Gut-Liver Axis Microphysiological System Fabricated by Multilayer Soft Lithography for Studying Disease Progression

Yang Jiandong

2023

Gut-Liver Axis Microphysiological System Fabricated by Multilayer Soft Lithography for Studying Disease Progression

Submitted by

Yang Jiandong

Department of Micro Engineering

In Partial Fulfillment of the Requirements

For the Degree of Doctor of Engineering

Kyoto University

Kyoto, Japan

2023

ABSTRACT

The microfluidic-based biomimetic cell cultivating system is termed as microphysiological system (MPS), an advanced *in vitro* model, which recapitulates human organ physiologically relevant conditions and demonstrates the mechanism of organ disease development. In particular, multi-organ MPSs with organ-to-organ communications, hold the potential for modeling disease progression. For example, the gut-liver axis (GLA)-MPS serves as the disease therapy evaluation model for non-alcoholic fatty liver disease (NAFLD) and disease progression, which progressively affects human health but doesn't have an available drug. However, in the previous GLA-MPSs with transwell inserts, there are issues with the interface between the macro-scale cell culture insert and the microfluidic flow perfusion. It is associated with the individual accessibility of physiologically relevant flow and disease progression research for two-connected organs. Furthermore, it has a low tissue-to-systemic liquid ratio, leading to insufficient GLA interaction due to the dilution of the large-volume circulating medium. To address the above issues, we use the multilayer soft lithography method to fabricate the microfluidic cell culture device at the wafer level and control the cell-culture microenvironment for compartmentalized treatment (mechanical stimulus and individual treatment for each organ) and organ-to-organ communication (GLA interaction) in an integrated device.

First, to generate the circulation flow between organs, microactuator-based-perfusion systems with pressure-driven microvalve or micropump were designed and characterized. For the microvalve, the three-dimensional fabrication process was optimized to fabricate a resist mold for the semi-round shape channel, which achieved a completely closed fluid path and flow control. For the micropump, an analytical model of a polydimethylsiloxane (PDMS) peristaltic micropump was developed. This model was based on fluid-structure interaction analysis and allowed the estimation of the volumetric flow rate as a function of an operating sequence of pneumatic actuation. Furthermore, the simulated results revealed that the micropump with nozzle-diffuser channel provided a higher pumping performance for medium recirculation in a complex microchannel network of MPS.

Then, to interconnect the GLA with flexible accessibility, a multi-sets microvalve system was fabricated via digital micromirror device (DMD)-based grayscale lithography and multilayer soft lithography, to control circulatory loop perfusion. By culturing the gut (Caco-2) and liver (HepG2) cells, the GLA-MPS could emulate *in vivo*-like GLA communications, containing cytokines and metabolites circulation flow. The initiation and progression of NAFLD could be investigated, which showed the NAFLD-like fatty acid accumulation phenotype with a cell apoptosis death and gene expression pattern. A protective effect of co-culture GLA interaction was presented, which indicated potential relationships in the further progression state of NAFLD.

Next, for mimicking the *in vivo*-like GLA physiologically relevant flow and investigating inflammation disease progression, we advanced the GLA-MPS with the multilayered structure and circulation flow, which allowed compartmentalized fluid shear stress (FSS) stimulus and individual treatment. The device was fabricated by multilayer soft lithography to integrate the compartmentalized cell culture chamber, PDMS porous membrane, circulation channel, and micropump. The flow perfusion with each organ's physiological FSS improved both cell functions (Caco-2 tight junction and HepG2 albumin marker expression) and induced the Caco-2 microvillus-like barrier structure. Furthermore, we observed that individuals treated gut with inflammatory bowel disease (IBD) could induce a progression of inflammation from the gut to the liver. This inflammation process recapitulated the underlying disease progression and mimicked the important initial step of nonalcoholic steatohepatitis (NASH) via GLA.

In summary, the developed GLA-MPS are more distinctive platforms than the previous GLA-MPSs in resembling physiological flow perfusion, closed-loop inter-tissue communications, and individual accessibility in an integrated device. The present device with disease progression model holds considerable potential for revealing new therapies and insights into the GLA interaction mediated by NAFLD and inflammation progression.

Contents

List of Figures

List of Tables

List of Abbreviations

ADME-T	Absorption, distribution, metabolism, excretion, and toxicity
ALB	Albumin
BoC	Body-on-a-Chip or multi-organ-on-a-chip
BSA	Bovine Serum Albumin
C_AM	Calcein AM
CFD	Computational fluid dynamics
DAPI	4,6-diamidino-2-phenylindole
DDM	n-dodecyl -β-D-maltoside
Dex	Dexamethasone
DMD	Digital micromirror device
DMEM	Dulbecco's modified Eagle medium
DMSO	dimethyl sulfoxide
EDTA	Ethylenediaminetetraacetic acid
ELISA	Enzyme-linked immunosorbent assay
ER	Endoplasmic reticulum
FBS	fetal bovine serum
FEM	Finite element method
FEA	Finite element analysis
FFAs	Free fatty acids
FITC-dextran	Fluorescein Isothiocyanate-Dextran
FSS	Fluid shear stress
GLA	Gut-liver axis
GLA-MPS	Gut-liver axis microphysiological system
HCA	High-content analysis
hPSCs	human pluripotent stem cells
Hst	Hoechst 33258
IBD	Inflammatory bowel disease
iGLC	integrated gut–liver-on-a-chip
iNOS	Inducible nitric oxide synthase
iPS cells	induced pluripotent stem cells
LPS	Lipopolysaccharides
MEA	Microelectrode array
MEMS	Micro Electro mechanical Systems
MPS	Microphysiological system
NAFLD	Non-alcoholic fatty liver disease
NASH	Nonalcoholic steatohepatitis
NEEA	Nonessential amino acids
OA	Oleic acid
OoC	Organ-on-a-Chip
P/S	Penicillin/streptomycin
PA	Palmitic acid

PAMPs	Pathogen associated molecular patterns
PBS	Phosphate-buffered saline
PC	Phase-contrast
PDMS	Polydimethylsiloxane
PET	Polyester, usually as PET porous membrane
ROS	Reactive oxygen species
STS	Staurosporine
TEER	Trans-epithelial electrical resistance
TNF-α	Tumor necrosis factor alpha
t-SNE	t-Distributed Stochastic Neighbor Embedding
ZO-1	Zona Occludens 1

Chapter 1 General introduction

1.1 Microphysiological system

"Microphysiological system (MPS)" or "Organ-on-a-Chip (OoC)" is the microfluidic-based *in vitro* cell-culture model, which is designed to mimic specific functions of human tissues.[1–4] For example, as shown in **Fig. 1-1a and b**, the lung on a chip[4], mimicked the lung breathing process on a microfluidic chip. Unlike conventional cell-culture models (such as T-flask and well-plate cell culture), the MPS incorporated the physiologically relevant cell culture environment, which included the mechanical stimulus, flow perfusion, molecular gradient, and so on. Microfluidic-based cell-culture models can be more predictive of *in vivo* biology owing to the dynamic cell culture environment control in the microfluidic system for cell growth, differentiation, migration, and maturation. Notably, they has been used in disease modeling for drug discovery. For example, the pulmonary edema disease was modeled on a lung-on-a-chip (**Fig. 1-1c**), showing the disease of inflammation, liquid leakage, and fibrosis for anti-inflammatory drug development.[5]

However, currently, most of the MPSs are single-organ systems mimicking one specific human organ. A single-organ system has the limitation of predicting drug absorption, distribution, metabolism, excretion, and toxicity (ADME-T). Therefore, compartmentalized multi-organ platforms with the circulatory system, known as multi-organ-on-a-Chip or Body-on-a-Chip (BoC) (**Fig. 1-1d**),[6–9] hold great potential for advancing drug development, and precision medicine, because they can mimic the blood flow in the human body with closed-loop culture medium by means of microactuators.[10] Such medium circulation recapitulates organ-organ interactions and helps emulate the dynamic exposure of organ cells to drugs and drug metabolites, offering valuable insights into systemic toxicity.[11–13]

Furthermore, the disease progression, time-dependent disease development and deterioration, is often related to multi-organ communications. These multi-organ MPS disease models may provide designed organ-to-organ communications for studying the disease progression. For example, type 2 diabetes involved blood glucose level, liver metabolism, and islet insulin adjustment. Thus, the liver/ islet on a chip could be used to model the progression of type 2 diabetes progression, for new therapeutic methods and drug development.[14] It proved the new crucial application of multi-organ MPSs. The concept of the disease progression model with organ crosstalks may be closer to the disease mechanism, which will be the next generation for disease modeling.

In addition, these devices are expected to replace animal models, which are often inaccurate in predicting human physiology. Even though the current animal disease model shows the *in vivo* relevant data, it involved complicated organ networks, hard for the disease mechanism study. Also, it takes time and money for a series of animal assays. Most importantly, the significant species difference between animals and humans potentially leads to misleading results, raising concerns about the reliability of the

data.[15,16] Instead, the application of MPS could provide a more reliable preclinical assay model, leading to reduced costs and time in pharmaceutical research and disease therapy development.[17,18]
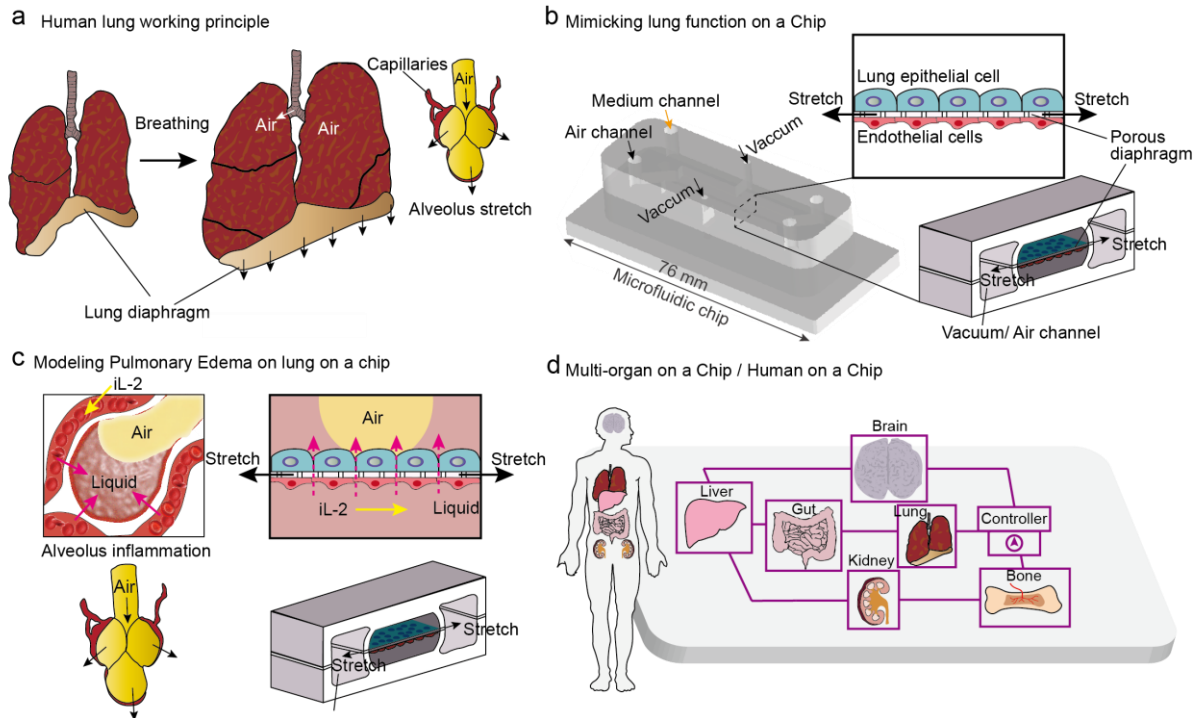
Figure 1-1 Organ-on-a-Chip and Body-on-a-Chip for modeling human organ-level function and organ-to-organ communications. (a) and (b) concept of the lung on a Chip, adapted from [4]; (c) concept of recapitulating pulmonary edema disease on the lung on a chip, adapted from [5];(d) concept of Body-on-a-Chip, adapted from [9].

To clearly understand the MPS disease modeling, several general features of MPS from the previous research domain are necessary. They can be divided into cell-culturing microenvironment control, multi-parameter monitoring, and multi-organ MPS, summarized as follows:

1) Cell-culturing microenvironment control

Fluid perfusion control: It is reported the reasonable fluid perfusion has a significant improvement in cell function[19] and differentiation[20]. However, high flow rate perfusion, inducing high fluid shear stress (FSS), is harmful to cells, especially hepatocyte-like cells, which do not receive flow directly.[21] Therefore, rebuilding physiological level FSS and perfusion is necessary for MPS to recapitulate *in vivo* organ state. To get the optimized FSS condition on the MPS, precise flow control can be conducted,

based on the micro actuators, such as the microvalve and micropump (**Fig. 1-2**). It can control the pico to microlitter fluidic perfusion.
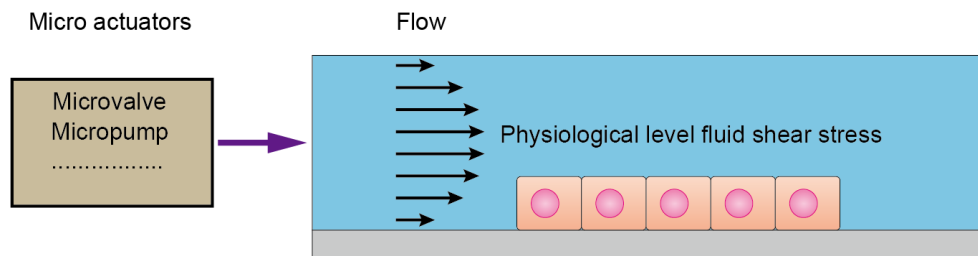
Figure 1-2 Concept of using microactuator to precisely control the fluid shear stress

Molecular transport control: One of the important fluid features of microfluidics is the laminar flow. It is easy to generate the two-phase interface during the stable and constant flow. For molecular transport, in this way, it could generate a concentration gradient to study the drug effect.[22] And it also could be designed with a well-mixing structure for molecular even distribution to increase cell-to-cell communications (cytokine molecular crosstalk) for the multi-organ system. Therefore, microfluidic cell culture systems have advantages in flexible control of cell culture molecular distributions.

Mechanical stress control: *In vivo* cells also experience mechanical physiological stimuli, induced by flow perfusion, liquid pressure, and cell-to-cell or substrate or extracellular matrix compression and stretch. MPS can be used to emulate the mechanical stress experienced by *in vivo* cells, allowing for the prediction of cellular response and the identification of key factors that improve cell function. For example, MPS device, fabricated from polydimethylsiloxane (PDMS) by using the microfabrication methods, can recapitulate cellular physiological levels stimuli, such as tensile stress and shear stress. [4,23,24] It rebuilds an advanced cell culture environment that mimics the *in vivo* phenotype and protein expression functions of cells.

2) Multi-parameter monitoring

High-content analysis and real-timing sensing: Traditional cell assay methods were a kind of end-point assay, which could not monitor the cell behavior and the detailed cells' reaction to stimuli. The microfabricated MPS device could utilize the Micro Electro mechanical Systems (MEMS) and semiconductor fabrication technology. It has the advantage of incorporating high-content imaging analysis (HCA) (e.g., high-speed single-cell profiles) and high sensitive electrode array, which could record the cell phenotype and function change in detail mode.[25,26] These points are important to improve the cell-based assay efficiency of MPS.

3) Multi-organ MPS

Organ-to-organ communication is an important part of the human inner environment system but is very complicated to study. Multi-organ MPS provided the opportunity for the designed organ communication system, such as the heart-liver communications for studying cardiac drug effect[27], and gut-liver communications for drug metabolism[28]. Currently, the connecting of multi-organ MPS mainly consisted of off-chip tubing[29], transwell-insert upper/bottom diffusing[30], and on-chip circulation[28]. Every method has its pros and cons. From the perspective of disease modeling, the on-chip circulation provides more intensified organ-to-organ communications with the possibility of a high-integration system.[31] Furthermore, the on-chip circulation has precise flow control and may emulate the *in vivo* drug distribution process.[32]

Overall, in this thesis, we will focus on the microfabrication methods to develop the multi-organ MPS device with the on-chip loop circulation system. In this way, a well-controlled cell culture microenvironment could be established to improve cell function and organ-to-organ communications for disease modeling.

1.2 Gut-liver axis for disease progression

Non-alcoholic fatty liver disease (NAFLD) encompasses a spectrum of conditions characterized by the accumulation of fat or lipids in the liver. Usually, the liver biopsy is the method to diagnose the disease. Accordingly, a fat amount of over 5% to 10% of the liver weight is identified as NAFLD. Recently, NAFLD has become an epidemic disease. It was around 20-30% of the adult population in the U.S. affected by this disease (**Fig. 1-3**). And 20% of NAFLD patients have liver inflammation,i.e. non-alcoholic steatohepatitis (NASH). It was mainly induced by the NAFLD progression. Because NAFLD is often referred to as a "silent" disease with no symptoms in the early stages, it can progress for years without causing any noticeable symptoms and is often not diagnosed until a more severe stage. NAFLD patients with NASH have a 15% risk of developing liver cirrhosis and further causing liver failure.[33] Therefore, fatty liver and NASH are important early stages for curing the disease. However, there is no available drug.[34]
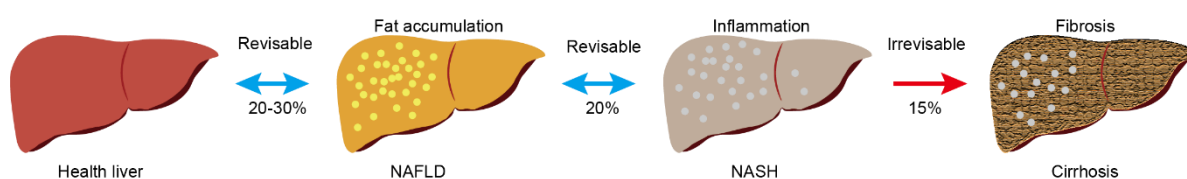
Figure 1-3 The NAFLD development and disease progression. NAFLD: non-alcoholic fatty liver disease. NASH: non-alcoholic steatohepatitis.

To develop the drug, in priority, it is necessary to setup models to understand the disease and design the drug evaluation method. In this research, the gut-liver axis model is discussed in detail. The gut-liver axis (GLA) plays a critical role in NAFLD progression, which is related to fatty liver and inflammation development.[35] This is because of their close relationship, termed GLA interaction.
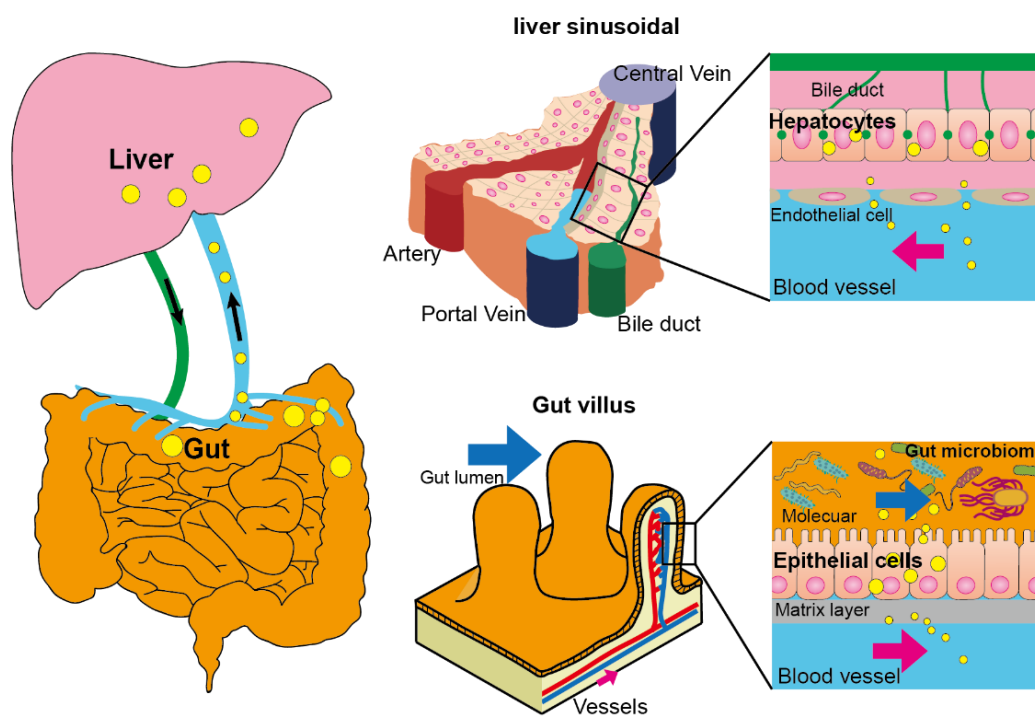
Figure 1-4 Gut and liver tissue structure and their interaction, termed gut-liver axis.

The GLA interaction is a bidirectional relationship in the human body (**Fig. 1-4**), and is important for human physical health.[36] In the GLA, gut epithelial cells, severing as a barrier against hostile external environments (e.g. gut microbiome and lipopolysaccharide: LPS), and are selectively responsible for nutrient absorption (e.g. lipids and free fatty acids: FFAs). For the liver, the liver parenchymal cells, hepatocytes, living in the space of Disse, are responsible for metabolism, detoxification, protein synthesis, and innate immunity.[37] In addition, the liver non-parenchymal cells, such as kupffer cells, sinusoidal endothelial cells and stellate cells, interact with hepatocytes to form liver function. Besides, the bidirectional relationship is established by the bile duct, portal vein, and blood systemical circulation which enables the transport of gut-derived products directly to the liver, and feedback of bile and metabolism secretion from the liver to the intestine. Hence, unbalance of the GLA interaction will cause diseases, such as obesity, non-alcoholic fatty liver disease (NAFLD), and inflammatory bowel disease (IBD).[38] The gut is strongly influenced by gut microbiota and dietary carbohydrates, and these may

accelerate NAFLD.[39–41] Inflammatory products, nutrients, and substances absorbed from food and microbiota via the intestinal barrier are carried by venous blood to the liver. In addition, products generated by hepatocytes are delivered to the small intestine. Thus, the gut and liver are closely interconnected, both physiologically and pathologically.

According to the multiple-hit hypothesis,[38] the GLA may be related to dietary modification and inflammation development (**Fig. 1-5**). For example, lipid accumulation in the gut may have a side effect on the fatty liver state. Also, the inflammatory gut has a further inflammation step to the liver, by pro-inflammation cytokines. Therefore, understanding the mechanism of GLA interaction is important for disease curing and new therapeutic drug development. But, there is a lack of methods to investigate their interaction and model the NAFLD progression on the GLA.
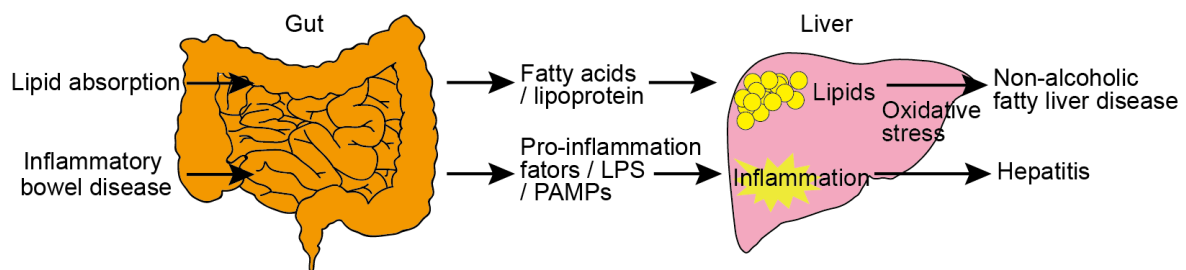
Figure 1-5 Gut-liver axis interaction for liver disease progression. LPS: lipopolysaccharides; PAMPs: Pathogen-associated molecular patterns.

1.3 GLA-MPS for disease modeling

In vitro disease model was important for investigating the disease mechanism and drug screening. However, the conventional *in vitro* model does not recapitulate many physiological processes of GLA, such as molecular transport, fluid shear stress, and gut-liver communications, resulting in poor predictions of disease progression and drug efficacy.[42] Therefore, there is an urgent need to find an efficient alternative method for the disease models, which should show human-related reactions with designed GLA.[43]

GLA-MPS recapitulates the GLA interaction on the MPS for disease modeling. For example, NAFLD could be modeled by administrating the free fatty acids (FFAs) in the gut, releasing the lipid to the liver, and observing the liver lipid accumulation (**Fig. 1-6**).[44]
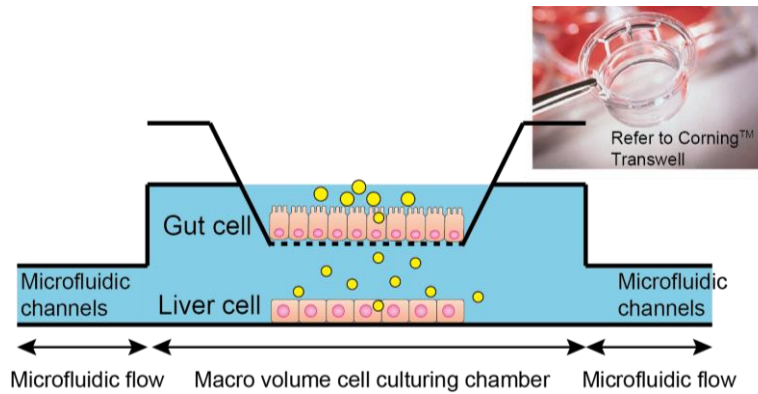
Figure 1-6 Previous gut-liver axis microphysiological system for modeling the free fatty acids transport from the gut to the liver. Yellow color molecular is the free fatty acids.

However, there are still left some issues for the previous GLA-MPS, such as microenvironment control and lower tissue-to-systemic liquid ratio with cytokine dilution,[32] leading to low GLA interaction. In addition, the GLA-MPS shall not only present the basic physiological initiation phenotype of gut and liver disease but also the GLA-MPS may reveal the pathological progression process from organ to organ by individual accessibility and treatment, which is crucial to understand the mechanism of NAFLD progression.

To overcome the above issues, this thesis reports a microfabricated GLA-MPS, by mimicking a physiologically relevant microenvironment and closed loop circulation (**Fig. 1-7**). First, the precisely controlled microactuators (e.g. microvalve, micropump) are set up for closed-loop circulation to enhance GLA interaction. Then, to obtain important insights into the GLA, a physiologically relevant flow perfusion with individual accessibility will improve cell function. Then, the *in vivo*-like structure and GLA interaction will be modeled in the device to present the process of disease progression.
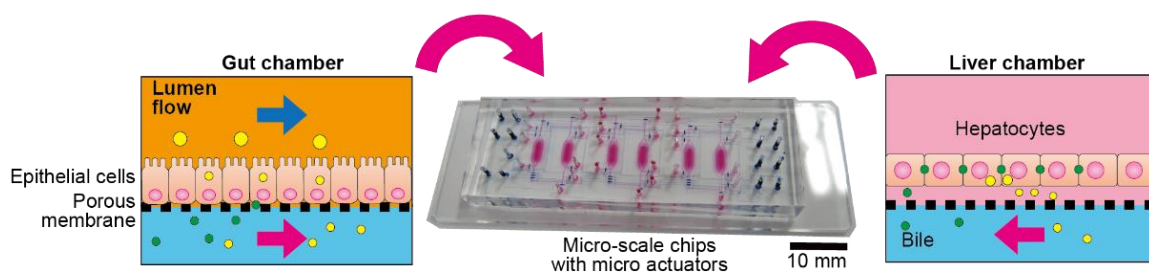
Figure 1-7 Concept of this thesis research contents 'Integrating gut and liver organs into the microphysiological system with micro-scale closed-loop circulation' [27,45].

1.4 Research objectives

The previous GLA-MPS for NAFLD modeling has not been fully accomplished in several aspects. For example, the physiologically relevant organ cell-cultivating microenvironment was not recapitulated. Also, a demonstration of the disease progression through GLA should be further investigated. In this study, we fabricated the GLA-MPS, by multilayer Soft lithography, and investigated the NAFLD and inflammatory progression via GLA, aiming to provide an advanced NAFLD disease progression model. To accomplish this goal, the objective of the thesis can be divided in detail as following steps:

First, in order to solve the issue of circulation flow control and microscale integration for GLA-MPS, we want to find a useful method to design the structures and microfabrication methods for the microactuators (microvalve and micropump). We will develop a simulation model of the finite element method (FEM), coupling fluidic flow and structure interface, to optimize the structure of the microactuators. To flexibly integrate each micro-scale component, the multilayer soft lithography shall be designed with multi-step fabrication.

Second, to solve the issue of GLA interaction, we will integrate the gut and liver cells in a designed circulation loop. We want to investigate the NAFLD initiation and progression via GLA, which provides improved gut and liver cell communications. This applies to investigating the GLA interaction during the NAFLD progression.

Third, to solve the issue of physiologically relevant flow stimulus and disease progression assay, we want to advance the GLA-MPS with a multilayered structure. We want to achieve individual flow accessibility to improve both organ cell functions. Also, we want to use individual treatment to observe the inflammation disease progression from one organ to another organ.

As the primary objective, we want to model the NAFLD and inflammation progression via GLA, which contributes to disease modeling and new drug evaluation.

1.5 Thesis outline

This thesis has 6 chapters (**Fig. 1-8**), including chapter 1 for a general introduction, chapter 2 for a review of previous MPS, chapter 3 for a fundamental theatrical analysis, optimization, and microfabrication of microactuators, chapter 4 and chapter 5 for GLA-MPS cell-based assay and disease modeling, and the last chapter of conclusions and insights for future works.

Chapter 1 is an overview of the concept of GLA-MPS devices, namely a brief introduction to the basic knowledge, including microphysiological system (MPS), gut-liver axis (GLA), and GLA-MPS. This chapter highlights the importance of GLA interaction for NAFLD progression and the need for GLA-

MPS modeling of NAFLD. Based on these motivations, the main objectives and structural arrangement of this thesis were specifically discussed.

Chapter 2 is a review of previous MPS development. In this chapter, the 20-year history of MPS was summarized. During this history, the MPS-disease models were developed since the year of 2012. The organ-to-organ communication model accounts for about 40% of the current disease model, which indicated the importance of multi-organ MPS for modeling the disease. Then, a review of previous microfabrication methods was introduced, with a focus on multilayer soft lithography. Finally, the mechanical stimulus from the flow of MPS was discussed. The case of porous membrane-based cell culture was mainly introduced. And the micropump for MPS flow control was also listed. In each part, the current state of this thesis' research was discussed by comparing it to previous studies.

Chapter 3 is a fundamental chapter for **chapters 4 and 5**. In this chapter, the pneumatic actuators, microvalve, and micropump were intensively investigated to meet the requirement of the MPS device. By finite element (FE) simulation of the diaphragm, the microvalve semi-round shape channel structure and working pressure were optimized. It was fabricated by grayscale lithography and multilayer soft lithography according to optimization results. For a specific closed-loop circulation MPS (**Chapter 4 device**), three microvalves could help generate enough circulation flow rate. Moreover, by simulating the three circular diaphragms' sequenced actuating and deformation, the micropump performance was analyzed. The flow volume was simulated with different conditions of hydraulic resistance, related to the microfluidic cell culture system. We found a diffuser/ nozzle channel works better than a normal straight channel in flow perfusion (**Chapter 5 device**).

Chapter 4 is the starting chapter of the discussion of the internal communication between the gut and liver, based on cell culturing and treatment. We utilized advanced grayscale lithography and multilayer soft lithography to fabricate the GLA-MPS with closed-loop circulation. By co-culturing the gut (Caco-2) and liver (HepG2) cells, we found their intensive communications via the HCA method and RNA-sequencing analysis. Also, these communications presented a protective effect against cell apoptosis death during the progression of non-alcoholic fatty liver disease (NAFLD) in micro-scale closed-loop circulation. Importantly, in this chapter, we also presented the *in vitro* modeling of NAFLD, which holds considerable potential for disease assay models.

Chapter 5 reports an advanced GLA-MPS, developed based on the device of **chapter 4** and **chapter 3**. By utilizing the multilayer soft-lithography, we fabricated a multilayered GLA-MPS. The device can achieve individual physiological flow perfusion for each organ in the cell-culture chamber, form barrier tissue structure on a porous membrane, and connect two organs with circulation flow. Furthermore, the inflammatory progression was presented via GLA interaction. It succeeded in generating an inflammatory bowel disease of the gut, then it had a further inflammation effect on the liver. This may be served as a disease progression model for the NAFLD of **Chapter 4**.

Chapter 6 provides a summary and conclusion of this work. We concluded the research of this thesis has contributed to enhancing the realism of the gut-liver axis model. And the developed disease model could help understand the importance of GLA interaction for NAFLD progression. It holds considerable potential for NAFLD therapeutic assay model. We also discussed the limitations of the developed devices. For the future works of GLA-MPS, the developed GLA-MPS devices could also be applied to other organ-to-organ communication systems. And to increase reliability, the integration of an electrode array for real-time cell state monitoring was discussed.
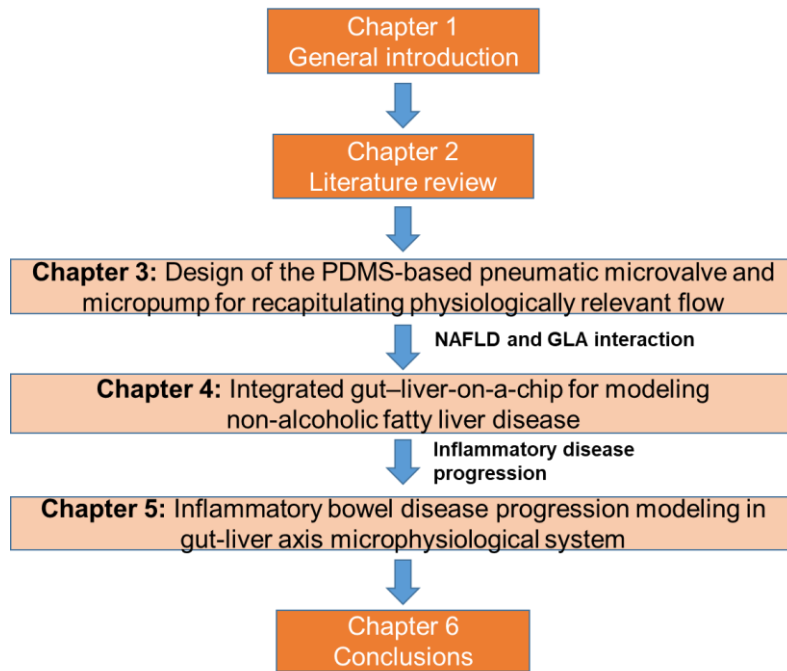
Figure 1-8 The structure and connections between each chapter of this thesis.

Chapter 2 Literature review

Microfluidics was a research field for manipulation or dealing with the flow in channels from 100 nm to 1 mm scale.[46] Over 30 years of development, microfluidics has turned out to be an important technology in diverse fields,[47] which are involved with the point-of-case device, droplet technology, multi-phase interface, and cell-based assay.[46] Especially, in recent years, microphysiological systems (MPSs) achieved high success as advanced *in vitro* pre-clinical assay models.

For MPSs, driving and manipulation of the fluidic flow for cell culture are the fundamental techniques. There are several available flow-driven methods of microfluidics, including electrokinetics,[48] thermal driving[49], electrical surface wetting[50], and pressure driving flow. Electrokinetics, such as electroosmotic flow[51] and dielectrophoresis[52], was widely studied in the minimized bioassay system. However, it has limitations in the application of biological cell culture, due to the electrochemical stability and joule heating issues.[53] Thermal driving employed the heat-dependent expansion or stress response of a material, which was limited by the high requirement of material, the low actuating flow rate, and the heating-cooling circuit.[54] Electrical surface wetting applied the electrolytic solution or surface charge forming a capacitive-like force to deliver fluid flow. It was typically used in droplet cases but was rarely used in biological cell culture.[55] The pressure-driving fluidic flow was the most common method for flow control. It could be transferred to a hydraulic equivalent system with high flexibility and reliability to control the complex microfluidic cell culture system.[56] Therefore, in this research, the flow perfusion for the MPSs was presented as the pressure-driven microfluidic flow.

In this literature review, we will review the emerging technology of MPSs and the current application for disease modeling on MPS. Also, the fabrication methods for the MPS were further discussed. Finally, a new sight into the porous membrane-based flow perfusion with related stress on cells and circulation flow for multi-organ MPSs was discussed.

2.1 The history of organ on a chip and MPS

The initial stage of the Organ-on-a-Chip (OoC) could be traced back to around 2000 (**Fig. 2-1**), with the development of 3D tissue perfusion culture. Linda G. Griffith et al developed the bioreactors array for 3D liver culture. The device was fabricated from a silicon scaffold.[57] Also, at the same time, polydimethylsiloxane (PDMS) started to become a widely used material for microfluidic systems.[58] Then, Michael L. Shuler et al developed the micropatterned cell culture analogs.[59] Paul J. Hung et al advanced the microfluidic cell bioreactor with high-throughput and continuous perfusion methods to the main long-term culture.[60] However, during this stage, the main work on the microfluidic cell culture was the high throughput cell culturing, due to the small scale and low consumption of the microfluidic system. After that, there was a growth of mimicking organ-specific flow perfusion structure on the

microfluidic cell culture system. The term biomimetic and artificial chip was incorporated. For example, Luke P. Lee et al presented the artificial liver sinusoid microfluidic chip with an endothelial-like barrier, for perfusion culture primary hepatocyte.[61] The real concept of 'Organ-on-a-Chip' was announced around the year 2010, the development of 'Lung–on–a–Chip', by Donald E. Ingber et al.[4] The chip was fabricated by soft-lithography of PDMS materials. The device mimicked physiological organ functions, such as lung-level breathing movements and proinflammatory activity. Also, another concept of 'human-on-chip' was described at a similar time by Hanry Yu et al around the year 2009. The multiple types of cells, fat, kidney, liver and lung, were co-cultured in a single microfluidic system, to study organ-to-organ communications.[62] Since that, the OoC achieved rapid growth. Later, in the year of 2013, 'Microphysiological tissue' was described on the microfluidic platform with larger-scale vascularized tissue arrays by Abraham P. Lee et al.[63] One important milestone of this stage was the application of human-pluripotent stem-cell-derived cell lines.[64,65] However, until the year of 2018, the idea of a 'patient-derived organ on a chip' for personalized medicine development was formed. On the other hand, Vernetti, L. et al developed a four-organ system, named 'Microphysiology System'. The intestine, liver, kidney proximal tubule, blood-brain barrier, and skeletal muscle were integrated into a single device.[66] At this moment, the idea of MPS was identified. With the development of MPS, the 'Body-on-a-Chip (BoC)' was formed by built-in micropumps with an internal circulation system. Long-term co-culture of human intestine, liver, skin, and kidney equivalents was succeeded.[10] These models could be used as pharmacokinetics (PK) models for preclinical trials.[67] Also, researchers recognized the importance of organ-to-organ communications for disease modeling. Furthermore, the traditional cell-based assay was an end-point assay. For real-time monitoring of the cell state, the electrode-based sensors were integrated into the MPS, by advanced MEMS technology.[68] Overall, the development of OoC or MPS technology has a trend to mimic the *in vivo* organ specific function, physiological conditions, and organ-to-organ communications, as the advanced *in vitro* model.

In this thesis, we focus on three points, the physiologically relevant cell culture, organ-to-organ communications modeling, and disease modeling. First, for disease modeling, providing a reliable disease model is the ultimate objective of this research. The new therapy development process should include a disease model for preclinical testing. The MPS of this research will make some progress in modeling the disease initiation and progression, severing as a considerable disease model for new drug and therapy screening. Second, for organ-to-organ communications modeling, a gut-liver axis system will be studied. The circulation flow, mimicking the human circulatory system, could be operated by on-chip micro actuators (e.g., microvalve and micropump). This reduces the circulation medium volume with a higher tissue-to-circulation liquid ratio, compared with the off-chip pumping system, leading to strengthening organ-to-organ communications. Third, the physiologically relevant cell culture can be regulated by microfluidic fluid control from a microfabricated cell culture system, including designed microchambers and channels. For a multi-organ system with designed distinct physiological perfusion

for each organ, individual assessability is taken into account by multilayered compartmentalized cell culture systems. This will improve the reliability of the MPSs.
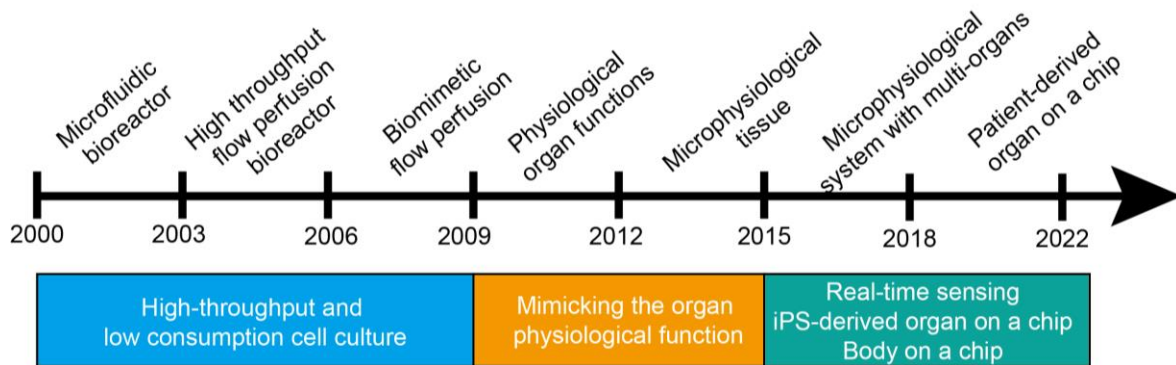
Figure 2-1 The development of the Organ-on-a-Chip and Microphysiological system.

2.2 Disease progression modeling on the MPS

With the development of MPS technologies, the application for disease modeling is gradually occupying the stage of history. The disease model is an important platform for investigating the disease mechanism and new therapeutic method development, particularly for modeling disease progression. Definitely, the danger of disease is always related to its progression, which is not 'silent' inside the human, but it will spread and change with time. Therefore, the disease progression model should include the initiation and progression (changing state) stage with the time-dependent axis.[69] It is vital to increase the disease modeling duration for understanding the disease progression and its therapeutic evaluation. However, the current animal model could not recapitulate the human disease, due to the species difference. It involved complicated tissue-crosstalks, leading to ambiguous disease progression data. Also, the high cost and ethics problems are growing issues for conducting the animal assay.[70] *In vitro* assay is an alternative method to overcome the complicated unwanted crosstalk happening *in vivo*. A well-designed *in vitro* model shall recapitulate the basic function of the human organ with human cell lines. The traditional two-dimensional cell culture model did not present high organ-level function in longer-term cell culture and failed in predicting disease progression. 'Human disease on a Chip' is an advanced technology to model the human disease progression on the microphysiological system (MPS), which shows a great achievement in revealing human disease mechanisms and organ-to-organ interactions.

Since the year of 2012, the concept of 'Pulmonary Edema-on-a-Chip[5]', the disease on a chip started to show great progress. **Table 2-1** lists the key MPS platform for modeling human disease. In only 10 years, there have been a lot of models, including lung, liver, kidney, vascular system, and brain for human disease modeling. For example, the SARS-CoV-2 infection were modeled to show the alteration of the blood-brain barrier.[71] From the trends (multi-organ disease model accounts for 40% of disease

models), we can conclude the organ to organ communications have become more and more important for modeling human diseases, such as fatty liver disease[72] and inflammation disease.[73] This is an important step to start studying the disease crosstalk progression.

Organ-to-organ communication is an important step for disease progressions, such as cancer metastasis[74] and nonalcoholic steatohepatitis (NASH) development[75]. The multi-organ MPSs with a circulation flow could mimic the *in vivo*-like organ-to-organ communications, which can be adopted for disease progression modeling. It may highlight the progression of the disease from one organ to another. It can be used to study their communication cytokines for disease mechanisms discover and therapy development. However, most of the listed disease models are mainly the initiation stage of the disease and demonstrate the relevant phenotype change. The involved mechanism was already well-known and did not show significant new findings for helping understand the disease. The progression stage was hardly investigated. For example, Gut-liver on a chip for hepatic steatosis[76] model presented the absorption of the gut via the gut barrier and lipid accumulation in the liver. However, there is no evidence to show the gut and liver interaction, also how this interaction affects the disease progression. Namely, is the co-culture of them have a positive direction for the disease progression or a negative direction for protective effect? A deep insight into liver disease progression were needed. Furthermore, the devices, which used the larger-scale Transwell insert and the microfluidic scale channel, were insufficient to induce the gut-liver interaction, due to dilution from low cell tissue-to-medium ratio in the bulk volume medium. Therefore, in this research, we propose modeling the disease progression via microfabricated multi-organ MPS with closed-loop circulation.

Table 2-1 10 years' development of disease modeling on MPS

Year	Name	Organ	Achievements
2012	Pulmonary Edema-on-a-Chip[5]	Lung	Inducing the pulmonary edema on the lung on a chip. Identification of the new therapeutics.
2016	Liver microphysiology platform[77]	Liver	The stellate cell was activated to elucidate fibrotic disease.
2016	Nonalcoholic fatty liver disease in a liver on a chip[78]	Liver	Mild liver damage with steatosis morphology
2016	Glomerulus-on-a-chip[79]	kidney	Glomerular mechanical forces increased glomerular leakage, which was observed in hypertensive nephropathy.
2017	Progeria-on-a-chip/ vascular on a chip[80]	vessels	Smooth muscle cells from iPS of Hutchinson-Gilford progeria syndrome patients showed an exacerbated inflammatory response to strain.
2017	Glomerulus-on-a-chip[81]	kidney	High glucose could induce critical pathological responses in diabetic nephropathy.

2017	Human pancreatic islets and liver spheroids on-a-chip[14]	Islets-liver	A functional feedback loop system between the liver and the insulin-secreting islet was demonstrated.
2018	Gut-liver on a chip for hepatic steatosis[76]	Gut-liver	The gut mimicked the absorption and the liver mimicked the accumulation of fatty acids
2019	Cancer metastasis-on-a-chip microphysiological system[74]	liver, lung, endothelial	Colorectal cancer enters the circulation system, preferentially home to the liver and lung constructs.
2019	Virus-induced kidney disease on a chip[82]	kidney	Pseudorabies-Virus-induced electrolyte regulation dysfunction in Na reabsorption.
2020	Gut-immune-liver microphysiological system[83]	Gut-liver	lipopolysaccharide (LPS) stimulated the inflammation response of immune cells.
2020	Lung-on-a-chip	Lung	The fibrosis-like transformation was modelled.
2020	Lymphatic vessel on a Chip[84]	vessel	Cyclical lymphatic flow of disease condition
2020	human blood-brain barrier[71]	endothelial	SARS-CoV-2 altered the barrier function
2021	Adipose model on a Chip[85]	Adipose	The device mimicked the insulin-resistant for adipose tissue.
2021	Human Nonalcoholic Steatohepatitis on a Chip[86]	Liver	Inflammatory and profibrotic markers were presented during NAFLD progression.
2021	Blood vessel/skin/liver/lung organ-on-a-chip[87]	vessel/skin /liver/lung	The jaundice disease model was established.
2021	Endothelium-on-a-Chip[88]	endothelial	Migration of T Cells was studied in the case of health and disease state.
2022	Human Liver-Islet Axis microphysiological system[89]	Liver-Islet	The liver and islet interaction of type 2 diabetes was modeled.
2022	Vasculature-on-a-chip[90]	vessel	SARS-CoV-2 infection was modeled.
2022	Interface-controlled-skin-on-chip[91]	skin	Propionibacterium acnes and sodium lauryl sulfate-induced inflammation process.
2022	Immune- skin-on-chip[73]	Skin-immune	Human HSV infection was modeled.
2022	Pancreas-Liver Crosstalk on a Chip[72]	Pancreas-Liver	Physiological timescales of glucose challenge were modeled for prediabetic hyperglycemia.
2022	Gut-liver-axis microphysiological system[92]	Gut-liver	Inflammatory bowel disease and gut-liver interaction were modeled.

2.3 MPS fabricated by multilayer soft lithography

The applications of microfluidics are dramatically growing, especially the above-mentioned MPS, and this development is indispensable for the advancement of chip fabrication technologies. At the beginning stage of microfluidics, the devices were usually made from glass-glass, glass-silicon, and glass-polymer.[93] They were fabricated by silicon-based MEMS processes and showed great interest in the minimized system. The application of microfluidic chips was limited due to the lack of optical transparency and flexible mechanical microactuator regulation. With the development of material science, polymer or plastic-based microfluidic system were attractive materials for the microfluidic device, due to integration friendly, optical transparency, biocompatibility, chemical stability, and mechanical properties.[58,94] Therefore, currently, the fabrication methods can be divided into prototyping and mold-free direct writing techniques (**Table 2-2**) at the laboratory level.[95] Prototyping methods generally need a replicable mold to get a designed microfluidic channel, followed by the bonding of each transferred layer, such as the soft lithography and injection.[96] Mold-free direct writing techniques are directly etching the microstructure or formation on the substrate, such as 3D printing and laser writing.[97] However, these methods may be combined, and also differ from laboratory to industry. For example, the PDMS material was widely used for the laboratory MPS device, fabricated by soft lithography. The mold was normally fabricated from photolithography. Conversely, due to the PDMS molecular absorption problem, the industry may use the thermoplastics for the fabrication of MPS device, by laser writing and thermal bonding. Therefore, a needs dependent fabrication is important for designing the MPS fabrication procress.

In this research, we want to control the microenvironment of the MPS device by designing the microstructures and on-chip microactuators. We utilize multilayer soft lithography for MPS device fabrication. By replica molding (mold fabricated based on the direct writing method), the cured PDMS can present the structure of the mold with high resolution.[58] With the development of microfluidic structure, a multilayer soft lithography is able to fabricate a three-dimension channels structure. Stephen R. Quake et al developed the monolithic microfabricated valves by sandwiching a PDMS diaphragm, which realized the microvalve and a microvalve pumping system.[96] Currently, by application of these techniques, a built-in micropump for MPS was widely developed.[27,98] It indicated a precise flow control could be realized by these microactuators. On the other side, a porous membrane is necessary for some epithelial or endothelial cells. It can be fabricated from PDMS (soft lithography) or PET (direct writing). To integrate into the MPS system, it was generated using the multilayer soft lithography and multilayer bonding method.[99] Recently, the compartmentalized cell culture of multi-organ MPS has become more and more important for individuals treating and culturing organ cells, which will solve the problem of co-culture medium.[100] The multilayer soft lithography techniques can generate a complicated structure for the MPS to realize the controlled cell microenvironment.

Table 2-2 The microfabrication methods for microfluidic chip (Adapted from Jing Wu et al[95])

	Methods	Advantages	Disadvantages
Prototyping method	Hot embossing[101]	Rapid replication microstructure, mass production	Only for thermoplastics, hard for 3D structure
	Injection[102]	Easy to fabricate 3D geometry, mass production, highly automated	Only for thermoplastics, high cost, difficult to form large undercut geometries
	Soft lithography [58]	Cost-effective, able to form complicated 3D structures, high resolution, good mechanical property	Material absorption, vulnerable to defect
Mold-free direct writing	3D print[97]	able to form complicated 3D structures, High throughput fabrication	Expensive, routine calibration, and diverse precision
	Laser writing[103]	Rapid, large scale	limited materials and precision
	Photolithography[104] X-ray lithography	High resolution, complicated 3D structure, MEMS fabrication, usually fabrication resist mold for Soft lithography	Difficulties in the master fabrication process and the clean-room facility were needed.

2.4 Microfluidic flow stimulus on cells

Owing to the development of microfluidics and related fabrication technologies, the microfluidic fluidic environment could be extended to the complicated environment with precise control by microscale structure and flow control units. Notably, this is very important in the application of microfluidic *in vivo*-mimicking cell culture platforms or MPSs. For example, the fluid environment of cells and the mechanical stimulus, such as shear stress and pressure, can be regulated by microactuators or external setups. Especially, currently, with the usage porous membrane cell culture method, fluidic perfusion is becoming a more physiologically relevant state. Therefore, in this section, the porous membrane-based cell perfusion methods and related stress are summarized (**Table 2-3**).

Generally, based on the cell culture methods, we divide them into four categories, static cell culture, flow perfusion[105], interstitial flow perfusion[106], and compression[107]. Inevitably, these cultural conditions may be combined with serval types of stresses.

Static cell culture is the traditional cell culture method, like cell culture on the Tranwell-insert. This method can get enough cell numbers for high throughput cell-based assay. However, as for epithelial cells, generally, due to the macro-culture space, it takes a long time (14-21 days) to form the barrier-like tissue. The open-well structure always causes variable optical interface and measurement results. Furthermore, the cells are a little different from *in vivo*-like polarized structures. A lot of functional markers are lower than in the microfluidic flow culture.[108]

Flow perfusion from a transverse direction is the most commonly used perfusion method. Cells experience fluid shear stress (FSS) during flow across the cell surface. The FSS value is directly proportional to the velocity of the surrounding fluid and viscosity. It was reported that flow perfusion increased epithelial cell maturation and function. It could improve the formation of *in vivo*-like tissue structures.[108,109] However, different tissue has own tolerance range of FSS. For example, the Caco-2 gut epithelial cell had a function improvement of FSS smaller than the 0.02 dyne cm^{-2}. The expression of protective mucus was highly upregulated.[110,111] On the other side, for the primary human proximal tubular epithelial cells, the FSS was much larger than the gut, it was evaluated as 0.2-20 dyne cm^{-2}.[105,112] The lower FSS could not induce full depolymerization of F-actin. In contrast, FSS above 1 dyne cm^{-2} accelerated the organization of F-actin.
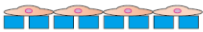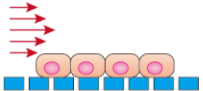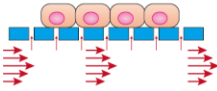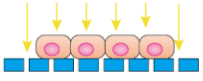
Interstitial flow perfusion is the flow penetrating across the extracellular matrix of tissues, cell-to-cell spaces, and porous membranes. The velocity is generally small than 4 µm/s.[113] Due to the tiny space, the FSS is hard to measure and evaluate. It depends on the tissue location and extracellular matrix. For the endothelial cell sprouting process, the FSS was around 10 dyne cm^{-2}.[114] However, for the cells, which did not experience flow perfusion directly, the interstitial flow FSS should be controlled as lower as possible. For example, the hepatocyte, the hepatocyte lived in the space of Disses (**Chapter 1**). The endothelial cells protected hepatocytes by forming a fenestrae structure on the outside of the liver sinusoid structure. The FSS was estimated smaller than 1×10^{-4} dyne cm^{-2}.[115] And the small FSS could improve hepatocyte functions.[116]

Compression is defined as the normal direction force on the cells. In the case of porous membrane cell culture, it could be generated by flow perfusion with pressure. The flow perfusion could generate compressive stress by flow perpendicular to the cell surface. For example, the liver bioreactor was developed to mimic the intra-abdominal pressure (0.09–0.9 kPa). The hepatocyte accelerated repolarization and formed cuboidal morphology. It maintained the hepatic functions for 14 days.[107] Also, for the hydrodynamic pressure or hydrostatic pressure,[63,117] endothelial cells were under compressive stress from 0 to 100 Pa in a microtissue chamber, which help generate vascular networks. This was applicable to form high throughput 3D vascular systems.

In this research, the fluid shear stress (FSS) is controlled on the fabricated multi-organ MPS device by individual accessibility. Because each organ has its requirement for the FSS or other stimulus, this

individual accessibility is important to functionalize the cells of each tissue, especially as above description the gut and liver cells. This research will be successful in reproducing the physiologically relevant flow on the multi-organ MPS.

Table 2-3 Microfluidic flow (directly or indirectly) stimulus on cells (on the porous membrane)

Culture method	Example	Stress type	Application example
Static cell culture		Cell-cell minor Compressive / tensile stress	Traditional cell culture/ simple.
Flow pefusion		Fluid shear stress	Improvement and maintenance of cell function [105]
Interstitial flow		Fluid shear stress Compressive stress (minor)	Angiogenesis / Cancer cell's invasion [106]
Compression (Flow pefusion/ Hydrostatic pressure)		Compressive stress (major) Fluid shear stress	Enhanced cell polarity and functions [107]

2.5 Circulation flow for multi-organ MPS

MPS with multi-tissue derived cells, connected by microfluidic channels were termed multi-organ MPS or Body on a Chip (BoC). To emulate human system circulation, a circulatory flow or medium crosstalk mixer was used to connect these tissues. Until now, there have been several methods for inducing medium communication between organs (**Fig. 2-2**). The traditional cell culture method was the transwell-cell culture with upper/bottom cell culture (**Fig. 2-2a**).[118] The medium crosstalk between multi-type cells was realized by molecular diffusing. The efficiency was worse when the static culture was used in the microfluidic channel. Also, small disturbances to the system could lead to larger variations or unrepeatable results.[32] Therefore, a circulation flow system was highlighted in the latter multi-organ MPS.

In the beginning, the circulation flow was driven by off-chip pumping systems[119] (**Fig. 2-2b**), such as peristaltic pump[119] and syringe pump[29]. However, it had the problem of complicated tube connections and enlarging the circulation medium volume.[31] It led to a higher systemic liquid-to-tissue ratio, which diluted the concentration of crosstalk cytokines in organs. Therefore, the on-chip micropump systems were developed with built-in micropumps. According to the actuating source, they could be divided into gravity-driven pumping[120] (**Fig. 2-2c**), magnetic/ piezoelectric micropumps[121] (**Fig. 2-2d**), and pneumatic micropump[10] (**Fig. 2-2e**). Both of these pumping methods have their pros and cons.

Magnetic/ piezoelectric micropumps and gravity-driven pumping were usually named valveless structures, working for simple and portable devices. But the pumping unit occupies most of the platform area and it had high bubble susceptibility. Especially, for the electric micropump components, the stable electrical resource was hard to keep in a relatively longer cell culturing time.[122] And for gravity driving, the circulation medium consumption was quite a lot. The pneumatic micropump was easily integrated into the multi-set parallel system and could actuate the circulation with several sets.[31,123] But it had a lot of accessory systems for compressed air actuating control, namely 3 to 6-phase sequenced loading or discharge of compressed air.[123]
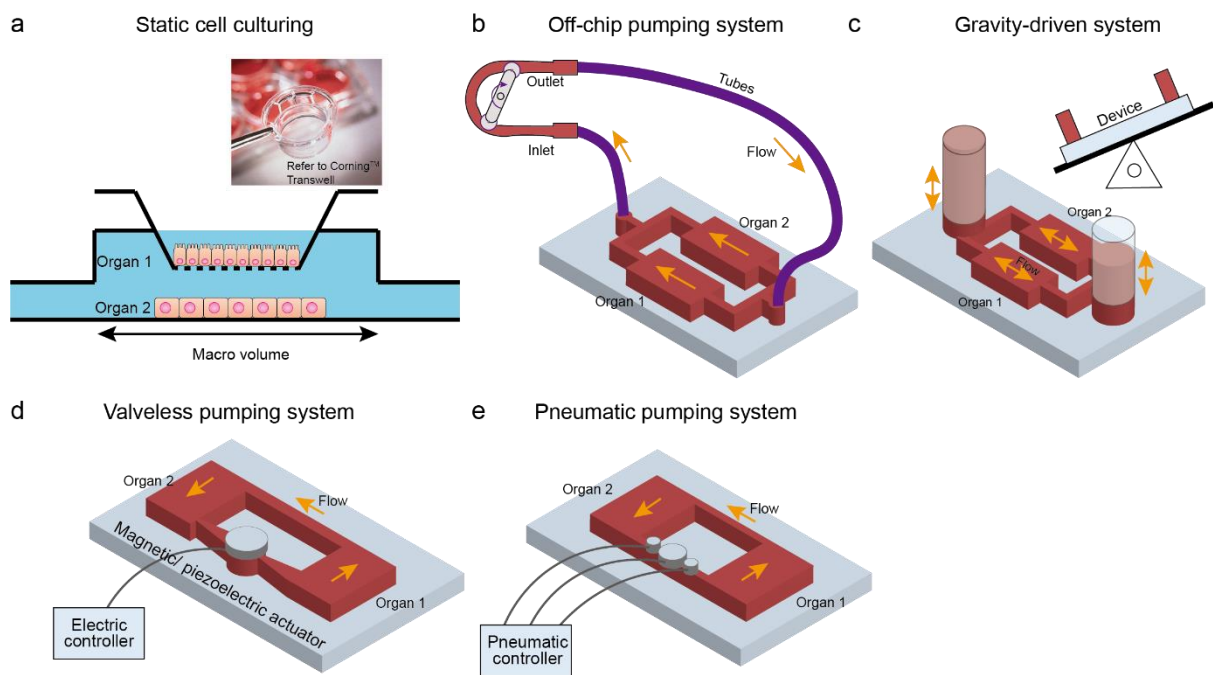
Figure 2-2 Generating multi-chamber medium crosstalks for organ-to-organ cytokine communications of multi-organ MPS. Adapted from [32,124]. (a) Transwell-insert static cell culture; (b) off-chip pumping system of the peristaltic pump; (c) Gravity driven system; (d) on-chip magnetic/ piezoelectric micropump; (e) on-chip pneumatic micropump.

To design and select the micropump for the multi-organ MPS circulation flow, several considerations shall be taken into account. First, the total system dimension is important to introduce the micropump and other components (e.g., cell culture chamber and channels). The biological experiment generally needs at least three duplicates or parallel sets. In the micro-scale MPS device, the pneumatic micropump is a favorable choice for system integration. Second, pumping performance was typically evaluated with the discharge pressure and flow rate.[125] A higher pump performance in the limited spaces (several square millimeters) shall be discussed, and the micropump design shall be optimized.

In this research, we employ PDMS-based pneumatic microactuators (e.g., microvalve and micropump), as the control and pumping unit. The size only ranges from 4×10^{-2} mm^2 (microvalve) to 6 mm^2 (micropump) with a small footprint. Therefore, a compact multi-organ MPS can be integrated into a single device. By using the computational fluid dynamics (CFD) simulation methods, the microvalve and micropump can be optimized in structure and actuating sequences for the application of MPS circulation flow. The developed system may work as a distinct unit for improving the reproducibility of the MPS.

2.6 Conclusions

In this chapter, the development of the MPS, MPS for disease progression modeling, MPS fabrication methods, the cell mechanical stimulus, and the micropump designs for MPS circulation flow were summarized and discussed.

From the development of MPS, we can find that physiologically relevant environment control and the application of disease modeling are becoming more and more important. Also, the concept of patient-derived organs on a chip holds great potential for personalized medicine, which will accelerate new drug development and disease therapeutic findings. The MPS disease model has a 10-year development and has shown great advantages compared with traditional methods. Especially, the multi-organ MPS disease model has proven the importance of organ-to-organ communications for the disease progression model. The MPS fabrication methods are advanced for more and more complicated three-dimension structures. By using multilayer soft-lithography, we can fabricate complicated multilayer structures. The mechanical stimulus and flow perfusion can be well-designed for precise cell culture microenvironment control. These technologies lead to control of the mechanical stimulus on cells. For the porous membrane cases, it helps cells form the polarized cell structure, and improve cell functions. Also, the on-chip micropump integration realizes the circulation volume reduction and scale-down for compact multi-organ MPS.

Overall, we will utilize the microfabrication method to fabricate the GLA-MPS with microactuators. We will also control circulation flow for organ-to-organ communications and the microenvironment for cell culture, especially the FSS and individual stimulus in the following chapters.

Chapter 3 Design of the PDMS-based pneumatic microvalve and micropump for recapitulating physiologically relevant flow

3.1 Introduction

Recently, the microfluidic cell culture platform, known as Organ on a Chip (OoC) or Micro Physiological System (MPS),[13,43] appeals to people's attention due to its advantages in recapitulating organ-specific culture environment and organ-to-organ communications.[27,126,127] It is expected to lead to reduced costs and time in pharmaceutical research and development, replacing the abuse of animal models.

One of the crucial points of the microfluidic cell culture platform is the fluidic control and driving for cell culturing, particularly for the circulation flow of a multi-organ system. In the early stage of microfluidic cell culture devices, the flow perfusion was realized by off-chip pumping systems[29], like a peristaltic external pumping system[119]. These systems were difficult to operate due to the tubes' connection and a higher amount of medium consumption. Then, the on-chip microactuators were developed for flow perfusion of the MPSs.[10] With the development of Micro Electro mechanical Systems (MEMS) fabrication technologies, the MPSs could be integrated with microvalve, and micropump for pressure-driven fluidic control,[128] by advanced microfabrication techniques. This improved function of MPS, for applying the physiological level flow stimulus on cells function and circulation flow to connect multi-cell culture chambers. Divided by actuating approaches, they could be pneumatic actuators[10], magnetic/ piezoelectric actuators[121], and gravity-driven actuators[120]. As the review of **chapter 2**, the pneumatic actuators were the widely favorite method for the MPS system circulation flow, because the pneumatic actuation method realizes large membrane deformation with an easily controllable hydraulic pressure and a small footprint than the other methods.[123]

In the MPS research domains, polydimethylsiloxane (PDMS) is still the main constructing material, with its good biocompatibility, elasticity, user-friendly practicability, and transparent property.[129] Therefore, PDMS-based pneumatic actuators are widely used for generating continuous fluidic flow for cell culture systems of MPS. The PDMS-based pneumatic actuators, coupled with several PDMS diaphragms driven by compressed air, can be divided into pneumatic microvalve[27,96] and micropump[98]. The microvalve controls the microfluidic flow routing, timing, and direction and is essential for multifunctional MPS devices. And the micropump is responsible for generating volumetric fluid flow on MPS,[130] especially the circulating medium flow for organ-to-organ communications.

The PDMS-based pneumatic actuators mainly consist of two layers, the flow perfusion liquid channel layer and the pneumatic pressure actuating channel layer, separated by PDMS diaphragms. For the

microvalve, there are mainly two types, check-valve[131] and Quake valve[96]. Compared with the check-valve, the Quake valve has the advantages of flexible flow control and simple integration. The Quake valve was widely used in the microfluidic system. The diaphragm was actuated by positive pneumatic pressure to close the flow channels, by the diaphragm contacting the liquid channel. The shape of the flow channel is important for sealing. For example, the rounded channel achieved a total close of around 40 kPa, but the rectangular would not completely close even above 200 kPa.[96] And for the micropump is generally composed of several microvalves or micro-pumping chambers with a sequencing actuating, for generating one-directional flow. The structure of microchamber size and diaphragm thickness affected the pumped flow rate. It was reported the circular shape chamber realized a much higher contact ratio, and was beneficial for the flow pumping.[132] Therefore, in this study, we focused on the Quake valve with a semi-round shape channel and micropump with circular chambers (**Figure 3-1**). From the viewpoint of single diaphragm actuating, the working principle of microvalve and micropump are similar to each other. A combination of investigation of them will be incorporated in this chapter.
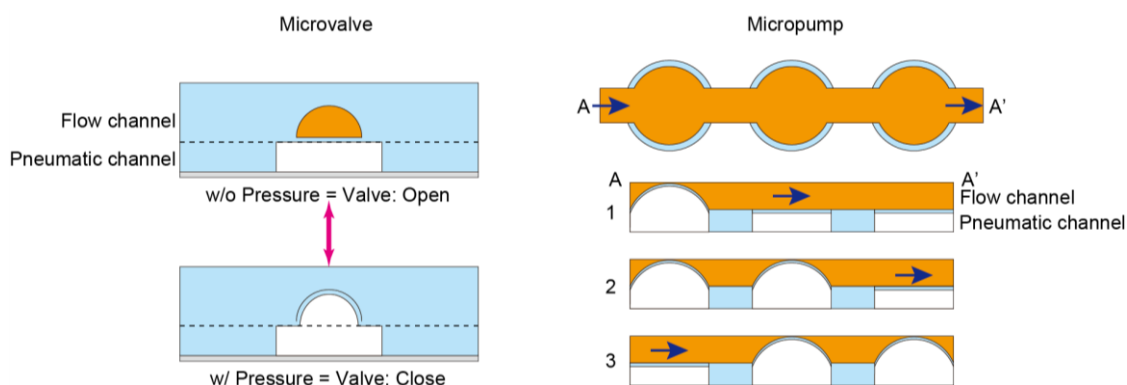
Figure 3-1 The illustration of PDMS-based pneumatic actuators from previous research. The Quake-type microvalve with a semi-round shape liquid channel; the micropump with a three-circular liquid channel and the same size diaphragms under 3-phase actuating.

Nowadays, fabricating controlled 3D microfluidic channel structures can be realized by digital-micromirror-device (DMD)-based grayscale lithography, with precisely controlled wafer-level scale.[133] The process parameters of grayscale lithography were gotten from a series process of optimization (**Appendix I Supplementary fig. S3-1**).[134] Furthermore, the coupling of pneumatic actuators and the microfluidic device is a crucial element for precisely controlling flow perfusion. A well-designed structure and actuating methods are necessary. To accomplish this work, an evaluation and design model is needed. Currently, with the development of computational fluid dynamics (CFD), researchers have established simulation models for finite element analysis (FEA) of the microvalve and micropump performance.[135–139] The studies of the pneumatic actuators' simulation of the diaphragm deformation were investigated from the configurations, response time, and contact pair.[136,140]

For the microvalve closing the liquid channel, to overcome the elements of birth/death in the contact area of the diaphragm, a high-viscosity region between the two contact surfaces was used, which reduced the calculation load.[137] Also, a high-resistance porous media mode was developed to solve the contact issues.[141] These models were avoiding the diaphragm contact, which more or less affected the microvalve dynamical function improvement. However, to obtain an optimized semi-round structure of the liquid channel with improved sealing properties, a three-dimensional contact analysis is needed. The diaphragm and fluid channel contact profile shall be used to optimize the fluid channel structure, which is applicable for practical usage.

For the micropump, a fluid-structure interaction (FSI) of finite element (FE) model was used to design the pumping chamber and diaphragm for flow volume estimation.[135] Similar to the microvalve, to reduce the calculation load, the contact of the diaphragm and flow channel was avoided in the simulation model. And, the micropump simulation model was estimated with single circular diaphragm flow volume generation.[142,143] The combination of three circular pumping chambers has little been investigated. One of the main obstacles was related to the conflict of backflow between each pumping chamber, i.e. obstacles of flow rectification,[144] leading to increased computational efforts. Also, the definition of phase sequencing and timing control was complicated during three diaphragm actuating.[123] Furthermore, a demonstration of pump capacity in a microfluidic system, like hydraulic resistance change, was a necessary factor for the complicated and variable microfluidic cell culture systems.[145]

Here, we analyze and characterize the performance of the PDMS-based pneumatic microvalve with a semi-round shape channel, modified from Quake's microvalve (**Fig. 3-2a**). Then, we characterize and design PDMS circular diaphragm-based micropump for higher pumping performance (**Fig. 3-2b**). This simulation model is based on fluid-structure interaction analysis and allows estimating the flow rate depending on the operation sequence of the pneumatic actuators, resulting in programmable medium recirculation in a complex microchannel network of BoC.
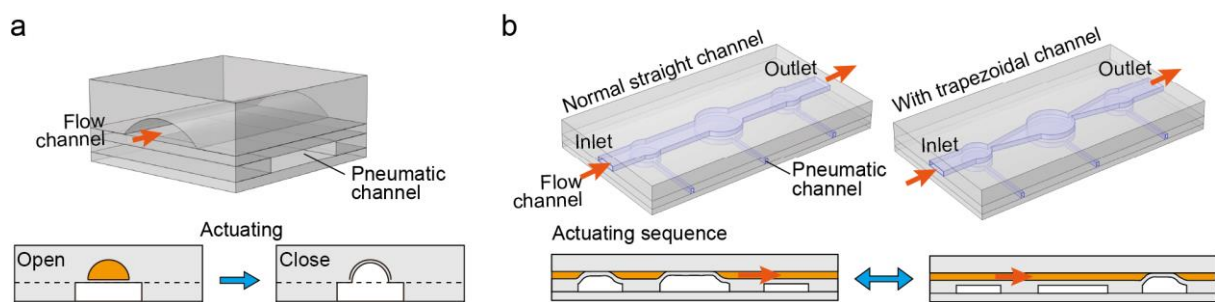
Figure 3-2 The conceptual illustration of the structure and actuating of the pneumatic actuated microvalve and micropump. (a) the microvalve with semi-round shape flow channel and actuating methods; (b) the micropump with normal straight channel and diffuser/ nozzle channel structure, and related working principle of the micropump in a two-phase actuating model.

3.2 Design and analysis of pneumatic actuators

3.2.1 Microvalve with semi-rounded channel

For the microvalve, the pressure was applied to the bottom pneumatic channel, which pushed up the diaphragm. Due to the semi-rounded shape of the flow channel, the deformed diaphragm can completely cover the flow channel. To achieve complete closure of the flow in a designed pressure, the shape of the rounded channel should be consistent with the deformed diaphragm (**Figure 3-3**). Furthermore, a well-matched structure has a larger occupancy ratio for flow driving.[27,146] The traditional microvalve rounded shape fabrication method mainly used the resist reflow method with uncontrollable shape.[96] To control the structure, wafer-level grayscale lithography was used to precisely fabricate the channel shape in this research.
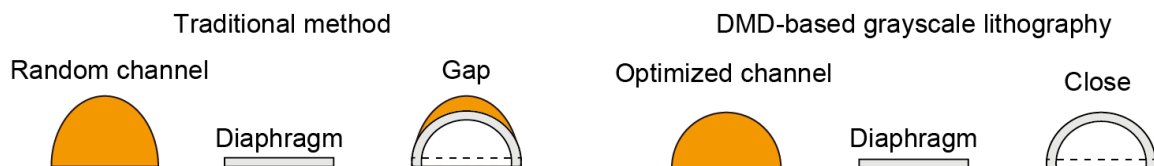
Figure 3-3 The structure of a semi-round shape channel for microvalve closing liquid channel in a designed pressure. DMD: digital micromirror device.

3.2.2 Peristaltic micropump and actuating sequence

The general pneumatic micropump consisted of three diaphragms, working in a peristaltic pattern (**Fig. 3-1**).[123] In this study, the micropump follows this classic design of three chambers with PDMS diaphragms (**Fig. 3-4a**). However, the actuating method is modified as two-phase sequences (**Fig. 3-4b**), based on the inertial mass difference micropump,[98] to reduce the actuating duration of one cycle and increase actuating frequency (one sequence actuating of three diaphragms), compared with **Fig. 3-1**. Namely, the center chamber size is larger than the two sides. When actuating two diaphragms at the same time, the response of deformation for the small diaphragm is faster than the big-size diaphragm, which makes a peristaltic movement pattern between two diaphragms in a phase pressure actuating (**Fig. 3-4b**). And coupling with another smaller diaphragm in phase 2, the flow could be continuously generated in one direction. Simultaneously, the purpose of this 'two phase' actuating method is also to simplify the actuating sequence, which reduces the efforts of frequency and pressure control from the pneumatic system. To be noted, here, the description of circular liquid channel shape was the same as the circular diaphragm shape.
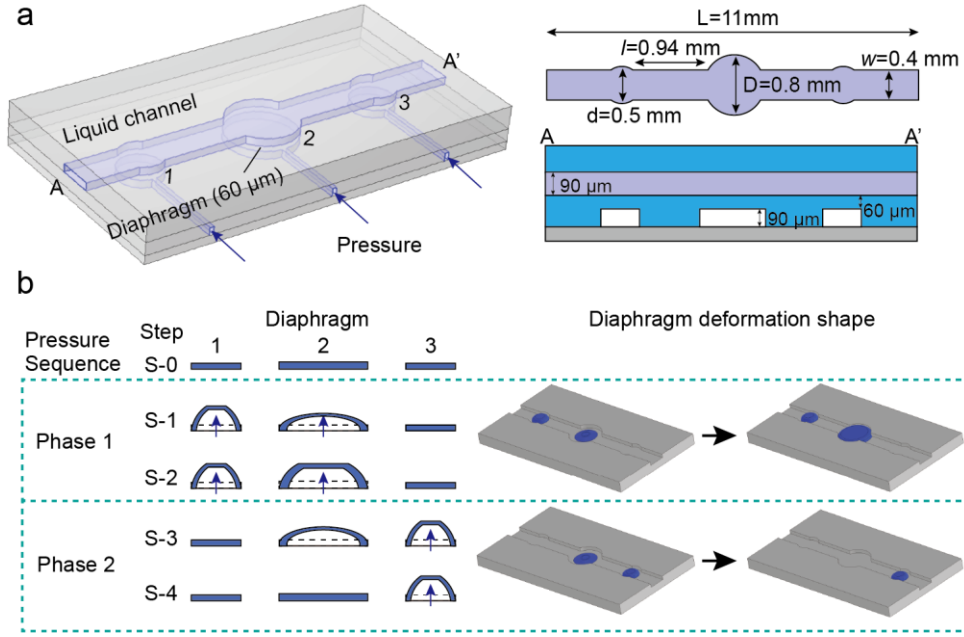
Figure 3-4 The illustration of micropump actuating in two-phase sequence mode. (a) Micropump structure and size; (b) micropump actuating sequence and diaphragm deformation shape. Note: the liquid channel shape was equal to the diaphragm shape.

3.2.3 Modeling the diaphragm deformation

To describe the nonlinear stress-strain characteristics of PDMS, a hyperelastic material model of solid mechanics in COMSOL Multiphysics (Ver. 6.0, COMSOL Inc.) was used in the analysis. A hyperelastic material model is a model in which the relationship between stress and strain is determined by a strain energy density function.[147] The Neo-Hookean model,[148–150] which is usually used for PDMS deformation analysis, was used in this study, as follows function.

$$W = \frac{1}{2}\mu(\overline{I_1} - 3) + \frac{1}{2}\kappa(J_{el} - 1), \qquad 3-1$$

where W is the strain energy density function, μ is the shear modulus, $\overline{I_1}$ is the invariant of the right Cauchy-Green deformation tensor, κ is the volume modulus, and J_{el} is the elastic volume modulus.

The shear modulus and volume modulus, which are constants in this function, can be obtained from Young's modulus and Poisson's ratio as follows equations.[147]

$$\mu = \frac{E}{2(1 + v)}, \qquad 3-2$$

$$\kappa = \frac{E}{3(1 - 2v)}. \qquad 3-3$$

Since PDMS is an incompressible material, Poisson's ratio is often set to 0.5. However, in the finite element method, if Poisson's ratio is set to 0.5, the denominator of the coefficient becomes 0 and the calculation cannot be performed. Therefore, a Poisson's ratio of 0.499 was used in this study.[151]

For the contact boundary setting between the deformed diaphragm and the upper surface of liquid channels, the penalty automatic method was used to model the contact conditions in case of spring with small deformation in the contact area.[152] The contact pressure in the normal direction is governed as follows equation.

$$T_n = \begin{cases} -p_n d_g & if \ d_g \ < 0 \\ 0 & if \ d_g \ \geq 0 \end{cases}, \qquad\qquad 3-4$$

$$p_n = \frac{E}{h_{min}}, \qquad\qquad 3-5$$

where T_n is the contact pressure in the normal direction, and p_n is the penalty factor. d_g is the gap (penetration) that is the distance between two existing contact nodes. E is the material Young's modulus. h_{min} is the minimum mesh size on the destination node.

3.2.4 Modeling the circular diaphragm-based micropump

For the fluidic dynamic analysis, it is difficult in dealing with the discontinuity of the fluid field for contact cases of the fluid-structure interaction (FSI), owing to the element of birth/death.[137] Therefore, to get smooth convergence of the flow simulation and reduce the computational effort, first, a contact analysis was used to simulate the diaphragm contact. Then, a liquid volume formed by the deformed PDMS diaphragm was converted into a cylinder with the same volume and height as the liquid channel (**Fig. 3-5a**). Finally, the fluidic simulation was converted into a 2D cross-section geometrical model of the micropump (**Figure 3-5b**). The diaphragm deformation process was equivalently simulated by the concentric circle that varies in radius.
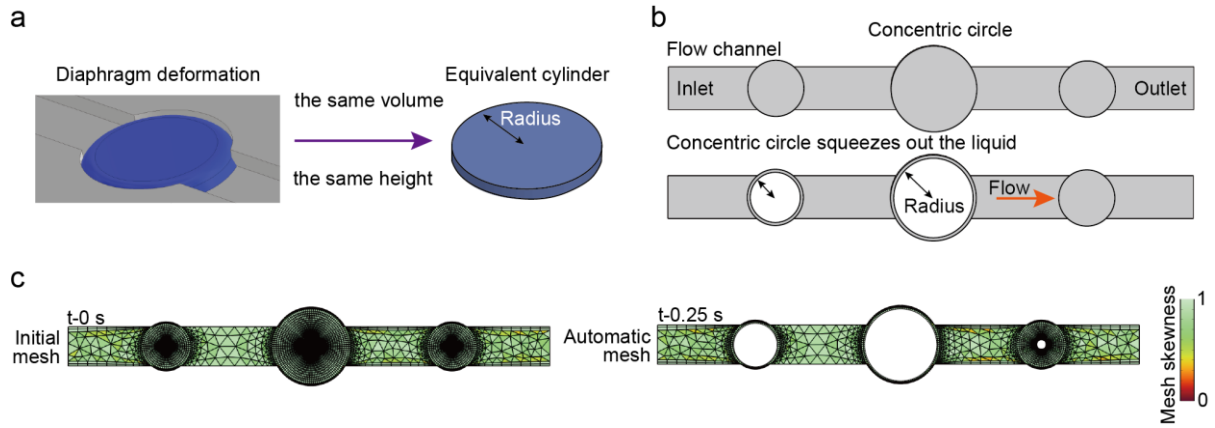
Figure 3-5 Numerical simulation model for the fluidic flow generation by three circular diaphragms. (a) The diaphragm deformation volume converting into a cylinder volume with the same volume and height; (b) the geometrical design and boundary setting of the simulation; (c) equivalent cylindrical circle radius change and auto-meshing methods for solving the deformed domain.

An auto-mesh function with normal direction moving mesh was used to mimic the three circular diaphragms suppressing the solution (**Figure 3-5c**). The equivalent circle radius change was used, which could be converted from the diaphragm volume change ratio (∂) of practical measurement as follows:

$$\partial = \frac{V_m}{V_{total}} = \frac{h \cdot S_c}{h \cdot S_{total}} = \frac{R_c^2}{R_{total}^2} \quad , \qquad\qquad 3-6$$

where V_m, V_{total} are the measured volume of the deformed diaphragm and the total volume of the micropump cylindrical chamber. h is the height of flow channels. S_c, S_{total} are equivalent cylindrical circle surface area of the moving mesh section and the cross-section surface area of the micropump chamber cylinder. R_c, R_{total} are the equivalent circle radius (moving mesh displacement) and the radius of the cross-section of the micropump circular cylinder.

Due to the micropump working in the low-frequency ranges in the microfluidic system, the Reynolds number (*Re*) was quite small. The flow could be calculated by the laminar flow module of COMSOL Multiphysics (Ver. 6.0, COMSOL Inc.).

The flow is assumed to be laminar Newtonian, viscous and incompressible flow without gravitation or other volume forces. And the Navier–Stokes equations in Arbitrary Lagrangian–Eulerian (ALE) formulation are used as the governing.[153]

$$\rho \frac{\partial u}{\partial t} - \nabla[-pI + \mu(\nabla u + (\nabla u))^T] + \rho((u - u_m)\nabla)u = 0, \qquad 3-7$$

$$\nabla u = 0, \qquad 3-8$$

where ρ is the fluid's density. u is the velocity field of the flow. p is the fluid pressure, I is the identity tensor. u_m is the mesh velocity due to the movement of the coordinate system, which was related to the time-dependent change of R_c. and ∇ is the differential operator with respect to the Eulerian coordinates. T is the absolute temperature.

And the inlet/ outlet was set as the open boundary. The original mesh size was physics-controlled finer mesh in deforming domain and coarser mesh in other parts. Due to the changing surface area, in the time-dependent solver, an automatic re-meshing was set with a Backward Euler consistent initialization (0.01 s), which kept the constant initial value.

The index of the pump performance was the pump flow volume and pumping pressure in the liquid channel by evaluating the pump against an external load. For the microfluidic system, the load mainly was the hydraulic resistance along the micro or nano scale fluidic channel. Therefore, the external hydraulic resistance was defined to represent the resistance, connecting two sides of the in- (R_{in}) and outlet (R_{out}) of the micropump (**Fig. 3-6**). A channel with two diffuser/ nozzle structures (nozzle angle θ: 0° - 30°) was designed into the micropump with the different liquid chamber (**Figs. 3-2b and 3-6**), which was typically designed in the micropump with the single liquid chamber to increase the flow rate.[121]
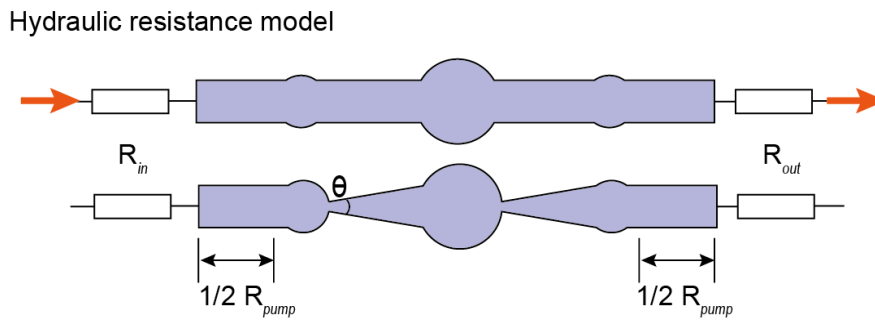
Figure 3-6 The simulation model for the micropump performance analysis.

To investigate the microfluidic flow for wide applications, a larger range of hydraulic resistance was taken into consideration. To clearly illustrate, the fluidic hydraulic resistance was simplified according to the below function with the initial hydraulic fluidic resistance of the inlet/out channel of micropump and resistance factor k.[56]

$$R = R_{in} + R_{out} = C_{geometry}\mu\frac{L}{A^2} = kR_{pump} \ (k \geq 1), \qquad\qquad 3-9$$

where R is the hydraulic resistance. $C_{geometry}$ is a geometric coefficient decided by fluidic channel shape, like $C_{geometry} = 12 \times (w/h)/(1 - (h/w) \times ((192/\pi^5) \times \sum(\cdots)))$ for the rectangular channel (h is the height of the channel, w is the width of the channel).[56] L is the length of the channel. μ is the fluidic viscosity. A is the surface area of the cross-section. R_{pump} is the original micropump hydraulic resistance of the inlet/outlet. For the present simulation model (**Fig.3-4** the sum of outlet and inlet channels-width 400 μm × height 90 μm × length 1 mm of viscosity μ 0.001 Pa·s), R_{pump} is estimated to be 8.23×10^{10} Pa·s/m³. k is the resistance factor to represent the magnitude of R resistance. When k=1, it means the micropump has no external resistance (empty load), the resistance is the micropump initial resistance of the simulation model.

3.3 Methods

3.3.1 Chip fabrication

The device was fabricated by using the multilayer soft-lithography method (**Fig. 3-7**).[154] For the microvalve, the round flow channel (perfusion layer) mold was fabricated by grayscale lithography. Generally, a positive resist (PMER P-LA900PM, Tokyo Ohka Kogyo) was spin-coated with a thickness of 45 μm on the wafer. Subsequently, digital micromirror device (DMD)-based grayscale lithography (DL-1000GS/KCH, NanoSystem Solutions) was performed using numerically optimized mask data[133] to achieve precise wafer-level mold fabrication (**Appendix I**). This allowed complete sealing of the microchannels with micro-valves and high-efficiency driving for the peristaltic micro-pumping system. And the pneumatic channel layer (control layer) mold was fabricated from a 30 μm thickness of negative photoresist (TMMR S2000, Tokyo Ohka Kogyo) and patterned by the standard photolithography method.

For the micropump, the resist mold was fabricated from a film-type negative photoresist (TMMF S2045, Tokyo Ohka Kogyo). The pneumatic channel layer (control layer) and flow liquid channel layer (perfusion layer) were 90 μm, which was controlled by the number of laminated sheets of TMMF. After UV exposure using a mask aligner (MUM-1000 Series, Japan Science Engineering)[155,156] with Cr- glass masks, the resist mold was patterned on the silicon wafer. For the development, the resist molds were put in a propylene glycol monomethyl ether acetate (PGMEA) solution (PM Thinner, Tokyo Ohka Kogyo) at 23 °C for 30 min.[155,156]

For the PDMS chip fabrication, the PDMS base and curing agent (Sylgard 184, Dow Corning) in a ratio of 10:1 were poured onto resist molds and cured at 25 °C over 48 h. The designed diaphragm thicknesses of the microvalve (20 μm) and micropump (60 μm) were tuned by spin coating to PDMS gel on the

control layer wafer. The perfusion layer was aligned and bonded on the upside of the control layer, after VUV surface activation (Min-Excimer SUS713, Ushio) in an oven at 80 °C for 2 h. Then, the peeled-off PDMS layers were bonded on the glass substrate and heated in an oven at 45 °C for 24 h.
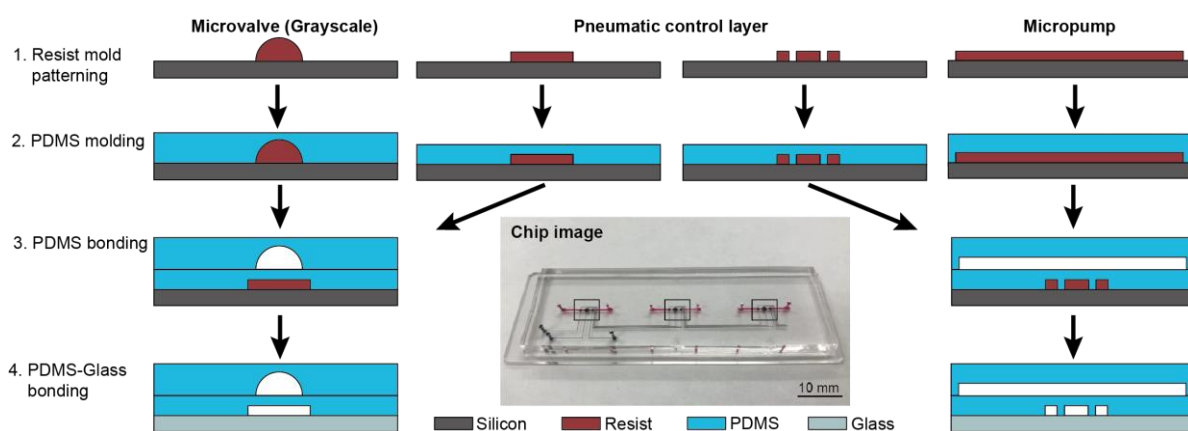
Figure 3-7 Microvalve and micropump fabrication process. Grayscale resist mold fabrication as described in **Appendix I**.

3.3.2 System operation and volumetric flow rate measurement

The experimental setup for microvalve and micropump actuating was shown in **Fig. 3-8a and b**. The pneumatic channel layer (control layer) was first filled with water to remove the risk of air bubble formation within the chips.[27] Then the chip was connected to the pneumatical control system. A solenoid valve was used to selectively actuate and release the pressure in the control layer channels. A LabVIEW program (Version 11.0, National Instrument Inc.) and NI cRIO controller board (National Instrument Inc.) were used to control the solenoid valve. The compressed air source was the control by the pressure regulator, which was connected to a mini-compressor (Anest Iwata Corporation). The pressure was released by directly opening the solenoid valve to the atmosphere.

The volumetric flow rate measurement (**Fig. 3-8c**) was realized by calculating the water-level moving in a Teflon tube (0.5 mm inner diameter, PILOT) with a designed time (5 min). Briefly, a water reservoir of a syringe shell (diameter 5 mm, TERUMO) was connected to the inlet of the chip by the Teflon tube. The outlet has also connected to the tube. A water head of the water reservoir was created at the beginning. Until the water level was not moving in the outlet tube. The system reached a balance to all the friction and capillary forces in the tube and chip channels. Then, the micropump was actuated and the water level moving distance in 5 min was recorded. Next, the volumetric flow rate was calculated as the mean flow volume of 1 min along the tube.

To characterize the flow velocity and performance of the microvalve and micropump, the microbeads (20 and 10 μm in diameter) tracing was used for visualizing the medium flow in the chip channel. Before

the experiments, the microfluidic chip was coated with 1% (w/v) bovine serum albumin (BSA, Sigma-Aldrich) in PBS for 2 h at 25 °C to prevent the nonspecific adhesion of beads on channels. The beads were suspended in a 1% BSA solution at 1×10^6 beads ml^{-1}; subsequently, a bead-suspended solution was introduced into the chip. The movement of the microbeads was captured using a microscope (GX53, Olympus) with a CMOS camera (Edomond Optics, 50 fps). The captured video data was divided by the imagJ software (Ver. 1.52a, National Institutes of Health) and analyzed in a program by Matlab (Ver. R2022a, MathWorks).
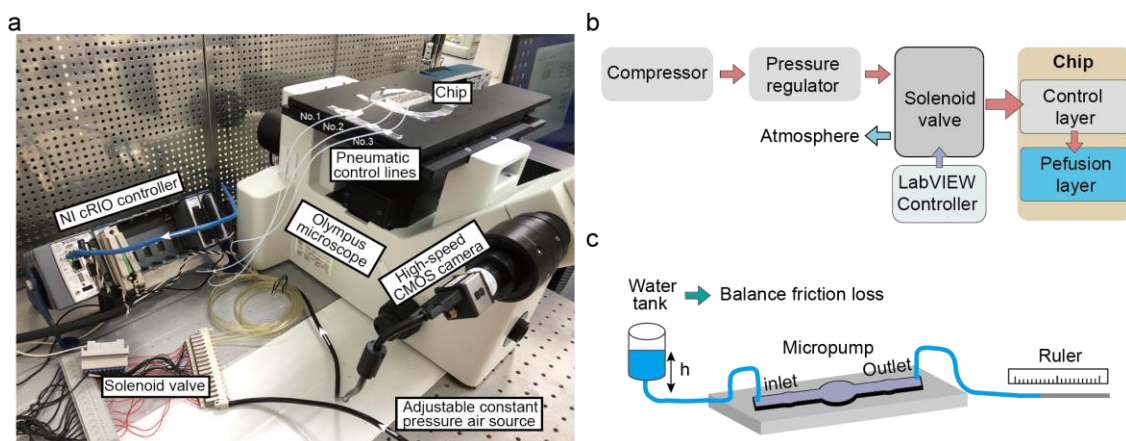
Figure 3-8 The experiment setup for the chip actuating and volumetric flow rate measurement. (a) the experiment system and equipment for chip evaluation experiment; (b) the control system for micropump actuating; (c) the principle of volumetrical flow rate measurement.

3.4 Results

3.4.1 The optimization of the semi-round shape channel

To design and optimize the semi-round shape structure of the microvalve, the validity of its pressure dependence on the diaphragm deformation was confirmed by the FEM results (**Fig. 3-9**), considering a contact analysis of the PDMS diaphragm deformation in the flow channel. The pressure of 50 kPa in the experiment agrees well with the pressure of 57 kPa in the analysis where the deformed PDMS starts to seal the 44.1 µm flow channel (**Figs. 3-9 a and b**), due to the fabrication error. But it could not completely close the channel, leaving a small gap. Instead, the 65 kPa has much better working performance. In addition, the flow channel of the valve was fully deformed at pressures over 140 kPa in the analysis, resulting in maximum diaphragm deformation (**Fig. 3-9c**). According to the simulation data, we refabricated the microvalve device by optimized grayscale lithography process (**Fig. 3-9d and Appendix I**), with a 45 µm height round flow channel and 200 µm ×200 µm diaphragm surface area. The photoresist mold profile of the fabricated microvalve was measured using a mechanical stylus profiler (Dektak XT-S, Bruker), which agreed well with the target profile of the 65 kPa simulation

diaphragm profile (**Fig. 3-9e**). However, the error between the measurements and FEA results, albeit small, may have resulted from the material properties of the PDMS. For example, Young's modulus of PDMS can vary from 50 kPa to 4 MPa depending on the process conditions.[149] The microvalve became less stable when the pressure was below 100 kPa. Therefore, a pressure of 150 kPa was generally selected because achieving a constant and reliable microvalve full deformation for sealing is important, particularly when integrated into MPS devices has high backflow pressure.
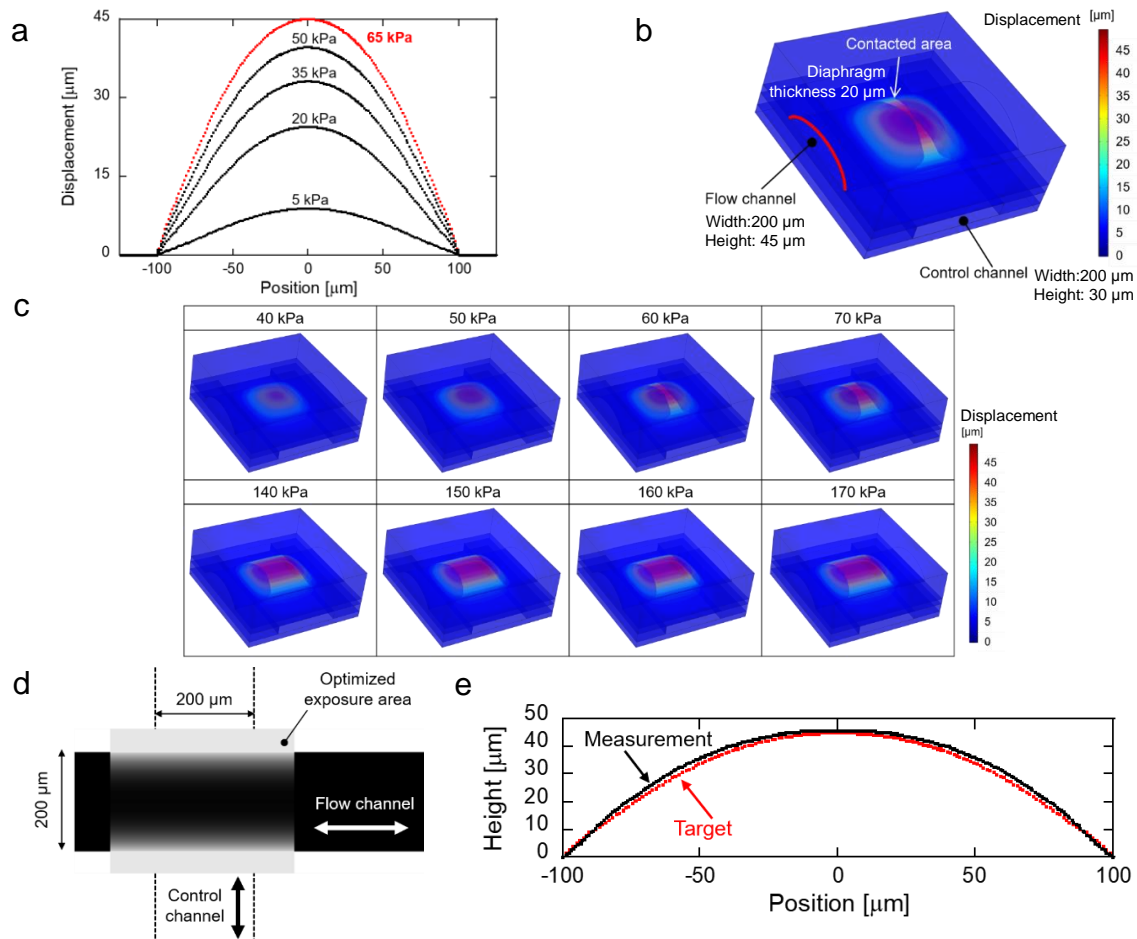
Figure 3-9 Characterizing the semi-round shape microvalve actuating. (a) The simulated cross-sectional profile of the deformed PDMS diaphragm. (b) 3D profile of the PDMS diaphragm deformed at a pressure of 57 kPa, which started to seal the liquid channel with a height of 44.1 μm. (c) Simulated 3D profiles of deformed PDMS diaphragm contacting the flow channel. (d) Optimized grayscale pattern for semi-round shape microvalve flow channel; (e) Comparison between the stylus measurement of fabricated microvalve and the target profile of 45 μm under diaphragm deformation of 65 kPa.

3.4.2 Three microvalves for interstitial flow pumping

The developed microvalve could successfully close the flow channel, as described in the previous section. Furthermore, the three connected microvalves with a sequencing actuating could also generate

a designed directional fluidic flow (**Fig. 3-10a**).[96] The driving pressure and actuation frequency of cyclic operation are two key factors affecting the performance of the microvalve pump. In the previous description, under 150 kPa, the diaphragm of the microvalve could achieve full deformation with smooth actuating. Therefore, we measured this microvalve working performance under 150 kPa. We measured the microbeads' movement path and related time, for calculating the flow rate. The flow rate shows a consistent trend with the driving frequency and almost linearly increases with the frequency until it reaches a peak value of 63.0 nL/min at a frequency of 3 Hz (**Fig. 3-10b**).

For the microfabricated MPS device with a total loop medium of 3 µl,[27] when pumping at 15-20 nL/min, this system has a flow velocity perfusion of nearly 1 µm/s (termed as an interstitial flow). And the closed loop circulation would obtain a total medium exchange within 3.3 min. Notably, this pumping performance is sufficient for recapitulating and enhancing the metabolite interaction of multi-organs MPS in this study (**Chapter 4**).
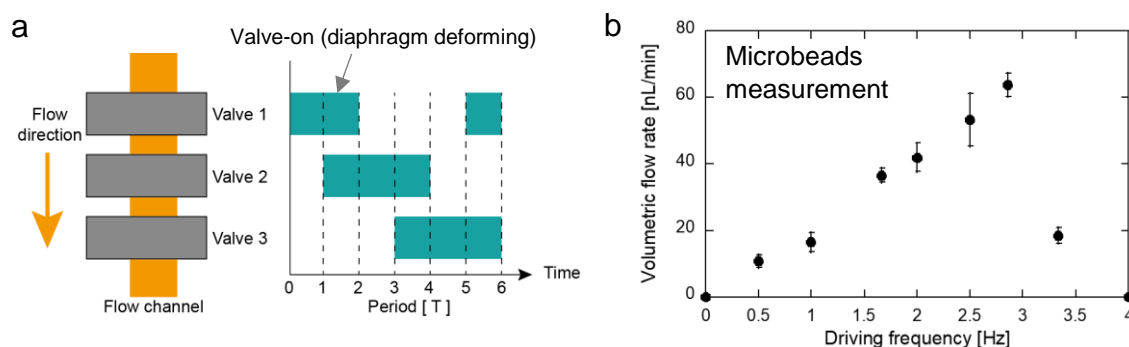
Figure 3-10 Microvalve for pumping the interstitial flow with nanoliter range. (a) Schematic illustration for the sequence of the microvalve pump actuation and intervals of actuation time for each solenoid valve. (b) The measured volumetric flow rate of the medium flow in the closed-loop MPS device[27] operated using the integrated three-connected microvalve under 150 kPa pneumatic pressure.

3.4.3 Modeling volumetric flow by three circular diaphragm-based micropump

The three microvalves set for flow pumping can generate a one-directional flow, however, it could not provide a larger range of the flow rate. Furthermore, in some cases, a simplified microactuator provides more reliable working performance for the MPS. [127,157,158] Therefore, we continue to analyze the micropump with different sizes of the circular diaphragm for flow perfusion.

For the micropump actuating process, the deformation volume of the circular diaphragm is one of the foremost elements for the micropump flow generation. The diaphragm deformation volume was equal to the squeezed liquid volume in the chamber. In this micropump, the diaphragm was deformed and attached to the upper surface of the fluidic channel, but it did not cover all the flow channels (**Fig. 3-**

11a). This deformed diaphragm profile was closed to a truncated cone shape. With the increase of applied pressure in the control channels, the big diaphragm started to attach to the liquid channel surface at around 10 kPa (**Fig. 3-11b**), and the small diaphragm was around 50 kPa. The simulation data (E=1.4 MPa) was consistent with the measurement data. Then, we measured the diaphragm deformation profile and calculated the volume formed by the deformed PDMS diaphragm (**Fig. 3-11c**). From 0 to 150 kPa, all the diaphragms' deformation volumes increased. But there is not so much difference between 150 kPa and 200 kPa. It indicated the 150 kPa would be close to the peak value for the currently designed dimension of the micropump.
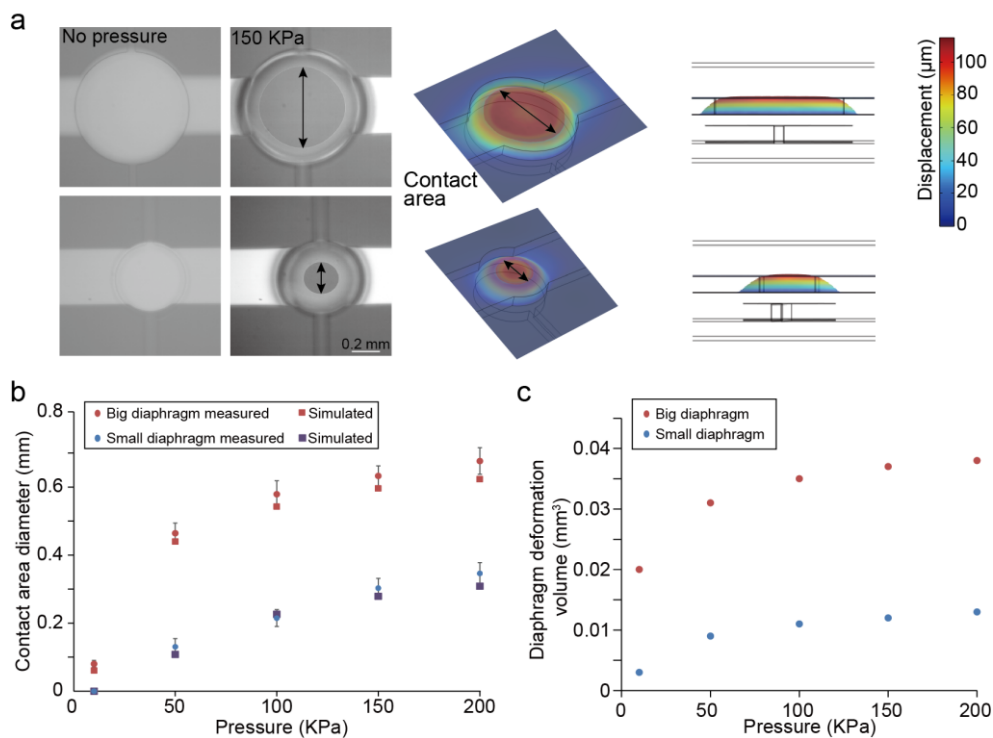
Figure 3-11 Measuring and analyzing the big (*D*-0.8 mm) and small (*d*-0.5 mm) diaphragm deformation and contact with the liquid channel upper surface. (a) the two diaphragm deformation and contact profiles from measurement and simulation results under 150 kPa pressure; (b) the measured and simulated (*E*=1.4 MPa) results of diaphragm contact area diameter; (c) the two diaphragm deformation volume dependent on the applied pressure.

In the fluidic simulation for micropump, the pushing down and up actuation of the diaphragm caused the fluid field to be changing between with and without continuity, which increased the FEA calculation effort and could not get convergence. Therefore, a 2D simulation model was developed. The top view of the micropump was taken into calculation. Due to the deformation profile of the diaphragm being closed to a truncated cone shape, the deformed diaphragm in the top view is a circle. The diaphragm deformation process can be thought of as a growing circular boundary to squeeze the liquid in the chamber (**Fig. 3-5**). Therefore, an equivalent volume sweeping of the diaphragm was converted to a

cylinder with the same volume and height. Namely, the diaphragm deformation volume in the liquid chamber was calculated and transformed to the change by a cylindrical circular interface with the same height (**Fig. 3-5**). Based on the aforementioned **equation 3-6 and Fig. 3-11c**, we got the radius value (**Table 3-1**).

Table 3-1 The cylindrical radius magnitude changing with applied pressure

Pressure (kPa)	50	100	150	200
D-0.5 Big-diaphragm radius (mm)	0.331	0.352	0.362	0.367
d-0.5 Small-diaphragm radius (mm)	0.178	0.197	0.206	0.214

The diaphragm deformation time-dependent manner is another crucial factor for the micropump actuating. In this study, the diaphragm push-up motion was realized by applying pressure, and the push-down motion was realized by its elastic property. Then, we measured the diaphragm deformation duration. The time consisted of pneumatic actuating time and diaphragm recovery time, which were related to the applied pressure (**Table 3-2**). It is also necessary to be noted that the recovery time was also depending on the adhesion force of the contact area. Here, we fixed the surface condition of the diaphragm and liquid channel, and the adhesion conditions were fixed. Furthermore, the small size diaphragm responded much faster than the big diaphragm. The two-phase sequence actuating could generate the peristaltic pattern movement. Notably, the duration represented the diaphragm actuating limitation range. For example, under 150 kPa, the big diaphragm takes about 0.63 s to finish a phase of actuating and recovery. If the pneumatic actuating period was faster than this diaphragm duration, the overlapping phenomenon would happen, and the diaphragm could not work under total deformation or recovery, which may reduce the generated flow by the micropump.

Table 3-2 The diaphragm deformation duration

Big-diaphragm (D=0.8 mm)			Small-diaphragm (d=0.5 mm)		
Pressure (kPa)	Actuating time (s)	Recovery time (s)	Pressure (kPa)	Actuating time (s)	Recovery time (s)
50	0.22	0.24	50	0.06	0.06
100	0.24	0.34	100	0.11	0.11
150	0.26	0.37	150	0.14	0.14
200	0.27	0.40	200	0.14	0.14

We combined the interface radius change (**Table 3-1**) and the diaphragm actuating duration time (**Table 3-2**) in an FEA model to simulate the micropump actuating and drive the fluidic flow. Based on the above measurement, we set up step radius functions for each diaphragm (**Figs. 3-12a and b**). The y-axis (radius change) and x-axis (time) of the step function were consistent with the corresponding data in **Table 3-1** and **Table 3-2**. In this way, we could simulate the micropump working with frequency and pressure dependence. First, the normal micropump with the same size pumping liquid chamber was

working under 3-phase actuating (**Fig. 3-1**). It was simulated as shown in **Fig. 3-12a**. Then, for the different size liquid chambers (different size diaphragms), the 2-phase actuating simulation was shown in **Fig. 3-12b and c**. It also modeled the diaphragm over-lap situation in this simulation. It demonstrated the three circular diaphragm deformations were simulated to drive the liquid flow. And this model could be used to study the micropump flow generation in the following sections.
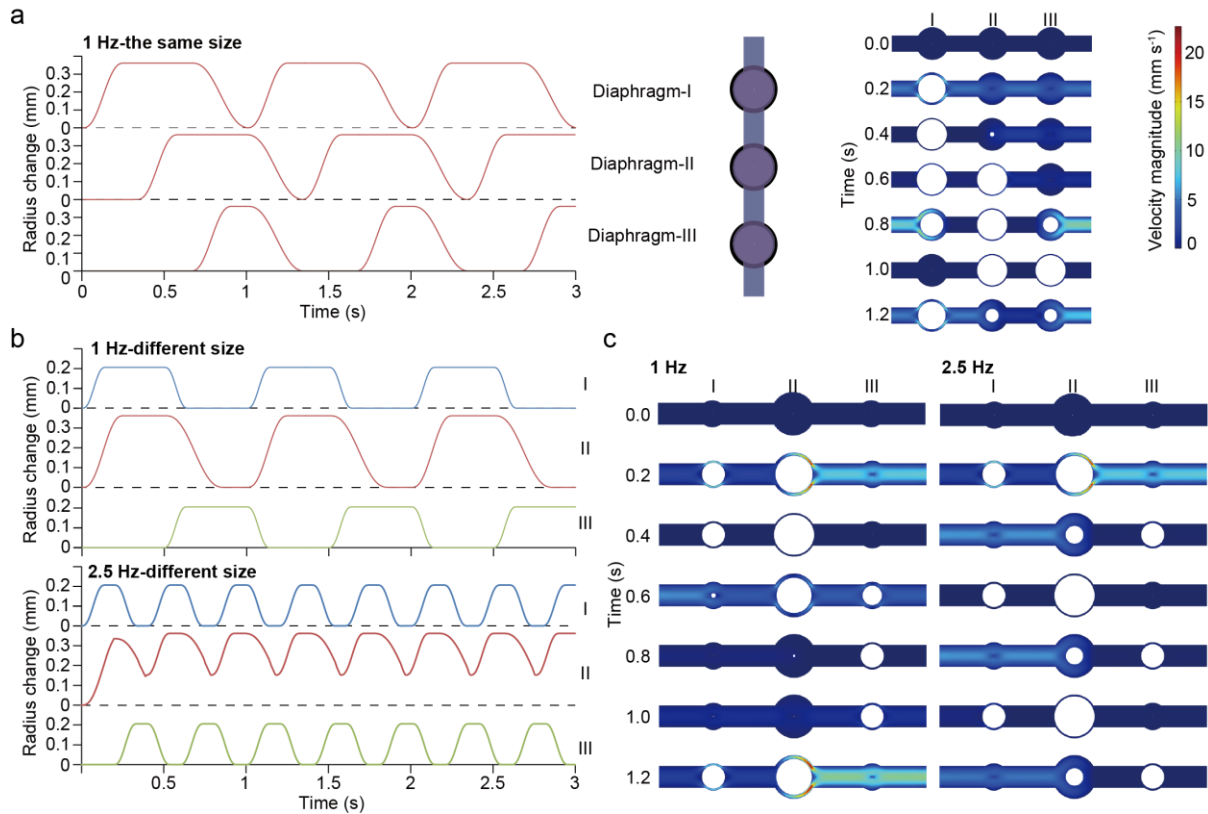
Figure 3-12 Simulating the three-circular diaphragm to drive the liquid flow. (a) simulating the flow velocity generated by a normal micropump with the same size liquid pumping chamber and 3-phase actuating (**Fig.3-1**) in 1 Hz frequency under 150 kPa pressure. (b) the radius function of three micropump diaphragms with different size liquid pumping chambers in 1 Hz and 2.5 Hz frequencies under 150 kPa pressure; (c) Simulating micropump with different size diaphragms driving the fluidic flow in one-single period cycle under 1 and 2.5 Hz with 150 kPa pressure actuating.

3.4.4 Characterizing the pumping performance

To characterize the micropump performance, we evaluated the parameter of pumping performance, namely the micropump-generated flow volume and flow pressure in the liquid channel. To begin with, pneumatic micropumps with the same size liquid chamber volume (straight channel ɵ=0°, all diaphragm diameter: 0.8 mm) were analyzed (**Fig. 3-13a**). In the simulated results of the micropump with the same size liquid chamber under the three-phase actuation mode (**Fig. 3-1**), the maximum flow volume of 2.02 µl/min was obtained at the frequency of 1 Hz when applying the pressure of 150 kPa; however, the flow

volume dropped to 1.03 μl/min at the frequency of 1.5 Hz. In contrast, the different size diaphragms could be used for two-phase actuation, owing to the inertia mass,[92] to improve the micropump flow rate. Accordingly, the volumetric flow rate of the micropump linearly increased to 3.79 μl/min under the same frequency and pressure conditions (**Fig. 3-13a**). The validity of this frequency dependence of the flow volume was confirmed by the experiment. The experimental results showed the flow rate has a similar frequency-pressure-dependent tendency to simulated results. Therefore, two small liquid chambers with diaphragms diameter of 0.5 mm with a short duration of deformation (1 s reduced to 0.67 s) was for faster responding to the one-directional flow perfusion, and one large liquid chamber with a diaphragm diameter of 0.8 mm was for increasing the pumping volume. These results demonstrated the validity of the simulation model to estimate the flow volume depending on the operation parameters. It indicated the improved pumping flow rate with two-different liquid chamber volumes.

Then, we used the simulation model to evaluate the structure of the micropump liquid channel and the pumping performance for the micropump design. For the fluidic channel of micropump shape, we modified it from a diffuser/nozzle structure or trapezoidal structure (**Fig. 3-13b**), which was widely used in the other diffuser/nozzle micropump to improve one-directional flow.[121] We also found the simulation results of flow rate matched the measured results with a similar frequency-dependent tendency.

To analyze the pumping performance (the pressure and flow rate of the liquid channel) for the system, the external hydraulic resistance of two discharge ports was increased for the 'power-load' relation curve. The basic hydraulic resistance of two inlet/outlet channels (R_{pump}) was 8.23×10^{10} Pa·s/m^3, calculated according to **equations 3-9**. To simply display the relationship, we used the resistance factor k to standard for the external resistance. The k has a wide range in the simulation for mimicking complicated system-level conditions of microfluidics.

For the pressure and resistance, with the increase of the hydraulic resistance, the pumping pressure was increased (**Fig. 3-13c**). This is the ability of the micropump against external resistance. For the straight channel ϴ=0°, the maximum pressure was 33 Pa. But the trapezoidal structure, ϴ=20°, and ϴ=30° achieved maximum pressure of 41 Pa and 55 Pa, respectively. In the present dimension design, the trapezoidal structure (ϴ=30°) could extend the pumping pressure. It indicated the trapezoidal structure has a higher capability against external resistance.

For further analysis with the simulation model, we evaluated the pumping volume of flow rate with fluidic resistance changing. As shown in Fig. **3-13d**, the mean flow volume was reduced by increasing the magnitude of resistance under the operation condition of 150 kPa and 1.5 Hz. In the case of the micropump with a straight channel, i.e. nozzle angle $\theta = 0°$, the higher flow volume was obtained when $k \leqslant 400$. In this magnitude range, the flow volume of the micropump with the nozzle angle of 30° is

constant and lower. But it is reversed with the straight channel when $k \geqslant 1000$. Therefore, the micropump with nozzle-diffuser channel provides a higher pumping performance for the medium perfusion with high hydraulic resistance (with a flow rate smaller than 1 µ/min), which is a normal condition of the interstitial flow of some MPSs.[159,160]
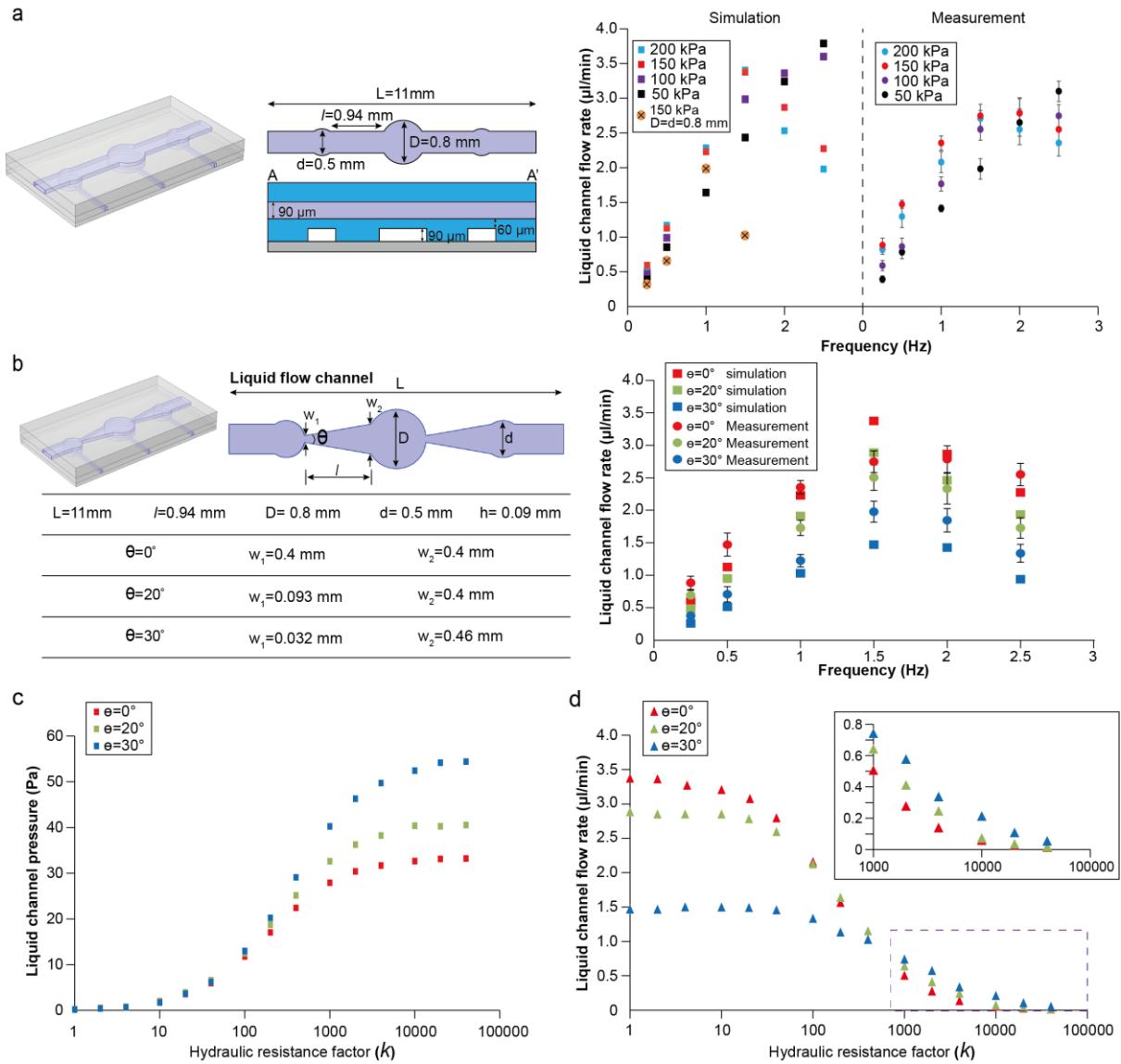
Figure 3-13 Micropump working performance evaluation with different liquid channel structures and channel hydraulic resistances. (a) The simulated and measured results of pressure-frequency-dependent flow volume of the normal straight channel. 150 kPa D=d= 0.8mm means the normal circular liquid channel micropump with the same size three liquid pumping chambers. And other conditions are the different size liquid pumping chambers. (b) The micropump working performance evaluation from simulation and measurement for the three angled channels, under 150 kPa actuating pressure. (c) The discharge pumping pressure in the liquid channel under a larger range of external channel resistance. (d) The discharge pumping flow volume in the liquid channel under a larger range of external channel resistance.

3.5 Discussions

3.5.1 The DMD-based grayscale lithography fabrication for microvalve

The traditional semi-round shape channel fabrication for Quake-type microvalve was the resist reflowing method.[161] To improve the reproducibility of this process, DMD-based grayscale lithography at the wafer level was employed to fabricate a high throughput with a controlled mold structure for a microvalve channel.[133] The design of a digital grayscale mask pattern was the most important step for this grayscale lithography. In the previous research, the digital grayscale mask pattern was designed by an FEA simulation of a diaphragm deformation.[134] However, it did not consider the diaphragm deformation in a microfluidic channel. Also, the involved contact with the channel wall surface was neglected. To obtain a more precise grayscale pattern, in this research, a simulation of the three-dimensional profile of the deformed PDMS diaphragm was developed. The fabricated microvalve system could be integrated into an MPS system with high throughput valve sets (**Appendix I**), which realized higher performance of flow routing control.

3.5.2 The circular diaphragms with the same or different sizes for micropump

For the micropump, in this research, we designed three different size diaphragms with one big and two small sizes (**Fig. 3-4**), which could achieve a 2-phase sequence of actuating. The reason we did not use the same size liquid chamber (three diaphragms with a diameter of 0.8 mm) with 3 phases was the narrow actuating frequency range and low flow volume. The three diaphragms of the same size liquid chamber take a total of 1 s duration for one-period deformation. To avoid the overlap of each diaphragm acting, the actuating frequency shall be less than 1 Hz (**Fig. 3-12a**). It also leads to a low pumping flow rate with a maximum flow rate of 2.02 μl/min under 150 kPa pressure. While the micropump used in this research (2-phase with different-size diaphragms) has a relatively faster period of 0.63 s and could get a maximum of 3.37 ul/min at the same condition. It demonstrated that the 2-phase actuating system not only reduced the control system's working steps but also improved the flow volume. With a wider range of flow rate control, it is better suited for the microfluidic cell culture system.

3.5.3 Simulating the microfluidic hydraulic resistance change

In the microfluidic cell culture system, the volumes of fluids were from microliters to nanoliters, even to femtoliters.[162] This is correlated to the micro-to-nano size fluidic channel or cell culturing conditions, which induces variable hydraulic resistance against the pumping flow rate. In this research, we used a larger range of variable hydraulic resistance factor k to evaluate the micropump performance. Thus, the microfluidic channel resistance in different cases can be simulated. To calculate the k, first, the initial

$k=1$ indicated the R_{pump}, the initial resistance of the micropump discharge part in the simulation. Then, according to **equations 3-9**, the external resistance can be changed from microfluidic viscosity μ and dimensions L/A^2 to calculate each system R. Therefore, we used the k number to standard for the external resistance, which is R/R_{pump}. Therefore, the k and R have the same control factors, viscosity μ and dimensions L/A^2. For the viscosity change cases by gels of microfluidic channels, the fluidic channel k changed to 1000 after being filled with gel for cell culture.[163] For the cases of vascularized tissue arrays with multi-sets, the k could be regulated from 1000 to 100000, during the vessel development.[63] For some cases of dimension change, for example, the holes of the porous diaphragm were covered by cells during cell growth, and the k would be regulated from 10 to 200.[164]

Recently, with the application of diaphragm structure,[165] the microfluidic cell culture system can be extended to a multilayered structure. Also, for the multi-organ MPS, a loop circulation system is important.[92] These conditions may generate a more complicated hydraulic resistance system (compared with the normal open system), and it is suitable to use the electric circuit analogy to analyze the flow features.[56] In this research, we provide the pump performance analysis method, considering the external resistance. It may serve as a considerable component for the electric circuit analogy model and promote understanding of the complicated multilayered structure and multi-organ MPS circulation.

Besides, in this research, the resistance factor k of closed-loop channels is around 1000 (**Chapter 4**).[27,92] However, the multilayered structure (**Chapter 5**) will generate a back pressure around 50 Pa (about 5 mm H_2O level), which increases the load of circulation flow. According to pumping pressure evaluation results, it indicates the trapezoidal structure is more suitable for the circulation flow of the microfluidic cell culture system, especially for the multilayered structure MPS.[92]

3.6 Conclusions

The MPS devices, using an external micropump for fluidic circulation, have troubles with complicated tube connections and larger volume medium occupation.[7,30,31] To precisely control the cell microenvironment perfusion and circulation flow of MPS, we need to design the on-chip microvalve and micropump. In this chapter, we characterized the performance of the PDMS-based pneumatic microvalve with a semi-round shape channel and micropump consisting of three circular diaphragms. We designed the microvalve and micropump by the FEA-based simulation, applying the contact analysis and fluid-structure interaction methods. In addition, we demonstrated the usage of the micropump with different size circular diaphragms (2-phase actuating) in wide-flow hydraulic resistance to mimic the case of the MPS system. We found the diffuser/ nozzle structure could control a more robust pump capacity than the normal straight channel, leading to a suitable flow for MPS.

The purpose of this chapter is to provide the concept of precise cell culturing microenvironment control by controlling the microactuators (**Fig. 3-14a**). As presented in the above section, the microvalve and micropump can be integrated into a micro-scale GLA-MPS system (**Fig. 3-14b**), for generating and controlling the circulation flow rate. In the following chapter, we will use the microvalve and micropump to build into the MPS, to achieve cell function improvement by the microenvironment control.
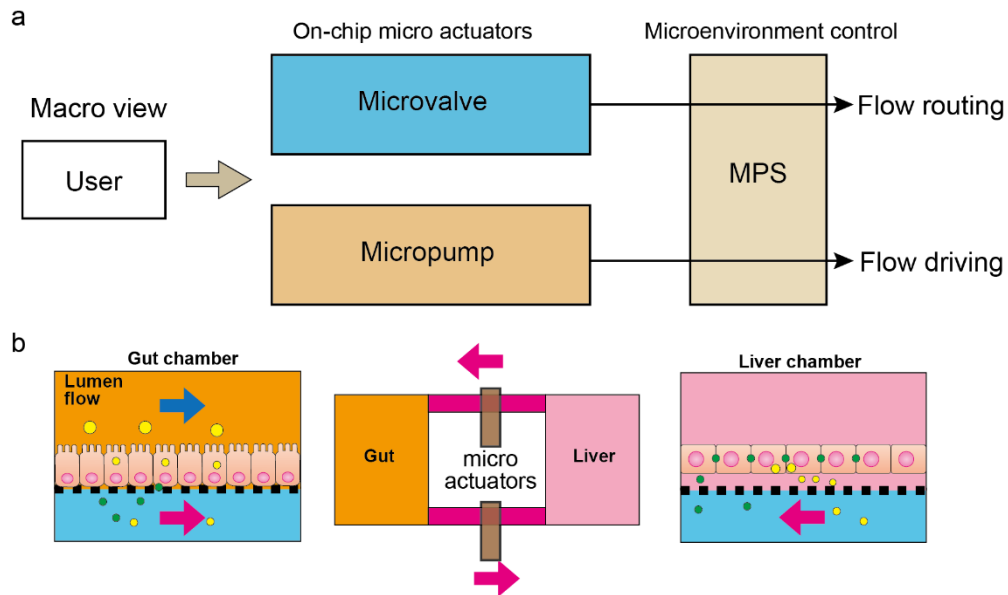
Figure 3-14 The concept of cell fluidic culture microenvironment control by controlling the microactuators for GLA-MPS. (a) The cell culture environment control by microvalve and micropump; (b) the microfabricated GLA-MPS with microactuators.

Chapter 4 Integrated gut–liver-on-a-chip for modeling non-alcoholic fatty liver disease

4.1 Introduction

In chapter 1, the gut-liver axis (GLA) interaction was thought as one of the most important factors, leading to the non-alcoholic fatty liver disease (NAFLD) progression. Therefore, in this chapter, we focus on understanding the NAFLD initiation and progression via GLA. To enhance the GLA, We use microfabricated closed-loop circulation with improved medium exchanging (pre-discussed in **chapter 3**).

As we discussed in chapter 1, non-alcoholic fatty liver disease (NAFLD) is a common chronic liver disease that can result in hepatic steatosis, liver cirrhosis, liver cancer, and cardiovascular diseases.[166–169] it is expected to afflict 33.5% of the United States population over 15 years of age by 2030.[170] Despite the urgent need for intervention at various stages of chronic fatty liver disease, the disorder mechanism is largely unknown due to the complicated processes that occur at multiple layers, which is known as the 'multiple hit theory'. For example, fat accumulation, oxidative stress, endoplasmic reticulum (ER) stress, and genetic or epigenetic modifications can take place at the cellular level, and insulin resistance and inflammatory responses can take place in multiple organs depending on the individual and environment.[35] To find new therapies for NAFLD, a thorough understanding of all of these processes are required.

In this study, we focused on the gut-liver axis (GLA) because it is one of the most important factors in the development and progression of NAFLD.[171,172] GLA dysfunctions, including intestinal dysbiosis, bacterial overgrowth, and alteration of mucosa permeability, caused by NAFLD, are potential therapeutic targets;[173,174] but no drug has been made commercially available to date. This is largely because conventional preclinical animal tests do not accurately represent the problems of the multiple hit theory, lack accessibility to individual organs in living animals, and have a species difference. Therefore, establishing a simplified and robust model to study the GLA with NAFLD is crucial to obtaining deeper insights into the underlying mechanisms to discover new drugs, treatments, and diagnostic tools.

As discussed in **Chapter 1** and **Chapter 2**, Organs-on-chips (OOCs), also known as micro-physiological systems (MPSs), have significant potential for *in vitro* preclinical testing[12,175–177] and disease modelling.[178] Notably, several important features should be emphasized to better understand the MPSs. First, it enables to exert of spatiotemporal control over cellular microenvironments to functionalize tissue cells. Second, a flow circulation of the cell culture medium can be generated to model multi-organ interactions involving paracrine and endocrine signaling. Finally, MPSs, associated

with cutting-edge cellular assays such as high-content analyses and the omics approach, provide quantitative and multi-parametric insights into biology that animal experiments do not.[179]

MPSs have been used to mimic the GLA *in vitro* and demonstrate the role of GLA crosstalk in pathological situations, including fatty liver disease[76,180] and inflammation[181], for *in vitro* pharmacokinetic studies.[28] However, to model the GLA, MPSs must be strengthened, and this requires the following four characteristics: a closed circulation loop, accessibility to individual chambers, tissue flow perfusion, and prevention of molecule concentration reduction from dilution and material absorption. First, the closed circulation loop is required for medium circulation to recapitulate inter-tissue interactions in the GLA. Then, individual accessibility is necessary to introduce tissue cells into the desired chamber and harvest them after treatment without cross-contamination from other cells. The closed circulation loop and individual accessibility seem to be contradictory features, but both need to be accomplished to investigate the crosstalk between the gut and liver. Tissue flow perfusion is crucial in obtaining functional tissue cells *in vitro*, particularly for the gut.[182]. Some OOCs require the use of additional cell culture inserts (e.g. Transwell) to co-culture two or more types of cells separated by a porous membrane. Due to the macroscale medium dilution, it reduced the GLA crosstalk cytokine concentration. Moreover, they cannot be used for microfabrication and therefore frequently lack the benefits of microfluidic technology, such as control over the flow dynamics in the cell culture chamber and the cellular microenvironment. Moreover, these additional inserts often interfere with the microscopic observation of cells because they increase the working distance and light diffraction by the membrane's pores. Polydimethylsiloxane (PDMS) is a widely used material for microfluidic cell culture systems, due to its biocompatibility, transparency, and elasticity properties. It is necessary to prevent PDMS absorption because PDMS causes the absorption of hydrophobic molecules and the loss of molecules such as metabolites, hormones, drug candidates, fatty acids, lipids, and fluorescent indicators, which can influence cellular phenotypes and assay results. In particular, free fatty acids (FFAs) are a critical factor in NAFLD.

In this chapter, we present an integrated gut–liver-on-a-chip (iGLC) platform as a simplified *in vitro* human model of the GLA (**Fig. 4-1**), and this model can help obtain deeper insights into the underlying mechanisms of NAFLD for the development of new therapies. The iGLA platform[27] has micro-valves and a microvalve pump to achieve individual accessibility for each cell culture chamber and a closed medium circulation flow to enhance GLA communication. The integrated microvalve pump controls the perfusion interstitial flow to activate cultured gut cells. The iGLC platform does not require additional cell culture inserts; therefore, it allows high-quality cell monitoring to achieve microscopic single-cell profiling. A simple surface coating with amphipathic molecules and an auto medium exchange timing control prevent the absorption of FFAs into PDMS. We co-cultured gut and liver cells with a closed circulation flow. To highlight initial and progressive NAFLD, we also induced a NAFLD-like cellular state by administering FFAs to the platform for two periods (1 and 7 days). Finally, using

microscopic single-cell profiling in combination with mRNA sequencing (mRNA-seq), we will explore the distinct cellular phenotypic alterations and associated gene networks for the GLA in a cellular state resembling NAFLD.
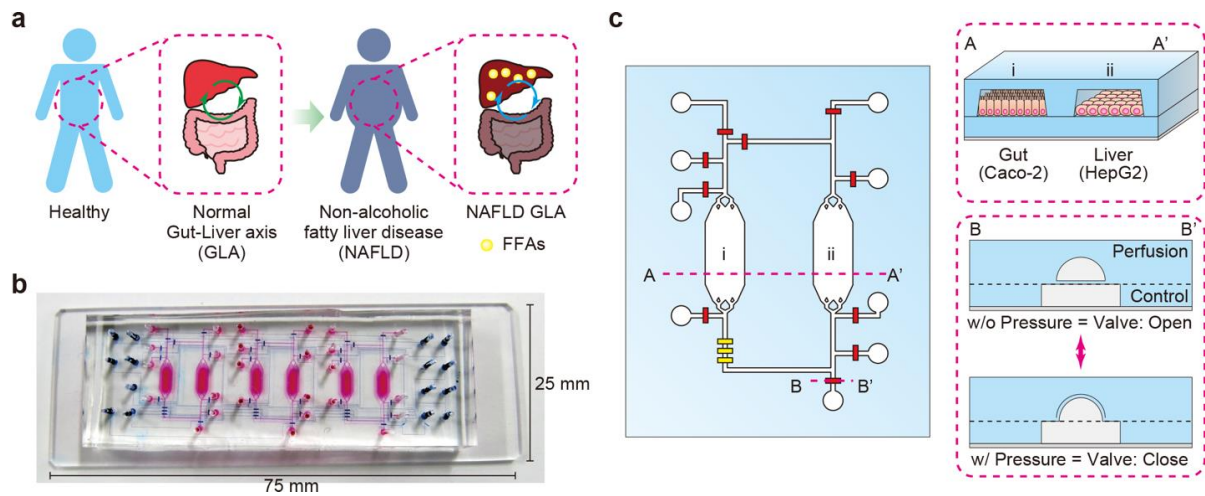
Figure 4-1 Design of the integrated gut–liver-on-a-chip (iGLC) platform to recapitulate NAFLD. (a) Schematic for NAFLD progression by free fatty acids (FFAs) via the gut-liver axis (GLA). (b) Photograph of an iGLC platform. The perfusion and control layers are colored in pink and blue, respectively. (c) Illustration of the iGLC platform used for NAFLD. Two cell culture chambers with cells (Caco-2 and HepG2) are linked by a microfluidic channel. Owing to microvalve, cell culture chamber is accessible without cross-contamination. A – A' shows gut and liver cell culture chambers. B-B' depicts microvalves that are open and closed. By applying pressure to the control layer's microfluidic channel, the elastic PDMS diaphragm closes the normally open valve.

4.2 Methods

4.2.1 Chip fabrication and surface treatment

(a) Chip fabrication. Following prior findings, the iGLC platform was constructed from flexible PDMS (SYLGARD 184, Dow Corning) polymer using a multilayer soft lithography replica molding approach (**Fig. 4-2, and Appendix I**).[133,134] The control layer consisted of microchannels supplying hydraulic pressure that was cast from a 30 µm-thick negative photoresist mold (TMMR S2000, Tokyo Ohka Kogyo) and patterned using a typical photolithography tool. The perfusion layer comprises of two cell culture chambers (225 µm in height and 2.1 mm in width) joined by 45 µm in height and 200 µm in width semi-elliptical microchannels. Combining traditional photolithography (cell culture chambers) and greyscale lithography, the perfusion layer mold creation technique adhered to the multilayer lithography principle (micro-channels). On the silicon wafer, a negative resist layer (TMMF S2045, Tokyo Ohka Kogyo) with a thickness of 180 µm was patterned first. Next, a 45 µm thick layer of a positive resist (PMER P-LA900PM, Tokyo Ohka Kogyo) was spin-coated onto the wafer. To accomplish precision wafer-level mold fabrication, digital micromirror device (DMD)-based grayscale

lithography (DL-1000GS/KCH, NanoSystem Solutions) was done with numerically optimized mask data.[133] This enabled perfect microchannel sealing with micro-valves and high-efficiency drive for the peristaltic micro-pump system. After the manufacture of the mold, the PDMS base and curing agent were thoroughly combined with a weight ratio of 10:1. For the control layer, the PDMS mixture was spin-coated with a 50 µm thickness on the mold to provide a 20 µm regulated PDMS thickness at the diaphragm region. PDMS for the control and perfusion layers was cured at 80 °C for 4 min on a hotplate and 40 min in a convection oven. Using the partial PDMS curing process, the perfusion layer was then peeled off, precisely aligned, and glued to the control layer. The constructed structure was baked at 80 °C for two hours before being peeled off the silicon wafer. The inlet and outlet wells were finally opened. The assembled structure was firmly bonded to a tiny slide glass (25 mm× 75 mm) using O$_2$ plasma (FA-1, SAMCO).
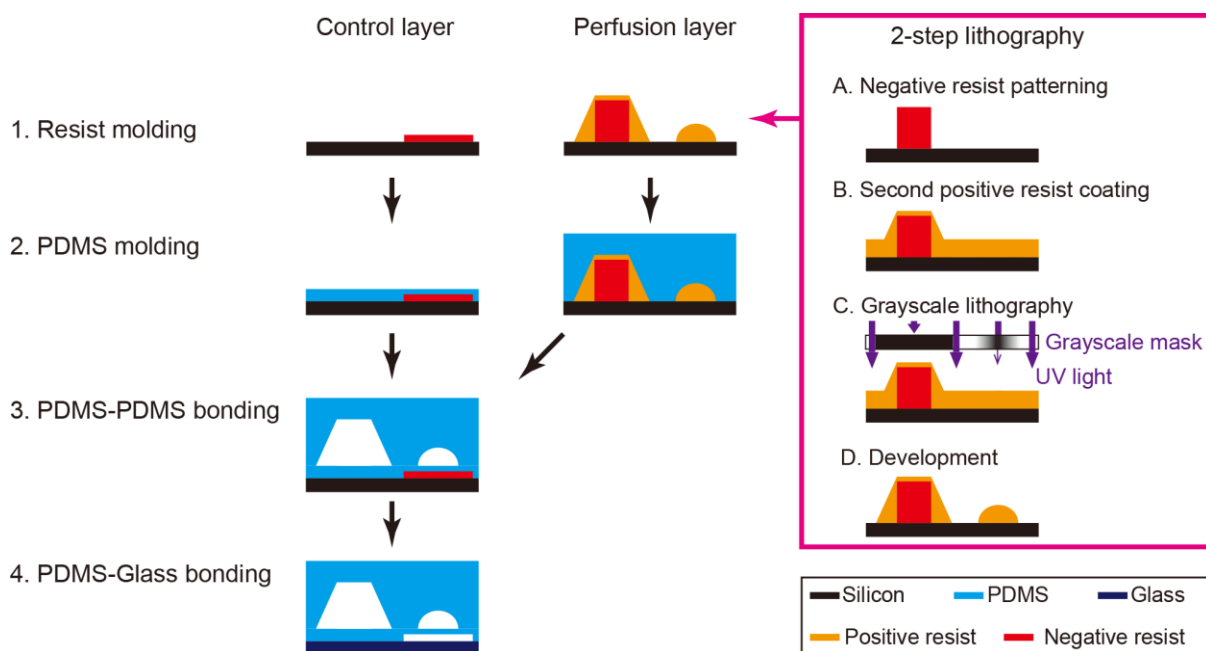
Figure 4-2 The illustration of fabrication procedure for the iGLC platform. Adapted from [27].

(b) Device control. The micro-valves and micro-pump were controlled by positive hydraulic pressure through control channels that were interconnected. A 1 mL syringe was used to fill the control channel within the chip with distilled water to prevent gas permeation over the PDMS. Then, metal pins and Teflon tubing (Pilot Corporation) were utilized to connect the control channels and pneumatic system's inlet wells to a compressed nitrogen gas supply (regulated at 0–200 kPa). The pressure actuation and release of the valves were regulated and operated via solenoid valves (Microfluidic System Works Inc. and THE LEE Company) and a controller board (VC3 8 controller [ALA Scientific Instruments] and NI USB-6501 [National Instruments]) with LabVIEW (Version 11.0, National Instrument) software. The microvalve pump was comprised of three adjacent micro-valves with serial actuation to provide a cyclic peristaltic motion for medium recirculation in the chip.

(c) Chip surface treatment. Prior to cell seeding, the platform was sterilized by cleaning it with 70% ethanol and placing it in a biosafety cabinet under ultraviolet radiation for 30 min. The cell culture chambers were next coated with 0.1% (w/v) DDM (n-dodecyl-β-D-maltoside) in PBS at 4 °C for 24 hours, followed by coating with Matrigel hESC-qualified matrix (Corning) diluted to 1.3% (v/v) with DMEM/F12 (Sigma-Aldrich) at 4 °C for 24 hours (**Figure 4-3**). After removing excess Matrigel with DMEM, the chip was put in an incubator at 37 °C until further use.
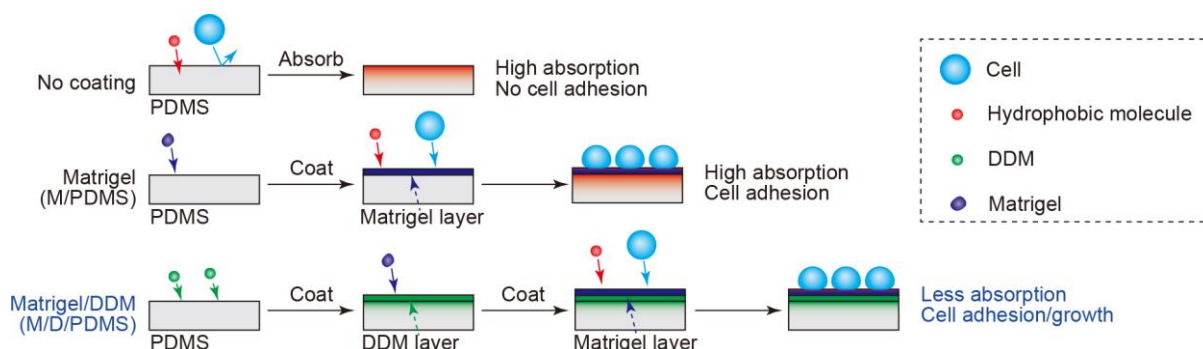
Figure 4-3 Schematic for PDMS coating with DDM and Matrigel to respectively prevent absorption of hydrophobic molecules in PDMS and promote cell adhesion and growth on PDMS.

4.2.2 Cell culture and cell-based assays

(a) Cell culturing. The American Type Culture Collection provided HepG2 human hepatocellular carcinoma and Caco-2 human colorectal adenocarcinoma cell lines. Cells were maintained in Dulbecco's modified Eagle medium (DMEM) (Sigma-Aldrich, St. Louis, MO, USA) incorporated with 10% (v/v) fetal bovine serum (FBS, Cell Culture Bioscience), 1% (v/v) nonessential amino acids (Thermo Fisher Scientific), and 1% (v/v) penicillin/streptomycin (Thermo Fisher Scientific) in a humidified incubator at 37 °C with 5% (v/v) CO_2. Every 3 and 5 days, HepG2 and Caco-2 cells were passaged with trypsin/EDTA (0.04% / 0.03%[v/v]) solutions at 1/5 and 1/10 ratios, respectively.

(b) Cell culturing on a platform. HepG2 and Caco-2 cells were collected from T-flasks with 1 mL of trypsin/EDTA (0.04% / 0.03% [v/v]) solution after incubation for 5 min at 37 °C. After centrifugation, the cells were resuspended at a concentration of 1.0×10^6 cells mL^{-1} in fresh cell culture medium. During cell seeding, the micro-valves adjacent to the cell culture chambers were closed to prevent cross-contamination (**Fig. 4-4**). Then, 5 µL of the Caco-2 cell suspension was pipetted into the well adjacent to the cell chamber at a concentration of 7.0×10^4 cells cm^{-2}. Meanwhile, 5 µL of the HepG2 cell suspension was introduced into another cell culture chamber. The platform was placed in a humidified incubator at 37 °C with 5% (v/v) CO_2. After one day, the cell culture medium was replaced to eliminate

dead cells that floated to the surface. The cell culture medium was then replaced every 6 hours using a coded program based on LabVIEW.

(c) Free fatty acid treatment. The FFA treatment solutions consisted of a 1:2 mixture of PA (Sigma-Aldrich) and OA (Sigma-Aldrich). To prepare the treatment solutions, PA was dissolved in dimethyl sulfoxide (DMSO; Nacalai Tesque Inc.) solution at 20 mg mL^{-1} to serve as the PA stock solution (78 mM). OA was dissolved in DMSO at 100 mg mL^{-1} to serve as the OA stock solution (354 mM). The PA and OA stock solutions were mixed (PA: OA=1:2) in DMEM (containing 1% BSA-fatty acid-free, 1% P/S, and 1 mM nonessential amino acids) to generate a series of FFA concentrations (0.1, 0.2, 0.5, 1, and 2 mM). Prior to FFA treatment, serum-free DMEM was added to both cell culture chambers for 12 hours to starve the cells. After that, the medium containing FFA was added to the cell culture chambers (**Fig. 4-4**). The platform was treated for seven days at 37 °C in a humidified incubator. During this time, the medium was replaced every six hours.
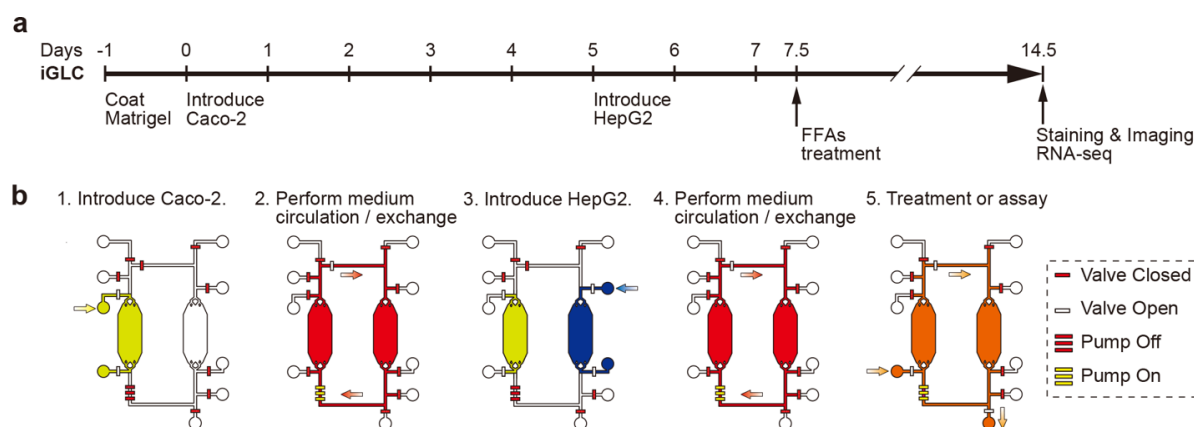
Figure 4-4 Experimental procedure to culture Caco-2 and HepG2 cells in an iGLC platform. (a) experiment timing control; (b) Microvalve controlling and procedures for on-chip cell culturing.

(d) Cell viability and apoptosis staining. Calcein AM (Dojindo Molecular Technologies, Inc.) and Annexin V-Alexa Fluor® 647 (Biolegend) dyes were used to stain viable and apoptotic cells, respectively. Hoechst 33258 (Dojindo Molecular Technologies, Inc.) was used for staining the nucleus. The staining solution was prepared by mixing 10 µL of Hoechst 33258 (1 mg mL^{-1} stock concentration), 10 µL of Calcein AM (1 mg mL^{-1} stock concentration), 10 µL of Annexin V (50 µg mL^{-1} stock concentration), 500 µL of Annexin V binding buffer (Biolegend), and 500 µL of DMEM. The wash buffer comprised 500 µL of Annexin V binding buffer and 500 µL of DMEM. After treatment, cells were washed twice with fresh DMEM, and subsequently, 10 µL of staining solution was introduced in a cell culture chamber using a pipette via the adjacent inlet. Cells were kept at 37 °C for 30 min. Then, the excess staining solution was removed by washing with 30 µL of wash buffer three times.

(e) AdipoRed staining. The lipid accumulation was visualized using an AdipoRed assay (Lonza) following the manufacturer's protocol. Briefly, 15 µL of AdipoRed assay reagent and 10 µL of Hoechst 33258 were mixed with 1 mL of DMEM to make the AdipoRed staining solution. The cell culture chambers and channels were washed with PBS twice. Then, 10 µL of AdipoRed staining solution was introduced and kept at 37 °C for 15 min. The chambers were washed with fresh DMEM solution three times.

(f) Immunocytochemistry. The cell-culture chambers were rinsed twice with 50 µL PBS after 7 days of FFAs treatment. The cells were fixed for 15 min in PBS with 4% paraformaldehyde (PFA, FUJIFILM Wako Pure Chemical) and permeabilized for 30 min in PBS with 0.1% (v/v) Triton X-100. After that, the cells were cultured at 4 °C for 24 hours in a blocking buffer, consisting of 5% normal goat serum (Vector); 5% normal donkey serum (Wako); 3% BSA (Sigma-Aldrich); and 0.1% Tween-20 (Nacalai Tesque, Inc., in PBS). After blocking, the cells were treated in a blocking solution for 24 hours with primary antibodies mouse anti-human albumin IgG (Thermo Fisher Scientific). After washing the primary antibodies three times with PBS-T, the cells were treated for 1 hour at 25 °C with secondary antibodies Alexa Fluor 647-labeled donkey anti-mouse IgG H&L (Jackson ImmunoResearch). The nuclei of the cells were stained with 300 nM of 4,6-diamidino-2-phenylindole (DAPI, Dojindo Laboratories) and incubated at 25 °C for 30 min before being rinsed with PBS.
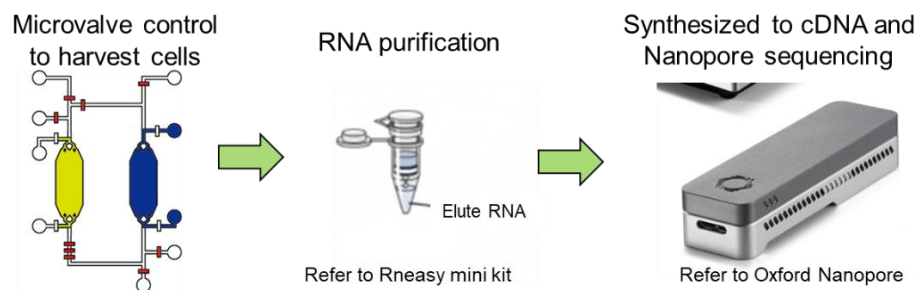
Figure 4-5 The process of RNA harvesting, purification and RNA-sequencing. The microvalves were operated to individually harvest gut and liver cells respectively.

(g) RNA harvesting and purification. RNA was purified from cells with RNeasy Mini Kit (Qiagen, Hilden, Germany) (**Fig. 4-5**). The micro-valves were initially closed to prevent cross-contamination between the HepG2 and Caco-2 cells. After the cells were washed with PBS, 10 µL of trypsin/EDTA (0.04% / 0.03%[v/v]) solution was introduced into the cell culture chambers and incubated with the cells at 37 °C with 5% CO_2 for 10 min. Subsequently, the cells were harvested with a 10-µL pipette and placed in 1.5-mL tubes. Cells were lysed by adding 350 µL of lysis buffer from the kit, and then, 350 µL of 70% (v/v) ethanol was added to the tubes. Each solution was transferred to an RNeasy Mini spin column placed in a 2-mL collection tube. The column was centrifuged for 15 s at 8000 × g, and the

flow-through was discarded. Next, 350 µL of buffer RW1 was added to the columns and centrifuged. Subsequently, 80 µL of DNase digestion buffer was added to the column and incubated at 25 °C for 15 min. Next, 350 µL of buffer RW1 was added to the column tube and centrifuged again. The column was washed with 500 µL of buffer RPE twice, placed in a new 2 mL tube, and centrifuged. The column was then placed in a new 1.5-mL collection tube, and 30 µL of RNase-free water was added to the column. This was followed by centrifugation for 1 min at $8000 \times g$ to elute RNA into the collection tube. The RNA quality was evaluated with Agilent 2100 Bioanalyser (Agilent Technologies, Inc., USA) (**Supplementary Figs. S4-4 in Appendix II**).

(h) RNA amplification and mRNA sequencing. mRNA-seq commissioned analysis was conducted by Takara Bio Inc or Oxford NANOPORE Technologies. For Takara Bio Inc, briefly, Using SMART-seq, 50 ng of total RNA from each sample was amplified and synthesized into cDNA (SMART-Seq v4 Ultra Low Input RNA Kit, Takara Bio). The cDNA was used to generate a library using the Nextera DNA Flex Library Prep Kit (Illumina), and the cDNA library was sequenced using the NovaSeq 6000. (Illumina). For Oxford NANOPORE Technologies, to prepare the cDNA library, 40 ng of total RNA was diluted with 9 µL of RNase-free water, combined with VN primer (Oxford NANOPORE Technologies, UK) and 1 µL of 10 mM dNTPs (New England Biolabs Inc. Ipswich, Massachusetts, USA), and then incubated at 65 °C for 5 min. The strand-switching buffer was composed of 4 µL of 5x RT Buffer (Thermo Fisher Scientific), 1 µL of RNaseOUT (Thermo Fisher Scientific), 1 µL of Nuclease-free water, and 2 µL of Strand-Switching Primer (Oxford NANOPORE Technologies). The two solutions were combined at 42 °C for 2 min, and then 1 µL of Thermo Fisher Scientific's Maxima H Minus Reverse Transcriptase was added. The mixture was incubated at 42 °C for 90 min, 85 °C for 5 min, and then stored at 4 °C until it was utilized as a cDNA library. 5 µL of cDNA library solution was combined with 25 µL of 2x LongAmp Taq Master Mix (New England Biolabs Inc.), 1.5 µL of Barcode Primers (Oxford NANOPORE Technologies), and 18.5 µL of nuclease-free water. The cDNA was barcoded for multiplexing using PCR (95 °C for 30 s, 18 cycles of 95 °C for 15 s, 62 °C for 15 s, and 65 °C for 50 s, and then 65 °C for 6 min). Until usage, PCR products were kept at 4 °C. After adding 1 µL of NEB Exonuclease 1 (New England Biolabs Inc.), the mixture was incubated at 37 °C for 15 min, followed by 15 min at 80 °C. The amplified DNA was purified using Agencourt AMPure XP beads (BECKMAN COULTER Life Science, Indianapolis, IN) and collected in 12 µL of Elution Buffer (Oxford NANOPORE Technologies). BioAnalyzer 2100 with a High Sensitivity DNA Kit (Agilent Technologies) was used to assess the quantity and quality of barcoded cDNA. Next, 50 fmol of barcoded cDNA was incubated with 1 µl of Rapid Adapter in a total volume of 11 µL for 5 min at 25 °C. 12 µL of the produced DNA library was combined with 37.5 µL of Sequencing Buffer (Oxford NANOPORE Technologies) and 25.5 µL of Loading Buffer for Nanopore sequencing (Oxford NANOPORE Technologies), which was added to the Nanopore Flow Cell (v9.4.1) and run for 24 hours.

4.2.3 Data acquisition and analysis

(a) Ultrahigh-performance liquid chromatography-tandem mass spectrometry (UHPLC-MS/MS). Firstly, 3 µL of the cell culture medium was collected from a chip and mixed with 96.95 µL of the working solution (50% isopropanol, 25% acetonitrile, and 25% water) and 0.05 µL of the internal standard solution (PA-d4: 5 mM, OA-d9: 5 mM, in isopropanol). The mixture was then vigorously mixed for 30 s and centrifuged at $16,000\times g$ for 10 min at 4 °C. Subsequently, 2 µL of the supernatant was injected and separated on a Nexera UHPLC system (Shimadzu, Kyoto Japan) by using a binary gradient with solvent A (50% Acetonitrile, 18% isopropanol, and 32% water) and solvent B (90% isopropanol, 10% acetonitrile, 10 mM ammonium formate, and 0.1% formic acid). The gradient program used was as follows: 0% B for 14 min, 100% B for 3 min, and 0% B for 3 min. An ACQUITY UPLC BEH C18 column (130 Å, 1.7 µm, 2.1 mm × 100 mm (Waters, Milford, MA)) was used at 40 °C. The UHPLC eluates were infused online to the LC-MS 8030plus (Shimadzu), which was set to negative electrospray ionization (ESI-) mode. The PA and OA responses were observed by pseudo multiple reaction monitoring (pMRM) with transitions at m/z 255.05 > 255.35 and 281.05 > 281.45, respectively. The pMRM transitions for PA-d4 and OA-d9 were 258.95 > 259.45 and 290.10 > 290.40, respectively. The pMRM transitions were optimized, and peak areas were calculated using LabSolutions software (Shimadzu). The PA and OA responses were normalized against those of PA-d4 and OA-d9 for each sample. All measurements were obtained in triplicate, and the averaged responses were used. Standard curves were generated by measuring a blank culture medium supplemented with increasing amounts of PA and OA.

(b) mRNA-seq analysis. Initially, mRNA-seq reads were mapped to the rRNA, tRNA, or mitochondrial genome sequences with BowTie (v.2.1.0).[183] The mapped reads were discarded and not used for the following analysis. The remaining reads were mapped to the human genome (GRCh38) with STAR Aligner (2.7.1a)[184] using ENCODE options considering gene annotation and Ensembl (ver.98).[185] After the mapping to the genome, gene expression values (Transcripts Per Million reads; TPM) were calculated using RSEM (ver. 1.3.0).[186] DEGs of the mono-cultured and co-cultured samples were calculated using DEseq2 (ver. 1.8.2).[187] If a gene satisfied the following criteria, the gene was defined as DEG: $p < 0.01$, abs ($\log_2$(Fold Change)) ≥ 0.263, base mean of raw reads ≥ 31, and average TPM in either sample ≥ 1. GO analysis for DEGs was performed with the WEB-based Gene Set Analysis Toolkit (WebGestalt[188]). 'Biological Process noRedundant' was selected for the database, and 'genome protein-coding' genes were selected for the reference set. The protein-coding genes among the DEGs were used as input.

To consider the FFA treatment conditions, we employed ANOVA to select DEGs and characterize samples. A gene was treated as a DEG if $p < 0.05$ and abs($\log_2$(Fold Change)) ≥ 0.263 for a combination

of any two samples. The expression values of DEG were used for PCA to characterize the samples. To compare DEG sets with FFA-minus and -plus under the mono-cultured condition, FFA-minus and -plus under the co-cultured conditions, and mono- and co-cultured samples under the FFA-minus condition, DEGs with a PC2 loading of ≥ 2 or ≤ 0.5 were used. The results were used to assess changes in gene expression related to the FFA treatment. To compare gene expression profiles according to FFA treatment under the mono- and co-cultured conditions, we employed Gene Set Enrichment Analysis (GSEA[189], ver.4.0.4) with DB files (msigdb.v7.1.symbols.gmt). The fold change values for the protein-coding genes were used as inputs. The bar plots show FDR q-values for the top four terms under either the mono- and co-cultured condition. In the analysis, the PCA plots were drawn with the ggplot2 package in R.

(c) Single-cell profiling based on microscopic images. Following microscopic image acquisition, the CellProfiler software (Broad Institute of Harvard and MIT, Version 3.1.9)[190] was used to estimate cellular features (e.g., cell size and fluorescent intensity). After loading the set of stained images (nuclei and cellular phenotype or function), all images were adjusted with the "correctilluminationCalcuate" and "correctilluminationApply" modules to reduce the uneven distribution of background signals. The settings of the manual were followed. Generally, the illumination function was calculated from "Background" with block size 20-100 for each image individually. And the Smoothing method was selected as the "Median filter", with a filter size of 50. Other options followed default settings. The mathematical methods of "correctilluminationApply" were "Subtract". With the corrected nuclei images, individual cells were identified by using Otsu's method[190] in the "IdentifyPrimaryObjects" module as primary objects, followed by "IdentifySecondaryObjects" to evaluate the cellular phenotype/function, automatically. Then, cellular features were calculated using the "MeasureObjectSizeShape" and "MeasureObjectIntensity" modules for both primary and secondary objects. Further analysis of single-cell morphological descriptors were performed with t-SNE in the open-source Orange 3 software (Version 3.23.1; Bioinformatics Laboratory, Faculty of Computer and Information Science, University of Ljubljana, Slovenia).[191]

(d) Statistical analysis. The Tukey–Kramer test and asymptotic Student's t-test were carried out with *R* software (ver. 3.5.2; https://www.r-project.org/). The data was provided in **Appendix III**.

(e) Data availability. The mRNA-seq data have been deposited to the NCBI Gene Expression Omnibus (GEO) under accession number GSE152091.

4.3 Results

4.3.1 iGLC platform for NAFLD modeling

A conceptual illustration of the integrated gut-liver on-a-chip (iGLC) platform is shown in **Fig. 4-1**. The design of the microfluidic platform is a critical factor for recapitulating the GLA *in vitro*. To elucidate inter-tissue interaction based on the multiple-hit-theory models, a single platform is needed that can both mono- and co-culture two or more cell types within the same format. In parallel, cross-contamination needs to be considered to allow analysis of each cell type and the influence of other cell types. We designed the iGLC platform to meet these requirements (**Figs. 4-1b and c**).[27] The iGLC platform is constructed of perfusion and control layers made from PDMS with gas permeability, biocompatibility, and transparency. Three sets of two cell culture chambers (2.1 mm width and 220 µm height) are linked by microfluidic channels (200 µm width and 45 µm height) in the perfusion layer. To integrate the micro-valves and pump, the control layer features a thin and flexible PDMS diaphragm (200×200 µm^2 area and 20 µm thickness), which allows open/close control with our previous microfabrication technology in **chapter 3** (**Fig. 4-2**).[27,192] Because most OoCs lack integrated microvalves, they necessitate the assembly and disassembly of tubes across several devices, reducing the accuracy of control over their interactions. The integrated micro-pump controls the perfused flow more precisely than an external pump within a microfluidic device. Furthermore, it lowers sample loss. Positive hydraulic pressure (150 kPa) delivered by computer-controlled solenoid valves activates the PDMS diaphragms. Individual cell culture chambers can be accessible without cross-contamination, and precise control over sample or reagent entry is possible by microvalves and pump. The integrated sets offer closed-loop medium circulation to recapitulate inter-tissue interactions like GLA, varying the flow rate between 0 and 20 nL min^{-1} by modifying its actuating cycle, which is sufficient for enhancing GLA interaction with a high medium exchange rate (**Chapter 3 section 3.4.2**).

Prior to the cell culture and FFA treatments, we coated the PDMS surface of the cell culture chambers with DDM [193,194] and then Matrigel to reduce the absorption of hydrophobic molecules (e.g. FFAs and AdipoRed fluorescent lipid marker) [195,196] and increase cell adhesion and growth (**Fig. 4-3**). This is a critical problem with using PDMS-based OOCs for drug discovery and *in vitro* disease modelling because small-molecule drug candidates and lipids are absorbed by the PDMS before reaching the target cells, and the concentrations differ from those in a microtiter plate. Under such conditions, the obtained results would be unreliable. DDM is a suitable amphipathic molecule to prevent PDMS absorption because its hydrophobic part binds with the PDMS surface, and the hydrophilic part prevents the absorption of hydrophobic molecules. However, DDM is not capable of promoting cell adhesion and growth on the PDMS surface. Therefore, we tested combining DDM with a subsequent layer of Matrigel. The DDM/Matrigel coating partially prevented the absorption of the AdipoRed fluorescent lipid marker into PDMS (**Fig. 4-6**).
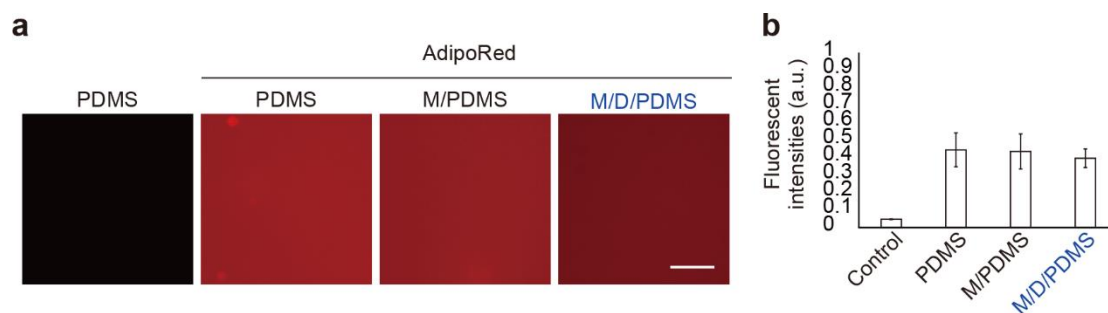
Figure 4-6 Absorption of hydrophobic molecules in PDMS. (a) Fluorescent micrographs of PDMS coated with Matrigel (M/PDMS), Matrigel and DDM (M/D/PDMS), and PDMS without any coating (PDMS) that were treated with the AdipoRed lipid fluorescent dye. The scale bar 100 μm. (b) Fluorescent intensities of AdipoRed dye absorbed in PDMS. The bars and error bars represent the mean ± standard deviations (n = 3).
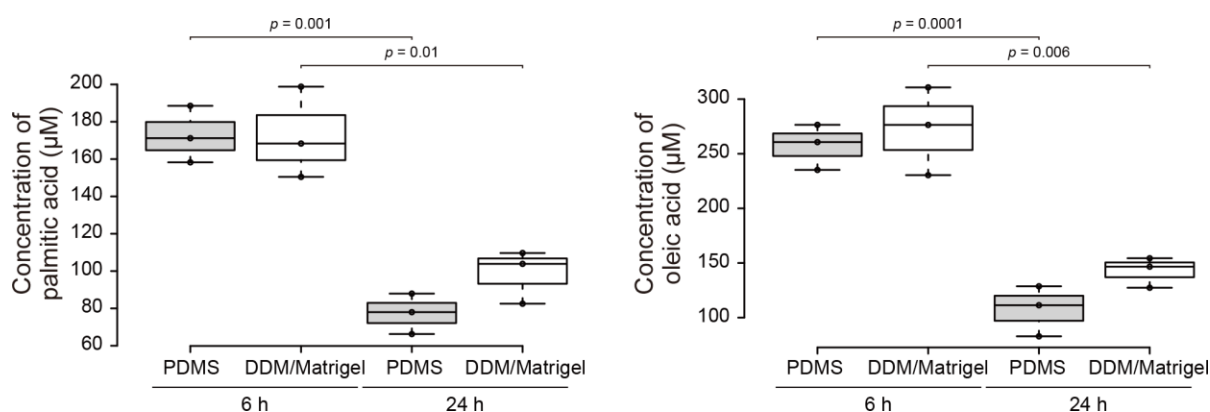
Figure 4-7 Lipid absorption in PDMS. FFA concentrations [left: palmitic acid (initial: 167 μM); right: oleic acid (initial: 333 μM)] in cell culture medium after incubation in PDMS or DDM/Matrigel-coated microfluidic channels for 6 and 24 h. The center lines show the medians. The box limits indicate the 25th and 75th percentiles. The whiskers extend 1.5 times the interquartile range from the maximum and minimum points; data points are plotted as circles. p values were estimated with Student's t-test (n = 3).

Then, we also measured the remaining FFAs [PA and OA molar ratio 1: 2; see Methods] in the cell culture medium after incubation with the coated PDMS (**Fig. 4-7**). PA was not absorbed with both the non-coated and DDM/Matrigel-coated PDMS after 6 h of incubation at 37 °C, whereas it showed absorptions of 53.7% and 40.9%, respectively, after 24 h of incubation. OA showed absorptions of 22.0% and 17.4%, respectively, after 6 h of incubation, and absorptions of 67.4% and 56.7%, respectively, after 24 h of absorption. These results suggest that, although the DDM/Matrigel coating slightly mitigated the absorption of both PA and OA into PDMS after 24 h of incubation, most of the FFAs were still absorbed. Therefore, we changed the medium every 6 h during the experiments. However, further improvements need to be made to prevent PDMS absorption, or other structural materials should be used for the OOCs.[12,197]

4.3.2 Closed-loop flow for gut and liver cell culturing

To recapitulate GLA *in vitro*, Caco-2 and HepG2 cells were introduced into individual cell culture chambers in the iGLC platform without cross-contamination but with a closed circulation flow (**Fig. 4-4b**). To confirm that the iGLC platform allows sustainable cell cultivation, the Caco-2 and HepG2 cells were cultured with a medium circulation flow of 15 nL min⁻¹ for 7 days and evaluated with a Calcein AM fluorescent cell viability indicator (**Figs. 4-8a** and **b**). Although Caco-2 cells generally take around 21 days to obtain functionality, perfusion conditions allow Caco-2 cells to express their functions within a shorter time, like 7 days.[99,198] Thus, we chose a 7-day cultivation time for recapitulating GLA *in vitro*. For comparison, we also tested separately cultured Caco-2 and HepG2 cells in cell culture chambers with a flow of 15 nL min⁻¹ and under static conditions. In light of computational fluid dynamics (CFD), 3.53×10^{-4} dyne cm⁻² of fluid shear stress (FSS) was generated on cells (**Fig. 4-9**). The flow condition did not affect the viability of HepG2 cells, which showed only some improvement with a circulation flow. The Caco-2 cells showed increased viability with a circulation flow than under static conditions. The fluorescent intensity of Calcein AM increased by approximately 7.4-fold with a circulation flow. Caco-2 cells have previously been reported to show improved functionality and viability when cultured under continuous perfusion on a microfluidic device within 1-week culture.[99,198] This proves that the iGLC platform provides better circulation flow conditions for both Caco-2 and HepG2 cells.
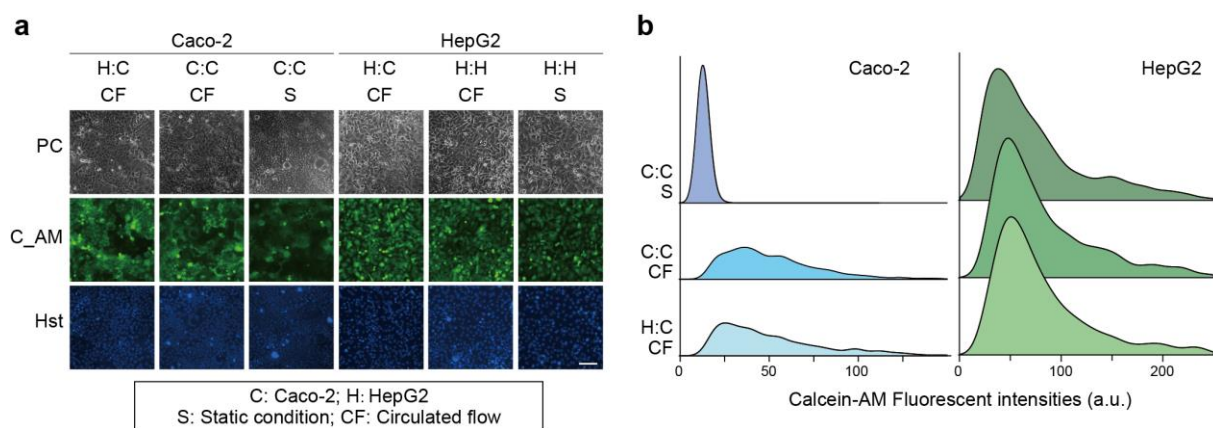
Figure 4-8 Establishment of the GLA in the iGLC platform. (a) Phase-contrast (PC) and fluorescent micrographs in the iGLC platform and stained with Calcein AM (C_AM) and Hoechst 33258 (Hst). Caco-2 (C:C) and HepG2 (H:H) cells under circulation flow (CF) and static conditions (S). Co-cultured Caco-2 and HepG2 cells (C:H). The scale bar represents 100 μm. (b) Ridgeline plots showing single-cell profiling of Caco-2 and HepG2 cells stained with Calcein AM. The *p*-values were estimated with the Tukey–Kramer test and are presented in Supplementary Table S4-1 for the Caco-2 and Supplementary Table S4-2 for HepG2 cells **Appendix III**.
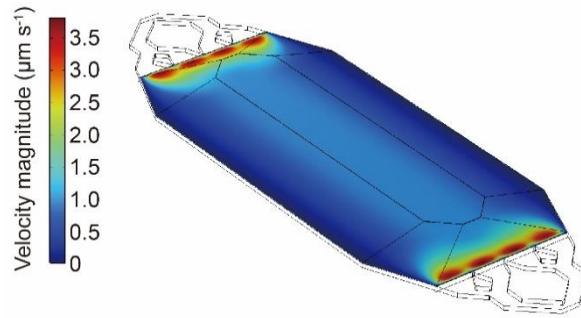
Figure 4-9 Simulated flow field profile in the cell culture chamber. Cell culture chamber flow profile was shown in a 0 to 1 μm s^{-1} flow velocity range; the estimated mean fluid shear stress on cells was around 3.53 × 10^{-4} dyne cm^{-2}.

4.3.3 Inducing the NAFLD

To induce NAFLD in the iGLC platform, we used FFAs represented by a mixture of PA and OA, which is typical of Western diets.[199] As shown in **Fig. 4-4a**, prior to the FFA treatment, Caco-2 and HepG2 cells were cultured in the iGLC platform with DMEM supplemented with 10%(v/v) FBS, and then, replaced to serum-free DMEM for 12 h to ensure cell starvation.
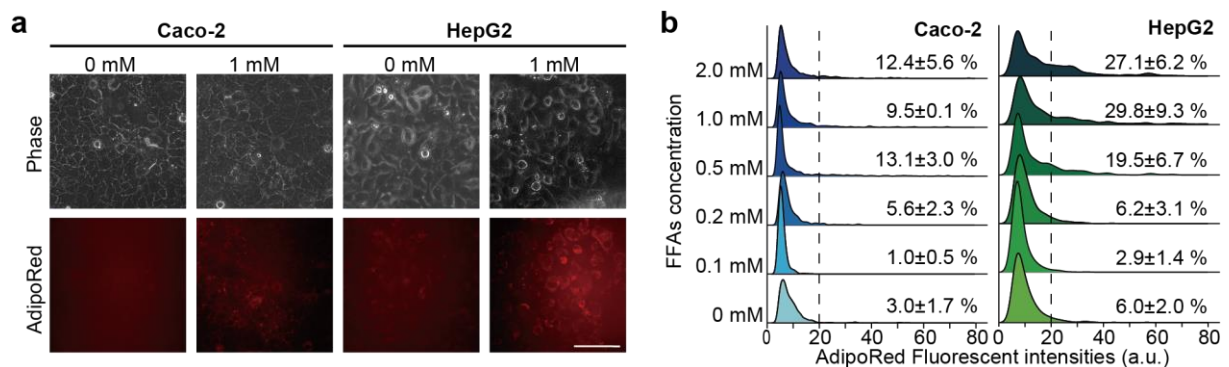
Figure 4-10 Evaluation of FFAs accumulation in Caco-2 and HepG2 cells for 1-day FFAs treatment. (a) Phase contrast and fluorescent micrographs of Caco-2 and HepG2 cells stained with AdipoRed lipid fluorescent dye. Scale bars represent 100 μm. (c) Ridgeline plots to evaluate FFA accumulation. The *p*-values were estimated with the Tukey–Kramer test and are presented in Supplementary Tables S4-3 and S4-4 for the Caco-2 and HepG2 cells, **Appendix III**.

Then, a series of FFA concentrations from 0 to 2 mM was introduced into the iGLC platform, and the cells were incubated for 24 h with medium circulation. To evaluate the FFA accumulation in the mono-cultured Caco-2 and HepG2 cells, the cells were stained with AdipoRed lipid fluorescent dye to visualize the intracellular lipids (**Fig. 4-10**). HepG2 cells showed intracellular FFA accumulation that was dose-dependent, and 1 mM FFAs treatment was used for further studies. Lipid droplet accumulation

in hepatocytes is a hallmark of NAFLD[200] and appeared in our model. During the FFAs treatments, because we used the serum-free medium supplemented with 1% (w/v) BSA to minimize the effects of cell proliferation, both mono-cultured Caco-2 and HepG2 cells showed the reduction of cell proliferation and would not interfere with the cell treatment because over cell growth (**Figure 4-11**).
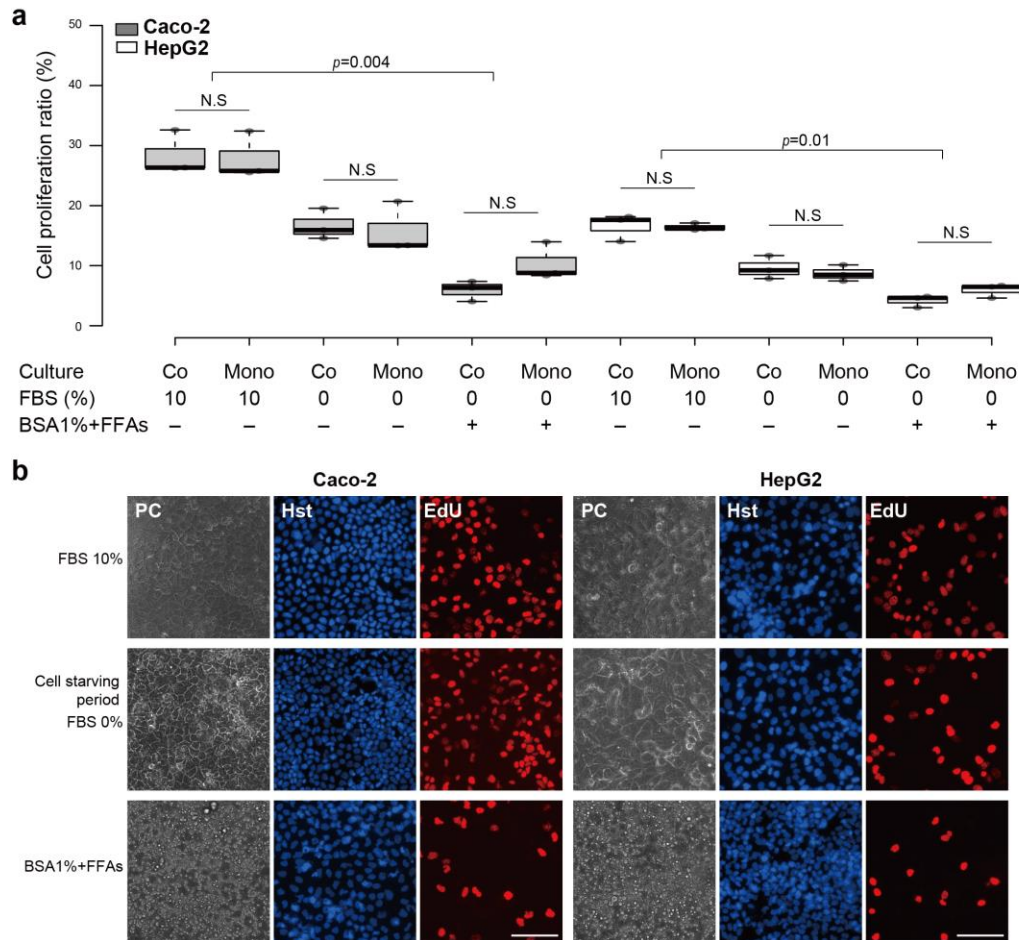
Figure 4-11 Evaluation of cell proliferation of Caco-2 and HepG2 cells in iGLC. (a) Box plot to evaluate cell proliferation of Caco-2 and HepG2 cells in DMEM cell culture with 10% FBS or 1% BSA (contained with 1 mM free fatty acids; FFAs), under co- or (Co) or mono-culture (Mono) conditions for 7-days. (b) Longer-term maintaining the cell culture of Caco-2 and HepG2 cells. The scale bar represents 100 μm. The center lines show the medians. The box limits indicate the 25th and 75th percentiles. The whiskers extend 1.5 times the interquartile range from the maximum and minimum points; data points are plotted as circles (n = 3). *P*-values were estimated with Student's t-test. N.S. means no significant difference. FBS 0% means the cell in starving period, i.e. day 7.5 in **Fig. 4-4**.

Then, we examined two treatment periods, such as 1 and 7 days, representing NAFLD initiation and progression, respectively. We also confirmed that the FFAs treatment for 7 days increased intracellular lipid accumulation in mono- and co-cultured Caco-2 and HepG2 cells (**Figs. 4-12a and b**). The co-

cultured Caco-2 cells showed less lipid accumulation than those of mono-cultured ones, but HepG2 showed increased lipid accumulation.
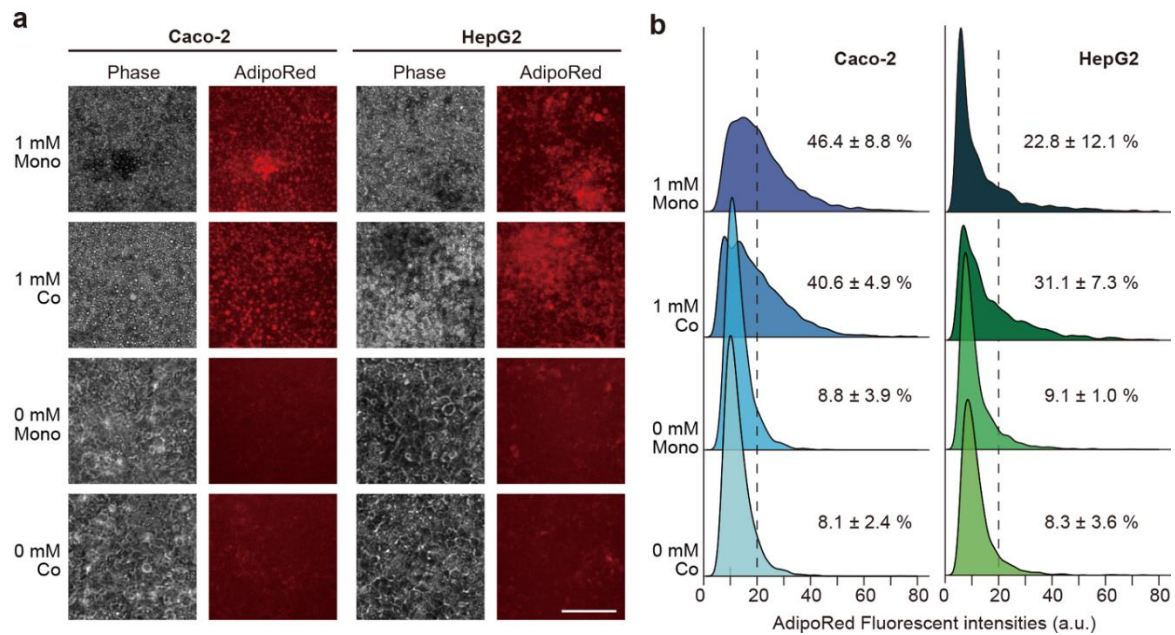
Figure 4-12 Lipids accumulated in both Caco-2 and HepG2 cells after 7-day FFAs treatment. (a) Phase contrast and fluorescent micrographs of Caco-2 and HepG2 cells treated with FFAs (0 and 1 mM) for 7 days stained with AdipoRed lipid fluorescent dye. The scale bars represent 100 μm. (b) Ridgeline plots to evaluate FFA accumulation in individual cells [Caco-2 (left) and HepG2 (right)] after FFA treatment for 7 days. The p-values were estimated with the Tukey–Kramer test and are presented in Supplementary Tables S4-5 and S4-6 for the Caco-2 and HepG2 cells, respectively **Appendix III**. Cells with over 20 of AdipoRed fluorescent intensity were considered as lipid accumulated cells.

We also carried out Annexin-V staining to evaluate the apoptotic status after FFAs treatment. For comparison, the cells were also treated with 1 μM of staurosporine (STS), which induces apoptosis. Although PA accumulation has been reported to cause cytotoxicity by 1-day of treatment,[201,202] the apoptotic staining (**Fig. 4-13a**) followed by quantitative single-cell profiling (**Fig. 4-13b**) results suggested that the 7-day FFA treatment induced apoptosis in mono-cultured Caco-2 and HepG2 cells, whereas 1-day treatment did not induce apoptosis (**Supplementary Fig. S4-1 in Appendix II**). But co-cultured Caco-2 and HepG2 cells showed a reduction of apoptosis. Notably, the expression of albumin (ALB), one of the functional markers of hepatocytes, in mono-cultured HepG2 cells was not changed by FFAs treatment, but co-cultured HepG2 cells demonstrated increased ALB expression (**Fig. 4-13c and 4-13d**). This suggests that HepG2 cells co-cultured with Caco-2 cells display improved functionality.
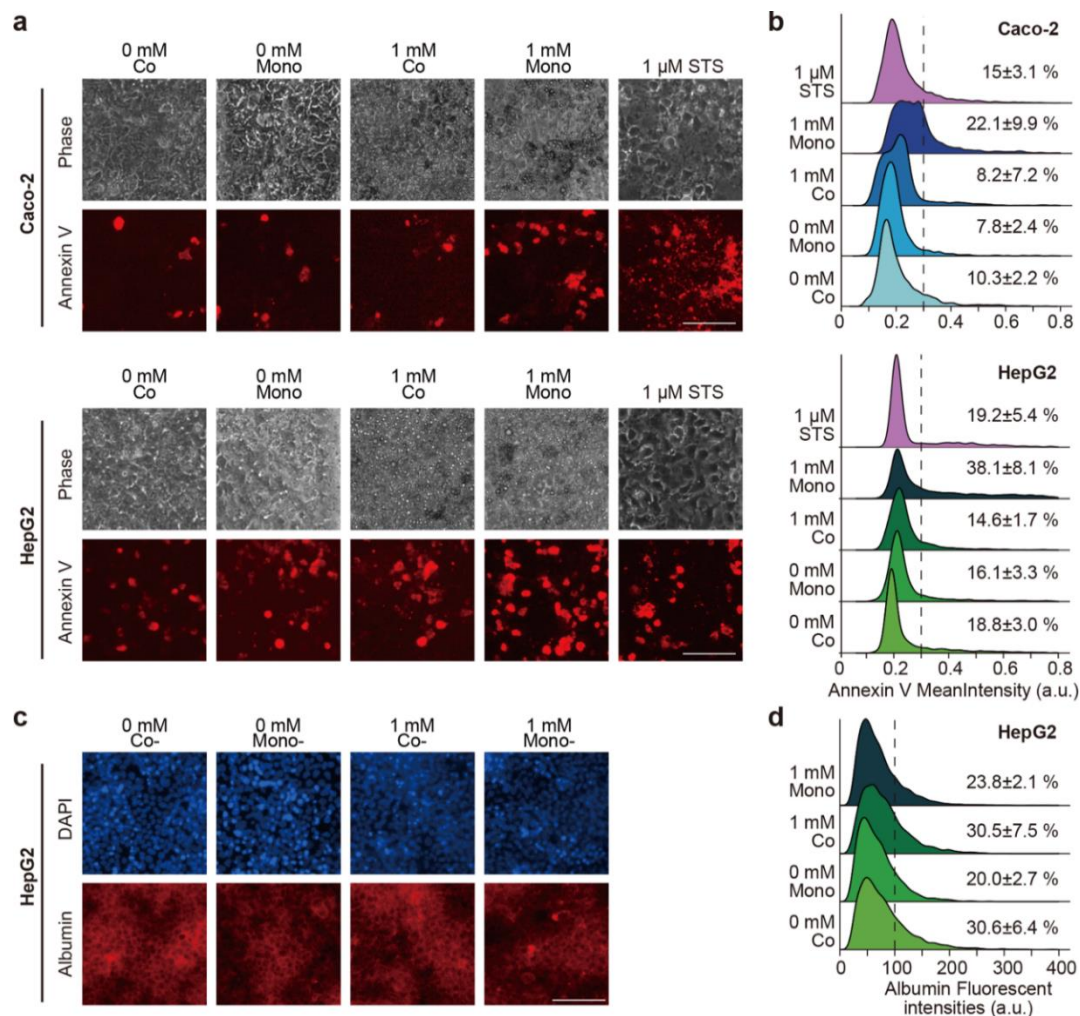
Figure 4-13 Apoptosis in both Caco-2 and HepG2 cells after FFAs treatment for 7 days. (a) Phase contrast and fluorescent micrographs. The scale bars represent 100 μm. (b) Ridgeline plots to evaluate individual apoptotic cells. For comparison, cells were treated with 1 μM of staurosporine (STS) for 24 h. Cells with over 0.3 of annexin V fluorescent intensity were considered as apoptotic cells. (c) Phase contrast and fluorescent micrographs of HepG2 albumin expression. (d) Ridgeline plots to evaluate individual HepG2 cells with human albumin expression. Cells with over 100 of ALB fluorescent intensity were considered as ALB-expressing cells. The *p*-values were estimated with the Tukey–Kramer test and are presented in Supplementary Table S4-7 for the Caco-2, Tables S4-8 and 4-9 HepG2 cells, respectively **Appendix III**.

To further evaluate the cellular phenotypes after the FFA treatment in detail, we stained cells with Calcein AM and Hoechst 33258 fluorescent dyes. This was followed by high-content analysis (HCA) using the CellProfiler computer-guided single-cell analysis software (**Fig. 4-14, Supplementary Figs. S4-2 and S4-3 in Appendix II**).[190,203] In general, the Calcein AM and Hoechst 33258 dyes are used as cell viability function, and nucleus markers. The Calcein AM staining can also be applied to evaluating the cell and nucleus morphologies to obtain cellular parameters for HCA.[204,205] Moreover, recent advances in single-cell profiling based on high-content images, like *t*-distributed stochastic neighbor

embedding (t-SNE), have allowed the quantitative understanding of individual cellular status with high-dimensional cellular parameters and visualizing such parameters in a two-dimensional map.[206] We analyzed microscopic images to quantify 68 cellular parameters (**Supplementary Table S4-10 in Appendix III**) for each cell of Caco-2 and HepG2 cells with 1 mM FFA for 7 days (**Fig. 4-14**). We identified specific parameters that could be distinguished between non-treated and FFA-treated cells that are associated with the cellular shape (AreaShape_FormFactor, AreaShape_MeanRadius and AreaShape_EquivalentDiameter), Calcein AM intensity (Intensity_LowerQuartileIntensity, Intensity_MeanIntensity, Intensity_MaxIntensity), nucleus shape (Nucleus_AreaShape_FormFactor), and Hoechst 33258 nuclei intensity (Intensity_LowerQuaterileIntensity, Intensity_MeanIntensity, Intensity_MaxIntensity and Intensity_MinIntensityEdge). Notably, for the Caco-2 cells, the most distinguishing features were the cellular shape (AreaShape_EquivalentDiameter), Hoechst intensity (Intensity_MaxIntensity) and Calcein AM intensity (Intensity_MaxIntensity) (**Fig. 4-14a**). However, for the HepG2 cells, the most distinguishing features were the Calcein AM intensity (Intensity_MeanIntensity and Intensity_MaxIntensity), nonetheless, the FFAs-treated HepG2 cells showed a reduction of these features (**Fig. 4-14b**). Thus, HCA-based on simple cell and nucleus staining can be used to identify minute cellular phenotypic changes upon FFA treatment that cannot be distinguished by molecular apoptotic markers. Because the iGLC platform does not require the use of cell culture inserts, it allows such HCA-based single-cell profiling to be carried out.
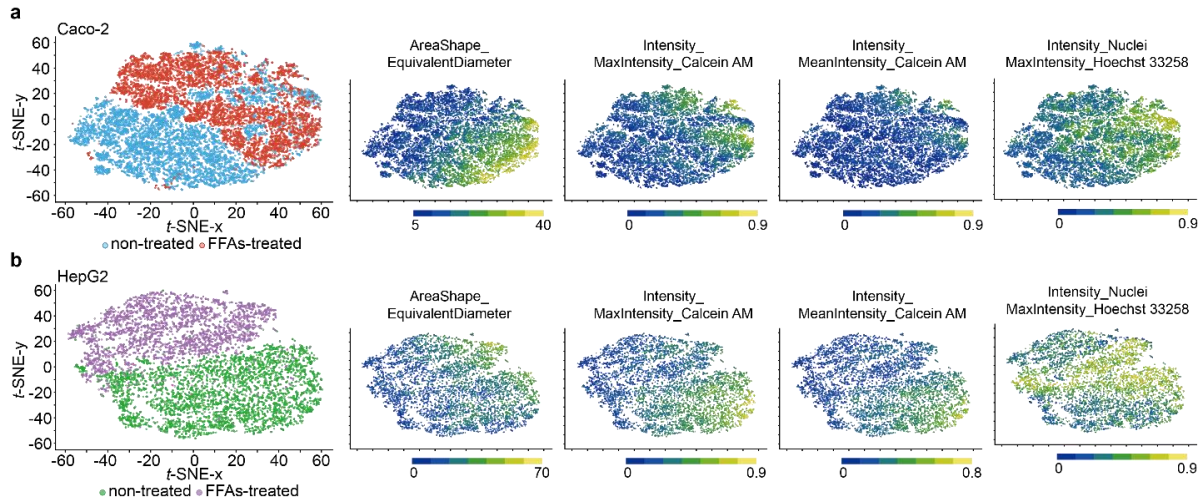
Figure 4-14 Single-cell profiling for the t-SNE analysis. a, b, Two-dimensional t-SNE plots of microscopic single-cell profiling of Caco-2 (a) and HepG2 (b) co-culture treated with 1 mM of FFAs or no treatment and stained with Calcein AM cellular and Hoechst 33258 nuclei markers. The most distinguishable cellular parameters are shown in the corresponding t-SNE plots as well as the boxplots in Supplementary Fig. S4-3 **Appendix II**. The *p*-values are presented in Supplementary Tables S4-11 and S4-12 **Appendix III**.

4.3.4 RNA-sequencing analysis of GLA interaction and NAFLD progression

To elucidate the effects of the FFA treatments and crosstalk via co-culturing on gene expression, we performed mRNA-seq, followed by PCA on the differentially expressed genes (DEGs), which were defined by an analysis of variance (ANOVA) (**Table 4-1, Table 4-2**, **Figs. 4-15a, 4-15b**, **Supplementary Figs. S4-4, S4-5 Appendix II**). We identified that 654 and 1330 genes in Caco-2 and HepG2 cells, respectively, were differentially expressed among the mono- and co-cultured conditions with or without 1 mM FFAs treatments for 7 days. In the case of Caco-2 cells, the PC1 axis distinguished mono- and co-cultured conditions, whereas the PC2 axis distinguished FFAs treatment. Notably, the co-cultured conditions showed less effects on gene expression altered by FFAs treatments. In contrast, in the case of HepG2 cells, the PC1 axis clearly distinguished HepG2 cells treated with 1 mM FFAs under the co-culture conditions from the other conditions. The PC2 axis in PCA of HepG2 also showed changes in gene expression associated with FFAs treatment; however, co-culturing reduced the changes of gene expressions by FFAs treatment.

The heat map of K-means clustering for DEGs in Caco-2 cells showed several clusters with similar up-regulated gene expression patterns by co-culture conditions, compared to mono-culture conditions (Clusters 1, 3, 5 and 10 in **Fig. 4-15c**). These clusters were related to cell cycle and metabolic processes, as suggested by gene-ontology (GO) terms (**Supplementary Figs. S4-6** and **S4-7 in Appendix II**). We also observed downregulated genes specific to the co-culture condition in Caco-2 cells (Clusters 2 and 6), however, the numbers of genes were too small to obtain sufficient interpretations from a GO analysis. In the case of HepG2 cells, Cluster 18 on the heat map for DEGs showed unique upregulated genes in the co-culture condition, whereas only Cluster 16 showed downregulated genes specific to the co-culture condition (**Fig. 4-15d,** and **Supplementary Figs. S4-8** and **S4-9 in Appendix II**).

We then compared the effects of FFA treatment under mono- and co-cultured conditions on gene expression in Caco-2 and HepG2 cells. The mRNA-seq results revealed that Caco-2 cells showed elevated expression of genes associated with mitosis (Cluster 8 in **Figs. 4-15a and 4-16a**), whereas the stress-responsive genes (Cluster 7 in **Figs. 4-15a and 4-16a**) were down-regulated. In contrast, HepG2 cells treated with FFAs displayed elevation in expression of genes related to the cell cycle (Clusters 12 and 17 in **Fig. 4-16b**),[207] and suppression in expression of genes associated with cell-cell adhesion and nucleic acid transport (Cluster 15 in **Fig. 4-16b**).

Overall, the differential gene expressions associated with co- and mon-culture were summarized into each cluster with their biological meaning by GO terms analysis in **Table 4-1 and 4-2**. The co- and mon-culture have a significant effect on the HepG2 and Caco-2 cell behaviors in both control and FFAs treatment conditions.
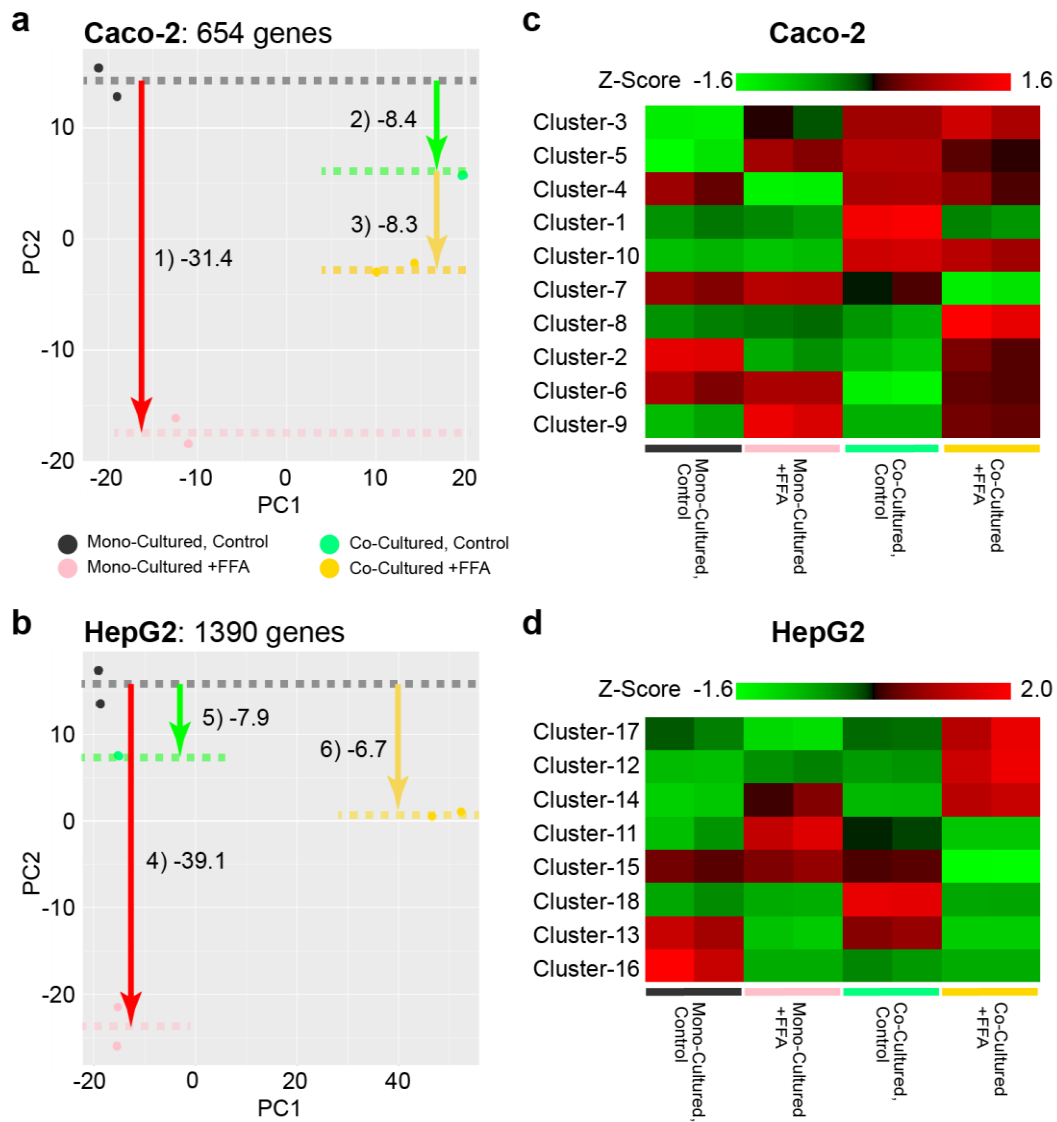
Figure 4-15 Gene expressions of the effects of FFAs treatment for 7 days and crosstalk with the *in vitro* human GLA model. a, b, PCA results for DEGs obtained from the Caco-2 (a) and HepG2 (b) experimental sets. The mean PC2 values among the replicates are shown with dotted lines. For these diagrams, the gene name and change direction shown in a, b were considered. c, d, Heat maps for the DEGs. Z-values of the expression profiles are shown.
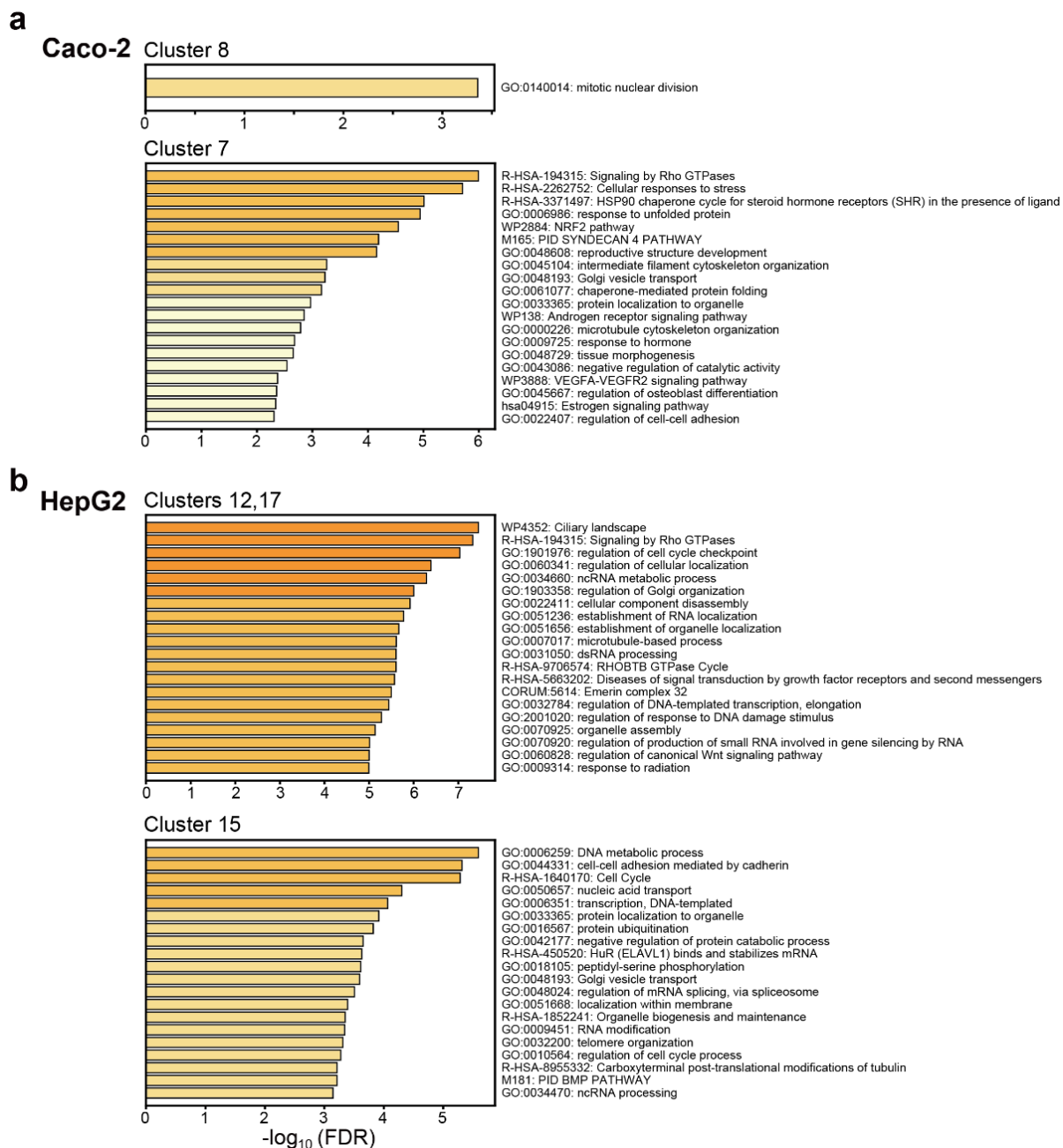
Figure 4-16 Bar graphs showing gene enrichment related to certain GO terms and pathways for representative K-means clusters of FFA-treated Caco-2 (**a**) and HepG2 (**b**) cells under mono- and co-cultured conditions. The other clusters were shown in Supplementary Fig. S4-6 to Fig. S4-9.

Table 4-1 Caco-2 cells Gene-ontology terms analysis of Co- and mono-culture conditions in each cluster. Co-culture as the comparing target.

Clusters	Conditions	Expression patterns	Biological meaning
Cluster 1	Control	Upregulation	Cell cycle and metabolic process
Cluster 2	Control	Downregulation	Antigen processing (non-obvious)
Cluster 3	Control	Upregulation	Cell cycle and metabolic process
Cluster 4	FFAs	Upregulation	Metabolic process
Cluster 5	Control	Upregulation	Cell cycle and metabolic process
Cluster 6	Control	downregulation	Viral process (non-obvious)
Cluster 7	FFAs	downregulation	Stress Response and tissue morphogenesis
Cluster 8	FFAs	Upregulation	Mitosis
Cluster 9	Control	non-obvious	RNA biosynthetic process (non-obvious)
Cluster 10	Control	Upregulation	Drug and small molecule metabolism process

Table 4-2 HepG2 cells Gene-ontology terms analysis of Co- and mono-culture conditions in each cluster. Co-culture as the comparing target.

Clusters	Conditions	Expression patterns	Biological meaning
Cluster 11	FFAs	Downregulation	Cellular responses to stress and intracellular signal transduction
Cluster 12	FFAs	Upregulation	Cell cycle
Cluster 13	Control	non-obvious	non-obvious
Cluster 14	FFAs	non-obvious	non-obvious
Cluster 15	FFAs	Downregulation	Cell-cell adhesion and nucleic acid transport
Cluster 16	Control	Downregulation	Microtubule-based movement
Cluster 17	FFAs	Upregulation	Cell cycle
Cluster 18	Control	Upregulation	Plasma membrane bounded cell projection assembly and glycerolipid metabolic process

4.4 Discussions

4.4.1 Enhanced GLA interaction through closed-loop perfusion

We established the human iGLC platform to investigate the GLA response to FFAs for a NAFLD model. Although OOCs have been used to study NAFLD, the iGLC platform demonstrates several advantages based on its application of microfabrication technology. Integrating the micro-valves and a pump in the platform enables both accessibility to individual cell culture chambers without undesired cross-contamination and closed medium circulation to mimic human GLA.

To investigate the effects of FSS by the closed circulation flow on the cells, we conducted CFD to estimate the FSS by closed-circulation flow, for which the result was 3.53×10^{-4} dyne cm^{-2} (**Fig. 4-9**). Under such a flow condition, Caco-2 cells showed increased cell viability (**Fig. 4-8a**), although HepG2 cells did not change (**Fig. 4-8b**). A number of previous reports suggested that Caco-2 cells functionality improved by applying the perfusion flow at over 0.0002 dyne cm^{-2}, which is similar to our tested FSS. [23,110,158,208] Additionally, functional activation by FSS in HepG2 cells has also been reported, but it requires a higher FSS of over 0.1 dyn cm^{-2}.[115,209]

Notably, co-culturing HepG2 and Caco-2 cells in a closed-loop perfusion environment increased crosstalk communications by a factor of 10 to 100 compared to the earlier gut-liver MPS platform.[210] It significantly changed gut and liver gene expression profiles, compared to mono-cultured cells (Clusters 1, 3, 5, 10 and 18 in **Figs. 4-15c, 4-15d,** and **Supplementary Figs. S4-6 to S4-9 in Appendix II**). The upregulated genes in the Caco-2 cells were related to 'Mitotic G1 phase and G1/S transition', 'Respiratory electron transport, ATP synthesis by chemiosmotic coupling, and heat production by uncoupling proteins', 'positive regulation of spindle checkpoint' and 'small molecule catabolic process'. Most of them are associated with cell cycle and metabolic processes, but the cell proliferation analysis did not show a significant difference between co- and mono-cultured Caco-2 cells (**Fig. 4-11**). Thus, such gene expressions in Caco-2 cells co-cultured with HepG2 cells did not have an impact on changing cell cycles and proliferation. In contrast, HepG2 cells upregulated genes showed GO terms of 'plasma membrane bounded cell projection assembly' (Cluster 18 in **Supplementary Fig. S4-9 in Appendix II**), and downregulated genes showed 'microtubule-based movement' (Cluster 16 in **Supplementary Fig. S4-9 in Appendix II**). Similarly, we could not observe obvious cellular phenotypes associated with gene expression changes.

4.4.2 GLA communications for NAFLD progression

To recapitulate the NAFLD-like GLA *in vitro*, FFAs were administered in the iGLC platform (**Fig. 4-4a**). Although lipid accumulation occurred in both Caco-2 and HepG2 cells treated with FFAs for 7 days (**Figs. 4-12a and b**), the numbers of apoptotic Caco-2 and HepG2 cells in the co-culture condition were significantly reduced compared with those of mono-culture conditions (**Fig. 4-13**).

In the case of Caco-2 cells, FFAs treatment for 1 day did not affect apoptotic cellular status in both conditions (**Supplementary Fig. S4-1 in Appendix II**). The enriched GO terms shown in **Supplementary Fig. S4-5 in Appendix II** were associated with the cellular response to copper ions. Copper is an essential trace element for human physiological processes, including enzymatic metabolism.[211] Dysregulation of intracellular copper ions generates reactive oxygen species (ROS) and metabolic imbalance, which results in DNA damage and apoptosis.[212-214] Our results suggest that the Caco-2 cells treated with FFAs for 1 day did not show the apoptotic cellular state with cellular

membrane disruption but initiated DNA damage due to the cellular response to copper ions. In contrast, even though the prolonged 7-day FFAs-treated mono-cultured Caco-2 cells showed increase in the count of apoptotic cells ($22.9 \pm 9.9\%$), the 7-day FFAs-treated Caco-2 cells co-cultured with HepG2 cells had protective effects against lipid-induced apoptosis ($8.2 \pm 7.2\%$) and similar levels were observed in non-treated Caco-2 cells (mono-cultured, $7.8 \pm 2.4\%$; co-cultured, $10.3 \pm 2.2\%$). Previously, although intestinal cells treated with FFAs showed apoptosis due to lipid accumulation followed by an increase in the levels of reactive oxygen species,[215,216] our microscopic single-cell profiling suggests suppression of the apoptotic signaling, which is in agreement with mRNA-seq results shown in **Figs. 4-15a, 4-15c** and **4-16a**, indicating the down-regulation of 'Signaling by Rho GTPase', which is the typical apoptosis-associated signaling pathway.[217]

In addition to the apoptotic status of Caco-2 cells, we also further examined the correlation between phenotypic changes in cellular morphology with gene regulation networks for *in vitro* GLA in the NAFLD-like state by single-cell profiling results (**Fig. 4-14 and Supplementary Fig. S4-2 in Appendix II**). At the initiation stage of 1-day FFAs treatment, the Hoechst 33258 intensity was slightly higher in the non-treated Caco-2 cells than in the FFA-treated Caco-2 cells (**Supplementary Figs. S4-2 in Appendix II**), but at the progression stage by 7-day FFAs treatment, the Hoechst 33258 intensity showed the opposite result, where FFAs-treated Caco-2 cells showed higher intensity than the non-treated Caco-2 cells (**Fig. 4-14a**). In general, the cellular uptake of Hoechst 33258 can occur by either ABC transporters or diffusion via a damaged cellular membrane. The mRNA-seq results of Caco-2 cells treated with FFAs for 1 or 7 days (**Supplementary Figs. S4-5, S4-6, S4-7 in Appendix II**) did not indicate any enriched GO terms associated with transporters (i.e. ATP-binding cassette transporter ABCG2)[218] that may efflux Hoechst 33258 outside the cells. Thus, transporters did not affect the Hoechst 33258 intensity. Therefore, FFAs-treatment might damage the cellular membrane after FFAs treatment, resulting in the increase of the Hoechst 33258 intensity but not induction of apoptosis.

In contrast, the FFA-treated HepG2 cells had the most distinguishable features, such as Calcein AM intensity (Intensity_MeanIntensity and Intensity_MaxIntensity), and FFAs-treated HepG2 cells showed a reduction of these features (**Fig. 4-14b**). Considering that the intensity of Calcein AM represents the cell viability,[219] this result suggests FFAs reduced the viability of co-cultured HepG2 cells. In contrast, we could not see the increase of apoptotic HepG2 cells under co-culture conditions, confirmed by Annexin V staining (**Figs. 4-13a** and **b**). Notably, the mRNA-seq results revealed that HepG2 cells co-cultured with Caco-2 cells increased gene expression associated with cell cycles (Clusters 12 and 17 in **Fig. 4-16b**). In addition, the genes associated with cell-cell adhesion were reduced in FFAs-treated HepG2 cells under co-cultured conditions (Cluster 15 in **Fig. 4-16b**). These results suggested that, as FFAs treatment induced mild damage in HepG2 cells co-cultured with Caco-2 cells, the HepG2 cells transformed from the status of differentiated liver cells to proliferating cells. Cell cycles and cell division are essential to maintain tissue homeostasis, but in diseases, like NAFLD, they often highlight

the imbalance of cell cycle caused by disrupted metabolic signalling.[207] Overall, the results with our platform indicate that HepG2 cells co-cultured with Caco-2 cells were activated towards NAFLD-like gene expression networks with FFA treatment.

4.4.3 Extending the application of iGLC

To make an advanced *in vitro* NAFLD model, cell types used in the model are critical. Previously, the liver micro physiological system (L-MPSs) was reported to recapitulate liver steatosis to liver inflammation and used non-parenchyma cells in the disease progression, such as Kupffer cells, endothelial cells, and stellate cells.[220] Moreover, in this study, we used only Caco-2 and HepG2 cells to recapitulate GLA, but they were originally harvested from different donors, and represent more cancerous characteristics rather than the *in vivo* physiological tissue functions. Instead, the use of human pluripotent stem cells (hPSCs), such as embryonic[221] and induced pluripotent stem cells[222] (hES or iPS cells) will be valuable resources to obtain a variety of functional tissue cells from a single cell source. Because of the recent advancement of gene editing technologies, such as CRISPR/Cas systems,[223] it allows the creation of gene-modified hPSCs used for disease modeling, for which the primary cells are not applicable.

Moreover, as shown in this study, NAFLD was involved in organ-to-organ interaction. Recent reports have suggested that gut microbiota significantly impact NAFLD development and need to be considered for establishing a new NALFD model.[39–41] However, each organ often requires the optimal culture conditions to express its proper functions. Our present iGLC platform could only use the same cell-culture medium to interconnect two different tissues, therefore, the next generation of iGLC platform needs to overcome present co-culture medium issues.

4.5 Conclusions

The iGLC platform represents a new *in vitro* human model for recapitulating physiological and NAFLD pathological conditions with a focus on the GLA. By co-culturing human gut and liver cell lines interconnected via microfluidics in a closed circulation loop, we created a gut–liver-on-a-chip (iGLC) platform as an *in vitro* human model of the gut–liver axis (GLA) for the initiation and progression of NAFLD by treatment with free fatty acids (FFAs) for 1 and 7 days respectively. As an *in vitro* human GLA model, the iGLC platform may serve as an alternative to animal experiments for the investigation of NAFLD mechanisms.

The device was fabricated by a combination of grayscale lithography and multilayer soft lithography with microvalves controlling the circulation flow and cell individual assessability. The gut and liver cells were co-cultured in a closed-loop circulation, with a high tissue-cell-to-circulation-medium ratio.

It was able to present the intensified gut-liver interaction, finding a protective effect of GLA during NAFLD progression. This may be contributing to a further understanding of this 'silent' disease (**discussed in Chapter 1**).

In near future, the iGLC platform combined with HCA and the omics approach may provide deeper insights into NAFLD development for the establishment of new drugs. The iGLC platform can contribute to the development of drugs for not only NAFLD but also a variety of disorders associated with GLA[38], such as inflammatory bowel disease, that do not have any *in vitro* experimental settings.

Therefore, we still need to build a physiologically relevant GLA-MPS, which could advance gut and liver cell function, such as the gut for transporting the molecular and the liver for metabolism. Also, for the NAFLD progression, inflammation development is a key point. These need further investigation and will be introduced in the following chapter (**Chapter 5**).

Chapter 5 Inflammatory bowel disease progression modeling in gut-liver axis microphysiological system

5.1 Introduction

In chapter 4, the non-alcoholic fatty liver disease (NAFLD) was modelled and analyzed with a hepatic steatosis phenotype, revealing the gut-liver axis (GLA) interaction, through the process of disease initiation and progression. We found a protective effect between gut and liver, which reduced the apoptotic cell status. And we found the co-culture has significantly changed their gene expression profiles. However, the device did not model the polarized state of cells, especially the selective permeability of molecular absorption and barrier function of gut epithelial cells. It was a critical concept for the individual treatment to induce disease in one organ and observe the disease progression to another organ. To solve this issue, in this chapter, we build a multilayered microfluidic device GLA-MPS by multilayer soft lithography. To further study the GLA interaction, the inflammation interaction between the gut and liver is studied, which is an important progression for NAFLD.

As discussed in **chapter 1**, GLA is a symmetric relationship that modulates the absorption/prevention of exogenous substances at the gut barrier and metabolic activities in the liver.[224,30] The disruption of GLA functions leads to liver disease progression and gastrointestinal disorders, such as NAFLD and Inflammatory bowel disease (IBD).[225] This is mainly related to the microbiome and bacteria-derived molecular (e.g., Lipopolysaccharides: LPS) in the gut. Consequently, there are ongoing breakthroughs in the research of GLA for disease modeling and therapeutic discovery. However, using animal models as references for GLA is ambiguous due to the complexity of the organ interactions that exist beyond GLA. Therefore, an *in vitro* physiological model must be established to analyze and understand GLA.

So far, GLA-MPS have been recognized as an advance *in vitro* GLA model for studying GLA for the metabolism and inflammation axis.[7,13,30,181,210,226] Compared to standard static cell-culture models, they exhibited superior ability to predict organ-to-organ interactions. However, concerns about flow perfusion control, organ functions, and inter-tissue interaction must be addressed with regard to GLA-MPS. First, distinct physiologically relevant flow perfusions for gut and liver cells must be realized by precise flow control within the chip. In addition, an individual-assessable treatment should be developed to observe the GLA interaction from one organ to another. Furthermore, the cellular polarity of gut and liver cells should be developed for molecular transport. Lastly, the circulatory system must connect two organs in order to enhance inter-tissue interactions.

In particular, the previous GLA-MPSs are based on two approaches: the cell-culture insert in the microtiter plates[210,226] and microfluidic devices.[27,45] For the cell-culture insert system, cellular uptake and transport across the cell barrier (e.g., endothelial cells and intestinal epithelial cells) can be studied with the porous membrane; under porous membrane, a circulation channel could be used to connect

two organs and apply flow perfusion. However, it is difficult to apply an appropriate uniform perfusion flow for the surface of each organ within the insert precisely, because of its macroscopic scale in the millimeter range and lack of a perfusion controlling system. To express their organ cell functions, gut epithelial cells require physiological relevant fluid shear stress (FSS) from the perfusion flow.[227,228] In contrast, using a microfluidic device allows the control of perfusion flow in the planar compartmentalized chambers and the interconnection of two or more tissue cells via a microfluidic channel with an on-chip micropump.[27,45,121] These microfluidic devices have some issues to be addressed; for example, we can apply only one flow rate for the introduced tissues, although the gut and liver require different flow rates to execute their functions properly.[109,115] Furthermore, the device cannot be applied to study organ molecular transport function across the gut barrier because it does not have an apical to basal side transport structure such as a porous membrane substrate on the bottom channel.[45] Thus, there is an urgent need to fulfill these requirements for establishing an advanced *in vitro* GLA model that (i) enables the application of appropriate perfusion flow for the gut and liver, (ii) studies molecular transports across the gut barrier for individual treatment, and (iii) interconnects the gut and liver to study their interactions within a single microfluidic device.
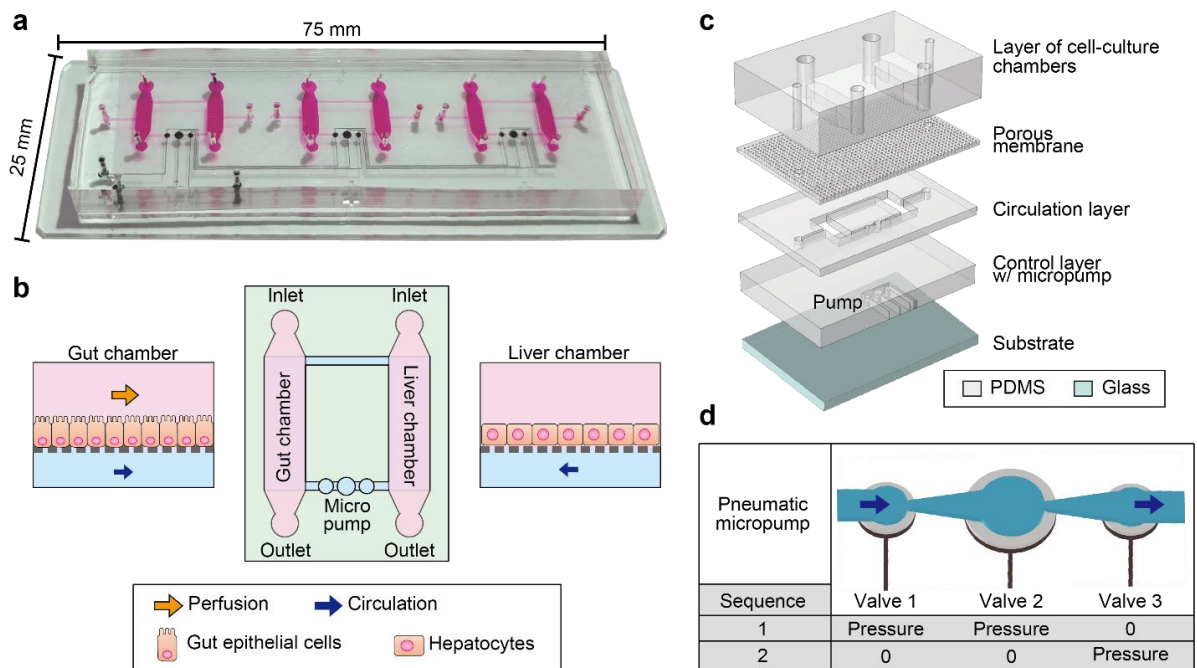
Figure 5-1 Conceptual illustration of the GLA-MPS. (a) Photograph of the GLA-MPS with three sets of *in vitro* GLA and an integrated micropump. (b) Illustration of microfluidic flow channels for establishing GLA-MPS. Gut epithelial cells and liver hepatocytes are cultured in separate cell-culture chambers, with optimal perfusion flow for each cell type and circulation flow connecting them. (c) Illustration of the GLA-MPS that comprises four PDMS layers and the bottom glass layer. (d) Schematic of actuating micropump.

In this chapter, we present a GLA-MPS device that can achieve individual physiological flow perfusion for each organ in the cell-culture chamber, form barrier tissue structure on a porous membrane, and connect two organs with circulation flow (**Fig. 5-1**). The device is fabricated with four-layered microfluidic structures such as a cell-culture layer, porous membrane, circulation layer, and control layer with an on-chip micropump structure. The FSS on cells is estimated by the computational fluid dynamic simulation. The Caco-2 intestinal epithelial and HepG2 hepatocyte-like cells are applied to their own physiologically relevant FSSs to enhance their functions. The circulation flow controlled by the micropump performed closed-loop circulation to interconnect the Caco-2 and HepG2 cell-culture chambers via a porous membrane. The lipopolysaccharide (LPS) and dexamethasone (Dex) were used to stimulate the GLA inflammation disease progression interaction. This device allows the modeling the GLA interaction as an *in vitro* disease model.

5.2 Methods

5.2.1 Chip design

(a) **Device concept and structure** The GLA-MPS device is shown in Figs. 5-1a and b. The GLA-MPS device consists of four polydimethylsiloxane (PDMS) layers and a glass substrate (**Fig. 5-1c and Supplementary Fig. S5-1 in Appendix II**). The four PDMS layers serve as a cell culture layer, porous membrane, circulation layer, and control layer integrated with a micropump. Owing to biocompatibility, gas permeability, and elasticity to enable micro pumping, PDMS meets the requirements as a structural material.[229] The cell-culture layer contains cell-culture chambers (length: 5.3 mm, width: 2 mm, height: 360 μm). A porous membrane has holes with a hole size of 5 μm, pitch of 20 μm, and thickness of 20 μm to prevent cell penetration through the holes and reduce the FSS for cells from the basal side. This membrane divides the cell-culture chamber and circulation channel to create two distinct flows; soluble substances are delivered through holes in the membrane. The control layer incorporates an on-chip micropump for closed-loop circulation. In addition, the external pump was linked to the chamber's inlet so that the FSS could be applied to the apical side of the gut epithelial cells.

(b) **Micropump actuation for closed-loop circulation** An approach that uses a pneumatic micropump-enabled integration with a microfluidic device. We fabricated a pneumatic micropump with PDMS circular diaphragm (**Chapter 3**) to perform closed-loop circulation (**Fig. 5-1d**). The circular diaphragm is integrated into the control layer, consisting of a flexible PDMS diaphragm and an underlying control channel. The diaphragm is actuated by varying the positive hydraulic pressure from the control channel as it bends towards the circulation channel. For easy alignment, this micropump uses three adjacent circular diaphragms with a larger size (diameter: 1 mm) and two smaller ones (diameter: 0.6 mm),

connected to a diffuser and nozzle structure[121](**Chapter 3**) for increasing the one-directional flow and pumping pressure by reducing backward flow. As discussed in the **chapter 3**, the purpose of this 'two phase' actuating method is to simplify the actuating sequence, which reduces the efforts of frequency and pressure control from the pneumatic system. Here, circulatory perfusion flow is controlled by selectively releasing ("0") and actuating ("Pressure") microvalves in the diaphragm "push-up" configuration. "sequence-1" represents actuating both valves 1 and 2 simultaneously, which keeps valve 3 free. Then, "sequence-2" represents the state where only valve 3 is actuating. The actuation time of the 1-mm microvalve is slower than that of the 0.6-mm microvalves because the larger volume of the control layer chamber leads to a high inertial mass.[98] Thus, valve 2 is slower than that of valves 1 and 3, which leads to a peristaltic valve motion to generate output flow in one direction during actuation.

5.2.2 Computational fluid dynamics for fluid shear stress

Computational fluid dynamics analysis was used to estimate the FSS of the cell surface using COMSOL Multiphysics (Ver. 5.6, COMSOL Inc.). In the calculation, the central cross-section along the gut chamber perfusion direction was adopted (**Fig. 5-1b**); the porous membrane's microhole structure was included. The cell-culture medium was defined as an incompressible and Newtonian fluid with identical properties to water at 37 °C (density: 997 kg m^{-3}, viscosity: 6.9×10^{-4} Pa s^{-1}). To model the cell layer, a 10-μm-thick layer covered the upper side of the porous membrane with no direct flow across via the interior wall setting. The channel walls were setting as non-slip boundary conditions. A laminar flow/stationary library was used to determine the net shear rate ($\dot{\gamma}$), and the FSS (τ) was calculated by multiplying the shear rate with the dynamic viscosity of water, as follows.

$$\tau = \dot{\gamma}_{xy}\mu = (\frac{dv_x}{dy} + \frac{dv_y}{dx})\mu \,, \qquad\qquad 5\text{-}1$$

Where $\frac{dv_x}{dy} + \frac{dv_y}{dx}$ is the net shear rate ($\dot{\gamma}_{xy}$) of a surface (x,y) obtained from Navier–Stokes equation in COMSOL, μ is the viscosity of medium.

5.2.3 Chip fabrication by multilayer soft lithography

The GLA-MPS device was fabricated using multilayer soft-lithography (**Fig. 5-2**).[154] For the resist mold of the cell-culture layer, a dry-film type negative photoresist (45 μm; TMMF S2045™, Tokyo Ohka Kogyo) was laminated 8 times to achieve a thickness of 360 μm; similarly, the TMMF was laminated 2 times to achieve a thickness of 90 μm for fabricating the resist mold of the circulation and control layers. The resist mold of the porous membrane layer was fabricated using a spin-coated 25-μm-thick negative photoresist (TMMR S2000™, Tokyo Ohka Kogyo). UV exposure was performed using a mask

aligner (MUM-1000 Series, Japan Science Engineering)[155,156] with Cr-patterned glass masks for the corresponding molds of each layer (cell culture layer: 1000 mJ cm^{-2}, porous membrane: 1500 mJ cm^{-2}, and circulation layer and control layers: 500 mJ cm^{-2}). For the development, the resist molds were put in a propylene glycol monomethyl ether acetate (PGMEA) solution (PM Thinner, Tokyo Ohka Kogyo)) at 23 °C for 20 min. [155,156] The PDMS base and curing agent (Sylgard 184, Dow Corning) mixed in a ratio of 5:1 (w/w) for the porous PDMS membrane and 10:1 for other layers were poured onto resist molds and cured at 25 °C for 48 h. The designed membrane thicknesses were tuned by spin coating to 25 μm for the porous PDMS membrane and 60 μm for the pump membrane.
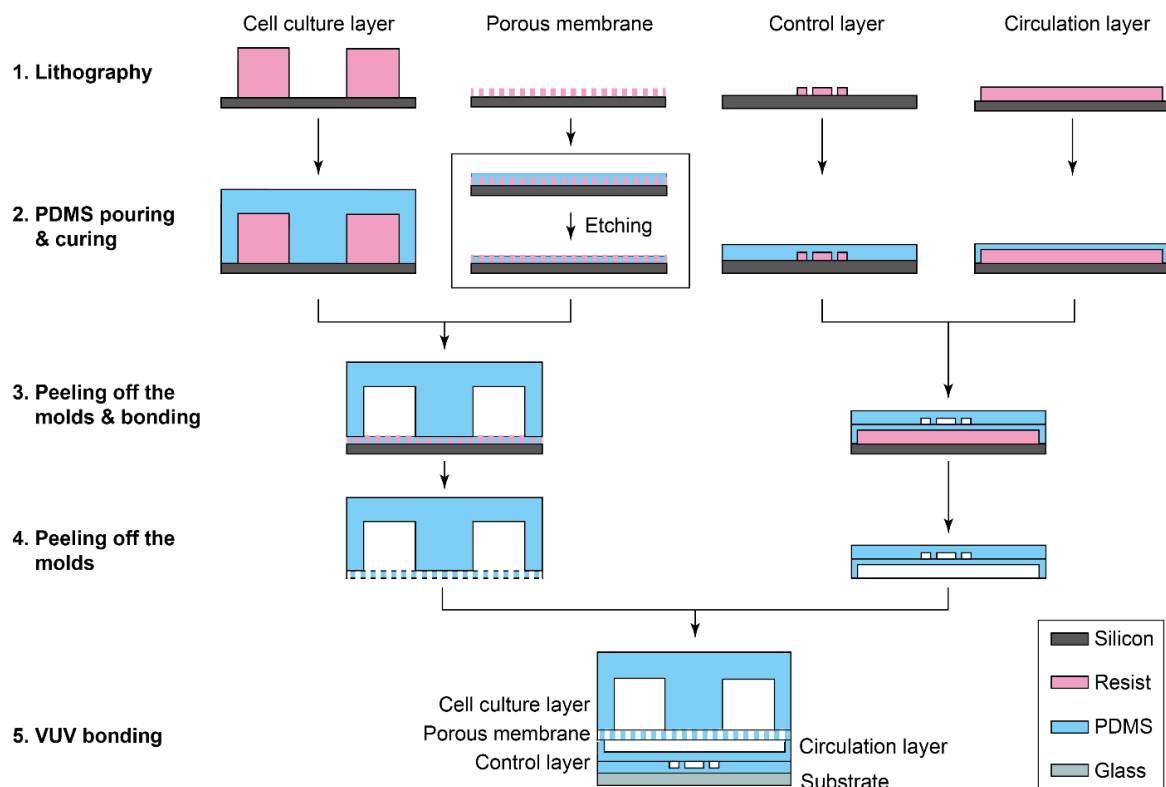
Figure 5-2 Multilayer soft lithography fabrication of the GLA-MPS. Each mold was fabricated with photolithography. The opening of the porous membrane well was conducted by dry etching method.

The cured PDMS layer of the porous membrane was etched with a 5-μm thickness using O$_2$ plasma (power 100 W: pressure 50 Pa: flow rate 50 sccm; FA-1, SAMCO) to open the through holes (**Fig. 5-3**). The cell-culture layer was bonded to the porous PDMS membrane, whereas the control layer was bonded to the circulation layer. The two assembled structures were peeled off from the substrate and bonded together using VUV surface activation (Min-Excimer SUS713, Ushio). Finally, the bonded PDMS layers were bonded on the glass substrate and cured in an oven at 45 °C for 24 h. Low-temperature bonding causes less deformations on the PDMS block, which prevents shrinkage and bending,[230] and leads to flat surfaces for multilayer bonding.
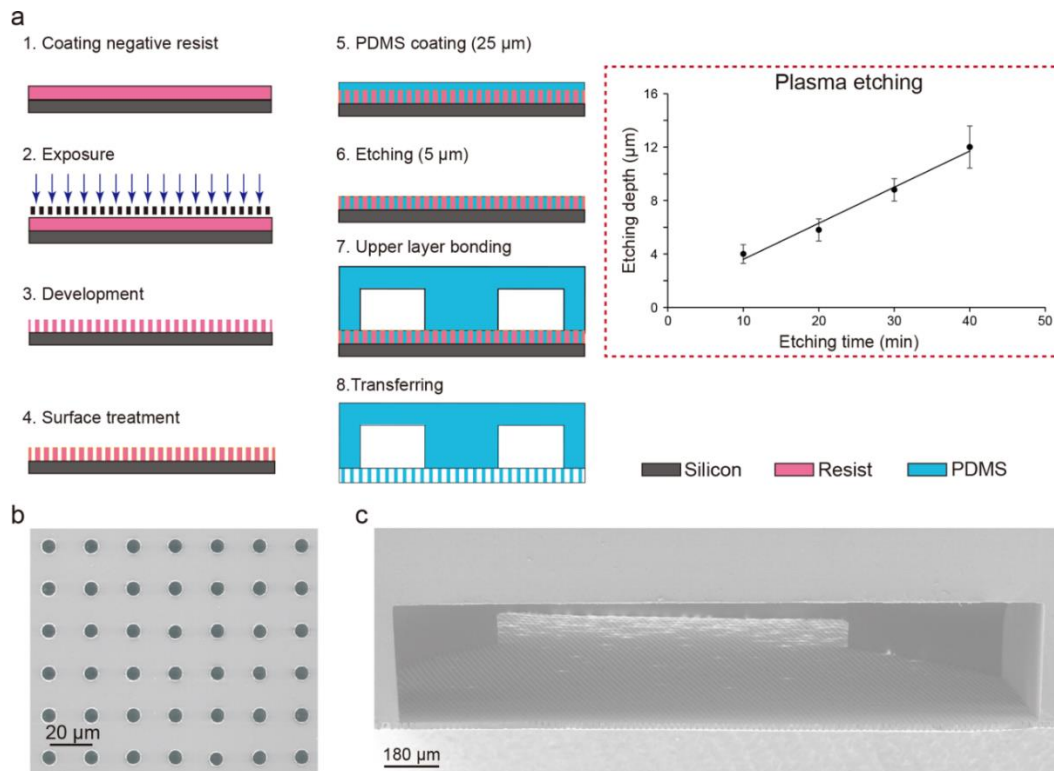
Figure 5-3 Microfabrication of porous PDMS membrane. (a) (1) Negative photoresist was uniformly coated on the silicon wafer with a thickness of 24 ± 1 μm. (2) Contact exposure was performed to generate patterns under a photomask. (3) After post-baking and development, the resist mold was fabricated. (4) The surface of the resist mold was treated with Shin-Etsu Barrier Coat No. 7 for easily peeling off the PDMS. (5) A 25-μm-thick PDMS layer was spin-coated on the resist mold wafer. (6) Plasma etching (O_2: CF_4 = 1:1) with a flow rate of 50 mL min^{-1} was used to etch the PDMS 5 μm and open the through holes. (7) The cell culture layer was bonded to the porous membrane after VUV surface activation. (8) Finally, the assembled structure was transferred to the cell culture layer and peeled off from the wafer. (b) Scanning electron micrographs of the porous PDMS membrane after plasma etching. (c) Cross-section view of the assembled structure with cell culture chamber after transferring a porous membrane.

5.2.4 Evaluating the micropump performance

In **chapter 3**, the micropump performance was evaluated on the open system. With the increase in hydraulic load, the flow rate was reduced. The multilayered GLA-MPS has closed-loop resistance and back-pressure effects. It needs to be measured in the loop system. Therefore, the microbeads tracing method was employed. The microbead tracing (4.5 μm in diameter) was used for visualizing the culture medium circulation flow to characterize the flow rate generated by the on-chip micropump; the flow distances of the beads were measured to measure the flow rate of the circulation loop. Prior to the experiments, the microfluidic channel was coated for 2 hours at 25 °C with 1% (w/v) bovine serum

albumin (BSA, Sigma-Aldrich) in PBS to prevent nonspecific adhesion of beads on flow channels and cell-culture chambers. The beads were suspended in a 1% (w/v) BSA solution at a concentration of 1×10^6 beads mL^{-1} before being introduced into the device. The microbead movement was recorded with a CMOS camera (EO-4010M, Edmond Optics) and a microscope (GX53, Olympus); the microbeads moving average velocity was analyzed with a custom-made MATLAB program (R2020b, MathWorks). Volumetric flow rates were calculated by multiplying the microbeads moving average velocity and the microfluidic channel's cross-sectional area.

5.2.5 Biology treatments and assays

(a) Cell culture From the American Type Culture Collection (ATCC), HepG2 human hepatocellular carcinoma, and Caco-2 human colorectal adenocarcinoma cell lines were obtained. The cells were cultivated in Dulbecco's modified Eagle medium (DMEM) (Sigma-Aldrich, St. Louis, MO, USA) facilitated with 10% (v/v) fetal bovine serum (FBS, Cell Culture Bioscience), 1% (v/v) nonessential amino acids (NEAA, Thermo Fisher Scientific), and 1% (v/v) penicillin/streptomycin (P/S, Thermo Fisher Scientific). Trypsin/EDTA (0.04%/0.03%[v/v]) was used to passage HepG2 and Caco-2 cells every 3 and 7 days, respectively.

(b) Cell culture on a chip and treatment The cell culturing followed the process in **Fig. 5-4**. The chips were sterilized with 70% (v/v) ethanol and ultraviolet light in a biosafety cabinet at 25 °C for 40 min prior to the cell culture on the chips. Then, two chambers in the cell-culture-chamber layer were filled with 1.3% (v/v) Matrigel hESC-qualified matrix (Corning) in DMEM/F12 (Sigma-Aldrich) at 25 °C for 2 h. The cell culture and circulation chambers were washed and filled with a cell-culture medium. The chips were incubated at 4 °C for 16 h to remove all air bubbles from the chips. The next day, after washing the chips with a cell-culture medium warmed at 37 °C, three microliters of cell suspensions of Caco-2 and HepG2 cells (5×10^6 cells mL^{-1}) were introduced into the corresponding cell culture chamber chips; the cell density was 1800 cells mm^{-2}. The chips were placed in a humidified incubator at 37 °C with 5% (v/v) CO$_2$. After 24 h, the cell culture medium was changed to remove the floating dead cells. For the circulation and perfusion, the inlet of the gut culture chambers was connected to a syringe pump (KDS LEGATO 210, KD Scientific Inc.); the micropump was actuated for medium recirculation. For a static cell culture, the cell culture and circulation chamber layers were changed with the cell culture medium every 6 h. The total cell culture on the chip was maintained for up to 9 days. Then, LPS (*Escherichia coli* O111:B4, Sigma-Aldrich) and Dex (Wako) were used to treat Caco-2 cells. LPS and Dex were dissolved in a cell-culture medium at 1 mg mL^{-1} and 200 µM, respectively, as the treatment solutions. After 9 days of culturing in the GLA-MPS, only Caco-2 cells were treated with the

treatment solutions for 4 days. For the 96-well-plate group, in the day 4, the Caco-2 cells was stained with Diaminofluorescein-FM diacetate (DAF-FMDA) to visualize the alive cell inflammation process.
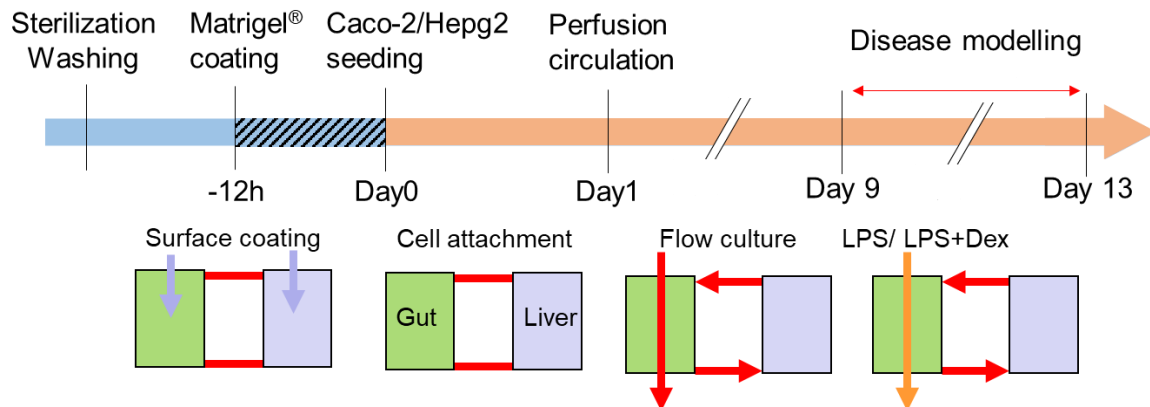
Figure 5-4 The cell culture schedule and treatment process. LPS: lipopolysaccharide; Dex: dexamethasone; Gut: Caco-2 cell; Liver: HepG2 cell.

(c) Live/dead cell assay A cell viability assay was conducted using the NucleoCounter NC-200, Via1-Cassette™ (Chemometec). After the cell culture or treatment, cells in the chips were washed with PBS once by adding 50 μL PBS through the cell culture chamber and the circulation channel. Then, 20 μL of trypsin/EDTA solution was added through the cell culture chambers and incubated at 37 °C for 10 min. After cell detachment, cells in both chambers were separately harvested into a 1-mL tube and diluted to 200 μL with the cell-culture medium. The homogenous cell suspension was aspirated into a Via1-Cassette™ to count the number and ratio of dead/live cells.

(d) Immunocytochemistry After the cell culture and treatment, the cell-culture chambers and circulation layer were washed twice with PBS containing 50 μL of PBS. The cells were fixed with 4% paraformaldehyde (PFA, FUJIFILM Wako Pure Chemical) in PBS for 15 min at 25 °C and permeabilized with 0.1% (v/v) Triton X-100 in PBS for 30 min at 25 °C. The cells were then incubated in a blocking buffer (5% normal goat serum, Vector; 5% normal donkey serum, Wako; 3% BSA, Sigma-Aldrich; and 0.1% Tween-20, Nacalai Tesque, Inc., in PBS) at 4 °C for 16 h. After blocking, the cells were incubated with primary antibodies such as rabbit anti-human ZO-1 IgG (Thermo Fisher Scientific), mouse anti-human albumin IgG (Thermo Fisher Scientific), and mouse anti-human inducible nitric oxide synthase (iNOS) IgG (R&D Systems) in a blocking buffer at 4 °C for 16 h. After washing the primary antibodies with PBS-T twice, the cells were incubated with secondary antibodies such as Alexa Fluor 488-labeled donkey anti-rabbit IgG and Alexa Fluor 647-labeled donkey anti-mouse IgG H&L (Jackson ImmunoResearch) in a blocking buffer at 25 °C for 1 h. The cell nuclei were stained with 300

nM 4,6-diamidino-2-phenylindole (DAPI, Dojindo Laboratories). The DAPI solution (50 μL) was introduced into the chambers and incubated at 25 °C for 30 min; the chambers were washed with PBS.

(e) Permeability assay across cell barrier FITC-dextran (4 kDa, Sigma-Aldrich) was used for the permeability assay.[231] It was dissolved into a cell-culture medium at a concentration of 1 mg mL^{-1} as the working solution. The working solution was introduced into the gut cell-culture chamber and incubated for 4 h. The FITC-dextran in the medium of the cell-culture chamber and circulation channel was separately collected and measured using the Synergy HTX microplate reader (BioTek Instruments). The hydraulic conductivity $K_{dextran}$ was calculated using

$$K_{dextran} = \frac{1}{A \cdot C_0} \cdot \frac{dQ}{dt},$$
5-2

where A, C_0, and dQ/dt represent the transporting surface area of the porous membrane (5.3 mm × 2 mm), original concentration of the FITC-dextran in the gut apical chamber, and amount of FITC-dextran transported across the membrane over the respective time interval, respectively.

(f) Enzyme-linked immunosorbent assays Enzyme-linked immunosorbent assay (ELISA) was performed to measure TNF-α secreted from the cells by following the manufacturer's instructions of RayBio Human TNF-α ELISA kit (RayBiotech). During 4-day stimulation, the cell culture medium from cell culture chambers and the circulation channel were collected, and the secreted TNF-α was measured at 450 nm absorbance by the Synergy HTX microplate reader (BioTek Instruments).

5.2.6 Data acquisition and analysis

(a) Imaging acquisition Confocal microscopic imaging was performed using an Andor Dragonfly 502 system (Andor, UK). This system is built on a Nikon ECLIPSE Ti2-E inverted fluorescence microscope (Nikon, Tokyo, Japan) and equipped with a Zyla 4.2 Plus scientific complementary metal oxide semiconductor (sCMOS) camera (Andor) driven by Fusion (Andor), a CFI Plan Apochromat Lambda 10x dry/0.45 NA (Nikon), motorized XY stage and stage piezo (Applied Scientific Instrumentation, MO, USA), and three lasers (405, 488, and 637 nm). For image acquisition, the lasers were set to 488 nm for ZO-1, 637 nm for albumin, and 405 nm for DAPI.

(b) Imaging quantification The imaging data quantification process was conducted using the CellProfilerTM (the Broad Institute of Harvard and MIT, version 4.07). To reduce the background

staining effect, a mathematically subtracting of the background signal was applied in every image in every calculating cycle using the correctilluminationCalcuate and correctilluminationApply functions (Median filter, 50). Using IdentifyPrimaryObjects, DAPI images were selected, and nuclei were identified. The parameters were set as follows: Typical diameter of objects, from 10 to 40; Threshold smoothing scale, 0.5; Threshold correction factor, 1; Lower and upper bounds on the threshold, 0 and 1; Method to distinguish clumped objects, intensity; Method to draw dividing lines between clumped objects, intensity; default values were used for the other parameters. In IdentifySecondaryObjects, stained total cell images were selected, and nuclei, as the input objects, were selected. The parameters were set as follows: Method to identify the secondary objects, Propagation; Threshold strategy, Global; Thresholding method, Otsu with two classes; Threshold smoothing scale, 0; Threshold correction factor, 1; Lower and upper bounds on the threshold, 0 and 1; Regularization, 0.05. Holes were filled in the identified objects. Objects touching the border of images were not discarded. In the MeasureObjectIntensity, the intensity of nuclei and cells of identified objects were measured.

(c) Statistical analysis The Student's t-test, asymptotic Wilcoxon signed-rank test, and Tukey's multiple comparison test were conducted using *R* software (ver. 3.5.2; https://www.r-project.org/). The *p*-value data was listed in **Appendix III**.

5.3 Results

5.3.1 Simulated results of FSS with the flow rate

The FSS was one of the most important physical factors affecting the cell function and morphology,[115,232] but the previous GLA-MPSs faced challenges in the control. The flow perfusion conditions should be investigated for each organ cell. In this device, we estimated the FSS and flow rates using **equation 5-1**, from COMSOL simulation to investigate whether the GLA-MPS provides proper FSS on cells (**Fig. 5-5**). When the medium perfusion in the gut chamber was performed from 2 to 5 μL min^{-1}, the surface FSS on the apical side of cells had a linear relationship with the external pumping flow rate (**Fig. 5-5a and b**). The mean FSS for the intestinal cells was in the range of 8×10^{-3} to 2×10^{-2} dyne cm^{-2}, which was in the physiologically relevant range[232,233] and could promote gut cell barrier formation and differentiation process.[110,158]

The FSS applied to cells from the basal side through the holes of the membrane was determined using the membrane thickness (h) and circulation flow rate (**Figs. 5-5c and d**). The FSS was reduced dramatically with an increase in membrane thickness. In our setup parameters (20-μm-thick membrane), we found that the surface FSS (1×10^{-8} to 1.2×10^{-7} dyne cm^{-2}) on the basal sides of cells by the

circulation flow were considerably smaller than those of the FSS on the apical side of gut epithelial cells. Thus, in the effect of circulation flow, we not only considered the effects of FSSs of basal sides for the later cell experiments, but we also recognized that circulation flow would mediate communication between the gut and liver cells.

In recent results for the gut on a chip[17], the Caco-2 cells on the porous membrane experienced flow perfusion in the apical side or basal side, which showed an improvement in cell functions. In our device, by using the simulation model, the FSS on cells is well-designed and can be clearly used for investigating their effect on cells from both sides.
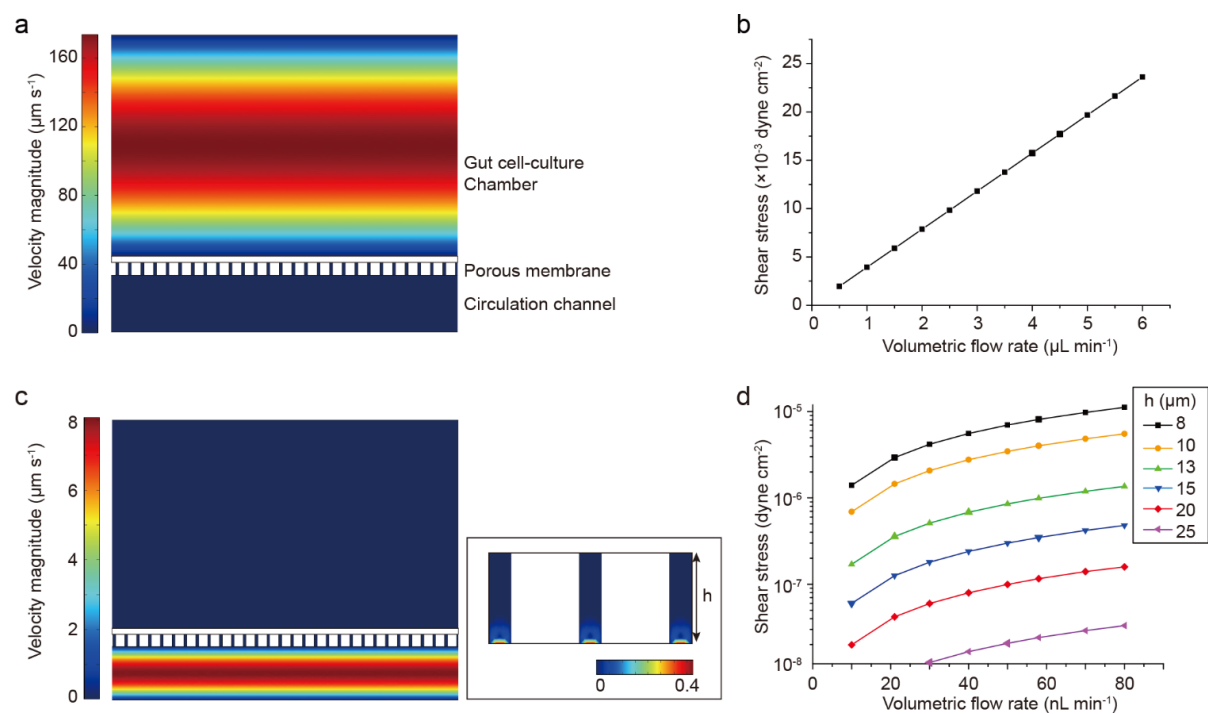
Figure 5-5 Simulated perfusion flow in the GLA-MPS. (a) Simulated perfusion flow in the gut cell culture chamber. (b) Simulated shear stress on the cell surface cultured on the porous membrane. (c) Simulated circulation flow in the circulation chamber. (d) Simulated shear stress by the circulation flow.

5.3.2 Enhancing GLA interaction by on-chip micropump

The micropump working flow rate was closely related to the working load, like fluidic resistance (**Chapter 3**). Especially, in the case of multilayered structures and closed loops, there was heavy load from the hydraulic resistance and back pressure. The hydraulic resistance was around 10^{12}-10^{13} Pa·s m^{-3}. The back pressure was around 50 Pa (5 mm H$_2$O height level).

Therefore, we measured again the flow rate generated by the micropump to induce the flow circulation between two multilayered organ chambers (**Fig. 5-6**). The mean flow rate increased with driving pressure (0–150 kPa) and pumping frequency (0–1.5 Hz). Working frequencies over 1 Hz exhibited no significant differences in the generated flow rates. However, for most of the multilayered structures, the

bonding strength and system leakage were limitations for improving the system's reliability.[234] In contrast, the GLA-MPS has not disassembled until applying over 150 kPa in the control layer for 14 days (data not shown). It was enough for most of the current MPSs to actuate.[234,235] Accordingly, the working pressure was set from 50 to 150 kPa to carry out cell culture and assay in the GLA-MPS; this gave flow rates from 22 to 61 nL min^{-1} for circulation at a 1-Hz working frequency.
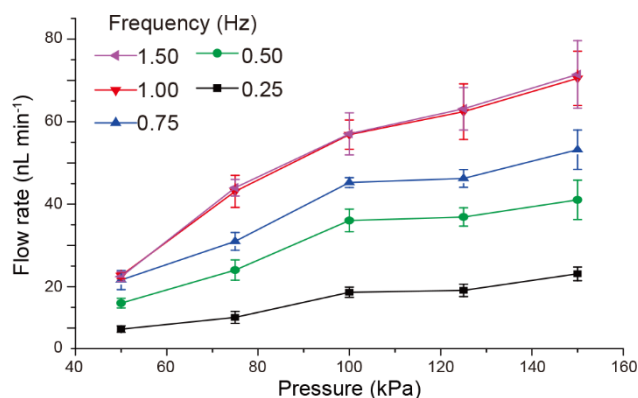
Figure 5-6 Measured mean flow rate of the micropump for pressure-dependent actuation from 0.25 to 1.5 Hz frequency. Each dot represents the mean ± standard deviation (SD) (n = 10).

The flow rate requirement for inducing two organ interactions could be estimated from the exchange ratio of circulation flow rate (q) and flow volume (Q), i.e., q/Q. In this device, the microfluidic system has a circulation flow volume of 1.5 µL. The exchange ratio is 1.5% to 9% in 1 min. In other GLA-MPSs,[30,210] the exchange ratio is approximately 0.25% to 1% in 1 min. Thus, our device realized a more intensified circulation flow (10 times) between the gut and liver. For 9-day cell culture, this flow is sufficient to induce the interaction between two organs compared with other GLA-MPS devices.[30,210] Besides, the on-chip micropump could realize a fine range of flow rate adjustment, which is consistent with the aforementioned FSS simulation circulation flow rate range. Therefore, we could couple the circulation flow with gut perfusion flow to improve the cell function and induce the organ to organ interaction for cell culture experiments.

5.3.3 Recapitulating physiological GLA

Caco-2 gut intestinal[236] and HepG2 hepatocyte-like cells[237] were used and cultured in GLA-MPS to establish *in vitro* GLA. Prior to the cell culture, the surface of the porous membrane should be coated with Matrigel for cell attachment. Here, the porous membrane has a porosity of 3.14% (hole size: 5 µm, pitch: 20 µm, thickness: 20 µm; **Figs.5-3b and c**), calculated based on previous research.[238] By applying the pressure barriers of caplillary[239], the Matrigel could be only coated on the surface of the cell-culture

chamber side (upper side), but not the surface of holes and circulation channel side (bottom side). This is to reduce cell attaching and migrating through the hole of the porous membrane (**Fig. 5-7a**).

After culturing for 1 day under the static conditions for the cell attachment, only Caco-2 cells, but not HepG2 cells, were subjected to the perfusion flow, since the apical side of hepatocytes in the physiological situation is not subjected to the perfusion flow (**Fig. 5-4**). Both Caco-2 and HepG2 cells were maintained for eight days with the circulation flow in the circulation channel. After the culture, Caco-2 and HepG2 cells showed 95% and 92% cell viability, respectively (**Fig. 5-7b**). It demonstrated that the cells could be maintained relatively high cell viability in this device.
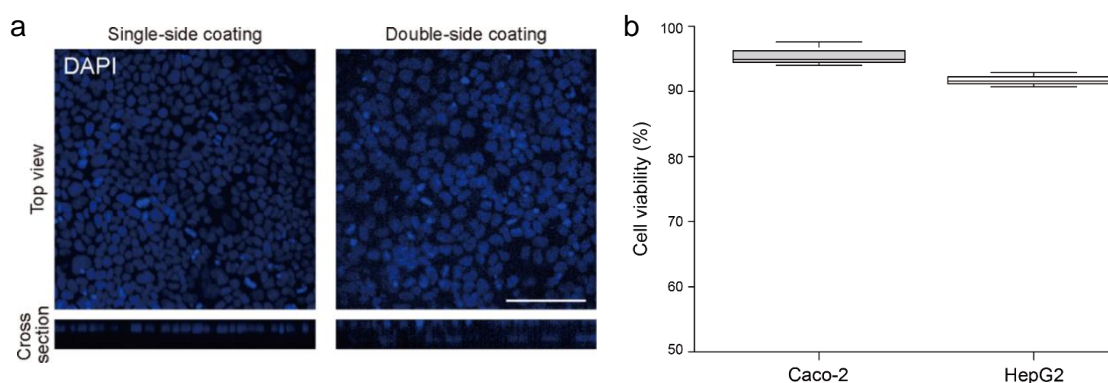
Figure 5-7 Cell culturing on the porous membrane and cell viability under flow perfusion. (a) the single-side coating preventing the Caco-2 cell from penetrating across the pore of the porous membrane compared with double-side coating. Scale bar: 100 μm. (b) Evaluation of cell viability of Caco-2 cells (2 μL min^{-1} of the perfusion flow; 61 nL min^{-1} of circulation flow) and HepG2 cells (without perfusion flow; 61 nL min^{-1} of circulation flow) in the GLA-MPS.

The expression of ZO-1 and albumin (ALB), as functional markers of the gut and liver, respectively, were observed by immunocytochemistry to confirm the functions of cells cultured in the GLA-MPS (**Fig. 5-8**). Caco-2 cells expressed ZO-1 tight-junction protein to form the gut barrier (**Fig. 5-8a**); the increase in flow rates of perfusion flows in the gut cell culture chamber induced the ZO-1 expression in the Caco-2 cells at 5 μL min^{-1} (FSS = 2×10^{-2} dyne cm^{-2}). Further, the circulation flow did not change the ZO-1 expression in the Caco-2 cells without perfusion flow; instead, it induced ZO-1 expression in addition to the perfusion flow (**Fig. 5-8b**). In light of the simulation results, FSS by circulation flow was considerably smaller than that by perfusion flows; however, the cultured cells could receive the FSS of basal sides. The cell-culture medium in the circulation channel could accumulate molecules (i.e., growth factors, cytokines, metabolites, and lipids) and exosomes secreted from Caco-2 and HepG2 cells. Thus, the medium contained both autocrine and paracrine factors and facilitated the interactions of Caco-2 and HepG2 cells by the circulation flow. Thus, the induction of

81

ZO-1 expression could be the outcome of the combinations of FSS by perfusion/circulation flows and molecular transport.
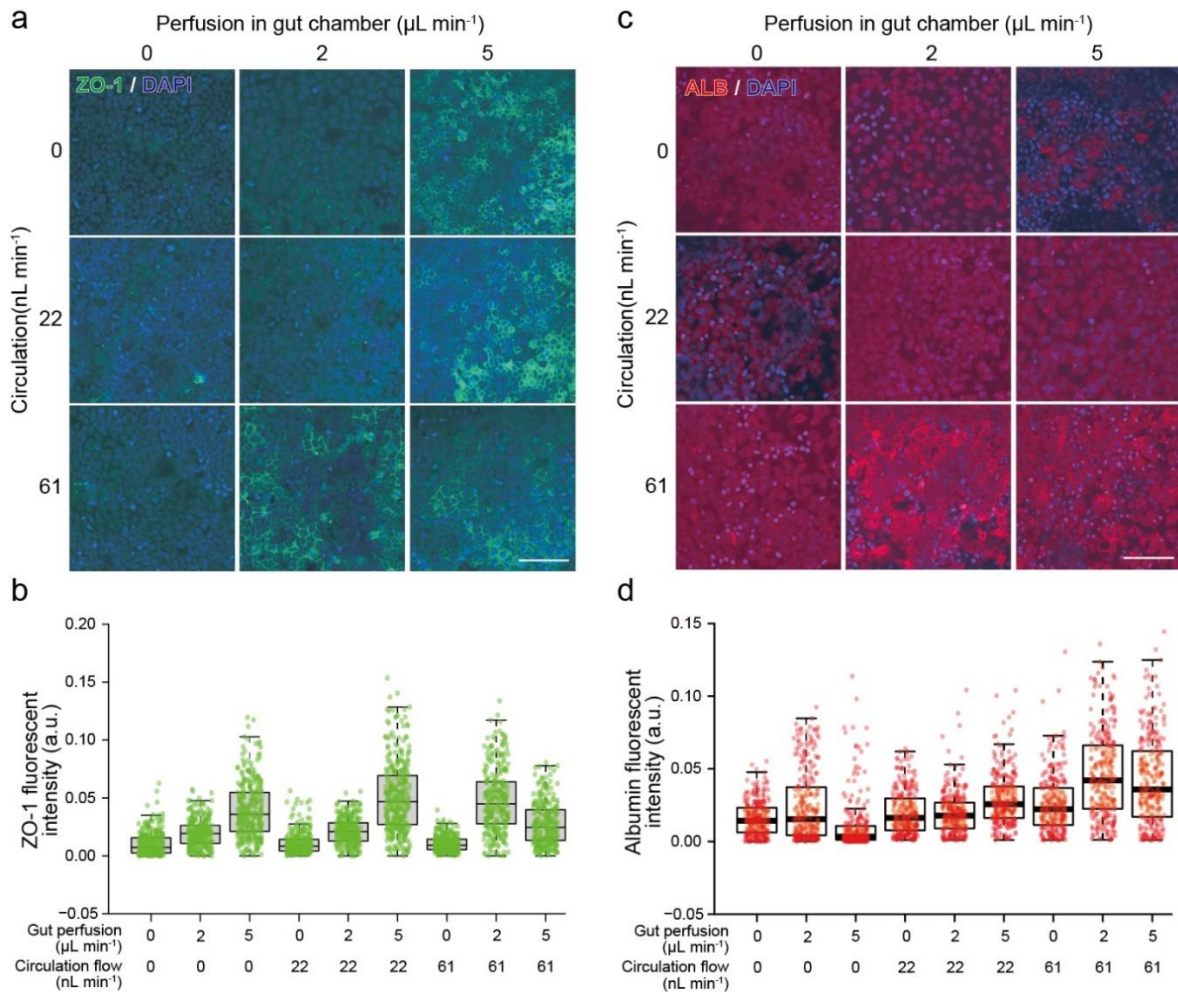
Figure 5-8 Optimal perfusion and circulation flows enhanced the expression of ZO-1 in Caco-2 cells and ALB in HepG2 cells. (a) Immunofluorescent micrographs of ZO-1 (green) expression in Caco-2 cells. (b) Quantitative single-cell profiling of ZO-1 expression in Caco-2 cells. *P* values estimated by Tukey's multiple comparison test were shown in **Table S5-1 Appendix III**. (c) Immunofluorescent micrographs of ALB (red) expression in Caco-2 cells. (d) Quantitative single-cell profiling of ALB expression in HepG2 cells. Center lines of box plots indicate medians; box limits indicate the 25th and 75th percentiles as determined by R software; whiskers extend 1.5 times the interquartile range from the 25th and 75th percentiles. *P* values estimated by Tukey's multiple comparison test were shown in **Table S5-2 Appendix III**. Nuclei were stained with DAPI. The scale bar represents 100 μm.

In the case of HepG2 cells, the HepG2 cells were not directly subjected to perfusion flow in the cell-culture chamber, since we focus to evaluate the effects of LPS from the circulation channel and there are several reports describing the effects of perfusion flow on hepatocytes;[240] also, increasing the gut cell culture chamber perfusion flow rates did not improve the ALB expression in HepG2 cells (**Fig. 5-8c**), while the increase in circulation flow rates from 0 to 61 nL min^{-1} significantly induced ALB

expression in HepG2 cells (**Fig. 5-8d**). These results suggest that HepG2 cells facilitated hepatic functions such as ALB production by FSS and as a molecular transport in the circulation channel.
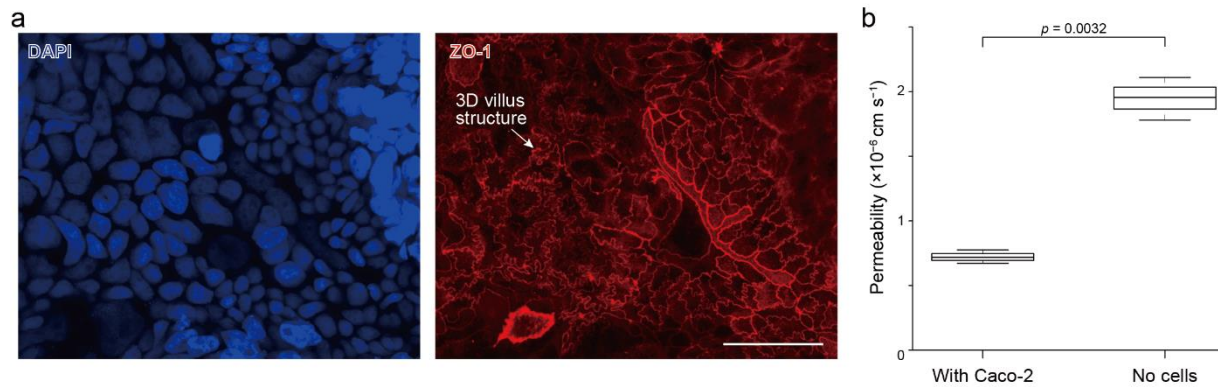
Figure 5-9 The three-dimensional villus structure development of Caco-2 cells and permeability assay for barrier function. (a) Immunofluorescent micrographs of ZO-1 (red) and nuclei (Blue) to show the three-dimensional villus structure after 9-days flow perfusion; (b) FITC-dextran to evaluate Caco-2 barrier function by observing transportation amount from the culture chambers to the circulation channel via the porous membrane (n = 3).

Thus, we selected the flow rates (gut perfusion flow: 2 µL min^{-1}; circulation flow: 61 nL min^{-1}) to establish *in vitro* GLA, which provided the highest expression of functional proteins in both Caco-2 and HepG2 cells among the tested conditions. Notably, in this optimal condition, the Caco-2 cells could generate a three-dimensional villus structure with 20-30 µm height (**Fig.5-9a**), which is a significant feature over conventional PET porous membrane cell culture MPS device.[241] This result is consistent with previous gut-on-a-chip devices.[109] Then, we also tested the permeability of Caco-2 cells after the 9-day culture, and we confirmed the cell barrier function (**Fig. 5-9b**). It indicated that Caco-2 cells formed an intact cell barrier to protect the transportation of 4-kD FITC-dextran across the porous membrane.

5.3.4 *In vitro* recapitulation of inflammatory bowel disease and progression

To demonstrate the interaction of the GLA-MPS for disease progression modeling, we selected to recapitulate inflammatory bowel disease (IBD)[210] *in vitro*. IBD is one of the chronic inflammatory intestinal disorders and is often caused by genetics, immune systems, microbiome, and environmental exposure, and their combinations. Importantly, IBD patients have a high risk of autoimmune liver disease via GLA[242]. It is related with NAFLD inflammation progression. But the underlying mechanisms of IBD and NAFLD progression are not fully understood yet. The feature of the presented GLA-MPS has an individual addressability for each cell-culture chamber. This feature is advantageous for modelling and investigating multiple organ diseases interactions such as IBD and liver disease.
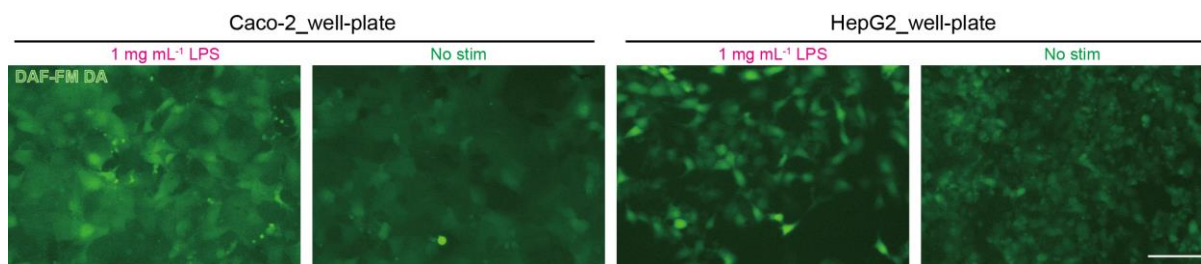
Figure 5-10 Four-day treatment of Lipopolysaccharides (LPS) inducing the inflammation marker expression on Caco-2 and HepG2, on 96-well-plate. DAF-FM DA is the live cell indicator to detect intracellular nitric oxide (NO) during the inflammation process. Scale bar: 100 μm.

To recapitulate IBD using the GLA-MPS, we utilized the bacterial endotoxin, LPS[243]. First, we investigated the LPS effect on the single type of cells based on the 96-well-plate experiment. We used the 1 mg mL^{-1} LPS to treat the Caoc-2 and HepG2 cells, respectively. And we found the LPS could significantly improve the DAF-FM DA (Diaminofluorescein-FM diacetate, an alive cell inflammation indicator) intensity for both cells (**Fig. 5-10**). It indicated the LPS could trigger the inflammation process on both cells in this concentration.
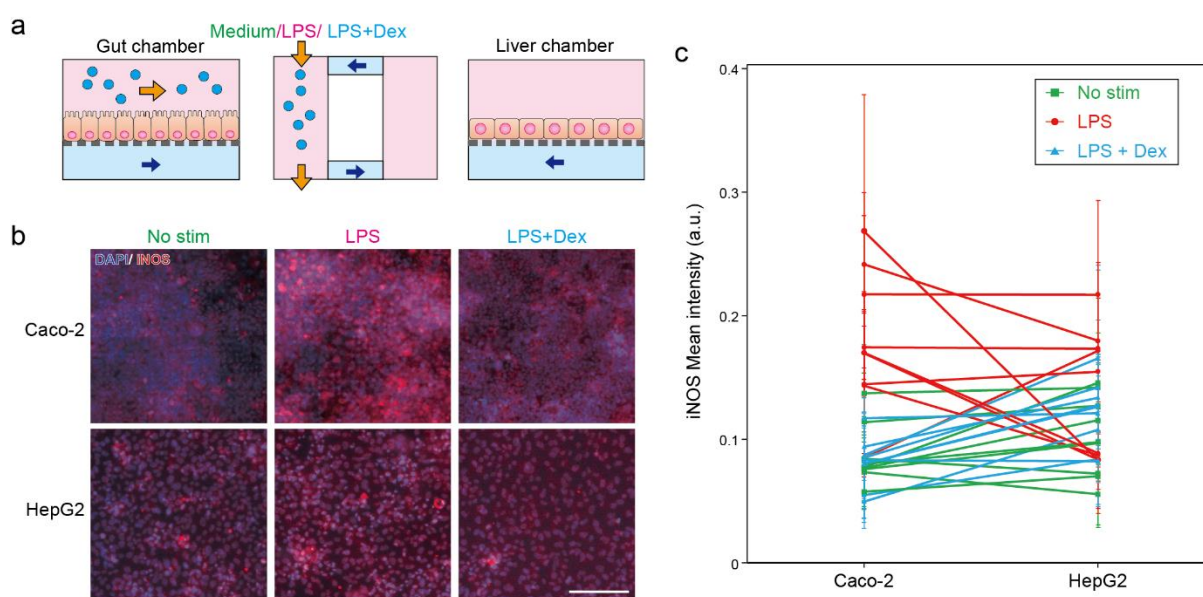
Figure 5-11 *In vitro* recapitulation of IBD in the GLA-MPS. (a) Experimental procedure of cell treatment. (b) Immunofluorescent micrographs of iNOS (red) expression in Caco-2 and HepG2 cells with no stimulation (No stim), 1 mg mL^{-1} LPS treatment (LPS), and 1 mg mL^{-1} LPS with 200 μM Dex treatment (LPS + Dex). Nuclei were stained with DAPI. The scale bar represents 100 μm. (c) Quantification of iNOS expression in individual Caco-2 and HepG2 cells based on the immunofluorescent micrographs shown in (b). Each bar and error bars represent the mean ± standard deviations (n=3). *P* values of Tukey's multiple comparison test are summarized in Tables S5-3 and S5-4 **Appendix III**.

a

LPS treatment

Apical side

ZO-1

100 μm

Circulation channel

b
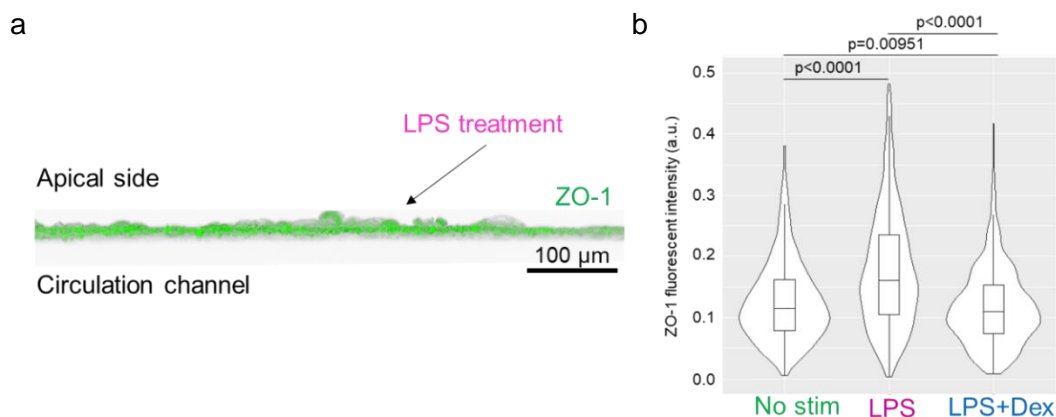
Figure 5-12 The LPS treatment inducing the improved expression of ZO-1 in Caco-2 cells. (a) Three-dimensional ZO-1 profile, Caco-2 forming barrier structure after flow perfusion cell culture. LPS was introduced in the apical side of the gut barrier and was limited to the circulation channel. (b) LPS treatment improved the ZO-1 expression of Caco-2.

Then, on the GLA-MPS, we administrated LPS in the Caco-2 culture chamber to induce gut inflammation. After the treatment with 1 mg mL^{-1} of LPS on Caco-2 cells for 4 days (**Figs. 5-4 and 5-11a**), most of the Caco-2 groups expressed iNOS, which is often observed in IBD[244]; the comparison with non-treated Caco-2 cells is shown in **Fig. 5-11b and c**. Notably, to confirm the integrity of the tight junction of the Caco-2 cells, we measured the ZO-1 intensity and three-dimensional profile (**Fig. 5-12a**). The results did not show a reduction in ZO-1 intensity (**Fig. 5-12b**) in the LPS treatment group, but the intensity increased. It indicated the leakage of the LPS into the circulation channel was limited. And the increase of ZO-1 may be also related to the function of LPS which promoted the proliferation of Caco-2 as previous research reported.[245]

Following the inflammatory induction of Caco-2 cells, iNOS expression was observed in 4 out of 9 samples of HepG2 cells, while no change in the iNOS expression was observed in the other 5 samples (**Fig. 5-11c**). Despite the use of established cell lines, such as Caco-2 and HepG2 cell lines, the complexity of the experimental setup could have caused the observed individual differences in the LPS stimulation. In contrast, the treatment of 200 μM of dexamethasone (Dex), an anti-inflammation agent, on the Caco-2 cells during 1 mg mL^{-1} LPS treatment suppressed the iNOS expression in both Caco-2 and HepG2 cells. Thus, inflammatory responses of HepG2 cells were induced by the LPS-treated Caco-2 cells.

To identify the inflammatory mediators that induced inflammatory responses of HepG2 cells via the circulation channel, ELISA was performed for TNF-α, which was elevated in the gut of IBD models[244]. However, TNF-α in the cultured medium was not observed because the amount of TNF-α within the

circulation channel with a limited volume (1.5 µL) was lower than the detection limit of ELISA (**Fig. 5-13**). Therefore, highly sensitive methods are required to detect the mediators within such a small volume to identify the mediators that influence the interaction between Caco-2 and HepG2 cells via the circulation channel.
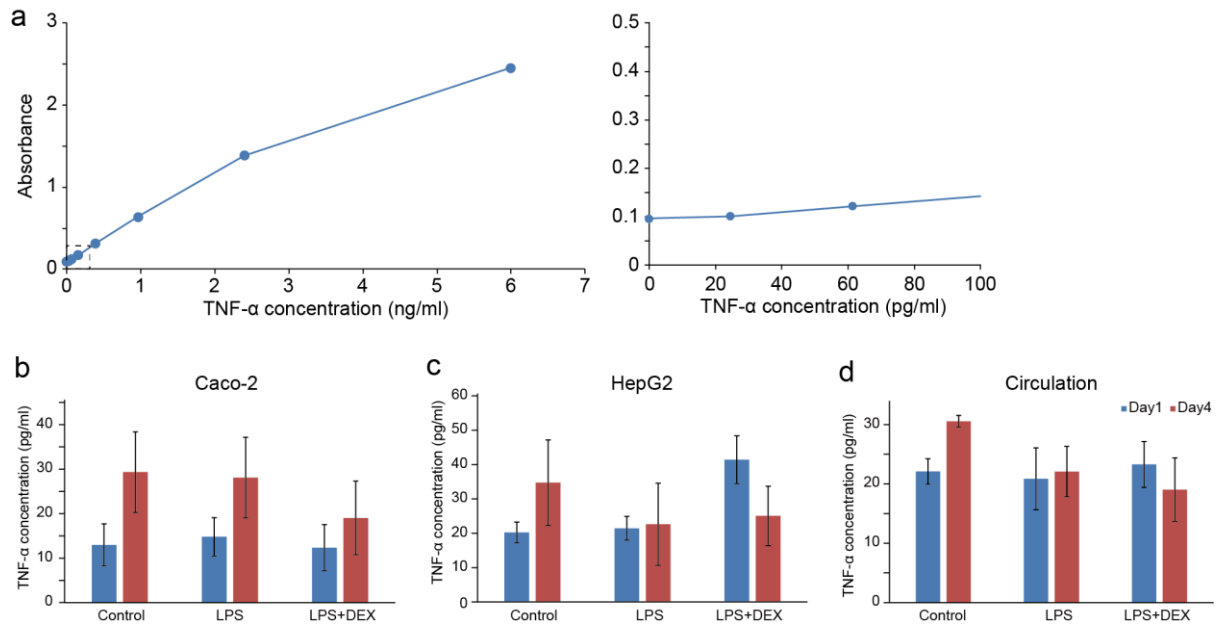
Figure 5-13 ELISA to measure the secreted TNF-α. (a) The calibration plot of TNF- α. The lower detection limit is approx. 60 pg mL^{-1}. (b-d) Amounts of TNF- α in the supernatants corrected from Caco-2 (b) and HepG2 (c) cell-culture chambers and the circulation channel (d). The measured concentrations were below the detection limit of this TNF- α ELISA. The blue color is a 1-day treatment; The red color is a 4-day treatment. Each bar and error bars represent the mean ± standard deviations. n=3.

5.4 Discussions

5.4.1 Physiological flow perfusion to recapitulate the GLA structure and function

In the previous research, it was reported that mechanical stretches and flow shear stress could promote the Caco-2 cell barrier function and the 3D villus structure.[99] In this research, we found the similar importance of a physiological flow stimulus on Caco-2 cells, which help generate the 3D microvillus structure. Also, the developed GLA-MPS achieved individual flow stimulus on gut cells and liver cells at the same time. We optimized the flow condition, which also help the HepG2 cells improve the expression of albumin.

As known to all, a polarized 'crypt-villus' structure for the gut is important to realize molecular absorption, transport, immune responses, and renewal.[246] There are several methods to help generate

this 3D structure, such the 3D scaffolds and gels.[247] However, these scaffolds and gels methods have increased the complicated interfaces, and scaffold-free cell-based tissue engineering is needed.[248] In the previous gut-on-a-chip system, the mechanical stimulus could promote the Caco-2 cell differentiation with a villus structure.[109] However, the specific details of how a mechanical stimulus might promote differentiation into a villus structure would depend on the specific conditions and parameters of the stimulus. The GLA-MPS device achieved the 3D structure by precisely controlling the FSS on Caco-2 cells in the microfabricated and multilayered structure. We got flow control parameters for these villus generations. This was realized by individual and compartmentalized FSS stimulus. It is also applicable for tissue engineering for other gut epithelial cell lines, such as induced Pluripotent Stem Cell-derived human intestinal cells. It can improve the differentiation stage of these cells.[249]

For the hepatocytes, flow perfusion importance was ambiguous. It is hard to know the exact physiological FSS or other mechanical stimuli on hepatocytes, due to the space of Disse.[115] In previous research, they introduced the effect of FSS on hepatocytes. It was known that high FSS may reduce cell function and cell viability.[116] However, the FSS may also maintain the hepatocyte's morphology for longer-term cell culture on chips.[250] In this device, we designed the porous membrane and circulation flow to control the FSS within the small interstitial flow range. It maintained a 9-days cell culture with improved cell function and viability. Therefore, it is also applicable to the cells, which do not receive flow perfusion directly, like neurocytes.

5.4.2 GLA-MPS for studying the inflammatory progression

The GLA-MPS device revealed the physiological level of fluidic control and enhanced the GLA function with intensive interaction for inflammatory progression. In the previous research, it was reported that LPS induced the secretion of pro-inflammation factors (e.g. iL-6, TNF-α) in Caco-2 cells,[251] which was related to Toll-like receptor 4 (TLR4).[252] In our study, we used a relatively high LPS concentration (1mg ml^{-1}) (low toxicity, derived from E.coli) to induce the inflammation of Caco-2 cells with highly expressed iNOS as the inflammation marker.[253] Even though we did not find obvious TNF-α upregulation by ELISA testing (**Fig. 5-13**). We still could confirm the inflammation state of Caco-2 cells, via comparing with Dex. Groups. The GLA communications were connected via the circulation channels. The medium crosstalk was nearly 10 times enhanced than traditional GLA-MPS (**Section 5.3.2**), which induced inflammatory communications between Caco-2 and HepG2. To analyze their interaction, we recognized the LPS did not directly cause the HepG2 inflammation. First, from the view of the Caco-2 tight junction, we did not find the reduction and breaking of the ZO-1 marker (**Fig. 5-12**). It indicated the leakage of LPS was limited. Second, in the previous research, HepG2 cells had a stronger reaction with the LPS and induced the iNOS expression.[254,255] If the LPS leaked into the circulation channel with 10 times enhanced micro-scale circulation, the HepG2 cells were supposed to

have a similar reaction with Caco-2 cells. However, only 4 of 9 chips presented positive iNOS conditions. This means only weak inflammation-inducing reactions. This is consistent with the observation of ELISA results. The weak interaction has a high possibility which lies in the pro-inflammation cytokine crosstalk. It indicated the Caco-2 released pro-inflammation factors which caused a further inflammation effect on HepG2 cells. It demonstrated the device could be used for individual treatment and studying organ-to-organ communications. It holds the potential to reveal gut-liver inflammatory communication, leading to the disease progression of NAFLD.[39]

5.4.3 Extending the application of multilayered GLA-MPS

Gut microbiome[256] plays critical roles in the pathophysiological scenarios in the gut; they can influence other organs, including the liver[39,169] and brain[257], and the immune system[258]. Instead of liver cells, our MPS device allows the introduction of other tissue cells like neurons, and we can investigate the interactions with the gut microbiome. Thus, our MPS is not limited to recapitulating only GLA, but it is also applicable to other organs and the microbiome.

Further, the presented GLA-MPS allows a collection of conditioned cell-culture medium from two cell-culture chambers and circulation channels separately for investigating the underlying molecular mechanisms of the GLA by biochemical assays such as ELISA and mass spectroscopy. Since these methods for the cell-culture medium are non-invasive for cultured cells, we will be able to determine the transitions of molecular contents in the medium during the experimental period to explore interesting molecular biomarkers. At the end of the experiments, GLA-MPS allows performing invasive cell-analytical methods like immunocytochemistry, as shown in this chapter, as well as multi-omics analysis (i.e., genomics, transcriptomics, proteomics, and metabolomics) to obtain deeper insights into normal and diseased GLA.

One advantage of using microfluidic technology for disease modeling is the minimization of the number of cells, such as the primary cells obtained from the patients. These cells are limited in their ability to recapitulate the patients' pathological conditions *in vitro*. The presented MPS requires only 1.5×10^4 cells for each cell culture chamber, which is considerably smaller than those of the 24-well cell culture inserts (3×10^5 cells). Therefore, we efficiently use precious patient samples, like biopsy specimens. In the present study, we used widely used cell lines (Caco-2 and HepG2) that can provide the standard performance of the presented GLA-MPS. Since patient-derived primary cells could have large patient-to-patient variations, it would be beneficial to obtain such standard datasets with the use of commonly used cell lines.

5.5 Conclusions

We developed a GLA-MPS platform, which was fabricated by multilayer soft lithography with a multilayered structure, capable of integrating the multilayer cell culture chamber, circulation channels, porous membrane, and on-chip micropump. The device can (i) cultivate gut and liver cells separately with applied different perfusion flows/FSS to improve their cell viabilities and functionalities, (ii) form 3D villus barrier tissue, and (iii) interconnect GLA via circulation channels.

The device is a more distinctive platform than the current GLA-MPS, resembling the physiological flow perfusion and circulation of *in vivo* GLA. It is also suitable for demonstrating individual accessibility to investigate the GLA interaction mediated by IBD and inflammation progress. However, the GLA-MPS still has some limitations that need to be improved in the future. For example, the device can be integrated with the organoid structure, which could extend the gut and liver organ functions for tissue engineering and disease modeling. In addition, the device should have capabilities beyond FSS control and effectively control the molecular transport gradient across the barrier tissues in the microenvironment to understand the GLA interaction.

Finally, our approach based on GLA-MPS has the potential for applications in understanding the GLA mechanisms associated with individual physiological flow perfusion and multi-organ interactions for NAFLD progression modeling.

Chapter 6 Conclusions

6.1 Summary of accomplishments

This thesis reported the novel GLA-MPS devices fabricated by multilayer soft lithography, which are more distinctive platforms than the previous GLA-MPSs in resembling the closed-loop inter-tissue communications, physiological flow perfusion, and circulation of mimicking *in vivo* GLA interaction for disease progression.

Non-alcoholic fatty liver disease (NAFLD) affected 20-30% of the adult population and has become an epidemic disease. Due to its 'silent' state, it has a heavy progression from hepatic steatosis to cirrhosis. Fatty liver and Inflammation of steatohepatitis (NASH) are recognized as two key steps. Currently, there is no available drug for curing the disease. This is mainly caused by a lack of precise disease progression models for new therapeutic methods and drug evaluations.

According to the multiple-hit hypothesis, to clarify the pathological roles of GLA for NAFLD, a GLA-MPS, recapitulating the GLA physiological organ-to-organ interaction, holds great potential for disease modeling. However, in the previous GLA-MPS, there is a problem with the interface between the macro-scale cell culture insert and the microfluidic flow perfusion. It is associated with the physiologically relevant flow for gut and liver cells' cultivation, and a low tissue-to-medium ratio leads to low GLA interaction. Furthermore, individual accessibility is lacking, leading to hard observation of the disease progression from one organ to another.

To address the issues of the previous GLA-MPSs, we used the advanced multilayer soft lithography method to fabricate the GLA-MPSs and controlled the cell-cultivating microenvironment (individual accessibility and mechanical stimulus, such as fluid shear stress) by microactuators, including microvalve and micropump. We aim to provide an advanced GLA-MPS for modeling NAFLD and related disease progression, via GLA interaction.

For designing advanced micro components for GLA-MPS, we characterized the performance of the PDMS-based pneumatic microvalve with a semi-round shape channel and micropump consisting of three circular diaphragms. We designed the microvalve and micropump by the FEA simulation, applying the contact analysis and fluid-structure interaction methods. In addition, the microwaves with a wafer-level high-accuracy fabrication could realize the liquid channel fully closed, which could be used to generate a flexible valve control system for individually assessing of multi-organ cell culture chamber. For the micropump, we demonstrated the usage of the micropump in high external hydraulic flow resistance cases to mimic the case of the MPSs. We found the diffuser/nozzle structure could control a more wide range of the flow rate than the normal straight channel, providing a more robust flow for MPSs.

For investigating the GLA interaction and demonstrating the initiation of NAFLD, NAFLD was modeled on the micro-scale closed-loop circulation system to enhance GLA communications. By multilayer soft lithography, we fabricated an integration of the gut–liver-on-a-chip (iGLC) platform. Human gut and liver cell lines were interconnected via microfluidics in a closed circulation loop. To model the initiation and progression of NAFLD, 1 and 7 days of free fatty acids (FFAs) treatment were conducted respectively. Co-cultured Caco-2 gut-like cells and HepG2 hepatocyte-like cells demonstrated the accumulated intracellular lipid droplets and the protective effects against apoptosis from FFAs treatment, whereas mono-cultured cells exhibited induced apoptosis. Gene expression analyses revealed that the FFA-treated liver cells showed an increase in gene expressions associated with a cellular response to copper ions and endoplasmic reticulum stress. Therefore, the present iGLC platform represents a new *in vitro* human model for recapitulating physiological and NAFLD pathological conditions with a focus on the GLA, allowing to advance *in vitro* model for NAFLD.

For mimicking the *in vivo*-like GLA interaction and inflammation disease progression, we developed a multilayered GLA-MPS, which allowed separate flow stimulus and individual treatment for gut and liver cells. The GLA-MPS was integrated with a layer of two- separated-cell-culture-chamber for individually applied perfusion flows, a porous membrane for polarized cell culture, and a circulation channel layer for GLA interaction. The on-chip micropump for driving circulation flow was fabricated under the circulation channel layer. These structures were achieved by multilayer soft lithography. Accordingly, we analyzed the fluid shear stress (FSS) with computational fluid dynamics simulations and confirmed that the physiologically relevant FSS could be applied to the gut (Caco-2) and liver (HepG2) cells. Under this FSS, the expression of functional proteins such as zonula occludens 1 (in Caco-2) and albumin (in HepG2) was enhanced. Particularly, the gut villus structure was generated. Afterward, the inflammatory bowel disease was recapitulated by applying lipopolysaccharide for only Caco-2 cells, which showed inflammatory proteins of inducible nitric oxide synthase (iNOS) expression. Subsequently, the HepG2 cells also showed iNOS expression. This process demonstrated an inflammation progression from the gut to the liver, which indicated an important progression step to NASH of GLA. It produces a more realistic model of GLA interactions in humans.

In conclusion, gut and liver diseases are strongly affected by environmental pathogenic factors. The GLA-MPS of this research presented the gut-liver disease initiation and progression. It is consistent with the current assumptions and findings of disease modeling. The present devices hold considerable potential for disease models to reveal new therapies and insights into the GLA interaction mediated by NAFLD and inflammation progression.

6.2 Limitations of this study

Even though we have got some achievements in this research, we still have several issues and limitations, such as chip fabrication materials, cell lines, and industrial applications.

First, the chips were fabricated from PDMS material. It has a high absorption of hydrophobic small molecules, such as fatty acids and cytokines. We have used several methods to maintain FFAs concentration, including surface coating and medium exchange timing control.[45] But the molecular concentration and organ-to-organ cytokines still got lost. It limited the application for the multilayered GLA-MPS for NAFLD modeling. Even though we have tried using a high concentration of FFAs, it seems the absorption still has some side effects, like background staining.[259] Therefore, we have not modeled the combination function of hepatic steatosis and inflammation development. Also, the micro-scale sample was quite limited, and a highly sensitive assay method was required. It will be our future work to gradually increase the system's complexity and find other methods to solve the absorption issue. Currently, thermoplastics[260], perfluoropolyether (PFPE) elastomer[261], off-stoichiometry thiol-ene (OSTE) polymer[262], or PDMS-PEG surface coating[263] has been developed with microfabrication methods. It may hold the potential for replacing the PDMS, as new material for the GLA-MPS.

Second, in this study, the HepG2 human hepatocellular carcinoma cell line and Caco-2 human colorectal adenocarcinoma cell line were used since they have been immortalized and widely used until now. However, such cell lines have genetic mutations and cannot express proper functions as actual hepatocytes[264] and intestinal cells.[265] In the case of hepatocytes, the HepaRG human hepatocellular carcinoma cell line has been used for liver disease modeling as well as toxicological research due to their relatively higher functionalities than those of HepG2 cells recently, but HepaRG cells also showed differences in lipid metabolism.[266] Moreover, cell lines generally form a pure cellular population, and cannot represent cellular diversity. For example, the liver contains hepatocytes and non-parenchymal cells (NPCs) such as Kupffer cells, endothelial cells, and stellate cells. In particular, since the liver microphysiological system (L-MPSs) was reported to recapitulate liver steatosis using NPCs,[220] NPCs are now recognized for their importance in hepatic disease modelling. In contrast, primary cells obtained from NAFLD patients showed similar cellular diversity and drug metabolic responses.[267] However, primary cells have limited cell growth capability and often lose their functions in vitro. Moreover, it is difficult to identify healthy donors to obtain a control sample. In addition to primary cells, human pluripotent stem cells (hPSCs), such as embryonic[221] and induced pluripotent stem cells,[65,268,269] can provide multiple cell types from a single cell source after induction of differentiation by applying growth factors and nutrients. However, the tissue cells derived from hPSCs could not fully cover the entire cellular diversity nor express their functionality in vivo. Therefore, it remains challenging for hPSCs to fully recapitulate the pathological conditions of NAFLD *in vitro*.

Finally, although several advances have already been made in this research, gaps remain between this laboratory work and its successful translation to industry and clinical settings. For example, the GLA-MPS is an *in vitro* assay model, and, currently, it can not directly represent the complicated networks of *in vivo* clinical data. However, this device has the potential for a therapeutic evaluation model, like drug screening. We also can provide proof of concept experiment data for the current assumption model (like multi-hit assumption) as *in vitro* investigation platform. For clinical application, a large amount of validation experiments is necessary. The microfluidic cell culture has the advantage of low cells and medium consumption for a multi-parallel system. It also will be our future work to improve the throughput of the GLA-MPS. Thus, we can calibrate our model based on a clinically relevant database or guidance, which will be used for the clinical prediction model.

6.3 Future works

There are still some subjects that can be extended to improve the function and application of the GLA-MPS in future research.

First, the FEA simulation, developed to analyze and optimize the microvalve and micropump, can be extended to use in other MPS systems. After converting to a 2D model, the calculation load is largely reduced, which increases the possibility of the simulation's complicated system. For example, the micropump model can be connected to a loop circulation system, and the actuating of the micropump generates a circulation flow, which may be used to furtherly study the molecular transport and diffusing model for multi-organ systems.

Second, instead of using the HepG2 and Caco-2 carcinoma cells, the use of human pluripotent stem cells (hPSCs), such as embryonic[221] and induced pluripotent stem cells[222] (hES or iPS cells) hold considerable promise to obtain a variety of functional tissue cells from a single cell source. Because of the recent advancement of gene editing technologies, such as CRISPR/Cas systems,[223] it allows the creation of gene-modified hPSCs used for disease modeling, for which the primary cells are not applicable. Therefore, hPSCs will be more suitable for establishing *in vitro* disease models, like NAFLD. It will be our future works by applying these techniques to model a human GLA-MPS model.

Finally, the devices were fabricated using the multilayer soft lithography microfabrication method with a several-layered planer microfluidic structure. Owing to this feature, it holds the capability to integrate electrical read-out sensors in cell-culture chambers and circulation channels, which allows for monitoring cell conditions and behaviors during cell culture and treatments in a real-time and non-invasive fashion.[270] Such sensors will provide temporal information on tissue formation, disease progression, and drug treatments. In the case of the GLA, the sensor for measuring trans-epithelial electrical resistance (TEER) was beneficial for evaluating gut barrier formation and causing damage

during disease progression. Until now, gut-on-a-chips integrated with TEER measurements have been reported.[25,68] However, the designs and fabrication processes need to be further improved for better accuracy and reproducibility, and integration with GLA-MPS. Currently, we are engaged in a topology optimization method to design the TEER electrode for high accuracy and real-time monitoring of gut barrier conditions and morphology changes.[25] This integrative approach will lead to the advancement of GLA-MPS for a better understanding of disease mechanisms and applications in drug discovery.

REFERENCES

1. Bhatia, S. N. & Ingber, D. E. Microfluidic organs-on-chips. *Nat. Biotechnol.* **32**, 760–772 (2014).

2. Park, S. M. *et al.* Reconstruction of in vivo-like in vitro model: Enabling technologies of microfluidic systems for dynamic biochemical/mechanical stimuli. *Microelectron. Eng.* **203**, 6–24 (2019).

3. Zhang, B. & Radisic, M. Organ-on-a-chip devices advance to market. *Lab Chip* **17**, 2395–2420 (2017).

4. Huh, D. *et al.* Reconstituting organ-level lung functions on a chip. *Science (80-.).* **328**, 1662–1668 (2010).

5. Huh, D. *et al.* A human disease model of drug toxicity–induced pulmonary edema in a lung-on-a-chip microdevice. *Sci. Transl. Med.* **4**, 159ra147-159ra147 (2012).

6. Lee, S. H. & Sung, J. H. Organ-on-a-chip technology for reproducing multiorgan physiology. *Adv. Healthc. Mater.* **7**, 1700419 (2018).

7. Sung, J. H. *et al.* Recent advances in body-on-a-chip systems. *Anal. Chem.* **91**, 330–351 (2018).

8. Ramadan, Q. & Zourob, M. Organ-on-a-chip engineering: Toward bridging the gap between lab and industry. *Biomicrofluidics* **14**, 41501 (2020).

9. Picollet-D'hahan, N., Zuchowska, A., Lemeunier, I. & Le Gac, S. Multiorgan-on-a-chip: a systemic approach to model and decipher inter-organ communication. *Trends Biotechnol.* **39**, 788–810 (2021).

10. Maschmeyer, I. *et al.* A four-organ-chip for interconnected long-term co-culture of human intestine, liver, skin and kidney equivalents. *Lab Chip* **15**, 2688–2699 (2015).

11. Wikswo, J. P. *et al.* Scaling and systems biology for integrating multiple organs-on-a-chip. *Lab Chip* **13**, 3496–3511 (2013).

12. Ronaldson-Bouchard, K. & Vunjak-Novakovic, G. Organs-on-a-Chip: A Fast Track for Engineered Human Tissues in Drug Development. *Cell Stem Cell* **22**, 310–324 (2018).

13. Fowler, S. *et al.* Microphysiological systems for ADME-related applications: Current status and recommendations for system development and characterization. *Lab Chip* **20**, 446–467 (2020).

14. Bauer, S. *et al.* Functional coupling of human pancreatic islets and liver spheroids on-a-chip: Towards a novel human ex vivo type 2 diabetes model. *Sci. Rep.* **7**, 1–11 (2017).

15. Hingorani, A. D. *et al.* Improving the odds of drug development success through human genomics: modelling study. *Sci. Rep.* **9**, 1–25 (2019).

16. Paul, S. M. *et al.* How to improve RD productivity: The pharmaceutical industry's grand challenge. *Nat. Rev. Drug Discov.* **9**, 203–214 (2010).

17. Esch, E. W., Bahinski, A. & Huh, D. Organs-on-chips at the frontiers of drug discovery. *Nat. Rev. Drug Discov.* **14**, 248–260 (2015).

18. Ayuso, J. M., Park, K.-Y., Virumbrales-Muñoz, M. & Beebe, D. J. Toward improved in vitro models of human cancer. *APL Bioeng.* **5**, 10902 (2021).

19. Theobald, J. *et al.* Liver-kidney-on-chip to study toxicity of drug metabolites. *ACS Biomater. Sci. Eng.* **4**, 78–89 (2018).

20. Arora, S., Srinivasan, A., Leung, C. M. & Toh, Y.-C. Bio-mimicking shear stress environments for enhancing mesenchymal stem cell differentiation. *Curr. Stem Cell Res. Ther.* **15**, 414–427 (2020).

21. Li, W. *et al.* Matrix stiffness and shear stresses modulate hepatocyte functions in a fibrotic liver sinusoidal model. *Am. J. Physiol. Liver Physiol.* **320**, G272–G282 (2021).

22. Xu, Z. *et al.* Application of a microfluidic chip-based 3D co-culture to test drug sensitivity for individualized treatment of lung cancer. *Biomaterials* **34**, 4109–4117 (2013).

23. Kulthong, K. *et al.* Microfluidic chip for culturing intestinal epithelial cell layers: Characterization and comparison of drug transport between dynamic and static models. *Toxicol. Vitr.* **65**, 104815 (2020).

24. Gerardo, H. *et al.* Soft culture substrates favor stem-like cellular phenotype and facilitate reprogramming of human mesenchymal stem/stromal cells (hMSCs) through mechanotransduction. *Sci. Rep.* **9**, 1–18 (2019).

25. Miyazaki, T., Hirai, Y., Kamei, K. ichiro, Tsuchiya, T. & Tabata, O. Design strategy of electrode patterns based on finite element analysis in microfluidic device for Trans-Epithelial Electrical Resistance (TEER) measurement. *Electron. Commun. Japan* **104**, 1–10 (2021).

26. Peel, S. *et al.* Introducing an automated high content confocal imaging approach for Organs-on-Chips. *Lab Chip* **19**, 410–421 (2019).

27. Kamei, K. I. *et al.* Integrated heart/cancer on a chip to reproduce the side effects of anti-cancer

drugs: In vitro. *RSC Adv.* **7**, 36777–36786 (2017).

28. Tsamandouras, N. *et al.* Integrated Gut and Liver Microphysiological Systems for Quantitative In Vitro Pharmacokinetic Studies. *AAPS J.* **19**, 1499–1512 (2017).

29. Imura, Y., Sato, K. & Yoshimura, E. Micro total bioassay system for ingested substances: assessment of intestinal absorption, hepatic metabolism, and bioactivity. *Anal. Chem.* **82**, 9983–9988 (2010).

30. Prot, J. M. *et al.* First pass intestinal and liver metabolism of paracetamol in a microfluidic platform coupled with a mathematical modeling as a means of evaluating ADME processes in humans. *Biotechnol. Bioeng.* **111**, 2027–2040 (2014).

31. Satoh, T. *et al.* A multi-throughput multi-organ-on-a-chip system on a plate formatted pneumatic pressure-driven medium circulation platform. *Lab Chip* **18**, 115–125 (2018).

32. Wang, Y. I., Carmona, C., Hickman, J. J. & Shuler, M. L. Multiorgan microphysiological systems for drug development: strategies, advances, and challenges. *Adv. Healthc. Mater.* **7**, 1701000 (2018).

33. Loomba, R., Friedman, S. L. & Shulman, G. I. Mechanisms and disease consequences of nonalcoholic fatty liver disease. *Cell* **184**, 2537–2564 (2021).

34. Santhekadur, P. K., Kumar, D. P. & Sanyal, A. J. Preclinical models of non-alcoholic fatty liver disease. *J. Hepatol.* **68**, 230–237 (2018).

35. Buzzetti, E., Pinzani, M. & Tsochatzis, E. A. The multiple-hit pathogenesis of non-alcoholic fatty liver disease (NAFLD). *Metabolism.* **65**, 1038–1048 (2016).

36. Stärkel, P. & Schnabl, B. Bidirectional Communication between Liver and Gut during Alcoholic Liver Disease. in *Seminars in Liver Disease* **36**, 331–339 (Thieme Medical Publishers, 2016).

37. Zhou, Z., Xu, M.-J. & Gao, B. Hepatocytes: a key cell type for innate immunity. *Cell. Mol. Immunol.* **13**, 301–315 (2016).

38. Albillos, A., de Gottardi, A. & Rescigno, M. The gut-liver axis in liver disease: Pathophysiological basis for therapy. *J. Hepatol.* **72**, 558–577 (2020).

39. Ohtani, N. & Kawada, N. Role of the Gut–Liver Axis in Liver Inflammation, Fibrosis, and Cancer: A Special Focus on the Gut Microbiota Relationship. *Hepatol. Commun.* **3**, 456–470 (2019).

40. Leung, C., Rivera, L., Furness, J. B. & Angus, P. W. The role of the gut microbiota in

NAFLD. *Nat. Rev. Gastroenterol. Hepatol.* **13**, 412–425 (2016).

41.   Marchesi, J. R. *et al.* The gut microbiota and host health: A new clinical frontier. *Gut* **65**, 330–339 (2016).

42.   Ma, C., Peng, Y., Li, H. & Chen, W. Organ-on-a-Chip: A New Paradigm for Drug Development. *Trends Pharmacol. Sci.* **42**, 119–133 (2021).

43.   Zhang, B., Korolj, A., Lai, B. F. L. & Radisic, M. Advances in organ-on-a-chip engineering. *Nat. Rev. Mater.* **3**, 257–278 (2018).

44.   Jeon, J. won, Lee, S. H., Kim, D. & Sung, J. H. In vitro hepatic steatosis model based on gut–liver-on-a-chip. *Biotechnol. Prog.* **37**, 1–13 (2021).

45.   Yang, J. *et al.* Integrated gut–liver-on-a-chip platform as an in vitro human model of non-alcoholic fatty liver disease. *bioRxiv* (2020). doi:10.1101/2020.06.10.141606

46.   Whitesides, G. M. The origins and the future of microfluidics. *Nature* **442**, 368–373 (2006).

47.   Convery, N. & Gadegaard, N. 30 Years of Microfluidics. *Micro Nano Eng.* **2**, 76–91 (2019).

48.   Li, D. *Electrokinetics in microfluidics*. (Elsevier, 2004).

49.   Kim, J.-H., Na, K.-H., Kang, C. J. & Kim, Y.-S. A disposable thermopneumatic-actuated micropump stacked with PDMS layers and ITO-coated glass. *Sensors Actuators A Phys.* **120**, 365–369 (2005).

50.   Yun, K.-S., Cho, I.-J., Bu, J.-U., Kim, C.-J. & Yoon, E. A surface-tension driven micropump for low-voltage and low-power operations. *J. microelectromechanical Syst.* **11**, 454–461 (2002).

51.   Alizadeh, A., Hsu, W., Wang, M. & Daiguji, H. Electroosmotic flow: From microfluidics to nanofluidics. *Electrophoresis* **42**, 834–868 (2021).

52.   Pesch, G. R. & Du, F. A review of dielectrophoretic separation and classification of non-biological particles. *Electrophoresis* **42**, 134–152 (2021).

53.   Green, N. G., Ramos, A., Gonzalez, A., Castellanos, A. & Morgan, H. Electrothermally induced fluid flow on microelectrodes. *J. Electrostat.* **53**, 71–87 (2001).

54.   Zhang, H. J. & Qiu, C. J. Characterization and MEMS application of low temperature TiNi (Cu) shape memory thin films. *Mater. Sci. Eng. A* **438**, 1106–1109 (2006).

55.   Mugele, F. & Baret, J.-C. Electrowetting: from basics to applications. *J. Phys. Condens. matter* **17**, R705 (2005).

56. Oh, K. W., Lee, K., Ahn, B. & Furlani, E. P. Design of pressure-driven microfluidic networks using electric circuit analogy. *Lab Chip* **12**, 515–545 (2012).

57. Powers, M. J. *et al.* A microfabricated array bioreactor for perfused 3D liver culture. *Biotechnol. Bioeng.* **78**, 257–269 (2002).

58. McDonald, J. C. *et al.* Fabrication of microfluidic systems in poly (dimethylsiloxane). *Electrophor. An Int. J.* **21**, 27–40 (2000).

59. Park, T. H. & Shuler, M. L. Integration of cell culture and microfabrication technology. *Biotechnol. Prog.* **19**, 243–253 (2003).

60. Hung, P. J., Lee, P. J., Sabounchi, P., Lin, R. & Lee, L. P. Continuous perfusion microfluidic cell culture array for high-throughput cell-based assays. *Biotechnol. Bioeng.* **89**, 1–8 (2005).

61. Lee, P. J., Hung, P. J. & Lee, L. P. An artificial liver sinusoid with a microfluidic endothelial-like barrier for primary hepatocyte culture. *Biotechnol. Bioeng.* **97**, 1340–1346 (2007).

62. Zhang, C., Zhao, Z., Rahim, N. A. A., van Noort, D. & Yu, H. Towards a human-on-chip: culturing multiple cell types on a chip with compartmentalized microenvironments. *Lab Chip* **9**, 3185–3192 (2009).

63. Hsu, Y.-H., Moya, M. L., Hughes, C. C. W., George, S. C. & Lee, A. P. A microfluidic platform for generating large-scale nearly identical human microphysiological vascularized tissue arrays. *Lab Chip* **13**, 2990–2998 (2013).

64. Mathur, A. *et al.* Human induced pluripotent stem cell-based microphysiological tissue models of myocardium and liver for drug development. *Stem Cell Res. Ther.* **4**, 1–5 (2013).

65. Takahashi, K. *et al.* Induction of pluripotent stem cells from adult human fibroblasts by defined factors. *Cell* **131**, 861–872 (2007).

66. Vernetti, L. *et al.* Functional coupling of human microphysiology systems: intestine, liver, kidney proximal tubule, blood-brain barrier and skeletal muscle. *Sci. Rep.* **7**, 1–15 (2017).

67. Sung, J. H., Kam, C. & Shuler, M. L. A microfluidic device for a pharmacokinetic–pharmacodynamic (PK–PD) model on a chip. *Lab Chip* **10**, 446–455 (2010).

68. Henry, O. Y. F. *et al.* Organs-on-chips with integrated electrodes for trans-epithelial electrical resistance (TEER) measurements of human epithelial barrier function. *Lab Chip* **17**, 2264–2271 (2017).

69. Mould, D. R. Models for disease progression: new approaches and uses. *Clin. Pharmacol. Ther.* **92**, 125–131 (2012).

70. Ingber, D. E. Human organs-on-chips for disease modelling, drug development and personalized medicine. *Nat. Rev. Genet.* **23**, 467–491 (2022).

71. Buzhdygan, T. P. *et al.* The SARS-CoV-2 spike protein alters barrier function in 2D static and 3D microfluidic in-vitro models of the human blood–brain barrier. *Neurobiol. Dis.* **146**, 105131 (2020).

72. Zandi Shafagh, R. *et al.* Bioengineered Pancreas–Liver Crosstalk in a Microfluidic Coculture Chip Identifies Human Metabolic Response Signatures in Prediabetic Hyperglycemia. *Adv. Sci.* 2203368 (2022).

73. Sun, S., Jin, L., Zheng, Y. & Zhu, J. Modeling human HSV infection via a vascularized immune-competent skin-on-chip platform. *Nat. Commun.* **13**, 1–15 (2022).

74. Aleman, J. & Skardal, A. A multi-site metastasis-on-a-chip microphysiological system for assessing metastatic preference of cancer cells. *Biotechnol. Bioeng.* **116**, 936–944 (2019).

75. Gil-Gómez, A., Brescia, P., Rescigno, M. & Romero-Gómez, M. Gut–liver axis in nonalcoholic fatty liver disease: the impact of the metagenome, end products, and the epithelial and vascular barriers. in *Seminars in Liver Disease* **41**, 191–205 (Thieme Medical Publishers, Inc., 2021).

76. Lee, S. Y. & Sung, J. H. Gut–liver on a chip toward an in vitro model of hepatic steatosis. *Biotechnol. Bioeng.* **115**, 2817–2827 (2018).

77. Vernetti, L. A. *et al.* A human liver microphysiology platform for investigating physiology, drug safety, and disease models. *Exp. Biol. Med.* **241**, 101–114 (2016).

78. Gori, M. *et al.* Investigating nonalcoholic fatty liver disease in a liver-on-a-chip microfluidic device. *PLoS One* **11**, e0159729 (2016).

79. Zhou, M. *et al.* Development of a functional glomerulus at the organ level on a chip to mimic hypertensive nephropathy. *Sci. Rep.* **6**, 1–13 (2016).

80. Ribas, J. *et al.* Biomechanical strain exacerbates inflammation on a progeria-on-a-chip model. *Small* **13**, 1603737 (2017).

81. Wang, L. *et al.* A disease model of diabetic nephropathy in a glomerulus-on-a-chip microdevice. *Lab Chip* **17**, 1749–1760 (2017).

82. Wang, J. *et al.* A virus-induced kidney disease model based on organ-on-a-chip: Pathogenesis exploration of virus-related renal dysfunctions. *Biomaterials* **219**, 119367 (2019).

83. Jeon, J., Choi, N., Lee, S. H. & Sung, J. H. Three-tissue microphysiological system for

studying inflammatory responses in gut-liver Axis. *Biomed. Microdevices* **22**, 1–11 (2020).

84. Fathi, P., Holland, G., Pan, D. & Esch, M. B. Lymphatic vessel on a chip with capability for exposure to cyclic fluidic flow. *ACS Appl. Bio Mater.* **3**, 6697–6707 (2020).

85. Tanataweethum, N. *et al.* Towards an insulin resistant adipose model on a chip. *Cell. Mol. Bioeng.* **14**, 89–99 (2021).

86. Freag, M. S. *et al.* Human Nonalcoholic Steatohepatitis on a Chip. *Hepatol. Commun.* **5**, 217–233 (2021).

87. Lei, F. *et al.* Multi-compartment organ-on-a-chip based on electrospun nanofiber membrane as in vitro jaundice disease model. *Adv. Fiber Mater.* **3**, 383–393 (2021).

88. de Haan, L. *et al.* A microfluidic 3D endothelium-on-a-chip model to study transendothelial migration of T cells in health and disease. *Int. J. Mol. Sci.* **22**, 8234 (2021).

89. Tao, T. *et al.* Microengineered Multi-Organoid System from hiPSCs to Recapitulate Human Liver-Islet Axis in Normal and Type 2 Diabetes. *Adv. Sci.* **9**, 2103495 (2022).

90. Lu, R. X. Z. *et al.* Vasculature-on-a-chip platform with innate immunity enables identification of angiopoietin-1 derived peptide as a therapeutic for SARS-CoV-2 induced inflammation. *Lab Chip* **22**, 1171–1186 (2022).

91. Quan, Q. *et al.* Analysis of drug efficacy for inflammatory skin on an organ-chip system. *Front. Bioeng. Biotechnol.* **10**, 939629 (2022).

92. Yang, J. *et al.* Gut-liver-axis microphysiological system for studying cellular fluidic shear stress and inter-tissue interaction. *Biomicrofluidics* **16**, 44113 (2022).

93. Harrison, D. J. *et al.* Micromachining a miniaturized capillary electrophoresis-based chemical analysis system on a chip. *Science (80-.).* **261**, 895–897 (1993).

94. Mukhopadhyay, R. When PDMS isn't the best. (2007).

95. Wu, J. & Gu, M. Microfluidic sensing: state of the art fabrication and detection techniques. *J. Biomed. Opt.* **16**, 080901 (2011).

96. Unger, M. A., Chou, H. P., Thorsen, T., Scherer, A. & Quake, S. R. Monolithic microfabricated valves and pumps by multilayer soft lithography. *Science (80-.).* **288**, 113–116 (2000).

97. Yu, F. & Choudhury, D. Microfluidic bioprinting for organ-on-a-chip models. *Drug Discov. Today* **24**, 1248–1257 (2019).

98.   Lai, H. & Folch, A. Design and dynamic characterization of 'single-stroke' peristaltic PDMS micropumps. *Lab Chip* **11**, 336–342 (2011).

99.   Kim, H. J. & Ingber, D. E. Gut-on-a-Chip microenvironment induces human intestinal cells to undergo villus differentiation. *Integr. Biol. (United Kingdom)* **5**, 1130–1140 (2013).

100.   Low, L. A. & Tagle, D. A. Organs-on-chips: Progress, challenges, and future directions. *Exp. Biol. Med.* **242**, 1573–1578 (2017).

101.   Qi, S. *et al.* Microfluidic devices fabricated in poly (methyl methacrylate) using hot-embossing with integrated sampling capillary and fiber optics for fluorescence detection. *Lab Chip* **2**, 88–95 (2002).

102.   Attia, U. M., Marson, S. & Alcock, J. R. Micro-injection moulding of polymer microfluidic devices. *Microfluid. Nanofluidics* **7**, 1–28 (2009).

103.   Rossier, J., Reymond, F. & Michel, P. E. Polymer microfluidic chips for electrochemical and biochemical analyses. *Electrophoresis* **23**, 858–867 (2002).

104.   Cao, H., Tegenfeldt, J. O., Austin, R. H. & Chou, S. Y. Gradient nanostructures for interfacing microfluidics and nanofluidics. *Appl. Phys. Lett.* **81**, 3058–3060 (2002).

105.   Jang, K.-J. *et al.* Human kidney proximal tubule-on-a-chip for drug transport and nephrotoxicity assessment. *Integr. Biol.* **5**, 1119–1129 (2013).

106.   Kim, S., Chung, M., Ahn, J., Lee, S. & Jeon, N. L. Interstitial flow regulates the angiogenic response and phenotype of endothelial cells in a 3D culture model. *Lab Chip* **16**, 4189–4199 (2016).

107.   Zhu, L. *et al.* A vertical-flow bioreactor array compacts hepatocytes for enhanced polarity and functions. *Lab Chip* **16**, 3898–3908 (2016).

108.   Kulthong, K. *et al.* Transcriptome comparisons of in vitro intestinal epithelia grown under static and microfluidic gut-on-chip conditions with in vivo human epithelia. *Sci. Rep.* **11**, 1–14 (2021).

109.   Shin, W., Hinojosa, C. D., Ingber, D. E. & Kim, H. J. Human Intestinal Morphogenesis Controlled by Transepithelial Morphogen Gradient and Flow-Dependent Physical Cues in a Microengineered Gut-on-a-Chip. *iScience* **15**, 391–406 (2019).

110.   Delon, L. C. *et al.* A systematic investigation of the effect of the fluid shear stress on Caco-2 cells towards the optimization of epithelial organ-on-chip models. *Biomaterials* **225**, 119521 (2019).

111. Fois, C. A. M., Schindeler, A., Valtchev, P. & Dehghani, F. Dynamic flow and shear stress as key parameters for intestinal cells morphology and polarization in an organ-on-a-chip model. *Biomed. Microdevices* **23**, 1–12 (2021).

112. Jang, K.-J. *et al.* Fluid-shear-stress-induced translocation of aquaporin-2 and reorganization of actin cytoskeleton in renal tubular epithelial cells. *Integr. Biol.* **3**, 134–141 (2011).

113. Ermis, M. *et al.* Hydrogels as a new platform to recapitulate the tumor microenvironment. in *Handbook of nanomaterials for cancer theranostics* 463–494 (Elsevier, 2018).

114. Galie, P. A. *et al.* Fluid shear stress threshold regulates angiogenic sprouting. *Proc. Natl. Acad. Sci.* **111**, 7968–7973 (2014).

115. Du, Y. *et al.* Mimicking liver sinusoidal structures and functions using a 3D-configured microfluidic chip. *Lab Chip* **17**, 782–794 (2017).

116. Rashidi, H., Alhaque, S., Szkolnicka, D., Flint, O. & Hay, D. C. Fluid shear stress modulation of hepatocyte-like cell function. *Arch. Toxicol.* **90**, 1757–1761 (2016).

117. Phan, D. T. T. *et al.* A vascularized and perfused organ-on-a-chip platform for large-scale drug screening applications. *Lab Chip* **17**, 511–520 (2017).

118. Choi, S. H., Nishikawa, M., Sakoda, A. & Sakai, Y. Feasibility of a simple double-layered coculture system incorporating metabolic processes of the intestine and liver tissue: application to the analysis of benzo [a] pyrene toxicity. *Toxicol. Vitr.* **18**, 393–402 (2004).

119. Sung, J. H. & Shuler, M. L. A micro cell culture analog (µCCA) with 3-D hydrogel culture of multiple cell lines to assess metabolism-dependent cytotoxicity of anti-cancer drugs. *Lab Chip* **9**, 1385–1394 (2009).

120. Esch, M. B., Ueno, H., Applegate, D. R. & Shuler, M. L. Modular, pumpless body-on-a-chip platform for the co-culture of GI tract epithelium and 3D primary liver tissue. *Lab Chip* **16**, 2719–2729 (2016).

121. Mi, S., Pu, H., Xia, S. & Sun, W. A Minimized Valveless Electromagnetic Micropump for Microfluidic Actuation on Organ Chips. *Sensors Actuators, A Phys.* **301**, 111704 (2020).

122. Hou, Y. *et al.* Recent trends in structures and applications of valveless piezoelectric pump-A review. *J. Micromechanics Microengineering* (2022).

123. Forouzandeh, F., Arevalo, A., Alfadhel, A. & Borkholder, D. A. A review of peristaltic micropumps. *Sensors Actuators, A Phys.* **326**, 112602 (2021).

124. Malik, M., Yang, Y., Fathi, P., Mahler, G. J. & Esch, M. B. Critical considerations for the

design of multi-organ microphysiological systems (MPS). *Front. Cell Dev. Biol.* **9**, (2021).

125. Haman, D. Z., Smajstrla, A. G. & Zazueta, F. S. Measuring Pump Capacity for Irrigation System Design. *Florida Coop. Ext. Serv. Univ. Florida, Inst. Food Agric. Sci. Gainesville, FL* (1994).

126. Azizgolshani, H. *et al.* High-throughput organ-on-chip platform with integrated programmable fluid flow and real-time sensing for complex tissue models in drug development workflows. *Lab Chip* **21**, 1454–1474 (2021).

127. Gómez-Sjöberg, R., Leyrat, A. A., Pirone, D. M., Chen, C. S. & Quake, S. R. Versatile, fully automated, microfluidic cell culture system. *Anal. Chem.* **79**, 8557–8563 (2007).

128. Ashraf, M. W., Tayyaba, S. & Afzulpurkar, N. Micro electromechanical systems (MEMS) based microfluidic devices for biomedical applications. *Int. J. Mol. Sci.* **12**, 3648–3704 (2011).

129. Miranda, I. *et al.* Properties and applications of PDMS for biomedical engineering: A review. *J. Funct. Biomater.* **13**, 2 (2021).

130. Au, A. K., Lai, H., Utela, B. R. & Folch, A. Microvalves and micropumps for BioMEMS. *Micromachines* **2**, 179–220 (2011).

131. Ball, C. S., Renzi, R. F., Priye, A. & Meagher, R. J. A simple check valve for microfluidic point of care diagnostics. *Lab Chip* **16**, 4436–4444 (2016).

132. Samuel, R., Thacker, C. M., Maricq, A. V. & Gale, B. K. Simple and cost-effective fabrication of microvalve arrays in PDMS using laser cut molds with application to C. elegans manipulation in microfluidics. *J. Micromechanics Microengineering* **24**, 105007 (2014).

133. Ma, X. *et al.* Experimental Study of Numerical Optimization for 3-D Microstructuring Using DMD-Based Grayscale Lithography. *J. Microelectromechanical Syst.* **24**, 1856–1867 (2015).

134. Kato, Y., Hirai, Y., Kamei, K., Tsuchiya, T. & Tabata, O. Microfluidic device to interconnect multiple organs via fluidic circulation: Towards body-on-a-chip. in *2015 Transducers - 2015 18th International Conference on Solid-State Sensors, Actuators and Microsystems, TRANSDUCERS 2015* 1549–1552 (IEEE, 2015).

135. Mazloum, J. & Shamsi, A. 3D design and numerical simulation of a check-valve micropump for lab-on-a-chip applications. *J. Micro-Bio Robot.* **16**, 237–248 (2020).

136. Liu, X., Li, S. & Bao, G. Numerical simulation on the response characteristics of a pneumatic microactuator for microfluidic chips. *J. Lab. Autom.* **21**, 412–422 (2016).

137. Shamsi, A. & Mazloum, J. Numerical study of a membrane-type micro check-valve for

microfluidic applications. *Microsyst. Technol.* **26**, 367–376 (2020).

138.   Gerasimenko, T. N., Kindeeva, O. V, Petrov, V. A., Khaustov, A. I. & Trushkin, E. V. Modelling and characterization of a pneumatically actuated peristaltic micropump. *Appl. Math. Model.* **52**, 590–602 (2017).

139.   Yao, P. *et al.* Combined experimental and numerical simulation study of PDMS pneumatic micropumps. in *The 7th IEEE International Conference on Nano/Molecular Medicine and Engineering* 130–133 (IEEE, 2013).

140.   Lau, A. T. H., Yip, H. M., Ng, K. C. C., Cui, X. & Lam, R. H. W. Dynamics of microvalve operations in integrated microfluidics. *Micromachines* **5**, 50–65 (2014).

141.   Wang, H. M., Chen, S., Li, K. L., Li, H. Q. & Yang, Z. Numerical Study on the Closing Characteristics of a Check Valve with Built-in Damping System. *J. Appl. Fluid Mech.* **14**, 1003–1014 (2021).

142.   Busek, M., Nötzel, M., Polk, C. & Sonntag, F. Characterization and simulation of peristaltic micropumps. *J. Sensors Sens. Syst.* **2**, 165–169 (2013).

143.   Whulanza, Y. *et al.* Design and evaluation of pneumatic micropump module for a portable polymerase chain reaction kit. in *AIP Conference Proceedings* **2062**, 20049 (AIP Publishing LLC, 2019).

144.   Bhadauria, R., Pidaparti, R. M. & Gad-el-Hak, M. Optimization of a peristaltic micropump with multiple moving actuators. *J. Microelectron. Electron. Packag.* **6**, 189–197 (2009).

145.   Zhang, H., Whalley, R. D., Ferreira, A. M. & Dalgarno, K. High throughput physiological micro-models for in vitro pre-clinical drug testing: a review of engineering systems approaches. *Prog. Biomed. Eng.* **2**, 22001 (2020).

146.   Zhang, D. *et al.* Microfabrication of polydimethylsiloxane–parylene hybrid microelectrode array integrated into a multi-organ-on-a-chip. *Jpn. J. Appl. Phys.* (2022).

147.   Bourbaba, H. & Mohamed, B. Mechanical behavior of polymeric membrane: comparison between PDMS and PMMA for micro fluidic application. *Energy Procedia* **36**, 231–237 (2013).

148.   Kim, T. K., Kim, J. K. & Jeong, O. C. Measurement of nonlinear mechanical properties of PDMS elastomer. *Microelectron. Eng.* **88**, 1982–1985 (2011).

149.   Johnston, I. D., McCluskey, D. K., Tan, C. K. L. & Tracey, M. C. Mechanical characterization of bulk Sylgard 184 for microfluidics and microengineering. *J. Micromechanics Microengineering* **24**, 35017 (2014).

150. Fuard, D., Tzvetkova-Chevolleau, T., Decossas, S., Tracqui, P. & Schiavone, P. Optimization of poly-di-methyl-siloxane (PDMS) substrates for studying cellular adhesion and motility. *Microelectron. Eng.* **85**, 1289–1293 (2008).

151. Müller, A., Wapler, M. C. & Wallrabe, U. A quick and accurate method to determine the Poisson's ratio and the coefficient of thermal expansion of PDMS. *Soft Matter* **15**, 779–784 (2019).

152. Freitas, D. N., Mongersun, A., Chau, H. & Araci, I. E. Tunable soft lithography molds enable rapid-prototyping of multi-height channels for microfluidic large-scale integration. *J. Micromechanics Microengineering* **29**, 35009 (2019).

153. Duarte, F., Gormaz, R. & Natesan, S. Arbitrary Lagrangian–Eulerian method for Navier–Stokes equations with moving boundaries. *Comput. Methods Appl. Mech. Eng.* **193**, 4819–4836 (2004).

154. Lai, A., Altemose, N., White, J. A. & Streets, A. M. On-ratio PDMS bonding for multilayer microfluidic device fabrication. *J. Micromechanics Microengineering* **29**, 107001 (2019).

155. Hirai, Y., Inamoto, Y., Sugano, K., Tsuchiya, T. & Tabata, O. Moving mask UV lithography for three-dimensional structuring. *J. Micromechanics Microengineering* **17**, 199–206 (2007).

156. Hirai, Y. *et al.* ALA-induced fluorescence detection with photoresist-based microfluidic cell sorter for bladder cancer diagnosis. *Sensors Actuators, B Chem.* **213**, 547–557 (2015).

157. Jalili-Firoozinezhad, S. *et al.* A complex human gut microbiome cultured in an anaerobic intestine-on-a-chip. *Nat. Biomed. Eng.* **3**, 520–531 (2019).

158. Kim, H. J., Huh, D., Hamilton, G. & Ingber, D. E. Human gut-on-a-chip inhabited by microbial flora that experiences intestinal peristalsis-like motions and flow. *Lab Chip* **12**, 2165–2174 (2012).

159. Liu, Y. *et al.* Angiogenesis and Functional Vessel Formation Induced by Interstitial Flow and Vascular Endothelial Growth Factor Using a Microfluidic Chip. *Micromachines* **13**, 225 (2022).

160. Figarol, A. *et al.* Interstitial flow regulates in vitro three-dimensional self-organized brain micro-vessels. *Biochem. Biophys. Res. Commun.* **533**, 600–606 (2020).

161. Studer, V. *et al.* Scaling properties of a low-actuation pressure microfluidic valve. *J. Appl. Phys.* **95**, 393–398 (2004).

162. Coluccio, M. L. *et al.* Microfluidic platforms for cell cultures and investigations. *Microelectron. Eng.* **208**, 14–28 (2019).

163. Amadi, O. C. *et al.* A low resistance microfluidic system for the creation of stable concentration gradients in a defined 3D microenvironment. *Biomed. Microdevices* **12**, 1027–1041 (2010).

164. Das, P. *et al.* Tunable microstructured membranes in organs-on-chips to monitor transendothelial hydraulic resistance. *Tissue Eng. Part A* **25**, 1635–1645 (2019).

165. Wu, J., Hirai, Y., Kamei, K., Tsuchiya, T. & Tabata, O. Novel microfluidic device integrated with a fluidic-capacitor to mimic heart beating for generation of functional liver organoids. *Electron. Commun. Japan* **102**, 41–49 (2019).

166. Chalasani, N. *et al.* The diagnosis and management of nonalcoholic fatty liver disease: Practice guidance from the American Association for the Study of Liver Diseases. *Hepatology* **67**, 328–357 (2018).

167. Younossi, Z. M. Non-alcoholic fatty liver disease – A global public health perspective. *J. Hepatol.* **70**, 531–544 (2019).

168. Byrne, C. D. & Targher, G. NAFLD: A multisystem disease. *J. Hepatol.* **62**, S47–S64 (2015).

169. Friedman, S. L., Neuschwander-Tetri, B. A., Rinella, M. & Sanyal, A. J. Mechanisms of NAFLD development and therapeutic strategies. *Nat. Med.* **24**, 908–922 (2018).

170. Estes, C., Razavi, H., Loomba, R., Younossi, Z. & Sanyal, A. J. Modeling the epidemic of nonalcoholic fatty liver disease demonstrates an exponential increase in burden of disease. *Hepatology* **67**, 123–133 (2018).

171. Wiest, R., Albillos, A., Trauner, M., Bajaj, J. S. & Jalan, R. Targeting the gut-liver axis in liver disease. *J. Hepatol.* **67**, 1084–1103 (2017).

172. Sumida, Y. & Yoneda, M. Current and future pharmacological therapies for NAFLD/NASH. *J. Gastroenterol.* **53**, 362–376 (2018).

173. Clemente, M. G., Mandato, C., Poeta, M. & Vajro, P. Pediatric non-alcoholic fatty liver disease: Recent solutions, unresolved issues, and future research directions. *World J. Gastroenterol.* **22**, 8078–8093 (2016).

174. Rotman, Y. & Sanyal, A. J. Current and upcoming pharmacotherapy for non-alcoholic fatty liver disease. *Gut* **66**, 180–190 (2017).

175. Abdalkader, R. & Kamei, K. I. Multi-corneal barrier-on-a-chip to recapitulate eye blinking shear stress forces. *Lab Chip* **20**, 1410–1417 (2020).

176. Sung, J. H., Wang, Y. I., Kim, J. H., Lee, J. M. & Shuler, M. L. Application of chemical

reaction engineering principles to "body-on-a-chip" systems. *AIChE J.* **64**, 4351–4360 (2018).

177. Abaci, H. E. & Shuler, M. L. Human-on-a-chip design strategies and principles for physiologically based pharmacokinetics/pharmacodynamics modeling. *Integr. Biol. (United Kingdom)* **7**, 383–391 (2015).

178. Schurdak, M. *et al.* Applications of the microphysiology systems database for experimental ADME-Tox and disease models. *Lab Chip* **20**, 1472–1492 (2020).

179. Grego, S. *et al.* Systems biology for organotypic cell cultures. *ALTEX* **34**, 301–310 (2017).

180. Müller, F. A. & Sturla, S. J. Human in vitro models of nonalcoholic fatty liver disease. *Curr. Opin. Toxicol.* **16**, 9–16 (2019).

181. Chen, W. L. K. *et al.* Integrated gut/liver microphysiological systems elucidates inflammatory inter-tissue crosstalk. *Biotechnol. Bioeng.* **114**, 2648–2659 (2017).

182. Costa, J. & Ahluwalia, A. Advances and Current Challenges in Intestinal in vitro Model Engineering: A Digest. *Front. Bioeng. Biotechnol.* **7**, 1–14 (2019).

183. Langmead, B. & Salzberg, S. L. Fast gapped-read alignment with Bowtie 2. *Nat. Methods* **9**, 357–359 (2012).

184. Dobin, A. *et al.* STAR: Ultrafast universal RNA-seq aligner. *Bioinformatics* **29**, 15–21 (2013).

185. Hunt, S. E. *et al.* Ensembl variation resources. *Database (Oxford).* **2018**, 1–12 (2018).

186. Li, B. & Dewey, C. N. RSEM: Accurate transcript quantification from RNA-Seq data with or without a reference genome. *BMC Bioinformatics* **12**, 323 (2011).

187. Love, M. I., Huber, W. & Anders, S. Moderated estimation of fold change and dispersion for RNA-seq data with DESeq2. *Genome Biol.* **15**, 550 (2014).

188. Wang, J., Vasaikar, S., Shi, Z., Greer, M. & Zhang, B. WebGestalt 2017: A more comprehensive, powerful, flexible and interactive gene set enrichment analysis toolkit. *Nucleic Acids Res.* **45**, W130–W137 (2017).

189. Subramanian, A. *et al.* Gene set enrichment analysis: A knowledge-based approach for interpreting genome-wide expression profiles. *Proc. Natl. Acad. Sci. U. S. A.* **102**, 15545–15550 (2005).

190. Carpenter, A. E. *et al.* CellProfiler: Image analysis software for identifying and quantifying cell phenotypes. *Genome Biol.* **7**, R100 (2006).

191. Demšar, J. *et al.* Orange: Data mining toolbox in python. *J. Mach. Learn. Res.* **14**, 2349–2353

(2013).

192.   Yu, Z. T. F. *et al.* Integrated microfluidic devices for combinatorial cell-based assays. *Biomed. Microdevices* **11**, 547–555 (2009).

193.   Kamei, K. I. *et al.* An integrated microfluidic culture device for quantitative analysis of human embryonic stem cells. *Lab Chip* **9**, 555–563 (2009).

194.   Huang, B., Wu, H., Kim, S. & Zare, R. N. Coating of poly(dimethylsiloxane) with n-dodecyl-β-D-maltoside to minimize nonspecific protein adsorption. *Lab Chip* **5**, 1005–1007 (2005).

195.   Kamei, K. I. *et al.* Phenotypic and Transcriptional Modulation of Human Pluripotent Stem Cells Induced by Nano/Microfabrication Materials. *Adv. Healthc. Mater.* **2**, 287–291 (2013).

196.   Regehr, K. J. *et al.* Biological implications of polydimethylsiloxane-based microfluidic cell culture. *Lab Chip* **9**, 2132–2139 (2009).

197.   Wong, I. & Ho, C. M. Surface molecular property modifications for poly(dimethylsiloxane) (PDMS) based microfluidic devices. *Microfluid. Nanofluidics* **7**, 291–306 (2009).

198.   Kulthong, K. *et al.* Implementation of a dynamic intestinal gut-on-a-chip barrier model for transport studies of lipophilic dioxin congeners. *RSC Adv.* **8**, 32440–32453 (2018).

199.   Gómez-Lechón, M. J. *et al.* A human hepatocellular in vitro model to investigate steatosis. *Chem. Biol. Interact.* **165**, 106–116 (2007).

200.   Marra, F. & Svegliati-Baroni, G. Lipotoxicity and the gut-liver axis in NASH pathogenesis. *J. Hepatol.* **68**, 280–295 (2018).

201.   Hirsova, P., Ibrabim, S. H., Gores, G. J. & Malhi, H. Thematic review series: Lipotoxicity: Many roads to cell dysfunction and cell death lipotoxic lethal and sublethal stress signaling in hepatocytes: Relevance to NASH pathogenesis. *J. Lipid Res.* **57**, 1758–1770 (2016).

202.   Ogawa, Y. *et al.* Palmitate-induced lipotoxicity is crucial for the pathogenesis of nonalcoholic fatty liver disease in cooperation with gut-derived endotoxin. *Sci. Rep.* **8**, 11365 (2018).

203.   McQuin, C. *et al.* CellProfiler 3.0: Next-generation image processing for biology. *PLoS Biol.* **16**, e2005970 (2018).

204.   Sirenko, O., Hesley, J., Rusyn, I. & Cromwell, E. F. High-content high-throughput assays for characterizing the viability and morphology of human iPSC-derived neuronal cultures. *Assay Drug Dev. Technol.* **12**, 536–547 (2014).

205.   Gilbert, D. F. *et al.* A novel multiplex cell viability assay for high-throughput RNAi screening. *PLoS One* **6**, e28338 (2011).

206. Van Der Maaten, L. & Hinton, G. Visualizing data using t-SNE. *J. Mach. Learn. Res.* **9**, 2579–2625 (2008).

207. Caldez, M. J., Bjorklund, M. & Kaldis, P. Cell cycle regulation in NAFLD: when imbalanced metabolism limits cell division. *Hepatol. Int.* **14**, 463–474 (2020).

208. Villenave, R. *et al.* Human gut-on-a-chip supports polarized infection of coxsackie B1 virus in vitro. *PLoS One* **12**, 1–17 (2017).

209. Wang, X. *et al.* Fluid shear stress promotes autophagy in hepatocellular carcinoma cells. *Int. J. Biol. Sci.* **14**, 1277–1290 (2018).

210. Trapecar, M. *et al.* Gut-Liver Physiomimetics Reveal Paradoxical Modulation of IBD-Related Inflammation by Short-Chain Fatty Acids. *Cell Syst.* **10**, 223-239.e9 (2020).

211. Camakaris, J., Voskoboinik, I. & Mercer, J. F. Molecular mechanisms of copper homeostasis. *Biochem. Biophys. Res. Commun.* **261**, 225–232 (1999).

212. Khan, S., Zafar, A. & Naseem, I. Redox cycling of copper by coumarin-di(2-picolyl)amine hybrid molecule leads to ROS-mediated modulation of redox scavengers, DNA damage and cell death in diethylnitrosamine induced hepatocellular carcinoma. *Bioorg. Chem.* **99**, 103818 (2020).

213. Parsekar, S. U. *et al.* DNA binding, cleavage and cytotoxicity studies of three mononuclear Cu(II) chloro-complexes containing N–S donor Schiff base ligands. *J. Biol. Inorg. Chem.* **23**, 1331–1349 (2018).

214. Foo, J. B. *et al.* Copper complex derived from S-benzyldithiocarbazate and 3-acetylcoumarin induced apoptosis in breast cancer cell. *BioMetals* **31**, 505–515 (2018).

215. Gori, M. *et al.* Palmitic acid affects intestinal epithelial barrier integrity and permeability in vitro. *Antioxidants* **9**, 417 (2020).

216. Storniolo, C. E., Cabral, M., Busquets, M. A., Martín-Venegas, R. & Moreno, J. J. Dual Behavior of Long-Chain Fatty Acids and Their Cyclooxygenase/Lipoxygenase Metabolites on Human Intestinal Caco-2 Cell Growth. *Front. Pharmacol.* **11**, 529976 (2020).

217. Embade, N., Valeron, P. F., Aznar, S., Lopez-Collazo, E. & Lacal, J. C. Apoptosis induced by Rac GTPase correlates with induction of FasL and ceramides production. *Mol. Biol. Cell* **11**, 4347–4358 (2000).

218. Simon, S. & Schubert, R. Inhibitory effect of phospholipids on P-glycoprotein: Cellular studies in Caco-2, MDCKII mdr1 and MDCKII wildtype cells and P-gp ATPase activity measurements. *Biochim. Biophys. Acta - Mol. Cell Biol. Lipids* **1821**, 1211–1223 (2012).

219. Berryman, S., Matthews, K., Lee, J. H., Duffy, S. P. & Ma, H. Image-based phenotyping of disaggregated cells using deep learning. *Commun. Biol.* **3**, 1–9 (2020).

220. Kostrzewski, T. *et al.* Modelling human liver fibrosis in the context of non-alcoholic steatohepatitis using a microphysiological system. *Commun. Biol.* **4**, (2021).

221. Thomson, J. A. Embryonic stem cell lines derived from human blastocysts. *Science (80-.).* **282**, 1145–1147 (1998).

222. Jaffe, R. B. Induction of pluripotent stem cells from adult human fibroblasts by defined factors: Commentary. *Obstet. Gynecol. Surv.* **63**, 153 (2008).

223. Makarova, K. S. *et al.* Evolutionary classification of CRISPR–Cas systems: a burst of class 2 and derived variants. *Nat. Rev. Microbiol.* **18**, 67–83 (2020).

224. Arakawa, H. *et al.* Kinetic analysis of sequential metabolism of triazolam and its extrapolation to humans using an entero-hepatic two-organ microphysiological system. *Lab Chip* **20**, 537–547 (2020).

225. Tripathi, A. *et al.* The gut-liver axis and the intersection with the microbiome. *Nat. Rev. Gastroenterol. Hepatol.* **15**, 397–411 (2018).

226. Shinha, K. *et al.* A kinetic pump integrated microfluidic plate (Kim-plate) with high usability for cell culture-based multiorgan microphysiological systems. *Micromachines* **12**, 1007 (2021).

227. Bein, A. *et al.* Microfluidic Organ-on-a-Chip Models of Human Intestine. *Cmgh* **5**, 659–668 (2018).

228. Tan, H. Y. *et al.* A multi-chamber microfluidic intestinal barrier model using Caco-2 cells for drug transport studies. *PLoS One* **13**, e0197101 (2018).

229. Halldorsson, S., Lucumi, E., Gómez-Sjöberg, R. & Fleming, R. M. T. Advantages and challenges of microfluidic cell culture in polydimethylsiloxane devices. *Biosens. Bioelectron.* **63**, 218–231 (2015).

230. Madsen, M. H., Feidenhans, N. A., Hansen, P.-E., Garnæs, J. & Dirscherl, K. Accounting for PDMS shrinkage when replicating structures. *J. Micromechanics Microengineering* **24**, 127002 (2014).

231. Frost, T. S., Jiang, L., Lynch, R. M. & Zohar, Y. Permeability of epithelial/endothelial barriers in transwells and microfluidic bilayer devices. *Micromachines* **10**, 533 (2019).

232. Lentle, R. G. & Janssen, P. W. M. Physical characteristics of digesta and their influence on

flow and mixing in the mammalian intestine: A review. *J. Comp. Physiol. B Biochem. Syst. Environ. Physiol.* **178**, 673–690 (2008).

233. Ishikawa, T., Sato, T., Mohit, G., Imai, Y. & Yamaguchi, T. Transport phenomena of microbial flora in the small intestine with peristalsis. *J. Theor. Biol.* **279**, 63–73 (2011).

234. Ma, L. D. *et al.* Design and fabrication of a liver-on-a-chip platform for convenient, highly efficient, and safe: In situ perfusion culture of 3D hepatic spheroids. *Lab Chip* **18**, 2547–2562 (2018).

235. Cameron, T. C. *et al.* PDMS Organ-On-Chip Design and Fabrication: Strategies for Improving Fluidic Integration and Chip Robustness of Rapidly Prototyped Microfluidic In Vitro Models. *Micromachines* **13**, (2022).

236. Sambuy, Y. *et al.* The Caco-2 cell line as a model of the intestinal barrier: Influence of cell and culture-related factors on Caco-2 cell functional characteristics. *Cell Biol. Toxicol.* **21**, 1–26 (2005).

237. Lasli, S. *et al.* A Human Liver-on-a-Chip Platform for Modeling Nonalcoholic Fatty Liver Disease. *Adv. Biosyst.* **3**, 1–12 (2019).

238. Quirós-Solano, W. F. *et al.* Microfabricated tuneable and transferable porous PDMS membranes for Organs-on-Chips. *Sci. Rep.* **8**, 1–11 (2018).

239. Wevers, N. R. *et al.* High-throughput compound evaluation on 3D networks of neurons and glia in a microfluidic platform. *Sci. Rep.* **6**, 1–10 (2016).

240. Lee, S. Y., Kim, D., Lee, S. H. & Sung, J. H. Microtechnology-based in vitro models: Mimicking liver function and pathophysiology. *APL Bioeng.* **5**, 41505 (2021).

241. Sasaki, Y. *et al.* Intestinal Permeability of Drugs in Caco-2 Cells Cultured in Microfluidic Devices. *Biol. Pharm. Bull.* **45**, 1246–1253 (2022).

242. Loftus, E. V. *et al.* PSC-IBD: A unique form of inflammatory bowel disease associated with primary sclerosing cholangitis. *Gut* **54**, 91–96 (2005).

243. Wu, X. X. *et al.* Paeoniflorin Prevents Intestinal Barrier Disruption and Inhibits Lipopolysaccharide (LPS)-Induced Inflammation in Caco-2 Cell Monolayers. *Inflammation* **42**, 2215–2225 (2019).

244. Fort, M. M. *et al.* A Synthetic TLR4 Antagonist Has Anti-Inflammatory Effects in Two Murine Models of Inflammatory Bowel Disease. *J. Immunol.* **174**, 6416–6423 (2005).

245. Lin, T.-Y., Fan, C.-W., Maa, M.-C. & Leu, T.-H. Lipopolysaccharide-promoted proliferation

of Caco-2 cells is mediated by c-Src induction and ERK activation. *Biomedicine* **5**, 1–6 (2015).

246. Santos, A. J. M., Lo, Y.-H., Mah, A. T. & Kuo, C. J. The intestinal stem cell niche: homeostasis and adaptations. *Trends Cell Biol.* **28**, 1062–1078 (2018).

247. Creff, J. *et al.* Fabrication of 3D scaffolds reproducing intestinal epithelium topography by high-resolution 3D stereolithography. *Biomaterials* **221**, 119404 (2019).

248. De Pieri, A., Rochev, Y. & Zeugolis, D. I. Scaffold-free cell-based tissue engineering therapies: advances, shortfalls and forecast. *NPJ Regen. Med.* **6**, 1–15 (2021).

249. Workman, M. J. *et al.* Enhanced utilization of induced pluripotent stem cell–derived human intestinal organoids using microengineered chips. *Cell. Mol. Gastroenterol. Hepatol.* **5**, 669–677 (2018).

250. Ishida-Ishihara, S., Takada, R., Furusawa, K., Ishihara, S. & Haga, H. Improvement of the cell viability of hepatocytes cultured in three-dimensional collagen gels using pump-free perfusion driven by water level difference. *Sci. Rep.* **12**, 1–11 (2022).

251. Wang, J. *et al.* Loganin alleviates LPS-activated intestinal epithelial inflammation by regulating TLR4/NF-κB and JAK/STAT3 signaling pathways. *Kaohsiung J. Med. Sci.* **36**, 257–264 (2020).

252. Park, B. S. & Lee, J.-O. Recognition of lipopolysaccharide pattern by TLR4 complexes. *Exp. Mol. Med.* **45**, e66–e66 (2013).

253. Panaro, M. A., Carofiglio, V., Acquafredda, A., Cavallo, P. & Cianciulli, A. Anti-inflammatory effects of resveratrol occur via inhibition of lipopolysaccharide-induced NF-κB activation in Caco-2 and SW480 human colon cancer cells. *Br. J. Nutr.* **108**, 1623–1632 (2012).

254. Kang, Y.-M., Eom, S.-H. & Kim, Y.-M. Protective effect of phlorotannins from Eisenia bicyclis against lipopolysaccharide-stimulated inflammation in HepG2 cells. *Environ. Toxicol. Pharmacol.* **35**, 395–401 (2013).

255. Zeng, J., Du, S., Zhou, J. & Huang, K. Role of SelS in lipopolysaccharide-induced inflammatory response in hepatoma HepG2 cells. *Arch. Biochem. Biophys.* **478**, 1–6 (2008).

256. Collins, S. L. & Patterson, A. D. The gut microbiome: an orchestrator of xenobiotic metabolism. *Acta Pharm. Sin. B* **10**, 19–32 (2020).

257. Muller, P. A. *et al.* Microbiota modulate sympathetic neurons via a gut–brain circuit. *Nature* **583**, 441–446 (2020).

258. Schluter, J. *et al.* The gut microbiota is associated with immune cell dynamics in humans. *Nature* **588**, 303–307 (2020).

259. Yang, J. *et al.* Multilayered Microfluidic Device for Controllable Flow Perfusion of Gut-Liver on a Chip. in *2021 21st International Conference on Solid-State Sensors, Actuators and Microsystems (Transducers)* 176–179 (IEEE, 2021).

260. Chuchuy, J. *et al.* Integration of electrospun membranes into low-absorption thermoplastic organ-on-chip. *ACS Biomater. Sci. Eng.* **7**, 3006–3017 (2021).

261. Wang, M. *et al.* Application of perfluoropolyether elastomers in microfluidic drug metabolism assays. *Int. J. Pharm.* **627**, 122253 (2022).

262. Saharil, F., Carlborg, C. F., Haraldsson, T. & van der Wijngaart, W. Biocompatible "click" wafer bonding for microfluidic devices. *Lab Chip* **12**, 3032–3035 (2012).

263. Gökaltun, A., Kang, Y. B. A., Yarmush, M. L., Usta, O. B. & Asatekin, A. Simple surface modification of poly (dimethylsiloxane) via surface segregating smart polymers for biomicrofluidics. *Sci. Rep.* **9**, 1–14 (2019).

264. Ramos, M. J., Bandiera, L., Menolascina, F. & Fallowfield, J. A. In vitro models for non-alcoholic fatty liver disease: Emerging platforms and their applications. *Iscience* **25**, 103549 (2022).

265. Grouls, M. *et al.* Differential gene expression in iPSC-derived human intestinal epithelial cell layers following exposure to two concentrations of butyrate, propionate and acetate. *Sci. Rep.* **12**, 1–15 (2022).

266. Green, C. J. *et al.* Studying non-alcoholic fatty liver disease: the ins and outs of in vivo, ex vivo and in vitro human models. *Horm. Mol. Biol. Clin. Investig.* **41**, (2020).

267. Ganji, S. H., Kashyap, M. L. & Kamanna, V. S. Niacin inhibits fat accumulation, oxidative stress, and inflammatory cytokine IL-8 in cultured hepatocytes: Impact on non-alcoholic fatty liver disease. *Metabolism* **64**, 982–990 (2015).

268. Yu, J. *et al.* Induced pluripotent stem cell lines derived from human somatic cells. *Science (80-.).* **318**, 1917–1920 (2007).

269. Lowry, W. E. *et al.* Generation of human induced pluripotent stem cells from dermal fibroblasts. *Proc. Natl. Acad. Sci.* **105**, 2883–2888 (2008).

270. Soucy, J. R., Bindas, A. J., Koppes, A. N. & Koppes, R. A. Instrumented Microphysiological Systems for Real-Time Measurement and Manipulation of Cellular Electrochemical Processes. *iScience* **21**, 521–548 (2019).

Appendix I - Digital micromirror device-based grayscale lithography

The semi-rounded shape fluidic channel was fabricated by grayscale lithography. The total process were included two steps (**Supplementary Fig. S3-1 and table S3-1**), grayscale lithography optimization and digital micromirror device (DMD) based grayscale lithography.

First, the profile of the semi-rounded shape fluidic channel was gotten by the FEA simulation method (described in **Chapter 3**). Then, the profile data was inputted into the optimization program.[133] A wafer-scale grayscale mask pattern was formed (**Supplementary Fig. S3-2**). Second, after a series process of positive resist coating, the wafer was put under the DMD system for exposure with a digital mask pattern and parameters. Finally, the wafer was put into developer solution with optimized development time, to get the designed semi-round shape channel mold.
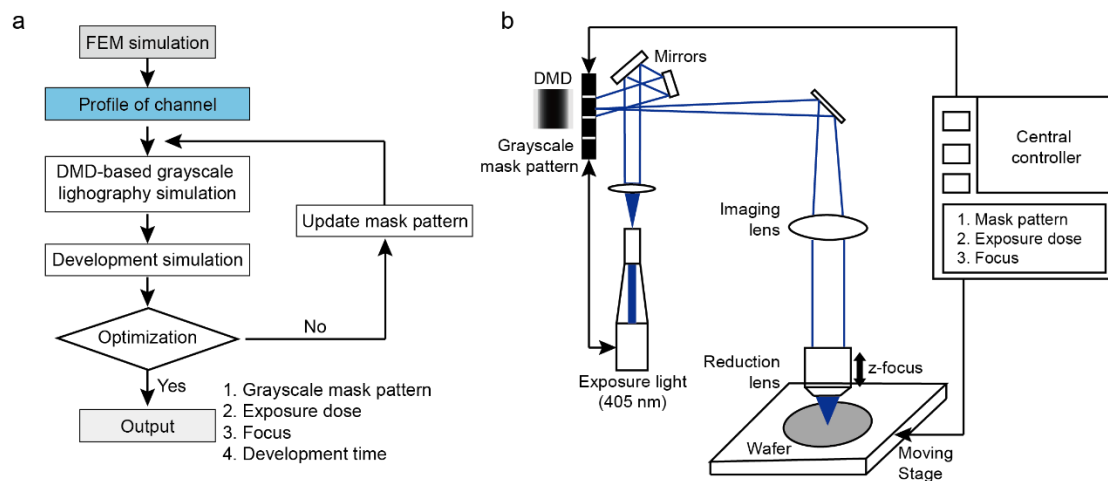
Supplementary Fig. S3-1 | The process of digital micromirror device-based grayscale lithography. (a) The grayscale lithography optimization flow chart; (b) The exposure controller of digital micromirror device lithography. DMD: digital micromirror device.
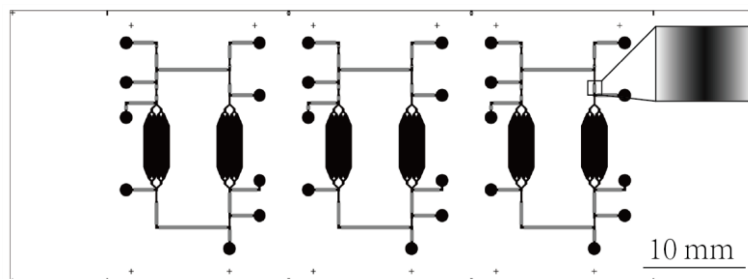
Supplementary Fig. S3-2 | Wafer-scale digital grayscale mask pattern (for chapter 4 device)

Supplementary Table S3-1 The grayscale lithography process for 45 μm semi-round channel mold fabrication

Process	Detial parameters
(1) Wafer cleaning	Pure water @10 min
(2) Dehydrated bake	Hotplate 150 @10 min
(3) Spin coating first layers positive photoresist (PMER P-LA900)	PMER P-LA900 spin coating (45 μm) Slope 2s 500rpm 38s 850rpm 15s
(4) Pre-bake	Oven 115°C @ 6 min
(5) Spin coating second layers positive photoresist (PMER P-LA900)	PMER P-LA900 spin coating (45 μm) Slope 2s 500rpm 38s 850rpm 15s
(6) Pre-bake	Oven 115°C @ 12 min
(7)Room temperature	Over 60 min (Moisture absorption)
(8) Grayscale Exposure (DMD)	Wave length 405 Dose 2000 mJ/mc^2 Off set 0.02-0.0225 mm
(9) Development	P-7G positive resist developer @ 550s Pure water clean @ 1min
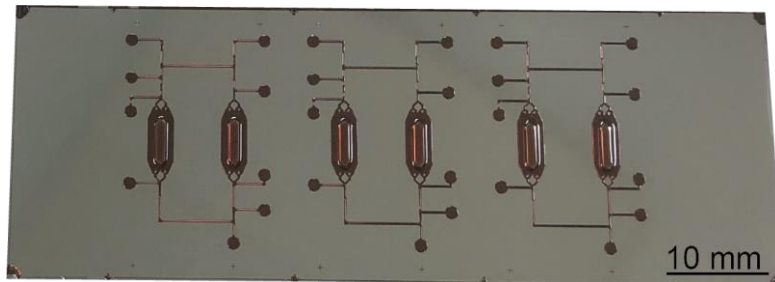
Supplementary Fig. S3-3 | DMD-based grayscale lithography fabricated mold (for chapter 4 device)

Appendix II - Supplementary Figures
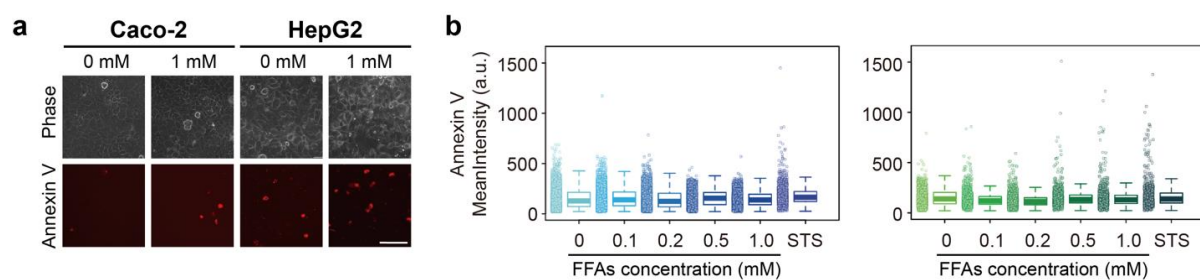
Supplementary Fig. S4-1 | FFAs treatment for 1 day did not affect apoptotic cellular status. a, Phase contrast and fluorescent micrographs of Caco-2 and HepG2 cells treated with FFAs (0 and 1 mM) stained with the Annexin V apoptotic cell marker. The scale bars represent 100 µm. b, Box plots to evaluate individual apoptotic cells [Caco-2 (left) and HepG2 (right)] after FFA treatment for 24 h. For comparison, cells were treated with 1 µM of straurosporine (STS) for 24 h. The center lines of the boxplots show the medians. The box limits indicate the 25th and 75th percentiles. The whiskers extend 1.5 times the interquartile range from the 25th and 75th percentiles.
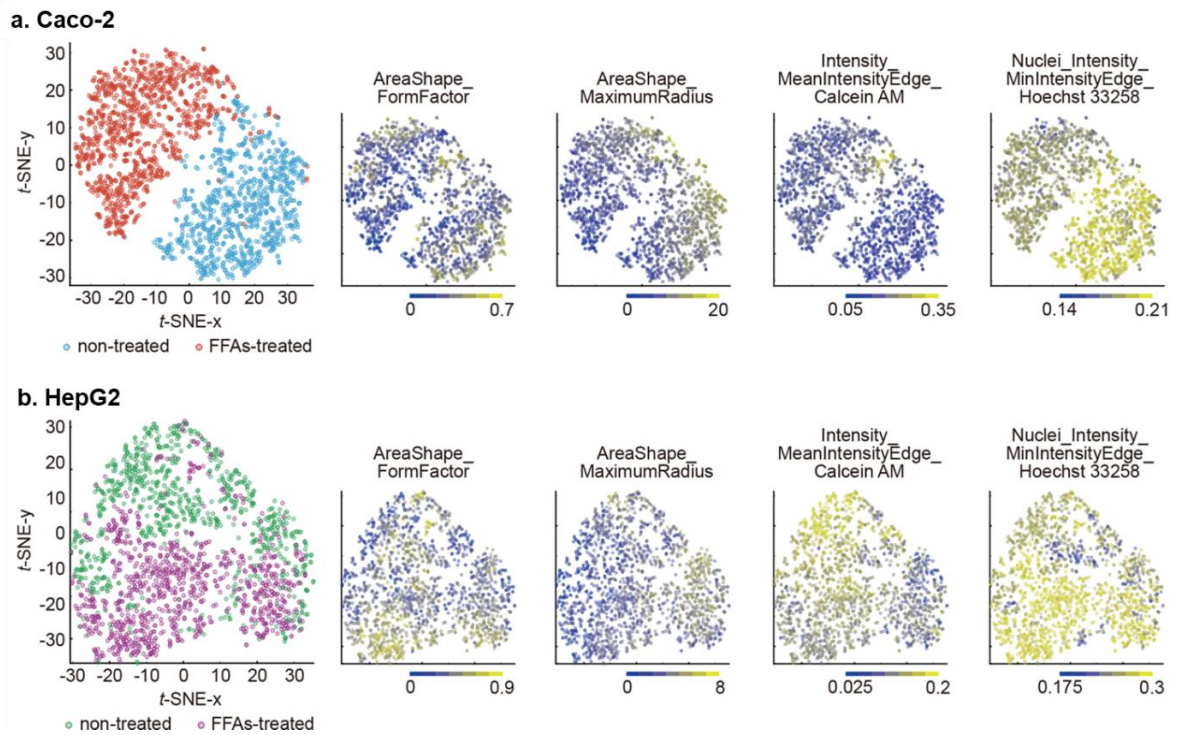
Supplementary Fig. S4-2 | Single-cell profiling cell viability and t-SNE analyses of the 1-day free fatty acids treatment. a, b, Two-dimensional t-SNE plots of microscopic single-cell profiling of Caco-2 (c) and HepG2 (d) treated with 1 mM of FFAs or no treatment and stained with Calcein AM cellular and Hoechst 33258 nuclei markers.
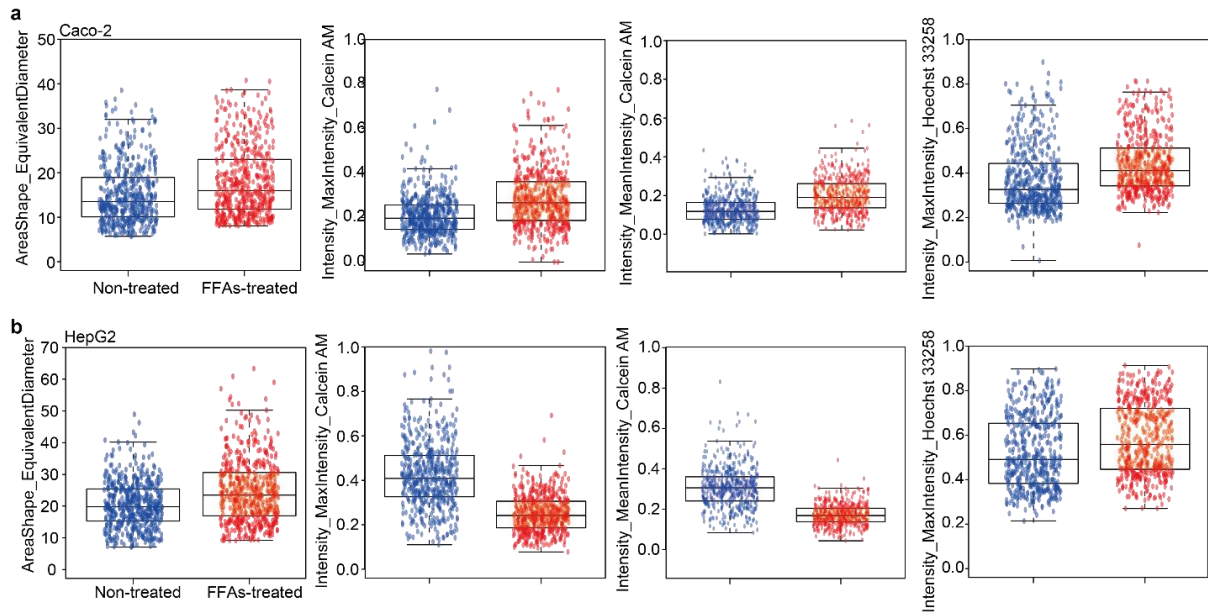
Supplementary Fig. S4-3 | Boxplots comparing cellular parameters of non-treated and FFAs-treated Caco-2 and HepG2 cells of 7 days FFAs treatment. The centrelines of the boxplots show the medians. The box limits indicate the 25th and 75th percentiles. The whiskers extend 1.5 times the interquartile range from the 25th and 75th percentiles. p-values were estimated with the Tukey-Kramer test and are presented in **Supplementary Table S4-11 and Table S4-12 in Appendix III**.
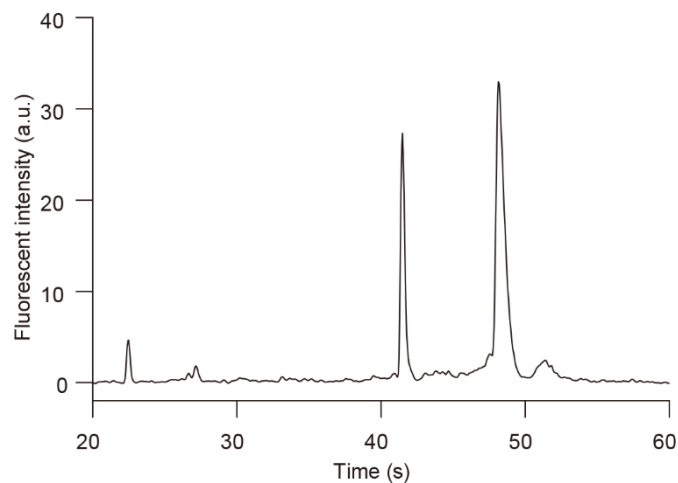
Supplementary Fig. S4-4 | Typical electropherogram of total RNA obtained from Caco-2 cells cultured on a chip with Agilent 2100 Bioanalyzer. The electropherogram shows that 18S and 28S ribosomal RNA (rRNA) bands were clearly detected without smeared bands, and the RNA integrity number (RIN), which is used to standardize RNA quality control, was over 7.0. This result indicates that the total RNA harvested from the chip was sufficient to be applied to RNA sequencing.
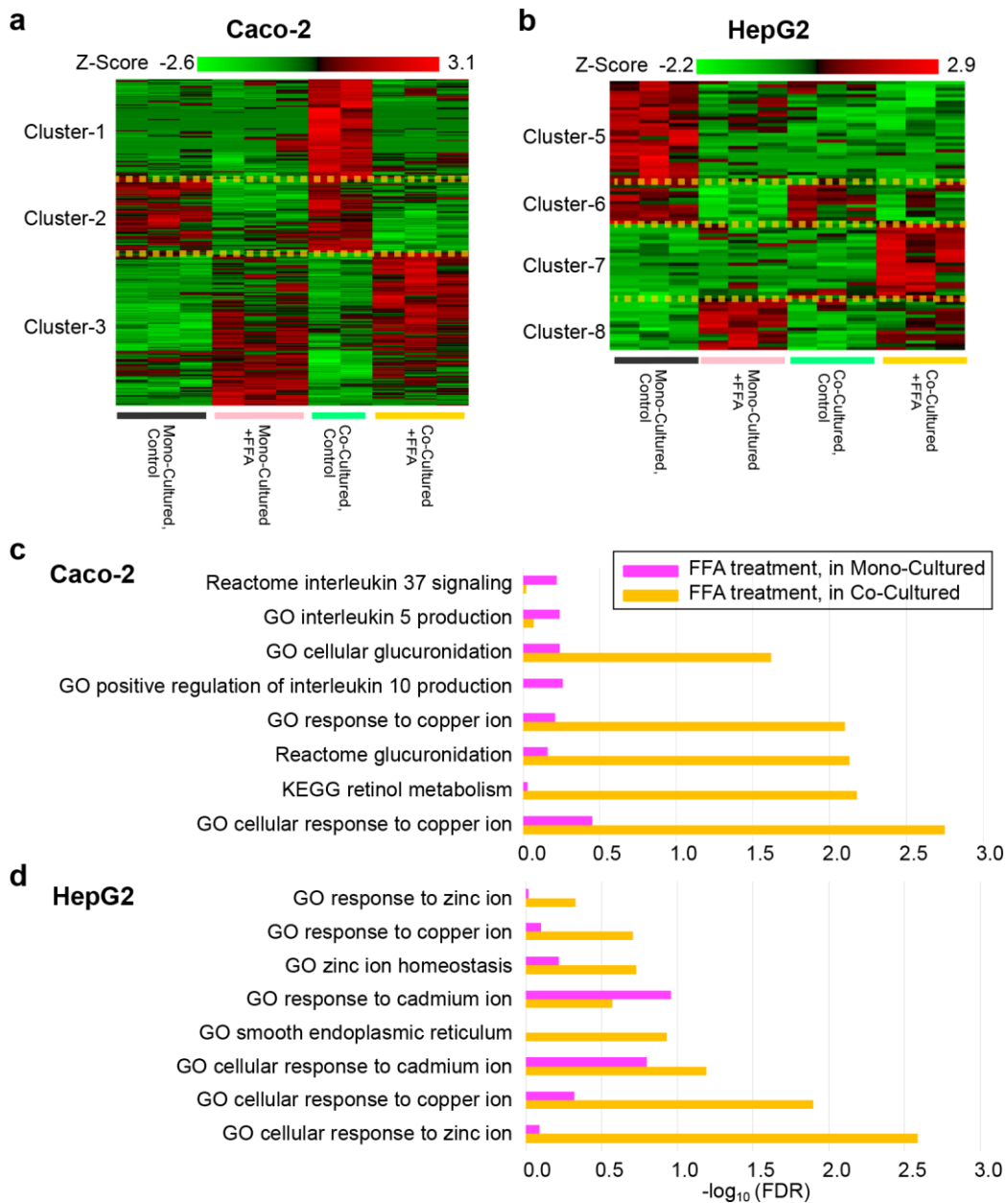
Supplementary Fig. S4-5 | Gene expressions of the effects of FFA treatment for 1 day and crosstalk with the *in vitro* human GLA model. a, b, Heat maps for the DEGs obtained from the 1-day FFAs-treated Caco-2 (**a**) and HepG2 (**b**) experimental sets. Z-values of the expression profiles are shown. **c, d,** Bar charts showing gene enrichment related to certain GO terms and pathways for FFA-treated Caco-2 (**c**) and HepG2 (**d**) cells under mono- and co-cultured conditions.
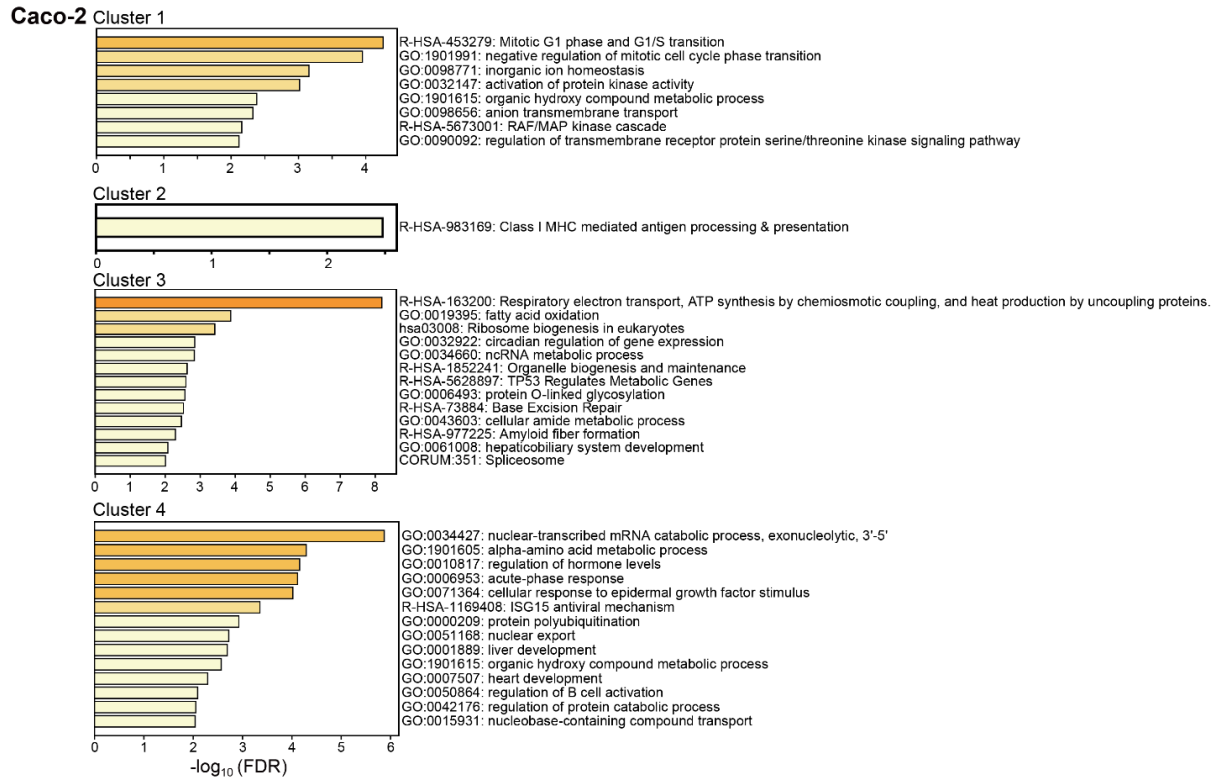
Supplementary Fig. S4-6 | Gene-ontology (GO) terms of Clusters 1 to 4 for Caco-2 cells
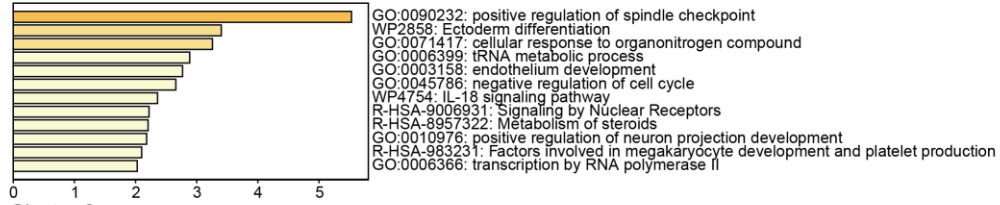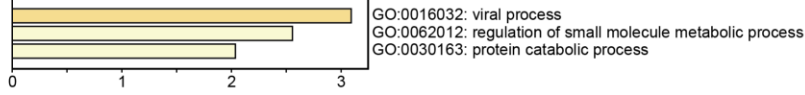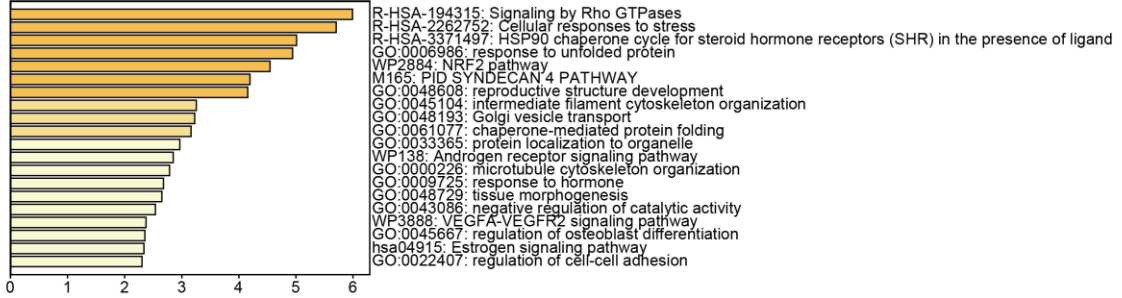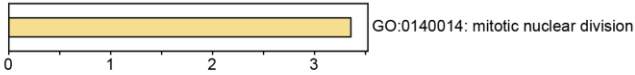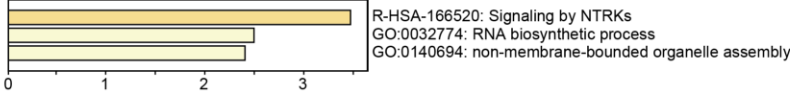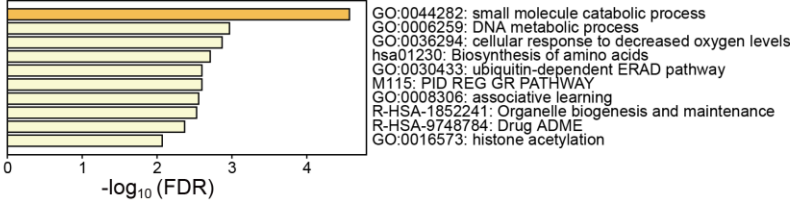
Supplementary Fig. S4-7 | Gene-ontology (GO) terms of Clusters 5 to 10 for Caco-2 cells
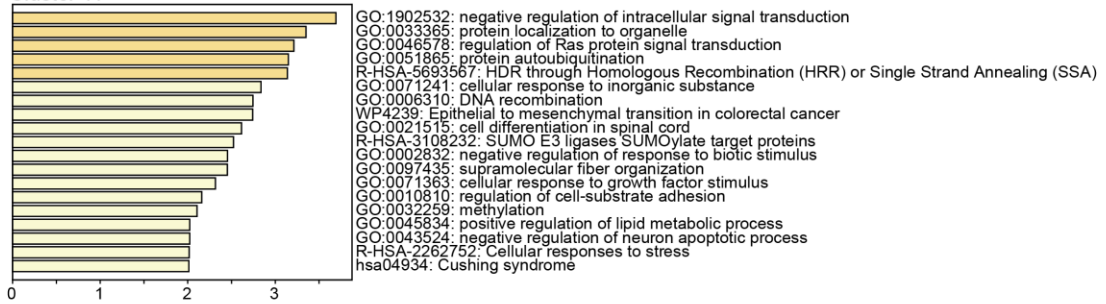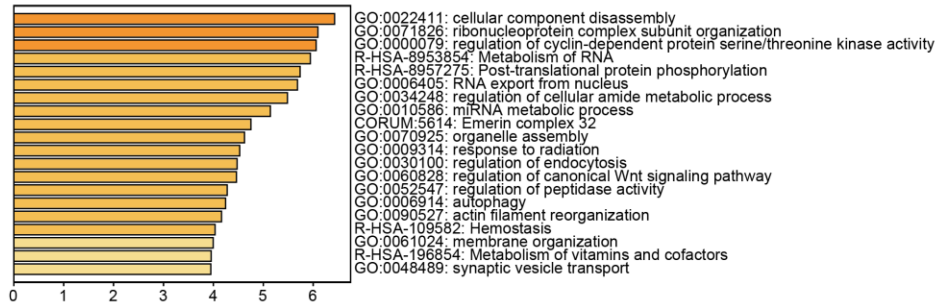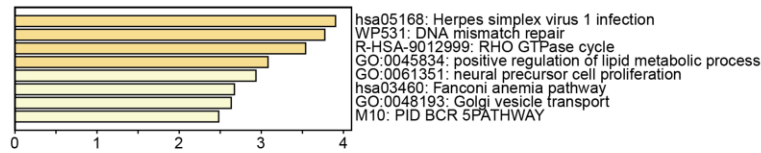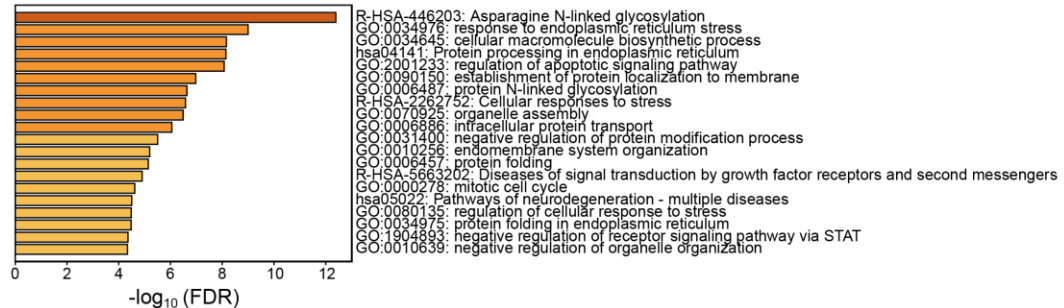
Supplementary Fig. S4-8 | Gene-ontology (GO) terms of Clusters 11 to 14 for HepG2 cells
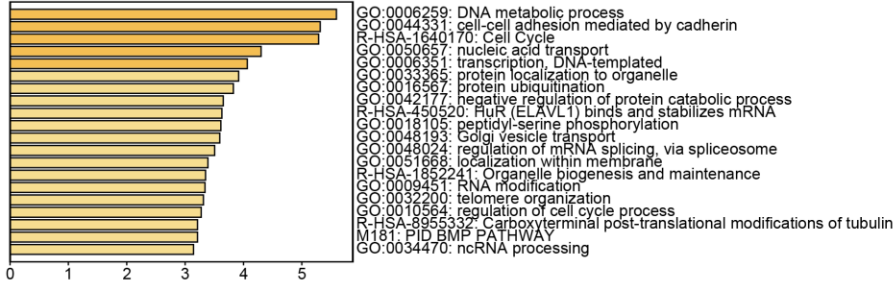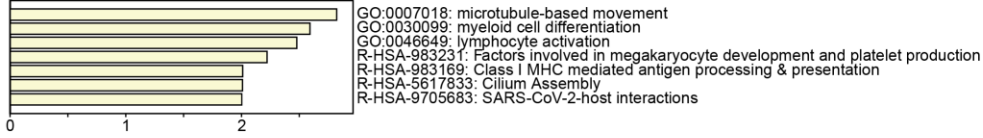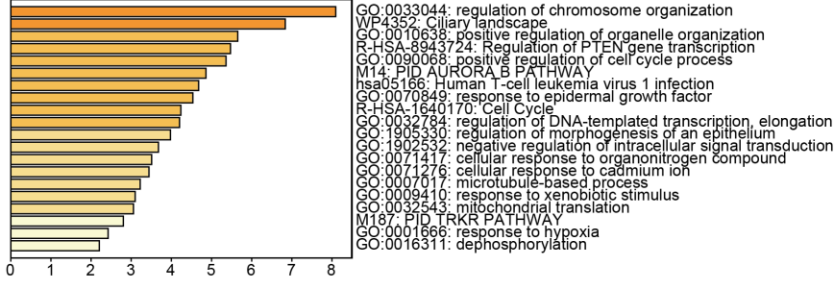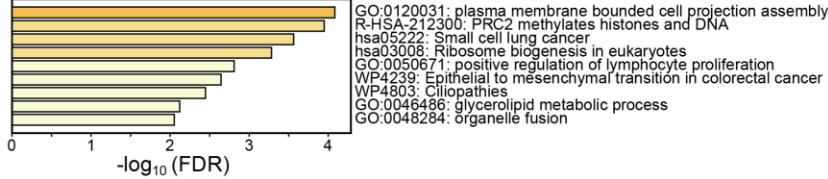
Supplementary Fig. S4-9 | Gene-ontology (GO) terms of Clusters 15 to 18 for HepG2 cells
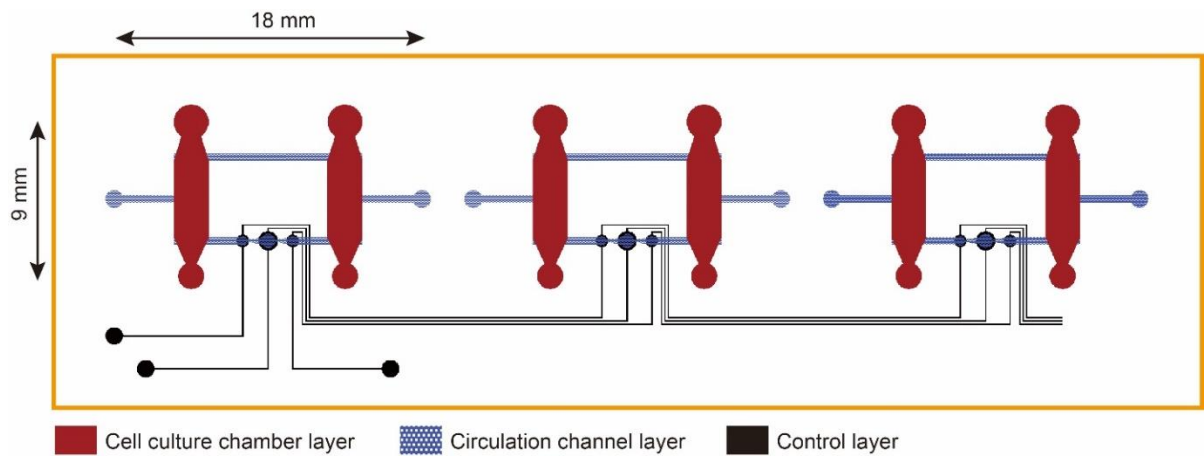
Supplementary Fig. S5-1 | Mask pattern design of GLA-MPS.

Appendix III - Supplementary Tables

Supplementary Table S4-1 | *p*-values by Tukey-Kramer test for single-cell profiling for viability staining in Caco-2 cells visualized by Calcein AM.

Sample A	Sample B	Lower	Upper	*p* value
C:H CF	C: C CF	-6.112719475	0.385090584	0.097
C:H CF	C: C S	-45.33705147	-40.09039401	0
C: C CF	C: C S	-42.47323702	-37.22657956	0

C: Caco-2; H: HepG2

S: Static condition; CF: Circulated flow

Supplementary Table S4-2 | *p*-values by Tukey-Kramer test for single-cell profiling for viability staining in HepG2 cells visualized by Calcein AM.

Sample A	Sample B	Lower	Upper	*p* value
C:H CF	C: C CF	-9.751347416	5.209697104	0.757
C:H CF	C: C S	-7.954678346	7.010102229	0.988
C: C CF	C: C S	-5.680112927	9.277187123	0.839

C: Caco-2; H: HepG2

S: Static condition; CF: Circulated flow

Supplementary Table S4-3 | *p*-values by Tukey-Kramer test for single-cell profiling of FFAs accumulation in Caco-2 cells for 1-day treatment visualized by AdipoRed staining

Sample A	Sample B	Lower	Upper	*p* value
0.1 mM	0.2 mM	0.223113	4.250708	0.0193
0.1 mM	0.5 mM	3.169775	7.19737	8.99E-09
0.1 mM	0 mM	0.185112	4.212706	0.0229
0.1 mM	1.0 mM	1.250067	5.277662	5.79E-05
0.1 mM	2.0 mM	2.544007	6.571602	1.08E-08
0.2 mM	0.5 mM	0.932865	4.960459	0.000443
0.2 mM	0 mM	-2.0518	1.975796	1
0.2 mM	1.0 mM	-0.98684	3.040751	0.694
0.2 mM	2.0 mM	0.307096	4.334691	0.0131
0.5 mM	0 mM	-4.99846	-0.97087	0.000351
0.5 mM	1.0 mM	-3.93351	0.094089	0.0719
0.5 mM	2.0 mM	-2.63957	1.388029	0.95
0 mM	1.0 mM	-0.94884	3.078753	0.659
0 mM	2.0 mM	0.345098	4.372693	0.0109
1.0 mM	2.0 mM	-0.71986	3.307737	0.445

Supplementary Table S4-4 | *p*-values by Tukey-Kramer test for single-cell profiling of FFAs accumulation in HepG2 cells for 1-day treatment visualized by AdipoRed staining

Sample A	Sample B	Lower	Upper	*p* value
0.1 mM	0.2 mM	-0.15943	4.633305	0.0834
0.1 mM	0.5 mM	3.120136	7.912872	0
0.1 mM	0 mM	-1.11966	3.673077	0.652
0.1 mM	1 mM	8.310987	13.10372	0
0.1 mM	2 mM	5.696866	10.4896	0
0.2 mM	0.5 mM	0.883199	5.675935	0.00136
0.2 mM	0 mM	-3.3566	1.436141	0.863
0.2 mM	1 mM	6.07405	10.86679	0
0.2 mM	2 mM	3.459929	8.252665	0
0.5 mM	0 mM	-6.63616	-1.84343	7.14E-06
0.5 mM	1 mM	2.794483	7.587219	9.94E-09
0.5 mM	2 mM	0.180361	4.973097	0.0266
0 mM	1 mM	7.034278	11.82701	0
0 mM	2 mM	4.420156	9.212892	0
1 mM	2 mM	-5.01049	-0.21775	0.0232

Supplementary Table S4-5 | *p*-values by Tukey-Kramer test for single-cell profiling of 7 days FFAs accumulation in Caco-2 cells visualized by AdipoRed staining

Sample A	Sample B	Lower	Upper	*p* value
0 mM-co	0 mM-mono	-1.29137	0.194586	0.23
0 mM-co	1 mM-co	5.379399	6.865359	2.41E-11
0 mM-co	1 mM-mono	6.835213	8.321173	2.41E-11
0 mM-mono	1 mM-co	5.927792	7.413752	2.41E-11
0 mM-mono	1 mM-mono	7.383607	8.869567	2.41E-11
1 mM-co	1 mM-mono	0.712835	2.198795	2.92E-06

Supplementary Table S4-6 | *p*-values by Tukey-Kramer test for single-cell profiling of 7 days FFAs accumulation in HepG2 cells visualized by AdipoRed staining

Sample A	Sample B	Lower	Upper	*p* value
0 mM-co	0 mM-mono	-1.20778	0.646492	0.865
0 mM-co	1 mM-co	4.899882	6.754151	2.41E-11
0 mM-co	1 mM-mono	2.047212	3.90148	2.41E-11
0 mM-mono	1 mM-co	5.180524	7.034793	2.41E-11
0 mM-mono	1 mM-mono	2.327854	4.182122	2.41E-11
1 mM-co	1 mM-mono	-3.7798	-1.92554	2.42E-11

Supplementary Table S4-7| *p*-values by Tukey-Kramer test for single-cell profiling of apoptotic cells in 7-days FFAs-treated Caco-2 cells visualized by Annexin V staining

Sample A	Sample B	Lower	Upper	*p* value
0 mM-Co	0 mM-Mono	-0.03047	-0.01876	0
0 mM-Co	1 mM-Co	-0.01207	-0.00036	0.031
0 mM-Co	1 mM-Mono	0.054332	0.066037	0
0 mM-Co	STS	0.000587	0.012293	0.0226
0 mM-Mono	1 mM-Co	0.012549	0.024254	0
0 mM-Mono	1 mM-Mono	0.078947	0.090653	0
0 mM-Mono	STS	0.025203	0.036908	0
1 mM-Co	1 mM-Mono	0.060546	0.072251	0
1 mM-Co	STS	0.006801	0.018507	2.13E-08
1 mM-Mono	STS	-0.0596	-0.04789	0

Supplementary Table S4-8| *p*-values by Tukey-Kramer test for single-cell profiling of apoptotic cells in 7-days FFAs-treated HepG2 cells visualized by Annexin V staining

Sample A	Sample B	Lower	Upper	*p* value
0 mM-Co	0 mM-Mono	-0.004368062	0.012056966	0.705
0 mM-Co	1 mM-Co	-0.002436683	0.013988345	0.307
0 mM-Co	1 mM-Mono	0.095574898	0.111999926	0
0 mM-Co	STS	0.019753004	0.036178032	0
0 mM-Mono	1 mM-Co	-0.006281135	0.010143893	0.968
0 mM-Mono	1 mM-Mono	0.091730446	0.108155474	0
0 mM-Mono	STS	0.015908552	0.03233358	0
1 mM-Co	1 mM-Mono	0.089799067	0.106224095	0
1 mM-Co	STS	0.013977173	0.030402201	0
1 mM-Mono	STS	-0.084034408	-0.06760938	0

Supplementary Table S4-9| *p*-values by Tukey-Kramer test for single-cell profiling of albumin expression in 7-days FFAs-treated HepG2 cells visualized by albumin staining

Sample A	Sample B	Lower	Upper	*p* value
0 mM-Co	0 mM-Mono	-14.3585	-8.82408	0
0 mM-Co	1 mM-Co	-2.47111	3.06336	0.993
0 mM-Co	1 mM-Mono	-9.963	-4.42854	0
0 mM-Mono	1 mM-Co	9.120202	14.65467	0
0 mM-Mono	1 mM-Mono	1.628305	7.162773	0.000263
1 mM-Co	1 mM-Mono	-10.2591	-4.72466	0

Supplementary Table S4-10| 68 types of Cellular parameters for quantitative cellular phenotype analysis with Calcein AM and Hoechst 33258 staining

AreaShape_Area

AreaShape_BoundingBoxArea

AreaShape_BoundingBoxMaximum_X

AreaShape_BoundingBoxMaximum_Y

AreaShape_BoundingBoxMinimum_X

AreaShape_BoundingBoxMinimum_Y

AreaShape_Center_X

AreaShape_Center_Y

AreaShape_Compactness

AreaShape_Eccentricity

AreaShape_EquivalentDiameter

AreaShape_Extent

AreaShape_FormFactor

AreaShape_MajorAxisLength

AreaShape_MaxFeretDiameter

AreaShape_MaximumRadius

AreaShape_MeanRadius

AreaShape_MedianRadius

AreaShape_MinFeretDiameter

AreaShape_MinorAxisLength

AreaShape_Orientation

AreaShape_Perimeter

AreaShape_Solidity

Intensity_IntegratedIntensityEdge_Hoechst 33258

Intensity_IntegratedIntensityEdge_Calcein AM

Intensity_IntegratedIntensity_Hoechst 33258

Intensity_IntegratedIntensity_Calcein AM

Intensity_LowerQuartileIntensity_Hoechst 33258

Intensity_LowerQuartileIntensity_Calcein AM

Intensity_MADIntensity_Hoechst 33258

Intensity_MADIntensity_Calcein AM

Intensity_MassDisplacement_Hoechst 33258

Intensity_MassDisplacement_Calcein AM

Intensity_MaxIntensityEdge_Hoechst 33258

Intensity_MaxIntensityEdge_Calcein AM

Intensity_MaxIntensity_Hoechst 33258

Intensity_MaxIntensity_Calcein AM

Intensity_MeanIntensityEdge_Hoechst 33258

Intensity_MeanIntensityEdge_Calcein AM

Intensity_MeanIntensity_Hoechst 33258

Intensity_MeanIntensity_Calcein AM

Intensity_MedianIntensity_Hoechst 33258

Intensity_MedianIntensity_Calcein AM

Intensity_MinIntensityEdge_Hoechst 33258

Intensity_MinIntensityEdge_Calcein AM

Intensity_MinIntensity_Hoechst 33258

Intensity_MinIntensity_Calcein AM

Intensity_StdIntensityEdge_Hoechst 33258

Intensity_StdIntensityEdge_Calcein AM

Intensity_StdIntensity_Hoechst 33258

Intensity_StdIntensity_Calcein AM

Intensity_UpperQuartileIntensity_Hoechst 33258

Intensity_UpperQuartileIntensity_Calcein AM

NucleiAreaShape_Area

NucleiAreaShape_Compactness

NucleiAreaShape_Eccentricity

NucleiAreaShape_EulerNumber

NucleiAreaShape_Extent

NucleiAreaShape_FormFactor

NucleiAreaShape_MajorAxisLength

NucleiAreaShape_MaxFeretDiameter

NucleiAreaShape_MaximumRadius

NucleiAreaShape_MeanRadius

NucleiAreaShape_MedianRadius

NucleiAreaShape_MinFeretDiameter

NucleiAreaShape_MinorAxisLength

NucleiAreaShape_Perimeter

NucleiAreaShape_Solidity

Supplementary Table S4-11| *p*-values by Tukey-Kramer test for single-cell profiling of FFAs-treated Caco-2 cells with the most distinguishable cellular parameters based on Calcein AM and Hoechst 33258 staining

Items	A	B	Lower	Upper	*p* value
AreaShape_EquivalentDiameter	FFAs-	Non-	-2.36536	-0.56856	0.0014
Intensity_MaxIntensity_Calcein AM	FFAs-	Non-	-0.10853	-0.08029	0
Intensity_MeanIntensity_Calcein AM	FFAs-	Non-	-0.11294	-0.09258	0
Intensity_MaxIntensity_Hoechst 33258	FFAs-	Non-	-0.086	-0.05159	0

Supplementary Table S4-12| *p*-values by Tukey-Kramer test for single-cell profiling of FFAs-treated HepG2 cells with the most distinguishable cellular parameters based on Calcein AM and Hoechst 33258 staining

Items	A	B	Lower	Upper	*p* value
AreaShape_EquivalentDiameter	FFAs-	Non-	-4.44339	-2.25715	2.53E-09
Intensity_MaxIntensity_Calcein AM	FFAs-	Non-	0.15985	0.190296	0
Intensity_MeanIntensity_Calcein AM	FFAs-	Non-	0.1563806	0.1764105	0
Intensity_MaxIntensity_Hoechst 33258	FFAs-	Non-	-0.04341	-0.00386	0.0192

Supplementary Table S5-1. Tukey's multiple comparison test for ZO-1 expression in Caco-2 cells

levelA	levelB	p-values	levelA	levelB	p-values
0P0C	0P22C	1	0P61C	5P0C	1.00E-11
0P0C	0P61C	0.999	0P61C	5P22C	1.00E-11
0P0C	2P0C	0.00074	0P61C	5P61C	1.01E-11
0P0C	2P22C	1.75E-05	2P0C	2P22C	0.997
0P0C	2P61C	1.00E-11	2P0C	2P61C	1.00E-11
0P0C	5P0C	1.00E-11	2P0C	5P0C	1.00E-11
0P0C	5P22C	1.00E-11	2P0C	5P22C	1.00E-11
0P0C	5P61C	1.01E-11	2P0C	5P61C	3.22E-07
0P22C	0P61C	0.999	2P22C	2P61C	1.00E-11
0P22C	2P0C	0.000643	2P22C	5P0C	1.01E-11
0P22C	2P22C	1.48E-05	2P22C	5P22C	1.00E-11
0P22C	2P61C	1.00E-11	2P22C	5P61C	2.40E-05
0P22C	5P0C	1.00E-11	2P61C	5P0C	5.41E-06
0P22C	5P22C	1.00E-11	2P61C	5P22C	0.493
0P22C	5P61C	1.01E-11	2P61C	5P61C	1.01E-11
0P61C	2P0C	2.54E-05	5P0C	5P22C	0.0376
0P61C	2P22C	3.44E-07	5P0C	5P61C	8.91E-08
0P61C	2P61C	1.00E-11	5P22C	5P61C	1.01E-11

0P, 2P and 5P represent 0, 2 and 5 µL min^{-1} of the perfusion flow.

0C, 22C and 61C represent 0, 22 and 61 nL min^{-1} of the circulation flow.

Supplementary Table S5-2. Tukey's multiple comparison test for ALB expression in HepG2 cells

levelA	levelB	p-values	levelA	levelB	p-values
0P0C	0P22C	0.879	0P61C	5P0C	6.64E-08
0P0C	0P61C	0.00171	0P61C	5P22C	0.412
0P0C	2P0C	0.00577	0P61C	5P61C	2.13E-07
0P0C	2P22C	0.666	2P0C	2P22C	0.599
0P0C	2P61C	1.00E-11	2P0C	2P61C	1.01E-11
0P0C	5P0C	0.554	2P0C	5P0C	4.16E-07
0P0C	5P22C	1.86E-08	2P0C	5P22C	0.232
0P0C	5P61C	1.01E-11	2P0C	5P61C	3.29E-08
0P22C	0P61C	0.183	2P22C	2P61C	1.00E-11
0P22C	2P0C	0.343	2P22C	5P0C	0.00453
0P22C	2P22C	1	2P22C	5P22C	0.000352
0P22C	2P61C	1.00E-11	2P22C	5P61C	1.02E-11
0P22C	5P0C	0.0177	2P61C	5P0C	1.00E-11
0P22C	5P22C	5.99E-05	2P61C	5P22C	1.01E-11
0P22C	5P61C	1.01E-11	2P61C	5P61C	6.87E-05
0P61C	2P0C	1	5P0C	5P22C	1.02E-11
0P61C	2P22C	0.386	5P0C	5P61C	1.00E-11
0P61C	2P61C	1.01E-11	5P22C	5P61C	0.0081

0P, 2P and 5P represent 0, 2 and 5 μL min^{-1} of the perfusion flow.

0C, 22C and 61C represent 0, 22 and 61 nL min^{-1} of the circulation flow.

Supplementary Table S5-3. Tukey's multiple comparison test for iNOS expression in Caco-2 cells

levelA	levelB	ci.low	ci.up	p-values
LPS _DEX_A	LPS _DEX_B	0.048019962	0.071115542	0
LPS _DEX_A	LPS _DEX_C	-0.0144929	0.008602681	1
LPS _DEX_A	LPS _DEX_D	-0.040786656	-0.017691075	0
LPS _DEX_A	LPS _DEX_E	-0.014371806	0.008723775	1
LPS _DEX_A	LPS _DEX_F	-0.010886423	0.012209158	1
LPS _DEX_A	LPS_A	0.126969582	0.150065163	0
LPS _DEX_A	LPS_B	0.137727055	0.160822636	0
LPS _DEX_A	LPS_C	0.075333244	0.098452002	0
LPS _DEX_A	LPS_D	0.022710275	0.045805855	0
LPS _DEX_A	LPS_E	-0.016759601	0.00633598	0.985
LPS _DEX_A	LPS_F	0.035287864	0.058383445	0
LPS _DEX_A	No_stim_A	0.018130966	0.041226547	0
LPS _DEX_A	No_stim_B	-0.022435924	0.000659657	0.0922
LPS _DEX_A	No_stim_C	-0.004912769	0.01819438	0.867
LPS _DEX_A	No_stim_D	-0.040284222	-0.017188641	0
LPS _DEX_A	No_stim_E	-0.043725597	-0.020630016	0
LPS _DEX_A	No_stim_F	-0.041634876	-0.018539295	0
LPS _DEX_B	LPS _DEX_C	-0.074060652	-0.050965071	0
LPS _DEX_B	LPS _DEX_D	-0.100354408	-0.077258827	0
LPS _DEX_B	LPS _DEX_E	-0.073939558	-0.050843977	0
LPS _DEX_B	LPS _DEX_F	-0.070454175	-0.047358594	0
LPS _DEX_B	LPS_A	0.06740183	0.090497411	0
LPS _DEX_B	LPS_B	0.078159303	0.101254884	0
LPS _DEX_B	LPS_C	0.015765492	0.03888425	0
LPS _DEX_B	LPS_D	-0.036857477	-0.013761897	0
LPS _DEX_B	LPS_E	-0.076327353	-0.053231772	0
LPS _DEX_B	LPS_F	-0.024279888	-0.001184307	0.0144
LPS _DEX_B	No_stim_A	-0.041436786	-0.018341205	0
LPS _DEX_B	No_stim_B	-0.082003676	-0.058908095	0
LPS _DEX_B	No_stim_C	-0.064480521	-0.041373372	0
LPS _DEX_B	No_stim_D	-0.099851974	-0.076756393	0
LPS _DEX_B	No_stim_E	-0.103293349	-0.080197768	0
LPS _DEX_B	No_stim_F	-0.101202628	-0.078107047	0
LPS _DEX_C	LPS _DEX_D	-0.037841546	-0.014745965	0
LPS _DEX_C	LPS _DEX_E	-0.011426696	0.011668884	1
LPS _DEX_C	LPS _DEX_F	-0.007941313	0.015154268	1
LPS _DEX_C	LPS_A	0.129914692	0.153010273	0
LPS _DEX_C	LPS_B	0.140672165	0.163767746	0

LPS _DEX_C	LPS_C	0.078278354	0.101397111	0
LPS _DEX_C	LPS_D	0.025655384	0.048750965	0
LPS _DEX_C	LPS_E	-0.013814491	0.00928109	1
LPS _DEX_C	LPS_F	0.038232974	0.061328555	0
LPS _DEX_C	No_stim_A	0.021076076	0.044171657	0
LPS _DEX_C	No_stim_B	-0.019490814	0.003604767	0.608
LPS _DEX_C	No_stim_C	-0.001967659	0.02113949	0.255
LPS _DEX_C	No_stim_D	-0.037339112	-0.014243531	0
LPS _DEX_C	No_stim_E	-0.040780487	-0.017684906	0
LPS _DEX_C	No_stim_F	-0.038689766	-0.015594185	0
LPS _DEX_D	LPS _DEX_E	0.014867059	0.03796264	0
LPS _DEX_D	LPS _DEX_F	0.018352443	0.041448024	0
LPS _DEX_D	LPS_A	0.156208448	0.179304029	0
LPS _DEX_D	LPS_B	0.16696592	0.190061501	0
LPS _DEX_D	LPS_C	0.10457211	0.127690867	0
LPS _DEX_D	LPS_D	0.05194914	0.075044721	0
LPS _DEX_D	LPS_E	0.012479265	0.035574846	5.23E-11
LPS _DEX_D	LPS_F	0.06452673	0.087622311	0
LPS _DEX_D	No_stim_A	0.047369832	0.070465413	0
LPS _DEX_D	No_stim_B	0.006802942	0.029898523	4.54E-06
LPS _DEX_D	No_stim_C	0.024326097	0.047433246	0
LPS _DEX_D	No_stim_D	-0.011045356	0.012050225	1
LPS _DEX_D	No_stim_E	-0.014486732	0.008608849	1
LPS _DEX_D	No_stim_F	-0.01239601	0.010699571	1
LPS _DEX_E	LPS _DEX_F	-0.008062407	0.015033174	1
LPS _DEX_E	LPS_A	0.129793598	0.152889179	0
LPS _DEX_E	LPS_B	0.140551071	0.163646652	0
LPS _DEX_E	LPS_C	0.07815726	0.101276017	0
LPS _DEX_E	LPS_D	0.02553429	0.048629871	0
LPS _DEX_E	LPS_E	-0.013935585	0.009159996	1
LPS _DEX_E	LPS_F	0.03811188	0.061207461	0
LPS _DEX_E	No_stim_A	0.020954982	0.044050563	0
LPS _DEX_E	No_stim_B	-0.019611908	0.003483673	0.579
LPS _DEX_E	No_stim_C	-0.002088753	0.021018396	0.276
LPS _DEX_E	No_stim_D	-0.037460206	-0.014364625	0
LPS _DEX_E	No_stim_E	-0.040901581	-0.017806	0
LPS _DEX_E	No_stim_F	-0.03881086	-0.015715279	0
LPS _DEX_F	LPS_A	0.126308215	0.149403796	0
LPS _DEX_F	LPS_B	0.137065687	0.160161268	0
LPS _DEX_F	LPS_C	0.074671876	0.097790634	0
LPS _DEX_F	LPS_D	0.022048907	0.045144488	0
LPS _DEX_F	LPS_E	-0.017420968	0.005674613	0.951
LPS _DEX_F	LPS_F	0.034626497	0.057722078	0
LPS _DEX_F	No_stim_A	0.017469598	0.040565179	0

LPS _DEX_F	No_stim_B	-0.023097292	-1.71E-06	0.0499
LPS _DEX_F	No_stim_C	-0.005574137	0.017533012	0.943
LPS _DEX_F	No_stim_D	-0.04094559	-0.017850009	0
LPS _DEX_F	No_stim_E	-0.044386965	-0.021291384	0
LPS _DEX_F	No_stim_F	-0.042296244	-0.019200663	0
LPS_A	LPS_B	-0.000790318	0.022305263	0.103
LPS_A	LPS_C	-0.063184129	-0.040065371	0
LPS_A	LPS_D	-0.115807098	-0.092711517	0
LPS_A	LPS_E	-0.155276973	-0.132181393	0
LPS_A	LPS_F	-0.103229509	-0.080133928	0
LPS_A	No_stim_A	-0.120386407	-0.097290826	0
LPS_A	No_stim_B	-0.160953297	-0.137857716	0
LPS_A	No_stim_C	-0.143430142	-0.120322993	0
LPS_A	No_stim_D	-0.178801595	-0.155706014	0
LPS_A	No_stim_E	-0.18224297	-0.159147389	0
LPS_A	No_stim_F	-0.180152249	-0.157056668	0
LPS_B	LPS_C	-0.073941601	-0.050822844	0
LPS_B	LPS_D	-0.126564571	-0.10346899	0
LPS_B	LPS_E	-0.166034446	-0.142938865	0
LPS_B	LPS_F	-0.113986981	-0.0908914	0
LPS_B	No_stim_A	-0.131143879	-0.108048298	0
LPS_B	No_stim_B	-0.171710769	-0.148615188	0
LPS_B	No_stim_C	-0.154187614	-0.131080465	0
LPS_B	No_stim_D	-0.189559067	-0.166463486	0
LPS_B	No_stim_E	-0.193000442	-0.169904862	0
LPS_B	No_stim_F	-0.190909721	-0.16781414	0
LPS_C	LPS_D	-0.064193937	-0.041075179	0
LPS_C	LPS_E	-0.103663812	-0.080545054	0
LPS_C	LPS_F	-0.051616347	-0.028497589	0
LPS_C	No_stim_A	-0.068773245	-0.045654488	0
LPS_C	No_stim_B	-0.109340135	-0.086221377	0
LPS_C	No_stim_C	-0.091816974	-0.06868666	0
LPS_C	No_stim_D	-0.127188433	-0.104069676	0
LPS_C	No_stim_E	-0.130629808	-0.107511051	0
LPS_C	No_stim_F	-0.128539087	-0.10542033	0
LPS_D	LPS_E	-0.051017666	-0.027922085	0
LPS_D	LPS_F	0.001029799	0.02412538	0.0171
LPS_D	No_stim_A	-0.016127099	0.006968482	0.996
LPS_D	No_stim_B	-0.056693989	-0.033598408	0
LPS_D	No_stim_C	-0.039170834	-0.016063685	0
LPS_D	No_stim_D	-0.074542287	-0.051446706	0
LPS_D	No_stim_E	-0.077983662	-0.054888081	0
LPS_D	No_stim_F	-0.075892941	-0.05279736	0
LPS_E	LPS_F	0.040499674	0.063595255	0

LPS_E	No_stim_A	0.023342776	0.046438357	0
LPS_E	No_stim_B	-0.017224114	0.005871467	0.964
LPS_E	No_stim_C	0.000299041	0.02340619	0.0371
LPS_E	No_stim_D	-0.035072412	-0.011976831	1.81E-10
LPS_E	No_stim_E	-0.038513787	-0.015418206	0
LPS_E	No_stim_F	-0.036423066	-0.013327485	0
LPS_F	No_stim_A	-0.028704689	-0.005609108	3.28E-05
LPS_F	No_stim_B	-0.069271579	-0.046175998	0
LPS_F	No_stim_C	-0.051748424	-0.028641275	0
LPS_F	No_stim_D	-0.087119877	-0.064024296	0
LPS_F	No_stim_E	-0.090561252	-0.067465671	0
LPS_F	No_stim_F	-0.088470531	-0.06537495	0
No_stim_A	No_stim_B	-0.05211468	-0.029019099	0
No_stim_A	No_stim_C	-0.034591525	-0.011484376	5.51E-10
No_stim_A	No_stim_D	-0.069962978	-0.046867398	0
No_stim_A	No_stim_E	-0.073404354	-0.050308773	0
No_stim_A	No_stim_F	-0.071313633	-0.048218052	0
No_stim_B	No_stim_C	0.005975364	0.029082513	1.82E-05
No_stim_B	No_stim_D	-0.029396089	-0.006300508	1.06E-05
No_stim_B	No_stim_E	-0.032837464	-0.009741883	2.00E-08
No_stim_B	No_stim_F	-0.030746743	-0.007651162	1.03E-06
No_stim_C	No_stim_D	-0.046930812	-0.023823663	0
No_stim_C	No_stim_E	-0.050372187	-0.027265038	0
No_stim_C	No_stim_F	-0.048281466	-0.025174317	0
No_stim_D	No_stim_E	-0.014989166	0.008106415	1
No_stim_D	No_stim_F	-0.012898445	0.010197136	1
No_stim_E	No_stim_F	-0.009457069	0.013638512	1

LPS: 1 mg mL$-$1 LPS treatment

LPS_DEX: 1 mg mL$-$1 LPS with 200 µM Dex treatment

No_stim: No treatment

A~F: The sample IDs

Supplementary Table S5-4. Tukey's multiple comparison test for iNOS expression in HepG2 cells

levelA	levelB	ci.low	ci.up	pValue
LPS _DEX_A	LPS _DEX_B	-0.024905898	-0.000509754	0.0308
LPS _DEX_A	LPS _DEX_C	0.002269427	0.026665572	0.00458
LPS _DEX_A	LPS _DEX_D	-0.069185166	-0.044789021	0
LPS _DEX_A	LPS _DEX_E	0.010460718	0.034856863	1.45E-08
LPS _DEX_A	LPS _DEX_F	-0.066450021	-0.042053877	0
LPS _DEX_A	LPS_A	0.009487854	0.033883998	8.75E-08
LPS _DEX_A	LPS_B	-0.060116674	-0.035720529	0
LPS _DEX_A	LPS_C	-0.033414778	-0.009018633	2.03E-07
LPS _DEX_A	LPS_D	-0.079622943	-0.055226798	0
LPS _DEX_A	LPS_E	-0.083848495	-0.05945235	0
LPS _DEX_A	LPS_F	0.093657479	0.118053624	0
LPS _DEX_A	No_stim_A	0.002985504	0.027381648	0.00192
LPS _DEX_A	No_stim_B	-0.060634792	-0.036238648	0
LPS _DEX_A	No_stim_C	-0.029979194	-0.005583049	5.48E-05
LPS _DEX_A	No_stim_D	-0.083809967	-0.059413823	0
LPS _DEX_A	No_stim_E	-0.078670327	-0.054274182	0
LPS _DEX_A	No_stim_F	-0.045352549	-0.020956405	0
LPS _DEX_B	LPS _DEX_C	0.014977253	0.039373397	0
LPS _DEX_B	LPS _DEX_D	-0.05647734	-0.032081195	0
LPS _DEX_B	LPS _DEX_E	0.023168544	0.047564688	0
LPS _DEX_B	LPS _DEX_F	-0.053742196	-0.029346051	0
LPS _DEX_B	LPS_A	0.02219568	0.046591824	0
LPS _DEX_B	LPS_B	-0.047408848	-0.023012704	0
LPS _DEX_B	LPS_C	-0.020706952	0.003689193	0.581
LPS _DEX_B	LPS_D	-0.066915117	-0.042518972	0
LPS _DEX_B	LPS_E	-0.071140669	-0.046744524	0
LPS _DEX_B	LPS_F	0.106365305	0.13076145	0
LPS _DEX_B	No_stim_A	0.01569333	0.040089474	0
LPS _DEX_B	No_stim_B	-0.047926966	-0.023530822	0
LPS _DEX_B	No_stim_C	-0.017271368	0.007124777	0.994
LPS _DEX_B	No_stim_D	-0.071102141	-0.046705997	0
LPS _DEX_B	No_stim_E	-0.065962501	-0.041566356	0
LPS _DEX_B	No_stim_F	-0.032644724	-0.008248579	7.74E-07
LPS _DEX_C	LPS _DEX_D	-0.083652665	-0.05925652	0
LPS _DEX_C	LPS _DEX_E	-0.004006781	0.020389363	0.651
LPS _DEX_C	LPS _DEX_F	-0.080917521	-0.056521376	0
LPS _DEX_C	LPS_A	-0.004979645	0.019416499	0.836
LPS _DEX_C	LPS_B	-0.074584173	-0.050188029	0
LPS _DEX_C	LPS_C	-0.047882277	-0.023486133	0
LPS _DEX_C	LPS_D	-0.094090442	-0.069694297	0

LPS _DEX_C	LPS_E	-0.098315994	-0.073919849	0
LPS _DEX_C	LPS_F	0.07918998	0.103586124	0
LPS _DEX_C	No_stim_A	-0.011481996	0.012914149	1
LPS _DEX_C	No_stim_B	-0.075102292	-0.050706147	0
LPS _DEX_C	No_stim_C	-0.044446693	-0.020050548	0
LPS _DEX_C	No_stim_D	-0.098277466	-0.073881322	0
LPS _DEX_C	No_stim_E	-0.093137826	-0.068741681	0
LPS _DEX_C	No_stim_F	-0.059820049	-0.035423904	0
LPS _DEX_D	LPS _DEX_E	0.067447812	0.091843956	0
LPS _DEX_D	LPS _DEX_F	-0.009462928	0.014933216	1
LPS _DEX_D	LPS_A	0.066474947	0.090871092	0
LPS _DEX_D	LPS_B	-0.003129581	0.021266564	0.458
LPS _DEX_D	LPS_C	0.023572316	0.04796846	0
LPS _DEX_D	LPS_D	-0.022635849	0.001760295	0.207
LPS _DEX_D	LPS_E	-0.026861401	-0.002465257	0.00363
LPS _DEX_D	LPS_F	0.150644573	0.175040717	0
LPS _DEX_D	No_stim_A	0.059972597	0.084368742	0
LPS _DEX_D	No_stim_B	-0.003647699	0.020748446	0.572
LPS _DEX_D	No_stim_C	0.0270079	0.051404044	0
LPS _DEX_D	No_stim_D	-0.026822874	-0.002426729	0.0038
LPS _DEX_D	No_stim_E	-0.021683233	0.002712911	0.371
LPS _DEX_D	No_stim_F	0.011634544	0.036030688	1.49E-09
LPS _DEX_E	LPS _DEX_F	-0.089108812	-0.064712667	0
LPS _DEX_E	LPS_A	-0.013170936	0.011225208	1
LPS _DEX_E	LPS_B	-0.082775464	-0.05837932	0
LPS _DEX_E	LPS_C	-0.056073568	-0.031677424	0
LPS _DEX_E	LPS_D	-0.102281733	-0.077885589	0
LPS _DEX_E	LPS_E	-0.106507285	-0.082111141	0
LPS _DEX_E	LPS_F	0.070998689	0.095394833	0
LPS _DEX_E	No_stim_A	-0.019673287	0.004722858	0.794
LPS _DEX_E	No_stim_B	-0.083293583	-0.058897438	0
LPS _DEX_E	No_stim_C	-0.052637984	-0.02824184	0
LPS _DEX_E	No_stim_D	-0.106468757	-0.082072613	0
LPS _DEX_E	No_stim_E	-0.101329117	-0.076932973	0
LPS _DEX_E	No_stim_F	-0.06801134	-0.043615195	0
LPS _DEX_F	LPS_A	0.063739803	0.088135948	0
LPS _DEX_F	LPS_B	-0.005864725	0.01853142	0.941
LPS _DEX_F	LPS_C	0.020837171	0.045233316	0
LPS _DEX_F	LPS_D	-0.025370993	-0.000974849	0.0192
LPS _DEX_F	LPS_E	-0.029596545	-0.005200401	9.62E-05
LPS _DEX_F	LPS_F	0.147909428	0.172305573	0
LPS _DEX_F	No_stim_A	0.057237453	0.081633597	0
LPS _DEX_F	No_stim_B	-0.006382843	0.018013301	0.973
LPS _DEX_F	No_stim_C	0.024272755	0.0486689	0

LPS _DEX_F	No_stim_D	-0.029558018	-0.005161873	0.000102
LPS _DEX_F	No_stim_E	-0.024418378	-2.22E-05	0.049
LPS _DEX_F	No_stim_F	0.0088994	0.033295544	2.50E-07
LPS_A	LPS_B	-0.0818026	-0.057406456	0
LPS_A	LPS_C	-0.055100704	-0.030704559	0
LPS_A	LPS_D	-0.101308869	-0.076912724	0
LPS_A	LPS_E	-0.105534421	-0.081138276	0
LPS_A	LPS_F	0.071971553	0.096367698	0
LPS_A	No_stim_A	-0.018700422	0.005695722	0.926
LPS_A	No_stim_B	-0.082320719	-0.057924574	0
LPS_A	No_stim_C	-0.05166512	-0.027268975	0
LPS_A	No_stim_D	-0.105495893	-0.081099749	0
LPS_A	No_stim_E	-0.100356253	-0.075960108	0
LPS_A	No_stim_F	-0.067038476	-0.042642331	0
LPS_B	LPS_C	0.014503824	0.038899969	0
LPS_B	LPS_D	-0.031704341	-0.007308196	3.72E-06
LPS_B	LPS_E	-0.035929893	-0.011533748	1.82E-09
LPS_B	LPS_F	0.141576081	0.165972226	0
LPS_B	No_stim_A	0.050904105	0.07530025	0
LPS_B	No_stim_B	-0.012716191	0.011679954	1
LPS_B	No_stim_C	0.017939408	0.042335553	0
LPS_B	No_stim_D	-0.035891365	-0.011495221	1.97E-09
LPS_B	No_stim_E	-0.030751725	-0.00635558	1.70E-05
LPS_B	No_stim_F	0.002566052	0.026962197	0.00322
LPS_C	LPS_D	-0.058406237	-0.034010093	0
LPS_C	LPS_E	-0.062631789	-0.038235645	0
LPS_C	LPS_F	0.114874185	0.139270329	0
LPS_C	No_stim_A	0.024202209	0.048598354	0
LPS_C	No_stim_B	-0.039418087	-0.015021942	0
LPS_C	No_stim_C	-0.008762488	0.015633656	1
LPS_C	No_stim_D	-0.062593262	-0.038197117	0
LPS_C	No_stim_E	-0.057453621	-0.033057477	0
LPS_C	No_stim_F	-0.024135844	0.000260301	0.0633
LPS_D	LPS_E	-0.016423624	0.00797252	0.999
LPS_D	LPS_F	0.16108235	0.185478494	0
LPS_D	No_stim_A	0.070410374	0.094806519	0
LPS_D	No_stim_B	0.006790078	0.031186223	8.57E-06
LPS_D	No_stim_C	0.037445677	0.061841821	0
LPS_D	No_stim_D	-0.016385097	0.008011048	0.999
LPS_D	No_stim_E	-0.011245456	0.013150688	1
LPS_D	No_stim_F	0.022072321	0.046468465	0
LPS_E	LPS_F	0.165307902	0.189704046	0
LPS_E	No_stim_A	0.074635926	0.099032071	0
LPS_E	No_stim_B	0.01101563	0.035411775	5.02E-09

LPS_E	No_stim_C	0.041671229	0.066067373	0
LPS_E	No_stim_D	-0.012159545	0.0122366	1
LPS_E	No_stim_E	-0.007019904	0.01737624	0.992
LPS_E	No_stim_F	0.026297873	0.050694017	0
LPS_F	No_stim_A	-0.102870048	-0.078473903	0
LPS_F	No_stim_B	-0.166490344	-0.142094199	0
LPS_F	No_stim_C	-0.135834745	-0.111438601	0
LPS_F	No_stim_D	-0.189665519	-0.165269374	0
LPS_F	No_stim_E	-0.184525878	-0.160129734	0
LPS_F	No_stim_F	-0.151208101	-0.126811956	0
No_stim_A	No_stim_B	-0.075818368	-0.051422224	0
No_stim_A	No_stim_C	-0.04516277	-0.020766625	0
No_stim_A	No_stim_D	-0.098993543	-0.074597398	0
No_stim_A	No_stim_E	-0.093853903	-0.069457758	0
No_stim_A	No_stim_F	-0.060536125	-0.036139981	0
No_stim_B	No_stim_C	0.018457526	0.042853671	0
No_stim_B	No_stim_D	-0.035373247	-0.010977102	5.41E-09
No_stim_B	No_stim_E	-0.030233607	-0.005837462	3.75E-05
No_stim_B	No_stim_F	0.003084171	0.027480315	0.0017
No_stim_C	No_stim_D	-0.066028846	-0.041632701	0
No_stim_C	No_stim_E	-0.060889205	-0.036493061	0
No_stim_C	No_stim_F	-0.027571428	-0.003175283	0.00151
No_stim_D	No_stim_E	-0.007058432	0.017337713	0.993
No_stim_D	No_stim_F	0.026259345	0.05065549	0
No_stim_E	No_stim_F	0.021119705	0.04551585	0

LPS: 1 mg mL$-$1 LPS treatment

LPS_DEX: 1 mg mL$-$1 LPS with 200 µM Dex treatment

No_stim: No treatment

A~F: The sample IDs

LIST OF PUBLICATIONS

Journal papers

[1] **Yang, J.,** Hirai, Y., Iida, K., Ito, S., Trumm, M., Terada, S., Sakai, R., Tsuchiya, T., Tabata, O. and Kamei, K.I., (**2023**). Integrated gut–liver-on-a-chip platform as an in vitro human model of non-alcoholic fatty liver disease. *Communications biology*. Under review

<div align="center">

Pre-print available in *BioRxiv* / Completed Minor Revision Chapter 4

</div>

[2] **Yang, J.**, Imamura, S., Hirai, Y., Tsuchiya, T., Tabata, O., & Kamei, K. I. (**2022**). Gut-liver-axis microphysiological system for studying cellular fluidic shear stress and inter-tissue interaction. *Biomicrofluidics*, *16*(4), 044113

<div align="center">

Featured article / The cover of Journal / AIP Scilight reported paper Chapter 5

</div>

[3] Zhang, D., **Yang, J.,** Hirai, Y., Kamei, K. I., Tabata, O., & Tsuchiya, T. (2022). Microfabrication of polydimethylsiloxane–parylene hybrid microelectrode array integrated into a multi-organ-on-a-chip. *Japanese Journal of Applied Physics*. 62, 017002

<div align="center">

Contribute to the analytical analysis, chip fabrication, and experiment Chapter 3

</div>

[4] **Yang, J.**, Hirai, Y., Tsuchiya, T., Tabata, O., & Kamei, K. I. Characterize the flow volume generated by a PDMS-based pneumatic micropump consisting of three circular diaphragms.

<div align="center">

Under manucript prepartion Chapter 3

</div>

[5] Yoshimoto, K., Minier, N., **Yang, J.,** Imamura, S., Stocking, K., Patel, J., ... & Kamei, K. I. (2020). Recapitulation of Human Embryonic Heartbeat to Promote Differentiation of Hepatic Endoderm to Hepatoblasts. *Frontiers in bioengineering and biotechnology*, 1064.

<div align="center">

Contribute to the finite element analysis

</div>

International conferences and papers

[1] **Yang, J.,** Imamura, S., Hirai, Y., Kamei, K.I., Tsuchiya, T. and Tabata, O., 2021, June. Multilayered Microfluidic Device for Controllable Flow Perfusion of Gut-Liver on a Chip. In *2021 21st International Conference on Solid-State Sensors, Actuators and Microsystems (Transducers)* (pp. 176-179). IEEE. (**Oral presentation and paper**)

[2] Miyazaki, T., **Yang, J.,** Imamura, S., Hirai, Y., Kamei, K.I., Tsuchiya, T. and Tabata, O., 2021, January. Highly Accurate Measurement of Trans-Epithelial Electrical Resistance in Organ-on-a-Chip. In *2021 IEEE 34th International Conference on Micro Electro Mechanical Systems (MEMS)* (pp. 411-414). IEEE. (**Oral presentation and paper)**

[3] **Yang, J.,** Hirai, Y., Kamei, K.I., Trumm, M., Tsuchiya, T. and Tabata, O., 2020. In Vitro Modeling of Non-Alcoholic Fatty Liver Disease by Integrated Gut-Liver on a Chip. The 2020 MRS Spring/Fall Meeting and Exhibit, Online. (**Oral presentation**)

[4] **Yang, J.,** Hirai, Y., Kamei, K.I., Trumm, M., Tsuchiya, T. and Tabata, O., 2019, October. Integrated Gut-Liver on a Chip for Modelling Non-Alcoholic Fatty Liver Disease in vitro. The 23rd International Conference on Miniaturized Systems for Chemistry and Life Sciences (MicroTAS 2019) (pp. 376-377). (**Poster**)

Domestic conference

[1] 楊 建東, 今村 聡, 平井 義和, 亀井 謙一郎, 土屋 智由, 田畑 修. 2021. Gut liver on a chip with controllable flow perfusion via multilayered microfluidic device. 第 38 回「センサ・マイクロマシンと応用システム」シンポジウム. (**Oral presentation**)

[2] 亀井 謙一郎, 楊 建東, 飯田 慶, 寺田 志穂, 土屋 智由, 田畑 修, 平井 義和. 2020. 非アルコール性脂肪性肝疾患を再現する肝臓-小腸・オン・チップ. 「化学とマイクロ・ナノシステム学会」第 42 回研究会(Cheminas42). (**Poster**)

[3] **Yang, J.,** Hirai, Y., Kamei, K.I., Tsuchiya, T. and Tabata, O., 2019, October. A microfluidic gut-liver on a chip for modeling the non-alcoholic fatty liver disease. 「化学とマイクロ・ナノシステム学会」第 40 回研究会(Cheminas40). (**Poster**)

Award

[1] 2021 年 11 月 第 38 回センサ・マイクロマシンと応用システムシンポジウム 奨励賞

ACKNOWLEDGEMENTS

This is the sixth year of my Ph.D. study. During these six years, I have encountered many difficulties and hardships. With everyone's help, I can overcome and finally come to the end of graduation. I would like to express my deepest gratitude to my family, supervisor, tutors, friends, and classmates.

First, I want to give my deep thanks to my supervisor, Prof. Tsuchiya. Within the past six years, Sensei has given me a lot of help and encouragement. My research is related to cell culture experiments. It took a quite long time for one period of the experiment. Sensei understood my situation and give me advice for my research progress. Especially, from the viewpoint of microfabrication and mechanical engineering, Sensei gave me a lot of useful ideas to make great works on chip designs, fabrication, and evaluation. Sensei's deep insight, open mind, and positive attitude to academic research set an excellent example for my future academic career.

I would like to express my sincere thanks to Prof. Tabata. Tabata-Sensei gave me the chance to study in Japan and help me get the MEXT scholarship. I could focus on my research. During my doctoral studies, Sensei gave me a lot of support to polish my research proposal and research papers. Also, in daily life, Sensei helps me adapt to study and life in Japan.

I'm extremely grateful for the help of Prof. Kamei. At the beginning of my Ph.D. study, I did not know about cell biology. Kamei-Sensei gave me the chance to open a new world to my research life. It is a research field with unlimited possibilities. Sensei not only guided me in my research but also taught me how to conduct basic biological experiments. During the research progress, Sensei gave me great support from the research proposal, experiment plan to paper writing.

I would like to express my deepest thanks to Prof. Hirai. Hirai-Sensei has supported my whole Ph.D. research and life. For the research, Sensei helps me organize the research proposal and plan. Sensei help me improve the quality of my presentation and papers, so I could have excellent achievements for academic conferences and papers. For daily life, Sensei gave me research assistant opportunities to cover my daily expenses during my scholarship expiration. Also, Sensei help me solve a lot of troubles related to lectures and problems of living in Japan.

I would like to thank Prof. Hirotani and Prof. Amit for their comments and questions during the lab seminar. I am extremely grateful for the help from Dr. Imamura, Terada-San, and Yoshimoto-San for their kind support of the biological experiment. I am very grateful to Prof. Iida for his help of RNA-sequencing data analysis and suggestions.

I want to acknowledge my Ph.D. committee, Prof. Yokokawa and Prof. Adachi. They generously provided their valuable time and patience to review my thesis and offer me valuable advice that greatly helped to refine this thesis and my future research.

PERMISSIONS FROM PUBLISHER

Chapter 3: Author using for thesis. Paper from' Dongxiao Zhang, **<u>Jiandong Yang</u>**, Yoshikazu Hirai, Ken-ichiro Kamei, Osamu Tabata, and Toshiyuki Tsuchiya. Microfabrication of polydimethylsiloxane–parylene hybrid microelectrode array integrated into a multi-organ-on-a-chip. Japanese Journal of Applied Physics 62, no. 1 (2022): 017002.', '© IOP Publishing. Reproduced with permission. All rights reserved.'

Chapter 4: Author using for thesis. Material from: '**<u>Jiandong Yang</u>**, Yoshikazu Hirai, Kei Iida, Shinji Ito, Marika Trumm, Shiho Terada, Risako Sakai, Toshiyuki Tsuchiya, Osamu Tabata, and Ken-ichiro Kamei. Integrated gut–liver-on-a-chip platform as an in vitro human model of non-alcoholic fatty liver disease. *Communications biology*.' [2023].

Chapter 5: Author using for thesis. 'Reproduced from [**<u>Jiandong Yang</u>**, Satoshi Imamura, Yoshikazu Hirai, Toshiyuki Tsuchiya, Osamu Tabata, and Ken-ichiro Kamei. Gut-liver-axis microphysiological system for studying cellular fluidic shear stress and inter-tissue interaction. *Biomicrofluidics* 16, no. 4 (2022): 044113], with the permission of AIP Publishing'